NUMERICAL STUDY OF NONLINEAR SLOSHING AND ITS COUPLING WITH VESSEL MOTIONS

by

Chongwei Zhang

A thesis submitted for the degree of

Doctor of Philosophy

Department of Mechanical Engineering

University College London

2016

Declaration

I, Chongwei Zhang, confirm that the work presented in this thesis is my own. Where information has been derived from other sources, I confirm that this has been indicated in the thesis.

Signature: 

Date: Jun 1st, 2016

Abstract

The FLNG (floating liquefied natural gas) facility is a new ocean engineering application, proposed to exploit natural gas reserves under the sea bed. It is considered as a giant floating vessel with several huge tanks. This study aims to investigate two hydrodynamic problems related to the FLNG facility, i.e. nonlinear sloshing in liquid tanks and its coupling with vessel motions, within the potential-flow theory. The main body of the research contains three parts.

The first part considers the sloshing in wall-sided FLNG tanks. Nonlinear boundary conditions satisfied on the instantaneous free surface are considered. In-house FORTRAN codes based on paralleled BEM are developed for sloshing simulations. The numerical scheme is verified through the simulation of a series of classical sloshing problems. Particularly, a distinct resonance (i.e. second-order resonance) is observed in 3D rectangular tanks, which suggests that the resonant sloshing does not have to be triggered at the natural frequency.

In the second part, a design of FLNG vessel with wedged tanks is proposed, aiming to avoid the dangerous simultaneous occurrence of sloshing resonance in all tanks. A BEM-based approach is developed to numerically predict resonance conditions of these wedged tanks. Then, two types of sloshing resonances, i.e. the classical resonance and Faraday waves, in wedged tanks are investigated. In particular, an improved semi-Lagrangian procedure is introduced to accurately track the nonlinear free-surface motion near non-vertical tank walls.

In the third part, an analytical solution for the coupling between the vessel motion and liquid sloshing in multiple tanks is firstly derived. A method to determine natural frequencies of the coupling system is also given. The dynamic properties of the system are studied systematically. Then, time-domain simulations of floating vessels with nonlinear sloshing tanks are performed. An extended modal decomposition method is derived to decouple the motions of the floating vessel, external waves and sloshing liquids. The dynamic properties of the FLNG model is also investigated.

Acknowledgement

I wish to express my sincere gratitude to all the people that encouraged me to work on this subject and supported me over the past years.

First of all, I would like to thank my primary supervisor, Prof. Guo Xiong Wu. His rigorous academic attitude, sense of responsibility, logical way of thinking and caring heart on students have left a deep mark in my mind. He always provided me with valuable guidance, pathbreaking advice, and great freedom, which has helped me grow quickly and obtain the independent research ability.

I am so grateful to Dr Stavroula Balabani from UCL and Dr Qing Xiao from University of Strathclyde. They have carefully read the full thesis and given invaluable suggestions on how to amend this thesis in every detail. Many thanks also go to Prof. Giles Thomas, Dr. Mark Selfridge and Dr. Yuriy Semenov who also carefully read some part of my thesis and gave precious suggestions.

I would also like to thank my colleagues, Dr. Guodong Xu, Baoyu Ni, Zhen Wang and Mashujin Lai, Miss. Bingyue Song, Yajie Li and Dongni Yan, Mr. Qicheng Meng and Kang Ren. We have shared so many happy times together, which helps me remain positive at any time. I wish to express deep love to my dear wife, Tingting Li, whose endless understanding and encouragement supported me to come this far. My gratitude also goes to my parents whose everlasting love and prayers made my life path possible.

I gratefully acknowledge China Scholarship Council (CSC) (No. 201206680001) and Lloyd's Register Foundation (LRF) through the joint centre involving University College London, Shanghai Jiao Tong University and Harbin Engineering University for the financial support during my study in UCL.

Table of content

List of figures

List of tables

Symbols and nomenclature

A	wave amplitude
A_x, A_y, A_z	excitation amplitude in x, y and z direction
A_{Rij}	added-mass coefficient in impulse response function method
$\tilde{A}_{Rij}(\omega)$	added-mass of vessel in frequency domain
B	tank width
B_B	width of vessel
$B_{Rij}(\tau)$	retardation function
$\tilde{B}_{Rij}(\omega)$	damping coefficient of vessel in frequency domain
$C(t)$	function of time
$[C]$	matrix of restoring coefficients
E_K	kinetic energy of fluid
E_P	potential energy of fluid
$\mathbf{F}$	force acting on vessel
$\mathbf{F}_B$	restoring force acting on vessel
$\mathbf{F}_D$	wave diffraction force acting on vessel
$\mathbf{F}_d$	force acting on vessel from external domain
$\mathbf{F}_I$	Froude-Krylov force
$\mathbf{F}_{Rj}$	radiation force due to the j-th mode of vessel motion

$\mathbf{F}_s$	sloshing-induced force acting on vessel
$\mathbf{F}_e$	extra force acting on vessel
$G(\mathbf{x}_p, \mathbf{x})$	Green's function
H	initial liquid depth in tank
$\mathbf{H}$	angular momentum of vessel
H_B	draft of vessel
H_t	tank height
$[I]$	matrix of moment of inertia of vessel
$J(\xi, \varsigma)$	Jacobian matrix of transformation
K	number of vertexes on each element
L	tank length
L_B	length of vessel
L_l	free-surface length in tank
$\mathbf{M}$	moment acting on vessel
$[M]$	mass matrix
M_1, M_2 and M_3	number of elements along length, width and depth tank edge
N	number of liquid tanks
N_a	number of boundary elements on free surface
N_b	number of boundary elements on tank walls and bottom
N_{dri}	number of drive tanks

N_e	number of boundary elements
$N_k(\xi,\varsigma)$	k -th shape function of the boundary element
N_p	number of boundary nodes
N_{res}	number of response tanks
$O-xyz$	body-fixed coordinate system
$O'-x'y'z'$	local coordinate system
$O_1-x_1y_1z_1$, $O_2-x_2y_2z_2$ and $O_3-x_3y_3z_3$	intermediary systems for definition of Euler angles
$O_o-x_oy_oz_o$	earth-fixed coordinate system
R	radius
S	fluid boundary surface
S_B	body surface
$\overline{S}_B$	mean body surface
S_C	open boundary
S_D	sea bed
S_e	boundary element with index e
S_e'	2D mapped area of S_e
S_F	free surface
$\overline{S}_F$	mean free surface

T	excitation period
T_{ramp}	ramp time
$[T]$	transformation matrix between coordinate systems
U_g	gravity potential
V	fluid volume
$\widehat{V}$	vessel displacement volume
Z	implicit shape expression of free surface
a_j	coefficients for surface fitting
$c(\mathbf{x}_p)$	solid angle at collocation point
c_i	solid angle at i-th boundary node
$\mathbf{e}_x$, $\mathbf{e}_y$ and $\mathbf{e}_z$	unit vectors in the x, y and z direction
g	gravitational acceleration
$\mathbf{i}_o$, $\mathbf{j}_o$ and $\mathbf{k}_o$	unit vectors in x_o, y_o and z_o direction
k_n	wave number
m	mass of vessel
m_L	mass of liquid
$\mathbf{n}$	unit normal vector on boundary pointing outward the fluid
p	pressure
p_o	atmospheric pressure
$\mathbf{r}$	position vector of a point in body-fixed coordinate system
$\mathbf{r}_c$	position vector of origin of body-fixed coordinate system

t	time
Δt	time step
$\mathbf{v} = \{v_{xo}, v_{yo}, v_{zo}\}$	fluid velocity
$\hat{\mathbf{v}}$	velocity of 'sensor' on free surface
$\mathbf{v}_c = \{v_1, v_2, v_3\}$	translation velocity of vessel
$w(\mathbf{x}_n - \mathbf{x}_0)$	weight function between point $\mathbf{x}_0$ and $\mathbf{x}_n$
$\mathbf{x}$	position vector of a point
$\hat{\mathbf{x}}$	displacement of 'sensor' on free surface
$\{x_c, y_c, z_c\}$	coordinates of origin of body-fixed system
$\{x_k, y_k, z_k\}$	coordinates of the k-th node of a boundary element
$\mathbf{x}_p = \{x_p, y_p, z_p\}$	collocation point
z_b	centre of buoyancy
z_f	free-surface height in body-fixed coordinate system
Θ	maximum pitching angle
$\boldsymbol{\Omega} = \{\Omega_x, \Omega_y, \Omega_z\}$	angular velocity of vessel rotation
$\dot{\boldsymbol{\Omega}}$	angular acceleration of vessel rotation
α_1, α_2 and α_3	Euler angles
δ_j^i	Kronecker delta function
ε	a small parameter
$\varepsilon(e,k)$	global index of the k-th vertex on the e-th element

$\xi-\varsigma$	2D parametric plane
η	free-surface elevation in body-fixed coordinate system
η_{ini}	initial free-surface elevation
η_o	free-surface elevation in earth-fixed coordinate system
θ	incline angle of tank wall
ρ	liquid density
ρ_v	material density of vessel
τ	nondimensionalized time
$\tau_{disturb}$	time duration of initial disturbance
ϕ	disturbance velocity potential
$\overline{\phi}$	natural sloshing mode
φ	velocity potential
φ_t	partial time derivative of φ
γ_{ramp}	ramp function
χ	auxiliary function
ω	angular frequency
ω_a	frequency of incident waves
ω_{mn}	natural sloshing frequencies in 3D rectangular tank
ω_n	natural sloshing frequencies in 2D tanks
ω_v	natural frequency of vessel oscillation

ω_x, ω_y and ω_z	excitation frequency of surge, sway and heave

Operator

∇_o	gradient operator of scalar in earth-fixed coordinate system
∇	gradient operator of scalar in body-fixed coordinate system
$\partial/\partial t$	partial time derivative
$\nabla_o \times$	curl operator of vector in earth-fixed coordinate system
∇_o^2	Laplace's operator in earth-fixed coordinate system
∇^2	Laplace's operator in body-fixed coordinate system
D/Dt	material derivative, defined as $D/Dt = \partial/\partial t + \hat{\mathbf{v}} \cdot \nabla_o$
$\lvert\cdots\rvert$	modulus of vector
$[\cdots]^{-1}$	matrix inverse
$[\cdots]^t$	matrix transpose

Abbreviation

2D	two-dimensional
3D	three-dimensional
ALE	arbitrary-Lagrangian-Eulerian
BEM	boundary element method
BIE	boundary integral equation
BVP	boundary value problem
CCR	characteristic circumcircle radius
CIP	constraint interpolation profile

CFD	computational fluid dynamics
CL	characteristic length
CPU	computer processing unit
DoF	degree of freedom
FDM	finite difference method
FEM	finite element method
FFT	fast Fourier transform
FLNG	floating liquefied natural gas
FK	Froude-Krylov
FVM	finite volume method
GMRES	generalised minimal residual
IRF	impulse-response function
LBIE	local boundary integral equation
LES	large-eddy-simulation
LNG	liquefied natural gas
LPG	liquefied petroleum gas
MEL	mixed-Eulerian-Lagrangian
MLS	moving least square
MLPG	meshless local Petrov-Galerkin
MPI	message passing interface
MPS	moving particle semi-implicit
NASA	National Aeronautics and Space Administration

NS	Navier-Stokes
NTNU	Norwegian University of Science and Technology
PC	personal computer
PSM	pseudo-spectral method
RAO	response amplitude operator
SL	semi-Lagrangian
SPH	smoothed particle hydrodynamics
TLD	tuned liquid damper
VOF	volume-of-fluid

Chapter 1 Introduction

1.1 Background and motivation

The liquid sloshing, which means the free-surface motion inside a tank, has been investigated for a long time. The work of Faraday (1831) which concerns the liquid motion in a vertically oscillating tank is probably the earliest research on the sloshing subject. After that, scattered sloshing-related literature gradually emerges in academia (e.g. Lamb 1945). From the middle of the twentieth century, sloshing problems start to become one of the primary interests in various engineering areas. For example, since the early 1960s, fuel sloshing effects on space flights have become a major concern of aerospace engineers (Abramson 1966), while civil engineers and seismologists have been focusing on the earthquake-induced liquid sloshing in a large dam, onshore fuel storage tank, elevated water tower and tuned liquid damper (TLD, a type of liquid tanks installed on the top of high buildings to control the wind-induced oscillation) (Ibrahim 2005). Then, in the marine engineering, researchers have been paying attention to the sloshing effects in anti-roll tanks (Faltinsen and Timokha 2009). Within the recent two decades, the sloshing problems are raised in a new ocean engineering application, the floating liquefied natural gas (FLNG) facility.

Some background about the FLNG facility is firstly introduced here. It is known that the natural gas with environmental advantages over other fossil fuels has become increasingly significant in meeting the world's energy needs (IGU 2014). However, a great proportion of the present natural gas reserves is located below the bed of the deep sea. To overcome the exploitation difficulties, the design of the FLNG facility has been proposed. Many existing designs have taken the FLNG facility as a giant floating vessel (e.g. Fig. 1.1) moored above an offshore natural gas field. During the operation, the natural gas is chilled onboard into the liquefied natural gas (LNG) at -161 degree Celsius with approximately 1/600 the volume of its gaseous state, and stored in several huge tanks below the deck. Then, the produced LNG is offloaded to LNG carriers and transported to the land. It should be noted that there are not

FLNG systems actually in operation at present. Although the world's first FLNG facility (i.e. the 488m long 'Prelude') has started its construction, most of the FLNG projects are still on paper. Identification and subsequent mitigation of the high technical, commercial, and execution risks are the keys to make them real.

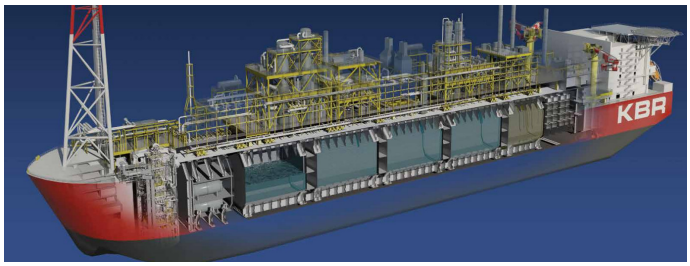

Fig. 1.1 A concept of FLNG facility (KBR 2016)

Unless docking for inspection and overhaul is required, the FLNG is continuously moored at the location for around 20-25 years. Thus, it could experience various complex sea states with any fill in the tanks during the period of service. Unlike oil, chemical or liquefied petroleum gas (LPG) vessel tanks that have internal structures to suppress the liquid sloshing, the LNG tanks have a clear internal surface. This is because, the tank surface is covered by the leakage-proof invar membrane (0.7mm), and it is not allowed to weld barriers or bulkheads through the fragile membrane in order to stand the extreme temperature and pressure. Thus, the vessel motion induced by external ocean waves could easily cause the violent liquid sloshing in partly filled tanks. Instantaneously, the massive liquid would react on the vessel and affect its motion in return. The vessel motion characteristics are closely related to the operation safety on board. However, the interaction mechanism among external waves, vessel motions, and sloshing liquids is still unclear, and presents a technical risk. What makes the problem more complicated is that even the nonlinear sloshing itself has not been systematically understood yet.

So, this thesis will investigate the nonlinear sloshing and its coupling with vessel motions, aiming to provide a deeper understanding of their mechanism. The investigations are mainly based on the numerical methods.

1.2 Outline of this study

Chapter 2 gives the mathematical equations used to describe the vessel motion, external flow, and liquid sloshing. These equations would be referred to frequently in later chapters. Chapter 3 to 11 form the main body of the research, which comprises three parts. Then, Chapter 12 draws conclusions and gives suggestions for the future work.

- **Part I (Chapter 3, 4 and 5): Sloshing in wall-sided tank**

Wall-sided tanks are normally considered for the benchmark test of sloshing simulations. By 'wall-sided' here, it means that the still free surface is perpendicular to tank walls. Aiming at the present application background, the term 'wall-sided' is specifically used to indicate 3D rectangular tanks.

Chapter 3 firstly reviews the popular methods that are used in the literature for sloshing simulations. Considering the scope of the objective, this thesis prefers to develop the in-house numerical scheme for nonlinear sloshing simulations, based on the 3D boundary element method (BEM).

Chapter 4 describes the technical details of the numerical scheme and then simulates a series of classical sloshing problems. The convergence and accuracy of the numerical scheme are verified. Comparisons with experiments are also performed to validate the mathematical model.

Chapter 5 further uses the developed numerical scheme to investigate a distinct sloshing resonance phenomenon, the 'second-order resonance'. This chapter aims to verify its existence in 3D rectangular tanks and observe its look.

- **Part II (Chapter 6, 7 and 8): Sloshing in non-wall-sided tank**

The FLNG vessel normally adopts wall-sided LNG tanks to efficiently utilise the internal space of the vessel hull. These tanks have similar dimensions and are filled to a similar level for the load balance. So, the liquid in each tank has similar natural sloshing frequencies. This suggests that, under certain ocean wave excitations, the sloshing resonance could occur simultaneously in all tanks, which would be one of the most dangerous situations in practice. In order to mitigate this risk, this part proposes an

alternative design. The wall-sided tanks are replaced with various wedged ones as in Fig. 1.2. This design could diversify natural sloshing frequencies in different tanks, without changing the total capacity of the tanks. Then, even though the resonance occurs in one tank, the sloshing in remaining tanks might still be gentle. The resultant sloshing effects on the vessel motions are expected to be much smaller.

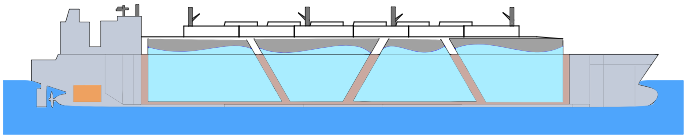

Fig. 1.2 Design of FLNG vessel with wedged tanks

Before verifying the effectiveness of the design, sloshing properties in 3D wedged tanks have to be identified.

Chapter 6 concerns the resonance conditions of the sloshing in these wedged tanks. A numerical approach with the help of BEM is developed to systematically investigate the natural sloshing frequencies and corresponding modes for wedged tanks.

To simulate the nonlinear sloshing in wedged tanks, the free-surface updating near non-vertical tank walls has to be dealt with. However, the traditional semi-Lagrangian (SL) procedure adopted in Part I is only available for wall-sided tanks. So, Chapter 7 specially develops an 'improved semi-Lagrangian procedure' to track the free-surface motion near non-vertical tank walls. It avoids the 'vertical-wall' limitation of the SL procedure. The accuracy of this procedure is verified through the result comparison with the open source CFD software OpenFOAM.

Then in Chapter 8, the resonant sloshing in wedged tanks is simulated. Two types of resonance are mainly considered. One is the classical resonance, which is induced by a lateral excitation on the tank. The other type is the Faraday waves due to the instability when the tank oscillates perpendicular to the undisturbed free surface plane. Featured sloshing phenomena in wedged tanks are observed, compared with those in rectangular tanks.

- **Part III (Chapter 9, 10 and 11): Coupling of sloshing and vessel**

motion

In this part, free vessel motions are taken into account.

Chapter 9 considers the multiple-tank vessel that moves freely on the horizontal plane. The vessel is only excited by the liquid sloshing in tanks. The analytical solution for this coupling problem is derived. Systematical analyses are performed to study the effect of the vessel mass, number of tanks, tank configuration, and free-surface deformation on the vessel motion, liquid sloshing, and mechanical energy components of the system.

Chapter 10 further takes the seakeeping problem (i.e. the interaction between the floating vessel and ocean waves) into account. An extended modal decomposition method is derived to decouple the seakeeping and sloshing problems. Using this method, the vessel's acceleration at any instant could be calculated explicitly in one step without iterations, which could greatly reduce the CPU consumption. A potential-flow numerical scheme based on this method is developed, which simulates the seakeeping and sloshing problems using the impulse-response function (IRF) and boundary element method, respectively.

In Chapter 11, the numerical scheme developed in Chapter 10 is firstly verified and validated through the comparison with analytical solutions and experimental measurements. Then, the sloshing effects on vessel motions are analysed in detail. Examples of the FLNG vessel are further simulated. The effectiveness of the designed FLNG vessel with wedged tanks is also verified.

1.3 Contributions to existing literature

The bulk of the thesis has been published in the following journal papers:

- Zhang, Chongwei*, Li, Yajie, Meng, Qicheng, 'Fully nonlinear analysis of second-order sloshing resonance in a three-dimensional tank', Computers & Fluids, 2015, 116: 88-104.
- Zhang, Chongwei*, 'Analysis of liquid sloshing in LNG carrier with wedge-shaped tanks', Ocean Engineering, 2015, 105: 304-317.
- Zhang, Chongwei*, 'Application of an improved semi-Lagrangian

procedure to fully-nonlinear simulation of sloshing in non-wall-sided tanks', Applied Ocean Research, 2015, 51: 74-92.

- Zhang, Chongwei*, 'Nonlinear simulation of resonant sloshing in wedged tanks using boundary element method', Engineering Analysis with Boundary Elements, 2016, 69: 1-20.
- Zhang, Chongwei*, 'Analytical study of transient coupling between vessel motion and liquid sloshing in multiple tanks', Journal of Engineering Mechanics (ASCE), 2016, 142: 04016034.
- Meng, Qicheng*, Zhang, Chongwei, 'A third-order KdV solution for internal solitary waves and its application in the numerical wave tank', Journal of Ocean Engineering and Science, 2016, 1: 93-108.
- Li, Yajie, Zhang, Chongwei*, 'Analysis of wave resonance in gap between two heaving barges', Ocean Engineering, 2016, 117: 210–220.

Chapter 2 Mathematical equations

2.1 Introduction

In this chapter, the mathematical equations used in later chapters are firstly given. An illustration of the problem under investigation is shown in Fig.2.1. This system is composed of three elements: the floating vessel, external ocean domain and sloshing liquid in the tank. Two types of Cartesian coordinate systems are defined: one is the earth-fixed coordinate system $O_o - x_o y_o z_o$ with z_o-axis pointing vertically upward; the other is the body-fixed coordinate system $O - xyz$ with O located at the mass centre of the vessel. The body-fixed system could undergo both translational and rotational motions with respect to the earth-fixed system. Initially, these two coordinate systems are coincident with each other.

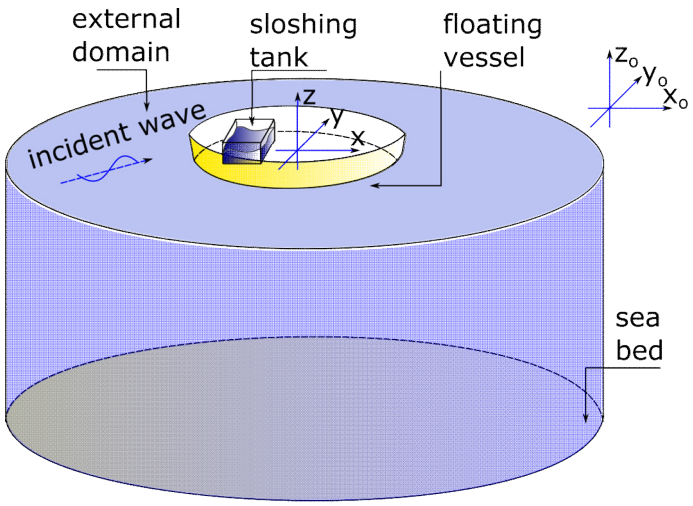

Fig. 2.1 Problem sketch and coordinate systems

This thesis will focus on the global liquid motion without considering the local phenomena (e.g. wave slamming, the formation of air pocket and gas-bubbles, wave breaking, the vibration of the elastic tank wall, and so on). Considering this large floating vessel, the potential-flow theory conventionally used for marine hydrodynamics is also adopted here to describe the external flow. For the sloshing problem, the interior of the tank is smooth. So the fluid viscous effects are limited to a 'boundary layer' close to the tank surface,

outside which the flow can be considered to be frictionless and irrotational. Since the sloshing flow is usually at a high Reynolds number, the boundary layer's thickness becomes very small compared to the dimensions of the tank, so that the presence of the boundary layer is negligible and the sloshing domain could also be regarded as the potential-flow region. Thus, both the external and sloshing flows are treated as potential flows by assuming the fluid to be inviscid, incompressible and flow-irrotational.

2.2 Vessel motions

2.2.1 Mathematical equations

The floating vessel is idealised to be rigid. According to Chasles' theorem, the general motion of a rigid body could be described as a translation of its mass centre plus a rotation about the mass centre. For a 3D unconstrained vessel, six equations of motions could be obtained. These motion equations include three 'Newton equations' and three 'Euler equations'

The Newton equations are determined by the Newton's second law. In the earth-fixed coordinate system $O_o - x_o y_o z_o$, the equation has the form

$$\frac{d\left(m\mathbf{v}_c\right)}{dt} = \mathbf{F}_o \tag{2.1}$$

where m is the vessel mass, $\mathbf{v}_c$ is the velocity of mass centre and $\mathbf{F}_o$ is the resultant force acting on the vessel. In this thesis, the subscript $_o$ is used to indicate a variable expressed in $O_o - x_o y_o z_o$. Since the origin O is fixed at the mass centre, this equation has defined the motion of O.

The Euler equations are determined by the conservation of the angular momentum about O. The rotational motion of the vessel could be described in the earth-fixed coordinate system as

$$\frac{d\mathbf{H}_o}{dt} = \mathbf{M}_o \text{ with } \mathbf{H}_o = \left[I\right]_o \boldsymbol{\Omega}_o \tag{2.2}$$

where $\boldsymbol{\Omega}_o$ is the angular velocity of $O-xyz$ about O, $\left[I\right]_o$ is a matrix related to the moment of inertia of the vessel, $\mathbf{H}_o$ is the angular momentum and $\mathbf{M}_o$ is the moment of forces. Note that the direction of $\mathbf{H}_o$ and $\boldsymbol{\Omega}_o$ are

usually not the same. The $[I]_o$ is a (3×3) matrix which describes the mass distribution of the vessel. It has the form

$$[I]_o = \begin{pmatrix} I_{xx} & I_{xy} & I_{xz} \\ I_{yx} & I_{yy} & I_{yz} \\ I_{zx} & I_{zy} & I_{zz} \end{pmatrix} \tag{2.3}$$

Assume that ρ_v is the material density at the position $\{x_o, y_o, z_o\}$ of the vessel. The elements of $[I]_o$ could be calculated by

$$\begin{aligned} &I_{xx} = \iiint \rho_v \left(y_o^2 + z_o^2\right) dV \,;\, I_{yy} = \iiint \rho_v \left(x_o^2 + z_o^2\right) dV \,; \\ &I_{zz} = \iiint \rho_v \left(x_o^2 + y_o^2\right) dV \,;\, I_{xy} = I_{yx} = \iiint \rho_v x_o y_o dV \,; \\ &I_{yz} = I_{zy} = \iiint \rho_v y_o z_o dV \,;\, I_{xz} = I_{zx} = \iiint \rho_v x_o z_o dV \end{aligned} \tag{2.4}$$

Here, I_{xx}, I_{yy} and I_{zz} are moments of inertia about the coordinate axes, while the remaining elements are called products of inertia. Notice that, even for the same vessel, different orientations would generally lead to a different $[I]_o$. In other words, as the vessel rotates, the $[I]_o$ varies with time, i.e.

$$\frac{d\mathbf{H}_o}{dt} = \frac{d[I]_o}{dt}\boldsymbol{\Omega}_o + [I]_o \frac{d\boldsymbol{\Omega}_o}{dt} \tag{2.5}$$

In practice, it is very inefficient to calculate $[I]_o$ at each instant. However, if the rotation is considered in the body-fixed system, the moment of inertia would be independent of time. In the body-fixed system, Euler equations could be written as

$$\frac{d\mathbf{H}}{dt} = [I]\frac{d\boldsymbol{\Omega}}{dt} + \boldsymbol{\Omega} \times \left([I]\boldsymbol{\Omega}\right) = \mathbf{M} \tag{2.6}$$

With a proper choice of the body-fixed system, all products of inertia could become zero and the matrix of moments of inertia could become diagonal. In this situation, the diagonal elements are called principal moments, and axes of the body-fixed system are called principal axes.

2.2.2 Orientation of the body-fixed system

The position and orientation of the body-fixed system $O-xyz$ could be obtained through four steps of operations on the earth-fixed system $O_o-x_oy_oz_o$ as in Fig.2.2.

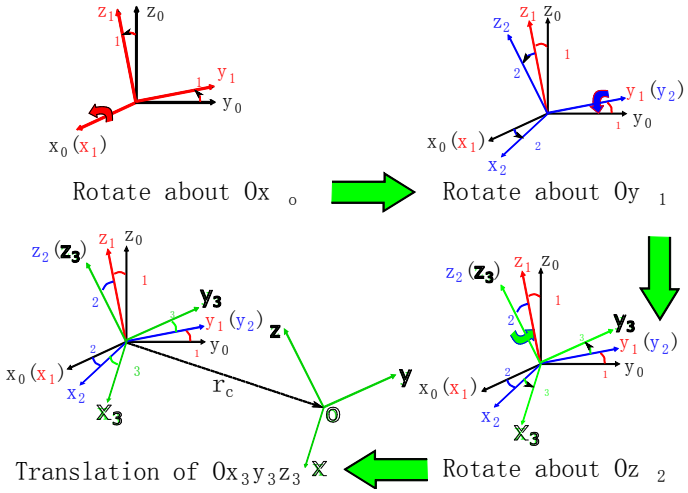

Fig. 2.2 Definition of Euler angles

In the first step, $O_o-x_oy_oz_o$ is rotated by an angle α_1 about the x_o-axis. The resultant system $O_1-x_1y_1z_1$ is expressed as:

$$\begin{Bmatrix} x_0 \\ y_0 \\ z_0 \end{Bmatrix} = \begin{bmatrix} 1 & 0 & 0 \\ 0 & \cos\alpha_1 & -\sin\alpha_1 \\ 0 & \sin\alpha_1 & \cos\alpha_1 \end{bmatrix} \begin{Bmatrix} x_1 \\ y_1 \\ z_1 \end{Bmatrix} = [T_1] \begin{Bmatrix} x_1 \\ y_1 \\ z_1 \end{Bmatrix} \tag{2.7}$$

The second step is a rotation of $O_1-x_1y_1z_1$ by an angle α_2 about the y_1-axis, which leads to the system $O_2-x_2y_2z_2$:

$$\begin{Bmatrix} x_1 \\ y_1 \\ z_1 \end{Bmatrix} = \begin{bmatrix} \cos\alpha_2 & 0 & \sin\alpha_2 \\ 0 & 1 & 0 \\ -\sin\alpha_2 & 0 & \cos\alpha_2 \end{bmatrix} \begin{Bmatrix} x_2 \\ y_2 \\ z_2 \end{Bmatrix} = [T_2] \begin{Bmatrix} x_2 \\ y_2 \\ z_2 \end{Bmatrix} \tag{2.8}$$

In the third step, rotate $O_2-x_2y_2z_2$ by an angle α_3 about the z_2-axis and obtain the system $O_3-x_3y_3z_3$:

$$\begin{Bmatrix} x_2 \\ y_2 \\ z_2 \end{Bmatrix} = \begin{bmatrix} \cos\alpha_3 & -\sin\alpha_3 & 0 \\ \sin\alpha_3 & \cos\alpha_3 & 0 \\ 0 & 0 & 1 \end{bmatrix} \begin{Bmatrix} x_3 \\ y_3 \\ z_3 \end{Bmatrix} = [T_3] \begin{Bmatrix} x_3 \\ y_3 \\ z_3 \end{Bmatrix} \tag{2.9}$$

After three rotations, the following relationship could be obtained

$$\begin{Bmatrix} x_0 \\ y_0 \\ z_0 \end{Bmatrix} = [T_1][T_2][T_3]\begin{Bmatrix} x_3 \\ y_3 \\ z_3 \end{Bmatrix} = [T]\begin{Bmatrix} x_3 \\ y_3 \\ z_3 \end{Bmatrix} \text{ or } \begin{Bmatrix} x_3 \\ y_3 \\ z_3 \end{Bmatrix} = [T]^{-1}\begin{Bmatrix} x_0 \\ y_0 \\ z_0 \end{Bmatrix} \tag{2.10}$$

$$[T] = \begin{bmatrix} \cos\alpha_2\cos\alpha_3 & -\cos\alpha_2\sin\alpha_3 & \sin\alpha_2 \\ \sin\alpha_1\sin\alpha_2\cos\alpha_3 + \cos\alpha_1\sin\alpha_3 & -\sin\alpha_1\sin\alpha_2\sin\alpha_3 + \cos\alpha_1\cos\alpha_3 & -\sin\alpha_1\cos\alpha_2 \\ -\cos\alpha_1\sin\alpha_2\cos\alpha_3 + \sin\alpha_1\sin\alpha_3 & \cos\alpha_1\sin\alpha_2\sin\alpha_3 + \sin\alpha_1\cos\alpha_3 & \cos\alpha_1\cos\alpha_2 \end{bmatrix} \tag{2.11}$$

where $[T]$ is the transformation matrix. Note that the inverse $[T]^{-1}$ has the same form as the transpose $[T]^t$. The $O-xyz$ could be obtained in the final step, through a translation of $O_3 - x_3y_3z_3$ along the vector $\mathbf{r}_c$. The coordinates in the earth- and body-fixed system have the following relationship

$$\begin{Bmatrix} x_o \\ y_o \\ z_o \end{Bmatrix} = \mathbf{r}_c + [T]\begin{Bmatrix} x \\ y \\ z \end{Bmatrix} \text{ or } \begin{Bmatrix} x \\ y \\ z \end{Bmatrix} = [T]^{-1}\left(\begin{Bmatrix} x_o \\ y_o \\ z_o \end{Bmatrix} - \mathbf{r}_c\right) \tag{2.12}$$

The angle α_1, α_2 and α_3 are called 'Euler angles' (Marion 1965), which could determine the orientation of the body-fixed coordinate system. When the body-fixed system rotates about an arbitrary axis, the angular velocity $\boldsymbol{\Omega}$ could be represented using Euler angles as $\boldsymbol{\Omega} = \dot{\alpha}_1\mathbf{e}_{x_1} + \dot{\alpha}_2\mathbf{e}_{y_2} + \dot{\alpha}_3\mathbf{e}_{z_3}$. Here, $\mathbf{e}_{x_i}$ denotes the unit vector of the $O_i - x_i$ axis. From Fig.2.2, it is known that $\mathbf{e}_{x_1} = \mathbf{e}_{x_2}\cos\alpha_2 + \mathbf{e}_{z_2}\sin\alpha_2$, $\mathbf{e}_{x_2} = \mathbf{e}_{x_3}\cos\alpha_3 - \mathbf{e}_{y_3}\sin\alpha_3$, $\mathbf{e}_{y_2} = \mathbf{e}_{y_3}\cos\alpha_3 + \mathbf{e}_{x_3}\sin\alpha_3$ and $\mathbf{e}_{z_2} = \mathbf{e}_{z_3}$. Thus, in the body-fixed system, the angular velocity $\boldsymbol{\Omega} = \Omega_x\mathbf{e}_x + \Omega_y\mathbf{e}_y + \Omega_z\mathbf{e}_z$ can be represented as

$$\begin{Bmatrix} \Omega_x \\ \Omega_y \\ \Omega_z \end{Bmatrix} = \begin{Bmatrix} \dot{\alpha}_1\cos\alpha_2\cos\alpha_3 + \dot{\alpha}_2\sin\alpha_3 \\ \dot{\alpha}_2\cos\alpha_3 - \dot{\alpha}_1\cos\alpha_2\sin\alpha_3 \\ \dot{\alpha}_3 + \dot{\alpha}_1\sin\alpha_2 \end{Bmatrix} \tag{2.13}$$

If the Euler angles are small, it can be obtained as $\cos\alpha_i \approx 1$ and $\sin\alpha_i \approx \alpha_i$. Then, Eq. (2.13) can be linearized as $\Omega_x = \dot{\alpha}_1$, $\Omega_y = \dot{\alpha}_2$ and $\Omega_z = \dot{\alpha}_3$.

2.3 Fluid motion in the external domain

2.3.1 Governing equations

For fluid motions in the external domain, equations are written in the earth-fixed coordinate system. Consider the ideal fluid. From the mass conservation law, the equation of continuity can be written as

$$\nabla_o \cdot \mathbf{v} = 0 \tag{2.14}$$

in which $\mathbf{v} = (v_{xo}, v_{yo}, v_{zo})$ is the fluid velocity and $\nabla_o = \mathbf{i}_o \frac{\partial}{\partial x_o} + \mathbf{j}_o \frac{\partial}{\partial y_o} + \mathbf{k}_o \frac{\partial}{\partial z_o}$. Here, $\mathbf{i}_o$, $\mathbf{j}_o$ and $\mathbf{k}_o$ are used to represent unit vectors in the x_o, y_o and z_o directions, respectively. According to the momentum conservation law, the fluid motion is described by

$$\frac{\partial \mathbf{v}}{\partial t} + (\mathbf{v} \cdot \nabla_o)\mathbf{v} = -\frac{1}{\rho}\nabla_o p - g\mathbf{k}_o \tag{2.15}$$

where ρ is the fluid density, p is the pressure and g denotes the gravitational acceleration.

When the fluid flow is further assumed to be irrotational (i.e. $\nabla_o \times \mathbf{v} = 0$), the potential-flow theory could be applied. The scalar velocity potential $\varphi(x_o, y_o, z_o, t)$ is introduced, which is defined as $\mathbf{v} = \nabla_o \varphi$. Then, the equation of continuity can be rewritten as the Laplace's equation

$$\nabla_o^2 \varphi = \frac{\partial^2 \varphi}{\partial x_o^2} + \frac{\partial^2 \varphi}{\partial y_o^2} + \frac{\partial^2 \varphi}{\partial z_o^2} = 0 \tag{2.16}$$

Meanwhile, taking $\nabla_o \times \nabla_o \varphi = 0$ into account, the momentum equations can be represented by

$$\nabla_o \frac{\partial \varphi}{\partial t} + \frac{1}{2}\nabla_o(\nabla_o \varphi \cdot \nabla_o \varphi) + \frac{1}{\rho}\nabla_o p + \nabla_o U_g = 0 \tag{2.17}$$

where U_g is defined as a gravitational potential with $\nabla_o U_g = g\mathbf{k}_o$. Integration of Eq. (2.17) leads to Bernoulli's equation

$$\frac{\partial \varphi}{\partial t} + \frac{1}{2}\nabla_o \varphi \cdot \nabla_o \varphi + \frac{p}{\rho} + U_g = C(t) \tag{2.18}$$

in which $C(t)$ is a time-dependent function. It should be pointed out that, since it is the potential derivative $\nabla_o\varphi$ instead the potential φ itself that is meaningful, adding constants or functions of time to the expression of φ will not affect the physics of the problem. By redefining φ appropriately, $C(t)$ could vanish without affecting the velocity field. Thus, for convenience, $C(t)$ may be set as $C(t)\equiv 0$ without any loss of generality.

The Laplace equation is the governing equation of the fluid motions. With appropriate boundary conditions, the velocity potential in the fluid domain can be solved. Then, the fluid velocity $\mathbf{v}$ can be obtained from the gradient of the velocity potential φ, and the pressure p can be calculated from Bernoulli's equation. Subsequently, forces and moments acting on the vessel can be obtained by an integration of the pressure on the body surface.

2.3.2. Boundary conditions

On the body surface S_B, the boundary condition requires that no fluid could pass through the surface. Thus, the motion of the fluid and vessel in the normal direction of the body surface must be equal, i.e.

$$\left(\frac{\partial\varphi}{\partial n}\right)_o=\left(\mathbf{v}_c+\boldsymbol{\Omega}\times\mathbf{r}\right)\cdot\mathbf{n} \tag{2.19}$$

where $\mathbf{r}=\{x,y,z\}$ is the position vector of a point on S_B, $\mathbf{n}$ is the unit normal vector pointing outward the fluid, $\mathbf{v}_c$ is the velocity of the origin O, and $\boldsymbol{\Omega}$ is the angular velocity of $O-xyz$. When the body surface is fixed, the boundary condition has a simpler form

$$\left(\frac{\partial\varphi}{\partial n}\right)_o=0 \tag{2.20}$$

Then, consider the boundary conditions on the free surface S_F. The variation of the atmospheric pressure and surface tension are neglected. Assuming that the free surface has an implicit shape expression $Z\left(x_o,y_o,z_o,t\right)=0$, the material derivative of Z must be zero at any instance

$$\frac{dZ}{dt} = \frac{\partial Z}{\partial t} + \hat{\mathbf{v}} \cdot \nabla_o Z = 0 \tag{2.21}$$

Here, $\hat{\mathbf{v}}(x_o, y_o, z_o, t)$ is the velocity of a 'sensor' on the free surface and the value of Z is recorded by the 'sensor'. Setting $\hat{\mathbf{v}}$ as the fluid velocity $\nabla_o \varphi$ at the same position leads to the kinematic free-surface boundary condition

$$\frac{dZ}{dt} = \frac{\partial Z}{\partial t} + \nabla_o \varphi \cdot \nabla_o Z = 0 \tag{2.22}$$

This means that the fluid particle on the free surface will remain on the free surface. Defining $Z(x_o, y_o, z_o, t) = z_o - \eta_o(x_o, y_o, t) = 0$ yields the Eulerian form kinematic free-surface boundary condition

$$\left(\frac{\partial \eta_o}{\partial t}\right)_o + \frac{\partial \varphi}{\partial x_o}\frac{\partial \eta_o}{\partial x_o} + \frac{\partial \varphi}{\partial y_o}\frac{\partial \eta_o}{\partial y_o} - \frac{\partial \varphi}{\partial z_o} = 0 \tag{2.23}$$

Since the free-surface position is not known a priori, an extra condition should be introduced for a deterministic solution. The dynamic free-surface boundary condition could be obtained by letting the pressure at the free surface equal to the atmospheric pressure p_0. The p_0 can be assumed to be a constant and taken as zero, i.e. $p_0 = 0$. According to Bernoulli's equation, the dynamic free-surface boundary condition can be written as

$$\left(\frac{\partial \varphi}{\partial t}\right)_o + \frac{1}{2}\nabla_o \varphi \cdot \nabla_o \varphi + g\eta_o = 0 \tag{2.24}$$

It should be pointed out that, since η_0 is a single-valued function, the Eulerian form free-surface conditions could not deal with overturning waves. Alternatively, the free-surface boundary conditions could be specified in the Lagrangian form. The kinematic and dynamic conditions are formed by following the fluid particle on S_F as

$$d\hat{\mathbf{x}}/dt = \nabla_o \varphi \tag{2.25}$$

$$\frac{d\varphi}{dt} - \frac{1}{2}\nabla_o \varphi \cdot \nabla_o \varphi + g z_o = 0 \tag{2.26}$$

where $\hat{\mathbf{x}}(x_o, y_o, z_o, t)$ denotes the position vector of the fluid particle.

It is clear that, although the Laplace's equation is linear, the free-surface boundary conditions are nonlinear. Also, above boundary conditions are satisfied on the instantaneous free and wetted body surface. Thus, the nonlinearities enter the fluid system via boundary conditions.

2.4 Fluid motion in liquid tanks

2.4.1 Governing equations

For the sloshing problem, it is more convenient to express the fluid motion in the body-fixed coordinate system $O-xyz$. The earth- and body-fixed systems are related through the Eq. (2.12). The spatial and time derivatives have the following relationship

$$\nabla = \nabla_o \tag{2.27}$$

$$\frac{\partial}{\partial t} = \left(\frac{\partial}{\partial t}\right)_o + \left(\mathbf{v}_c + \boldsymbol{\Omega}\times\mathbf{r}\right)\cdot\nabla \tag{2.28}$$

where $\partial/\partial t$ denotes the temporal derivative at a fixed position $\mathbf{r} = \{x, y, z\}$ in $O-xyz$. As a result, the Laplace's equation remains its form in $O-xyz$ as

$$\nabla^2\varphi(x, y, z) = 0 \tag{2.29}$$

but the Bernoulli's equation becomes

$$\frac{\partial\varphi}{\partial t} - \left(\mathbf{v}_c + \boldsymbol{\Omega}\times\mathbf{r}\right)\cdot\nabla\varphi + \frac{1}{2}\nabla\varphi\cdot\nabla\varphi + \frac{p}{\rho} + gz_o = 0 \tag{2.30}$$

2.4.2 Boundary conditions

The body surface boundary condition in the body-fixed system takes the same form as that in the earth-fixed system, which allows no flow to pass through or away from the tank wall

$$\frac{\partial\varphi}{\partial n} = \left(\mathbf{v}_c + \boldsymbol{\Omega}\times\mathbf{r}\right)\cdot\mathbf{n} \tag{2.31}$$

Assume the free surface is defined as $Z(x, y, z, t) = z - \eta(x, y, t) = 0$ in the body-fixed system. The kinematic free-surface boundary condition can be written in the following form

$$\frac{\partial \eta}{\partial t}+\left(\mathbf{v}_c+\boldsymbol{\Omega}\times\mathbf{r}\right)\cdot\left\{-\frac{\partial \eta}{\partial x},-\frac{\partial \eta}{\partial y},1\right\}+\frac{\partial \varphi}{\partial x}\frac{\partial \eta}{\partial x}+\frac{\partial \varphi}{\partial y}\frac{\partial \eta}{\partial y}-\frac{\partial \varphi}{\partial z}=0 \tag{2.32}$$

The dynamic condition can be expressed as

$$\frac{\partial \varphi}{\partial t}-\left(\mathbf{v}_c+\boldsymbol{\Omega}\times\mathbf{r}\right)\cdot\nabla\varphi+\frac{1}{2}\nabla\varphi\cdot\nabla\varphi+gz_c+g\left(T_{31}x+T_{32}y+T_{33}\eta\right)=0 \tag{2.33}$$

Both kinematic and dynamic free-surface boundary conditions are satisfied on the instantaneous free surface.

2.5 Hydrodynamic forces

The hydrodynamic force $\mathbf{F}$ and moment $\mathbf{M}$ acting on the vessel can be calculated by integrating the pressure over the wetted body surfaces. The pressure can be calculated by integrating the Bernoulli equation. After the surface integration, the following equations can be obtained

$$\mathbf{F}=-\rho\iint_{S_B}\left(\left(\frac{\partial \varphi}{\partial t}\right)_o+\frac{1}{2}\nabla_o\varphi\nabla_o\varphi+gz_o\right)\mathbf{n}dS \tag{2.34}$$

$$\mathbf{M}=-\rho\iint_{S_B}\left(\left(\frac{\partial \varphi}{\partial t}\right)_o+\frac{1}{2}\nabla_o\varphi\nabla_o\varphi+gz_o\right)\left(\mathbf{r}\times\mathbf{n}\right)dS \tag{2.35}$$

where $\mathbf{n}$ is the unit vector normal to S_B and pointing outwards. Once the velocity potential and its normal derivatives are solved, the spatial derivatives of the velocity potential can be obtained. Thus, the only unknown on the right-hand side of Eqs. (2.34) and (2.35) is the φ_t term (note that the subscript t is used to represent the partial time derivative). The value of φ_t might be obtained explicitly from the backward difference method, but this is not always accurate enough and may lead to numerical instabilities (Wang and Wu 2010). Alternatively, it could be solved from the boundary value problem (Wu and Eatock Taylor 1996)

$$\nabla_o^2\varphi_t=0 \text{, in } V \tag{2.36}$$

$$\varphi_t=-gz_o-\frac{1}{2}\nabla_o\varphi\nabla_o\varphi \text{, on } S_F \tag{2.37}$$

$$\frac{\partial \varphi_t}{\partial n} = \left(\dot{\mathbf{v}}_c + \dot{\Omega} \times \mathbf{r}\right) \cdot \mathbf{n} - \mathbf{v}_c \cdot \frac{\partial \nabla_o \varphi}{\partial n} + \Omega \cdot \frac{\partial}{\partial n}\left[\mathbf{r} \times \left(\mathbf{v}_c - \nabla_o \varphi\right)\right], \text{ on } S_B \tag{2.38}$$

where $\dot{\mathbf{v}}_c$ and $\dot{\Omega}$ are used to express the translational and rotational accelerations of the vessel. Numerical computation of the second-order differentiation term $\partial\left(\nabla_o \varphi\right)/\partial n$ and $\partial\left[\mathbf{r} \times \left(\mathbf{v}_c - \nabla_o \varphi\right)\right]/\partial n$ appears to be difficult. Since Eq. (2.38) could be rewritten as

$$\frac{\partial}{\partial n}\left(\varphi_t + \mathbf{v}_c \cdot \nabla_o \varphi + \nabla_o \varphi \cdot (\Omega \times \mathbf{r}) - \mathbf{v}_c \cdot (\Omega \times \mathbf{r})\right) = \left(\dot{\mathbf{v}}_c + \dot{\Omega} \times \mathbf{r}\right) \cdot \mathbf{n} \tag{2.39}$$

an auxiliary function $\chi = \varphi_t + \mathbf{v}_c \cdot \nabla_o \varphi + \nabla_o \varphi \cdot \left(\Omega \times \mathbf{r}\right) - \mathbf{v}_c \cdot \left(\Omega \times \mathbf{r}\right)$ could be constructed (Wu and Hu 2004). The χ could be calculated through the following boundary value problem

$$\nabla_o^2 \chi = 0 \text{, in } V \tag{2.40}$$

$$\chi = -g z_o - \frac{1}{2} \nabla_o \varphi \nabla_o \varphi + \mathbf{v}_c \cdot \nabla_o \varphi + \Omega \cdot \left(\mathbf{r} \times \nabla_o \varphi\right) - \Omega \cdot \left(\mathbf{r} \times \mathbf{v}_c\right) \text{, on } S_F \tag{2.41}$$

$$\frac{\partial \chi}{\partial n} = \left(\dot{\mathbf{v}}_c + \dot{\Omega} \times \mathbf{r}\right) \cdot \mathbf{n} \text{, on } S_B \tag{2.42}$$

2.6 Closure

This chapter gives the fundamental equations used to describe the vessel motion, external flow, and liquid sloshing. These equations will be referred to frequently in later chapters. This chapter is followed by Part I (Chapter 3 to 5) which focuses on the sloshing in wall-sided tanks (a benchmark test model) as the first step to start the sloshing subject.

Part I (Ch 3, 4 & 5) Sloshing in wall-sided tanks

Chapter 3 Methodology reviews on sloshing simulations

The sloshing problem could be investigated based on experimental and simulation (either analytical or numerical) methods, the latter of which is the interest of the present study. Before choosing a proper method for sloshing simulations, a methodology review is firstly given in this chapter.

3.1 Analytical method

By ‘analytical’, it means that the solution of the problem could be expressed mathematically with well-known functions, constants and operations. Since the analytical solution is presented as a mathematical expression, it offers a clear view into how variables and their interactions affect the result, which is helpful for uncovering the sloshing mechanism. The analytical solutions are also useful for verifying the numerical method and guiding systematic numerical studies. However, the sloshing is a complex phenomenon. Even if factors such as the capillary effect, surface tension, compressibility, viscosity and flow rotations are neglected, it is still difficult to obtain the analytical solution of this nonlinear system. If the amplitude of the free-surface elevation is further assumed to be small, analytical solutions in a ‘weakly-nonlinear’ sense can be obtained for some simple wall-sided sloshing tanks. Two typical analytical methods are mostly adopted. One is the perturbation method which solves the Laplace’s equation associated boundary conditions, and the other is the modal expansion method which solves the variational formulation. Both methods are based on the potential-flow theory.

The perturbation method assumes that the free surface oscillates about a mean position, and all quantities derivable from the flow (e.g. the free-surface elevation, pressure, and force) oscillate slightly around their mean value. Then, quantities on the instantaneous free surface could be expanded as Taylor series about the mean boundary position. These expansions are further substituted into the governing equation and nonlinear boundary conditions. Collecting terms of the same order, one may obtain a series of linear boundary value problems (BVPs) that might be solved analytically. This

method has been used in the following works. Faltinsen (1978) studied the sloshing in a 2D rectangular tank and derived analytical solutions up to the third order. Chapman and Porter (2005) presented the second-order solutions for the free sloshing in a 2D tank with vertical walls but a complex bottom. Wu (2007) analysed the second-order solution of sloshing in 2D rectangular tanks, and predicted a phenomenon of the second-order sloshing resonance. Overall, the perturbation method is effective for analysing the sloshing nonlinearities to different levels. However, besides the small-wave-slope restrictions, this method becomes impractical when considering the third and higher-order nonlinearities, because of the long inhomogeneous terms with higher-order derivatives in the equations.

An alternative method is the modal expansion method which is fundamentally from the ‘least action principle’. This principle originates from Maupertuis’ feeling that the perfection of the universe demands a certain economy in nature and is opposed to any needless expenditure of energy (Davis 1998). In the context of mechanics, natural motions must be such as to make some quantity a minimum. After the development by Lagrange, Euler, Maupertuis and Hamilton, this quantity comes to be known as the ‘action’ of an object (Faltinsen and Timokha 2009). At present, two types of action have been found: (1) In the Lagrangian variational theory, the action is defined as the time integration of the difference between the kinetic and potential energies in the fluid domain; (2) In the Bateman-Luke variational theory, the action is the time integration of the pressure. When using this method, the free-surface elevation and velocity potential are firstly expanded into infinite series with base functions and unknown time-dependent coefficients. Here, each base function should satisfy both the Laplace’s equation and the tank-wall condition. Then, the expansion series are substituted into the function of the action that implicitly contains the nonlinear free-surface conditions. The variational formulation is used to find the extreme, which leads to an infinite-dimensional system of differential equations in terms of the time-dependent coefficients.

Based on the modal expansion method, Faltinsen and his co-workers have studied the nonlinear behaviour of sloshing in 2D and 3D rectangular

tanks (e.g. Faltinsen et al 2000; Faltinsen and Timokha 2002; Faltinsen et al 2003; and Faltinsen et al 2005). La Rocca et al (2000) modelled the sloshing in tanks rotating around a horizontal axis. La Rocca et al (2002) and La Rocca et al (2005) investigated the interfacial waves in a tank fully-filled with two fluids. Love and Tait (2011, 2013) concerned the interaction between various wall-sided sloshing tanks and their supporting structures. However, it should be noted that the series of base functions are difficult to find for arbitrary tanks. For example, they require the tank wall to be vertical in the vicinity of the free surface, and they should be complete on the mean free surface and the whole fluid domain.

Other analytical methods for sloshing problems also exist. For example, Wu et al (2001) solved the linearized Navier-Stokes (NS) equations (also known as Stokes equations) using the Laplace transform method. The viscous liquid sloshing in a 2D rectangular tank was considered. This method is also restricted to the situation when the liquid disturbance is small, so that higher-order convective terms in NS equations could be neglected. The linearization is performed on the governing equations, instead of the boundary conditions as in the potential-flow theory.

3.2 Numerical method for potential flows

The numerical method, which is also known as the computational fluid dynamics (CFD) method, has become an important tool for sloshing analyses. A general procedure of the numerical solution contains several steps. (1) Choose a suitable mathematical model (i.e. governing equations and boundary conditions) for the concerned physical phenomenon, based on either the potential-flow theory or NS equations. (2) Discretize governing equations and boundary conditions using numerical discretization strategies, such as the finite difference method (FDM), finite element method (FEM), local boundary integral equation (LBIE) method, meshless Petrov-Galerkin (MLPG) method, boundary element method (BEM), finite volume method (FVM), smoothed particle hydrodynamics (SPH), moving particle semi-implicit (MPS) method and so on. (3) Form a system of linear equations. (4) Solve the equation system and update quantities to the subsequent time step.

Even though real fluids are always viscous to some degree, it could be reasonable to neglect the viscosity for sloshing in a smooth tank and regard the fluid domain as a potential-flow region, as discussed in Section 2.1. Compared with NS-based methods, the numerical methods for potential flows usually have efficiency advantages. The potential-flow methods most frequently used for sloshing problems are summarised as follows.

- **FDM**

The FDM can be used to solve the Laplace's equation with nonlinear free-surface conditions. The computation is performed only in the fluid domain and the mesh always conforms to the geometry of the fluid volume. The nonlinear free surface is tracked either by Lagrangian particles or implicitly by the mapping method. The mapping method transforms the curvilinear mesh in the physical domain to the computational domain with rectangular grids, and the governing equation and boundary conditions are modified accordingly. This method is effective when the free surface slope is not steep and no wave overturning occurs.

There are two categories of FDM approaches with respect to the calculation of spatial derivatives. The first category performs the numerical difference in a local area of grids. For example, Chen et al (1996) investigated the nonlinear liquid sloshing in 2D rectangular tanks undergoing horizontal excitation. Frandsen and Borthwick (2003) applied the σ -transformation method by mapping the physical mesh linearly between the tank bottom and free surface onto a fixed computational mesh, and simulated the 2D nonlinear sloshing in fixed or heaving rectangular tank. Frandsen (2004) further studied the nonlinear sloshing in a 2D tank which was accelerated both horizontally and vertically. Santos and Greaves (2007) used Lagrangian particles instead of the mapping method to track the free surface and studied the 2D free sloshing problems. Hernandez-Barrios et al (2007) simulated nonlinear sloshing responses in a cylindrical tank during the earthquake by the σ -transformation approach in the cylindrical coordinate system. The other category is usually called the 'pseudo-spectral method (PSM)'. It expands variables in terms of global functions and calculates their derivatives globally. For example, Chern et al (1999) simulated the nonlinear sloshing in 2D

rectangular tanks due to the horizontal excitation. The physical problem was mapped to regular grids through the σ -transformation. The distribution of the velocity potential along the horizontal and vertical grids was approximated by the Chebyshev polynomial. Chern et al (2001) and Chern et al (2012) extended this Chebyshev pseudo-spectral method to sloshing in annular cylindrical and 3D rectangular tanks, respectively. Similarly, Kim et al (1998) chose homogeneous solutions of the Laplace's equation (i.e. natural modes) as bases to approximate the velocity potential along the horizontal and vertical grids. It should be noted that the resulted matrix of the pseudo-spectral method would be denser than that of the former FDM.

- **FEM**

The FEM also requires a discretization of the internal fluid volume. It divides the fluid domain into small elements. The velocity potential values at nodes of each element are treated as unknown constants to be determined. The field variable within the element is approximated by an interpolation of the nodal values. Typical FEM works for 2D sloshing problems are as follows. Nakayama and Washizu (1980) simulated the nonlinear sloshing in a rectangular tank undergoing the sinusoidal pitching oscillation. Okamato and Kawahara (1990) carried out the analysis for large-amplitude sloshing waves in tanks with roofs and chamfers. The mesh nodes advanced in a Lagrangian manner. Wu and Eatock Taylor (1994) simulated the free sloshing induced by an initial free-surface disturbance. The second-order perturbation solution was also derived for comparison. Turnbull et al (2003a, b) adopted the σ -transformation and simulated the free and forced sloshing in a rectangular tank. The free surface was tracked by mixed Eulerian-Lagrangian (MEL) scheme and the fluid domain was discretized using Voronoi unstructured mesh at each time step. Wang and Khoo (2005) analysed the nonlinear sloshing in a rectangular tank undergoing prescribed horizontal random motion. Sriram et al (2006) studied the nonlinear waves in a flume. A cubic spline interpolation was used to calculate the fluid velocity. As a 3D case, Wu et al (1998) conducted an extensive research on sloshing waves in a rectangular tank undergoing translational motions.

- **LBIE and MLPG**

The LBIE and MLPG are two meshless methods for potential flows (Zhu et al 1998; Atluri and Zhu 1998). For LBIE, a number of nodes are distributed over the fluid domain and its boundary. Each node is encircled by a local surface on which the boundary integral equation (BIE) transformed from the Laplace's equation is applied. The integration over the local surface is calculated by the Gaussian quadrature method. The velocity potential at each Gaussian quadrature point is expressed by the moving least square (MLS) interpolation over its neighbour nodes. Traversing all the nodes leads to a system of linear equations in terms of the velocity potential. If the Green's function in LBIE is replaced by a user-defined test function, the MLPG method could be obtained. Pal and Bhattacharyya (2010) is a typical MLPG work that simulates the sloshing in 2D rectangular tanks. The LBIE and MLPG methods do not require a mesh discretisation of the fluid domain, and internal nodes do not have to be Lagrangian particles. However, to guarantee an accuracy interpolation value on each Gaussian point, a dense node distribution is necessary. Also, the fluid boundary still has to be determined, in order to calculate the solid angle in the local boundary integral equation at boundary nodes.

- **BEM**

The BEM has been widely used in free-surface wave problems. The governing Laplace's equation is firstly converted to BIE. Then, boundary elements are introduced to discretize the BIE. The BEM only requires the spatial discretization on the boundary surface instead of the entire flow field. This saves the trouble of generating interior mesh elements for a 3D fluid domain. This feature also considerably reduces the number of unknowns, leading to a small system of equations. For the sloshing problem, it only requires a few thousands of boundary elements to guarantee the numerical convergence. So, even though the resulted system of equations is normally dense, the simulations could run on a personal computer (PC) without much challenge of computing resources. The works of Faltinsen (1978) and Nakayama and Washizu (1981) that simulated the nonlinear sloshing in 2D rectangular tanks seem to be the earliest applications of BEM to sloshing problems. They adopted the MEL procedure to track the free surface, by

regarding free-surface mesh nodes as Lagrangian particles on the free surface. At any instant, the velocity and material derivative of the velocity potential on each node can be found by solving the BVP in the Eulerian frame. Then, the free-surface position and velocity potential on the free surface as boundary conditions can be updated to the next time step by following the Lagrangian-type nodes. Liu and Huang (1994) analysed the nonlinear sloshing in a 2D rectangular tank with a semi-Lagrangian (SL) method to track the free surface. In their method, the boundary nodes moved only in the vertical direction to represent the instantaneous free surface profile. Chen et al (2007) studied the sloshing behaviours in cylindrical and 3D rectangular liquid tanks. The second-order Taylor series expansion with respect to the time was used to update the free-surface boundary conditions.

3.3 Numerical method for Navier-Stokes equations

When the fluid viscosity is concerned in a sloshing problem, the Navier-Stokes (NS) equations should be adopted as governing equations. With respect to the numerical discretization strategy, the methods for NS equations could be classified as mesh-based and meshless methods.

The mesh-based methods can be further classified into two groups.

- **For single-phase flow**

In the first group, the calculation is only performed in the liquid domain, similar to the potential-flow methods. Here are some typical 2D examples. Ramaswamy (1990) simulated the free sloshing in rectangular and wedged tanks using FEM. The free surface was tracked using a particle method. Takizawa and Koshizuka (1992) studied the free-surface oscillation due to the liquid circulation in a rectangular tank using FDM with a mapping method. Chen and Chiang (1999) investigated the nonlinear sloshing in a rectangular tank subjected to coupled-horizontal-vertical excitations based on FDM. The mapping method was used to handle the time varying free surface. Chen and Nokes (2005) further studied the sloshing in the rectangular tank due to coupled surge, heave and pitch motions. For 3D studies, Ushijima (1998) simulated the nonlinear sloshing in a cylindrical tank with forced horizontal or vertical motion using FEM coupled by the MEL technique. Wu and Chen

(2009) investigated the sloshing in a 3D rectangular tank undergoing horizontal ground motion. The FDM coupled with the mapping procedure was used. Chen and Wu (2011) subsequently studied the sloshing due to coupled heave, surge and sway motions.

- **For two-phase flow**

In the second group, two phases including both the air and liquid in the tank are treated in the calculation. The numerical mesh is generated over the two-phase domain. The interface between two phases is a transition region within which the density and viscosity vary smoothly but rapidly. The free surface is usually captured by the 'volume-of-fluid (VOF)' (Hirt and Nichols 1981) or 'level-set' (Sussman et al 1994) techniques. Numerical methods in this group are usually capable to deal with complex flow phenomena such as the wave breaking without changing the fundamental algorithm. At present, large volumes of sloshing researches are based on the commercial software (e.g. Fluent, MSc.Dytran, CFX, and FLOW3D) which combines the FDM, FVM or FEM solver with the VOF technique. There are also studies based on in-house codes. For example, Celebi and Akyildiz (2002) developed an FDM code coupled with VOF and studied the 2D nonlinear sloshing in baffled and unbaffled rectangular tanks moving along a pre-defined path. Kishev et al (2006) applied the constraint-interpolation-profile (CIP) FDM to study violent sloshing in a rectangular tank. An interface capturing method coupled with stationary Cartesian grids was developed to predict the free surface. Liu and Lin (2008) introduced a 3D numerical model for the violent sloshing. The VOF technique of the second-order accuracy was used to simulate breaking free-surface waves. Chen et al (2009) applied the 3D FDM to study the impact pressure during the sloshing, with the level-set method for the free-surface capturing. It should be noted that mesh-based methods in this group also have some drawbacks. One is the simulation efficiency. Take the 3D simulation of Liu and Lin (2008) for example. Even if the domain was only discretized into 57*31*30 uniform grids, it took about 265 hours on Intel Xeon CPU X5355 (2.66 GHz) to simulate around 30 excitation periods. Another limitation is the simulation accuracy and stability. After a long time simulation, the free surface zone smears widely, which will cause numerical errors (Gao

2011). Gavrilyuk et al (2005) also pointed out that, without a sufficient care, the numerical errors may accumulate, resulting in a loss of the fluid volume.

For the meshless or particle method, the fluid domain is denoted by a set of particles according to certain rules. The topological relation of these particles is not needed. The SPH and MPS are the most popular meshless methods.

- **SPH**

The SPH method was originally introduced by Lucy (1977) and Gingold and Monaghan (1977) and then applied to sloshing problems by Monaghan (1994). Using this method, the fluid domain is represented by a set of Lagrangian particles. Each particle carries the information of mass, pressure, momentum and energy on itself. The continuous variables in the fluid are calculated by an interpolation of the values on particles. Having solved the Lagrangian form NS equations, the acceleration of each particle can be obtained to predict the particle position for the next time step. The impenetrable boundary condition could be defined in different means, such as using mirror particles and repulsive particles. Souto-Iglesias et al (2004) and Souto-Iglesias et al (2006) simulated the 2D sloshing in a rolling rectangular tank. Rudman and Cleary (2009) applied SPH to modelling sloshing in a 2D surging tank. Marsh et al (2010) studied the energy dissipation of a 2D rectangular TLD using SPH. Shao et al (2012) modelled viscous incompressible sloshing in the 2D rectangular tank.

- **MPS**

The MPS method was originally developed by Koshizuka et al (1995, 1996 and 1998) for incompressible fluids. Using this method, the fluid domain is firstly discretized into particles and the fluid density at the position of a particle is represented by the particle number density. The MPS scheme has the prediction and correction steps. In the prediction step, the fluid can be imagined to be compressible. Only the body force and viscosity terms are taken into account, and the velocity and displacement of fluid particles are explicitly updated to predicted values. In the correction step, the incompressible condition is enforced to redistribute the particle number

density and correct the pressure, velocity and position at each particle. Typical MPS simulations for sloshing problems are as follows. Khayyer and Gotoh (2010) simulated the violent sloshing in a 2D rectangular tank. Lee et al (2011) investigated the slamming loads in a rectangular tank. Gao (2011) proposed a modified MPS method and modelled both gentle and violent sloshing in a 2D surging rectangular tank. Pan et al (2012) simulated the sloshing in a 2D tank undergoing the surge and roll motions.

The meshless methods have some common disadvantages. For example, (1) the obtained pressure has a spiky behaviour and negative pressure cannot be obtained when there is 'suction' on the wall (Rudman and Cleary 2009); (2) A huge number of particles and small time steps are inevitable to guarantee the accuracy and stability, resulting in a high CPU consumption (Gomez-Gesteira et al 2010). Take Marsh et al (2010b) for example. A physical time of 10 seconds requires the CPU time for around 1 day for 2500 particles and two weeks for 50,000 particles, on the 3.2 GHz Intel Xeon processor. For MPS, the conservation of momentum is not satisfied, which means that the interaction from particle i to particle j does not always equal to interaction from j to i, which is not physically true.

3.4 Analogy method

For sloshing in tanks undergoing a lateral motion, the horizontal oscillation of the mass centre can be approximated by an equivalent mechanical system, i.e. the 'mechanical analogy'. The mechanical model could be the pendulum or mass-spring system. Although this analogy is crude, which may only provide a primitive description of some sloshing characters, its simulation time is much shorter than the physical time in reality. Thus, it may be regarded as a rapid method to approximate sloshing effects. However, it should be noted that the determination of parameters of the mechanical models (e.g. spring stiffness) is usually difficult and tricky.

Different mechanical models were described in detail in the NASA report of Abramson (1966) and its updated version of Dodge (2000). The mechanical analogy parameters (e.g. the mass and length of each pendulum and damping coefficients in the baffled tank) are determined using either

potential-flow results or experimental measurements. In Pilipchuk and Ibrahim (1997) and Ibrahim and EL-Sayad (1999), a simple pendulum model was adopted. The tank was supported by elastic structures, which was modelled as four massless rods restrained by four torsional springs at the base. The sloshing impact was approximated by a pendulum striking on the tank wall. Aliabadi et al (2003) used the pendulum model to analyse the liquid sloshing in a tanker truck. For liquid tanks at the low or moderate filling levels, the mechanical model could give results qualitatively comparable with the FEM solutions. Godderidge et al (2012a, b) developed a pendulum model with the fluid impact taken into account. It shows that the simulation time on a desktop PC was only 0.1% of the real physical time. The spring-type mechanical analogy was also widely adopted, e.g. by Shrimali and Jangid (2002a, 2002b and 2003), Damatty and Sweedan (2006) and Livaoglu (2008). Damatty and Sweedan (2006) considers the sloshing tank under the seismic excitation. The deformability of tank walls was taken into account in the motion equations. Livaoglu (2008) evaluated the sloshing effects when fluid-structure and soil-structure interactions matters during the earthquake.

3.5 Discussion

All methods reviewed in this chapter could be adopted to solve the sloshing problem defined in Chapter 2. This thesis aims to develop in-house CFD codes. So, conditions should be set to filter out the methods. The filter conditions are set in the following order, according to the factors that are considered mostly: (a) ‘Could the method be easily extended to simulate the sloshing in general tanks?’ (b) ‘Could the method give accurate enough results?’ (c) ‘Is the method efficient enough on a PC (based on our laboratory condition)?’ and (d) ‘Is the method technically easy to achieve (especially for the mesh processing)?’ The comparisons are listed in Table 3.1. If a method does not satisfy a condition well, it would be sifted out and will not be further checked by subsequent conditions. The symbol ‘-’ in the table means that the corresponding method has been disregarded at that stage. It can be seen that the BEM could be a proper option for sloshing simulations in this thesis.

Table 3.1 Comparison of methodology for sloshing simulation

	(a) General tank	(b) Accurate	(c) Efficient	(d) Easy meshing
				
Analytical method (e.g. Faltinsen 1978; Chapman & Porter 2005; Wu 2007; Faltinsen et al 2000; Faltinsen & Timokha 2002; Faltinsen et al 2003; Faltinsen et al 2005; La Rocca et al 2000; La Rocca et al 2002; La Rocca et al 2005; Love & Tait 2011; Love & Tait 2013; Wu et al 2001)	Unsuitable	-	-	-
Mechanical analogy (e.g. Abramson 1966; Dodge 2000; Pilipchuk & Ibrahim 1997; Ibrahim & EL-Sayad 1999; Aliabadi et al 2003; Godderidge et al 2012a,b; Shrimali & Jangid 2002a, 2002b, 2003; Dammaty & Sweedan 2006; Livaoglu 2008)	Good	Unsuitable	-	-
NS solver (e.g. Ramaswamy 1990; Takizawa & Koshizuka 1992; Chen & Chiang 1999; Chen & Nokes 2005; Ushijima 1998; Wu & Chen 2009; Chen & Wu 2011; Celebi & Akyildiz 2002; Kishev et al 2006; Liu & Lin 2008; Chen et al 2009; Souto-Iglesias et al 2004; Souto-Iglesias et al 2006; Rudman & Cleary 2009; Marsh et al 2010; Shao et al 2012; Khayyer & Gotoh 2010; Lee et al 2011; Gao 2011; Pan et al 2012)	Good	Good	Unsuitable	-
Potential-flow solver (domain discretization) (e.g. Chen et al 1996; Frandsen & Borthwick 2003; Frandsen 2004; Santos & Greaves 2007; Hernandez-Barrios et al 2007; Chern et al 1999; Chern et al 2001; Chern et al 2012; Nakayama & Washizu 1980; Okamato & Kawahara 1990; Wu & Eatock Taylor 1994; Turnbull et al 2003a, b; Wang & Khoo 2005; Sriram et al 2006; Wu et al 1998; Pal & Bhattacharyya 2010)	Good	Good	Good	Unsuitable
Potential-flow solver (BEM) (e.g. Faltinsen 1978; Nakayama & Washizu 1981; Liu & Huang 1994; Chen et al 2007)	Good	Good	Good	Good

Chapter 4 Numerical simulation of nonlinear sloshing in 3D rectangular tanks

4.1 Introduction

Over the past decades, it has been recognised that the sloshing problem exhibits nonlinearity (Faltinsen and Timokha 2009). In terms of the nonlinearity, one major difficulty is that the nonlinear boundary conditions have to be satisfied on the free surface not known *a priori*. This chapter would develop a numerical scheme to simulate the nonlinear sloshing in wall-sided tanks based on the BEM. Then, the numerical scheme will be verified and validated by a series of sloshing cases in 3D rectangular tanks. The rectangular tank has a length L, width B and initial liquid depth H. As defined in Chapter 2, the earth-fixed system $O_o - x_o y_o z_o$ and body-fixed system $O - xyz$ are used. The origin O is at the rotation centre and axes are parallel to edges of the rectangular tank. More parameters are illustrated in Fig. 4.1.

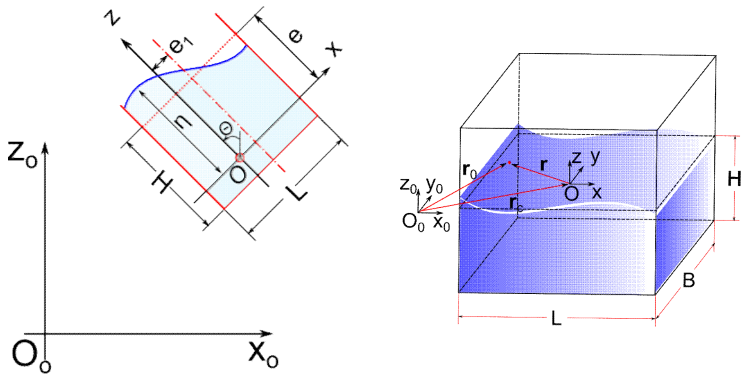

(a) (b)

Fig. 4.1 Sketch of (a) coordinate systems and (b) tank dimensions

The governing equation and boundary conditions of the sloshing problem are expressed by Eqs. (2.29)-(2.33). Aiming at wall-sided tanks, the notation $\delta/\delta t = \partial/\partial t + (\partial\eta/\partial t)\partial/\partial z$ is introduced into the dynamic free-surface boundary condition Eq. (2.33). This yields the semi-Lagrangian (SL) form of the dynamic free-surface condition

$$\frac{\delta\varphi}{\delta t}=\frac{\partial\varphi}{\partial z}\cdot\frac{\partial\eta}{\partial t}+\left(\mathbf{v}_c+\Omega\times\mathbf{r}\right)\cdot\nabla\varphi-\frac{1}{2}\nabla\varphi\cdot\nabla\varphi-gz_c-g\left(T_{31}x+T_{32}y+T_{33}\eta\right) \tag{4.1}$$

The operator $\delta/\delta t$ means the time derivative of a variable detected by a 'sensor' on S_F moving along the z axis.

Conservation laws of the fluid volume, momentum and energy are applied to test whether the numerical solutions are consistent with the governing equation and boundary conditions. The fluid volume V could be calculated according to the divergence theorem

$$V=\iiint_V dV=\frac{1}{3}\iiint_V\left(\nabla\cdot\mathbf{r}\right)dV=\frac{1}{3}\iint_S\left(\mathbf{r}\cdot\mathbf{n}\right)dS \tag{4.2}$$

where $\mathbf{r}$ is the position vector of a point on the surface. The centroid of V is

$$\begin{aligned} x_{ct}&=\frac{1}{V}\iiint_V xdV=\frac{\mathbf{i}}{2V}\cdot\iiint_V\nabla\left(x^2\right)dV=\frac{1}{2V}\iint_S x^2n_xdS;\\ y_{ct}&=\frac{1}{2V}\iint_S y^2n_ydS;\ \ z_{ct}=\frac{1}{2V}\iint_S z^2n_zdS \end{aligned} \tag{4.3}$$

where $\mathbf{i}$ denotes the unit vector of the Ox axis. As the momentum theorem states, the change of the fluid momentum is equal to the net impulse acting on the fluid, i.e.

$$\mathbf{M}_f\left(t\right)-\mathbf{M}_f\left(0\right)=\mathbf{I}_p\left(t\right)+\mathbf{I}_g\left(t\right) \tag{4.4}$$

where the momentum $\mathbf{M}$ is defined as

$$\mathbf{M}_f=\rho\iiint_V\left(\nabla_o\varphi\right)dV=\rho\iint_S\varphi\mathbf{n}dS \tag{4.5}$$

and the impulse $\mathbf{I}$ as a time integration of the force acting on the fluid is

$$\mathbf{I}_p\left(t\right)=-\int_0^t\left(\iint_S p\mathbf{n}dS\right)d\tau;\ \ \mathbf{I}_g\left(t\right)=-\rho gVt\ \mathbf{k}_o \tag{4.6}$$

The negative sign in Eq. (4.6) is due to the force direction. The pressure force acting on the tank is defined as $p\mathbf{n}$, while the tank has the reactive force $-p\mathbf{n}$ on the fluid. According to the work-energy theorem, the work done by all forces, including the gravity, acting on the fluid equals the change of the fluid's kinetic energy:

$$E_k(t) - E_k(0) = W_g(t) + W_p(t) \tag{4.7}$$

$$E_k = \iiint_V \frac{1}{2}\rho(\nabla_o\varphi \cdot \nabla_o\varphi)dV = \frac{\rho}{2}\iint_S \varphi\nabla_o\varphi \cdot \mathbf{n}dS = \frac{\rho}{2}\iint_S \varphi\varphi_n dS \tag{4.8}$$

$$W_p(t) = \int_0^t \left(\iint_S p\varphi_n dS\right)d\tau \tag{4.9}$$

$$W_g(t) = -\int_0^t \left(\iiint_V \rho g\mathbf{k} \cdot \nabla\varphi dV\right)d\tau = -\rho g\int_0^t \left(\iint_S \varphi n_z dS\right)d\tau \tag{4.10}$$

where E_k is the kinetic energy of the fluid, W_p is the work done by the pressure on the fluid boundary and W_g is the work done by the gravity.

4.2 Methodology description

4.2.1 Formulation of BEM

In order to solve the boundary value problem using BEM, the governing Laplace's equation of φ in V is firstly transformed into the boundary integral equation (BIE) over the entire fluid boundary S based on the Green's third identity (Newman 1977)

$$c(\mathbf{x}_p)\varphi(\mathbf{x}_p) = \iint_S \left[G(\mathbf{x}_p, \mathbf{x})\frac{\partial\varphi(\mathbf{x})}{\partial n} - \varphi(\mathbf{x})\frac{\partial G(\mathbf{x}_p, \mathbf{x})}{\partial n}\right]dS \tag{4.11}$$

where $\mathbf{x}_p = \{x_p, y_p, z_p\}$ denotes the collocation point, $\mathbf{x} = \{x, y, z\}$ presents the point on S, $c(\mathbf{x}_p)$ is the solid angle and $G(\mathbf{x}_p, \mathbf{x})$ denotes the Green's function which can be expressed as

$$G(\mathbf{x}_p, \mathbf{x}) = 1\Big/\left[(x - x_p)^2 + (y - y_p)^2 + (z - z_p)^2\right]^{1/2} \tag{4.12}$$

The BIE is numerically solved by the BEM. The boundary is firstly discretized into connected and non-overlapping elements. Let N_e be the total number of elements and S_e denotes the e-th element. Eq. (4.11) becomes

$$c(\mathbf{x}_p)\varphi(\mathbf{x}_p) + \sum_{e=1}^{N_e}\iint_{S_e}\left[\varphi(\mathbf{x})\frac{\partial G(\mathbf{x}_p, \mathbf{x})}{\partial n}\right]dS = \sum_{e=1}^{N_e}\iint_{S_e}\left[G(\mathbf{x}_p, \mathbf{x})\frac{\partial\varphi(\mathbf{x})}{\partial n}\right]dS \tag{4.13}$$

To carry out the integration, S_e can be mapped to a region S_e' on the two-dimensional $\xi-\varsigma$ plane. Coordinates of a point on the element can be approximated by

$$\begin{gathered} x(\xi,\varsigma)=\sum_{k=1}^{K} N_k(\xi,\varsigma)\,x_k;\quad y(\xi,\varsigma)=\sum_{k=1}^{K} N_k(\xi,\varsigma)\,y_k; \\ z(\xi,\varsigma)=\sum_{k=1}^{K} N_k(\xi,\varsigma)\,z_k \end{gathered} \tag{4.14}$$

where (x_k,y_k,z_k) are coordinates of the k-th node of the element, $N_k(\xi,\varsigma)$ are the shape functions and K is the total number of nodes on each element. In this thesis, the free surface is discretized by triangular elements ($K=3$), while the wetted tank surface is covered by quadrilateral elements ($K=4$). The expressions of $N_k(\xi,\varsigma)$ can be written as

$$\left.\begin{aligned} N_1(\xi,\varsigma)&=1-\xi-\varsigma \\ N_2(\xi,\varsigma)&=\xi \\ N_3(\xi,\varsigma)&=\varsigma \end{aligned}\right\}\ \text{for}\ K=3;\quad \left.\begin{aligned} N_1(\xi,\varsigma)&=0.25(1-\xi)(1-\varsigma) \\ N_2(\xi,\varsigma)&=0.25(1+\xi)(1-\varsigma) \\ N_3(\xi,\varsigma)&=0.25(1+\xi)(1+\varsigma) \\ N_4(\xi,\varsigma)&=0.25(1-\xi)(1+\varsigma) \end{aligned}\right\}\ \text{for}\ K=4 \tag{4.15}$$

The velocity potential and its normal derivative are assumed to be expressed in a similar way

$$\varphi(\xi,\varsigma)=\sum_{k=1}^{K} N_k(\xi,\varsigma)\,\varphi_k;\quad \frac{\partial\varphi(\xi,\varsigma)}{\partial n}=\sum_{k=1}^{K} N_k(\xi,\varsigma)\left(\frac{\partial\varphi}{\partial n}\right)_k \tag{4.16}$$

where φ_k and $\left(\frac{\partial\varphi}{\partial n}\right)_k$ are the values at the k-th node of the element.

All nodes on S are marked non-repetitively from 1 to N_p and $\varepsilon(e,k)$ is taken as the global index of k-th node of the e-th element. Eq. (4.13) becomes

$$\begin{aligned} &c_i\varphi_i+\sum_{e=1}^{N_e}\iint_{S_e'}\left[\sum_{k=1}^{K} N_k(\xi,\varsigma)\,\varphi_{\varepsilon(e,k)}\cdot\frac{\partial G(\xi,\varsigma)}{\partial n}\cdot\left|J(\xi,\varsigma)\right|\right]d\xi d\varsigma \\ &=\sum_{e=1}^{N_e}\iint_{S_e'}\left[\sum_{k=1}^{K} N_k(\xi,\varsigma)\left(\frac{\partial\varphi}{\partial n}\right)_{\varepsilon(e,k)}\cdot G(\xi,\varsigma)\cdot\left|J(\xi,\varsigma)\right|\right]d\xi d\varsigma \end{aligned} \tag{4.17}$$

where i is the global index of collocation point $\mathbf{x}_p$ and J is the Jacobian

matrix. The above equation can be written in a neater form

$$\sum_{j=1}^{N_p} H_{ij} \cdot \varphi_j = \sum_{j=1}^{N_p} G_{ij} \cdot \left(\frac{\partial \varphi}{\partial n} \right)_j \text{, for } i = 1, 2, \cdots, N_p \tag{4.18}$$

$$G_{ij} = \sum_{e=1}^{N_e} \sum_{k=1}^{K} \left[\iint_{S_e'} N_k(\xi, \varsigma) \cdot G(\xi, \varsigma) \cdot |J(\xi, \varsigma)| \, d\xi d\varsigma \right] \cdot \delta^j_{\varepsilon(e,k)} \tag{4.19}$$

$$H_{ij} = c_i \delta^i_j + \sum_{e=1}^{N_e} \sum_{k=1}^{K} \left[\iint_{S_e'} N_k(\xi, \varsigma) \cdot \frac{\partial G(\xi, \varsigma)}{\partial n} \cdot |J(\xi, \varsigma)| \, d\xi d\varsigma \right] \cdot \delta^j_{\varepsilon(e,k)} \tag{4.20}$$

where $\delta^i_j = \{1, i = j; 0, i \neq j\}$ is the Kronecker delta function. One can refer to Brebbia and Dominguez (1992) for details of numerical integrations in Eqs. (4.19) and (4.20). The solid angle is obtained geometrically as shown in Appendix A. Moving all the known terms to the right-hand side and the unknowns to the left could lead to a system of linear equations. After the solution of these equations, the value of φ and $\partial\varphi/\partial n$ on the full boundary surface could be known. The BVP of the auxiliary function χ could also be solved in the same way by replacing φ with χ.

4.2.2 Formulation of spatial derivatives

To calculate the tangential derivatives of φ at the free-surface node $\mathbf{x}_0$, a $\xi - \varsigma$ plane perpendicular to the normal vector is formed. The φ can be approximated as

$$\varphi^h(\mathbf{x}, \mathbf{x}_0) = \sum_{j=1}^{m} p_j(\mathbf{x}) a_j(\mathbf{x}_0) \tag{4.21}$$

where $\varphi^h(\mathbf{x}, \mathbf{x}_0)$ is the fitting function, $p_j(\mathbf{x})$ are the base functions and $a_j(\mathbf{x}_0)$ are the coefficients. The $p_j(\mathbf{x})$ can be chosen as polynomial functions. This gives the linear set $\{p_1, p_2, p_3\} = \{1, \xi, \varsigma\}$ for $m = 3$ and the quadratic set $\{p_1, p_2, \cdots, p_6\} = \{1, \xi, \varsigma, \xi^2, \xi\varsigma, \varsigma^2\}$ for $m = 6$.

To obtain the coefficients $a_j(\mathbf{x}_0)$, the weighted least-square method is used among $\mathbf{x}_0$ and its neighbouring nodes. Select N ($N \geq m$) nodes

$\mathbf{x}_n = \{\xi_n, \varsigma_n\}$ around $\mathbf{x}_0$. At each scattered node, it has

$$\begin{aligned} J^h(\mathbf{x}, \mathbf{x}_0) &= \sum_{n=1}^{N} w(\mathbf{x}_n - \mathbf{x}_0) \cdot \left[\varphi^h(\mathbf{x}_n, \mathbf{x}_0) - \varphi(\mathbf{x}_n)\right]^2 \\ &= \sum_{n=1}^{N} w(\mathbf{x}_n - \mathbf{x}_0) \cdot \left[\sum_{j=1}^{m} p_j(\mathbf{x}_n) a_j(\mathbf{x}_0) - \varphi(\mathbf{x}_n)\right]^2 \end{aligned} \tag{4.22}$$

where $w_n = w(\mathbf{x}_n - \mathbf{x}_0)$ is the weight function and $\varphi(\mathbf{x}_n)$ is the known value at the node $\mathbf{x}_n$. It should be noted that once the weight function $w_n = w(\mathbf{x}_n - \mathbf{x}_0)$ is constant, the expression of $J^h(\mathbf{x}, \mathbf{x}_0)$ is the same as the normal least-square method. To get a minimised value of $J^h(\mathbf{x}, \mathbf{x}_0)$, the following conditions should be imposed

$$\frac{\partial J^h}{\partial a_i} = 0, \text{ for } i = 1, 2, \cdots, m \tag{4.23}$$

i.e.

$$\begin{aligned} \frac{\partial J^h}{\partial a_i} &= 2\sum_{n=1}^{N} p_i(\mathbf{x}_n) \cdot w(\mathbf{x}_n - \mathbf{x}_0) \cdot \left[\sum_{j=1}^{m} p_j(\mathbf{x}_n) a_j(\mathbf{x}_0) - \varphi(\mathbf{x}_n)\right] \\ &= 2\sum_{n=1}^{N} p_i(\mathbf{x}_n) \cdot w(\mathbf{x}_n - \mathbf{x}_0) \cdot \left[\sum_{j=1}^{m} p_j(\mathbf{x}_n) a_j(\mathbf{x}_0)\right] - 2\sum_{n=1}^{N} p_i(\mathbf{x}_n) \cdot w(\mathbf{x}_n - \mathbf{x}_0) \cdot \varphi(\mathbf{x}_n) \\ &= 2\sum_{j=1}^{m} a_j(\mathbf{x}_0) \left[\sum_{n=1}^{N} w(\mathbf{x}_n - \mathbf{x}_0) \cdot p_i(\mathbf{x}_n) \cdot p_j(\mathbf{x}_n)\right] - 2\sum_{n=1}^{N} w(\mathbf{x}_n - \mathbf{x}_0) \cdot p_i(\mathbf{x}_n) \cdot \varphi(\mathbf{x}_n) \\ &= 0 \end{aligned} \tag{4.24}$$

Thus, a system of linear equations could be formulated

$$\sum_{j=1}^{m} A_{ij} a_j = B_i, \text{ for } i = 1, 2, \cdots, m \tag{4.25}$$

For $m = 6$ and $N \geq m$, A_{ij} and B_i have the form

$$A_{ij} = \sum_{n=1}^{N} w_n \beta_{ni} \beta_{nj}; \quad B_i = \sum_{n=1}^{N} w_n \beta_{ni} \varphi(\mathbf{x}_n) \tag{4.26}$$

$$\beta_{n1} = 1; \quad \beta_{n2} = \xi_n; \quad \beta_{n3} = \varsigma_n; \quad \beta_{n4} = \xi_n^2; \quad \beta_{n5} = \xi_n \varsigma_n; \quad \beta_{n6} = \varsigma_n^2 \tag{4.27}$$

In this study, the weight $w_n = w(\mathbf{x}_n - \mathbf{x}_0)$ is chosen to be a spline function

$$w(\mathbf{x}_n - \mathbf{x}_0) = 1 - 6(d_n/D)^2 + 8(d_n/D)^3 - 3(d_n/D)^4, \quad 0 \le (d_n/D) \le 1 \tag{4.28}$$

where d_n is the distance between $\mathbf{x}_n$ and $\mathbf{x}_0$. The size of the support domain D is chosen to be twice the size of the local element.

Known the coefficients $a_j(\mathbf{x}_0)$, the derivatives $\partial\varphi^h/\partial\xi$ and $\partial\varphi^h/\partial\varsigma$ can be obtained from a direct differentiation of Eq. (4.21). The tangential derivatives of φ could be transferred to $O-xyz$ as needed. By setting the $\xi-\varsigma$ plane as $O-xy$, one can also obtain the tangential spatial derivatives of η in a similar way.

4.2.3 Mesh handling technique

As mentioned above, to perform the BEM calculation, the fluid boundary surface should be firstly discretized into the surface mesh. In general, the surface mesh falls into two groups: structured and unstructured mesh. Structured mesh has regular connectivity, so that the neighbours of each mesh element are explicitly known. For example, if the index array (i,j) is used to represent a mesh node, this mesh node may have neighbour nodes with the indices of $(i\pm1,j)$ or $(i,j\pm1)$. The unstructured mesh, in contrast, is arranged in an arbitrary fashion, which has advantages in discretizing complicated surfaces but requires a more complex numbering system.

In the present study, a mixture of both meshes is to be adopted. The walls and bottom of the tank are covered by the structured mesh. In the depth direction of the side walls, mesh nodes are distributed rationally (Chung, 2002) as

$$z_i = \eta - (h+\eta)\frac{(\gamma+1)-(\gamma-1)\left(\frac{\gamma+1}{\gamma-1}\right)^{1-i/m}}{\left(\frac{\gamma+1}{\gamma-1}\right)^{1-i/m}+1}, i = 0,1,\cdots,m \tag{4.29}$$

where z_i is the vertical coordinate of each node, m is the number of mesh nodes in the vertical direction and $\gamma > 1$ is a constant. The larger the value of $(\gamma-1)$ is, the more uniform the node distribution will be. In this study, the value of γ is chosen as 1.5.

The free surface is covered by the unstructured mesh with triangular elements. This thesis has also developed an in-house mesh generation code based on the Delaunay triangulation technique. The technical details are provided in Appendix B. With the input coordinates of the boundary nodes, the program will automatically generate the unstructured mesh on the plane surface. It should be mentioned that it is a general-purpose mesh generation code, which is not restricted to cases of the rectangular domain considered in this chapter. As shown in Appendix B, a complex fluid domain such as multi-connected domain with outer and inner boundaries can also be well coped with.

During the time stepping, free-surface boundary conditions coupled with the 4th-order Runge-Kutta updating method are used to update the free-surface position and the velocity potential on it. The structured mesh on the tank walls is stretched accordingly, so that the wall nodes are always distributed rationally from the free surface to the bottom.

4.2.4 Parallel computation procedure

The BEM generally produces dense and non-symmetric matrices. For the present 3D calculation with a few thousand of unknowns, the computation of the matrix elements normally consumes the largest proportion of the CPU time. Since integrations in Eqs. (4.19) and (4.20) are independent of one another, the parallel procedure could be introduced to further improve the computational efficiency. The OpenMP parallel programming that relies on multiple CPU cores of the computer is applied in the present numerical scheme. Compared with serial acceleration algorithms (e.g. the fast multipole method and pre-corrected fast Fourier transform method) and the MPI parallel programming, the OpenMP is relatively easy to implement. One only needs to add a few lines to the traditional serial BEM codes to achieve the parallelism. The workflow of the parallel procedure is illustrated in Fig.4.2. The parallel region is defined within the matrix construction module. To be specific, the calculation of H_{ij} and G_{ij} for $i = 1 \sim N_1$ is performed on Core-1 of the CPU, the calculation for $i = N_1 + 1 \sim N_2$ is performed on Core-2, and so on. Thus, the calculation burden of matrix elements has been distributed on

multiple CPU cores, reducing the time consumption.

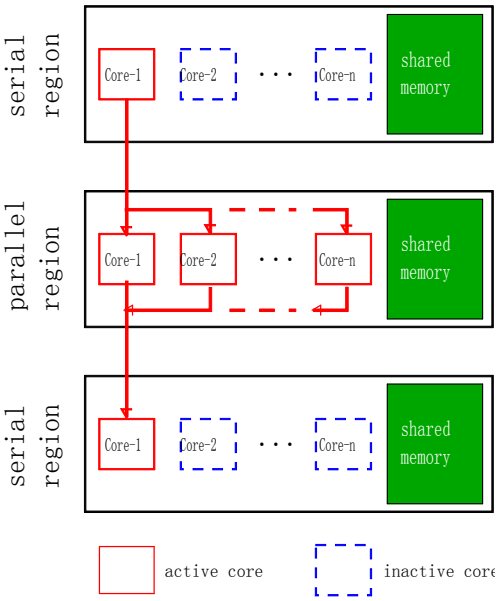

Fig. 4.2 Working principle of parallel procedure

4.3 Convergence study and efficiency test

The convergence of the numerical scheme is to be verified in this section. The natural sloshing frequencies of a 3D rectangular tank (Faltinsen and Timokha 2009) are denoted by ω_{mn}

$$\omega_{mn}=\sqrt{g\pi\sqrt{\left(\frac{m^2}{L^2}+\frac{n^2}{B^2}\right)}\tanh\left(\pi\sqrt{\left(\frac{m^2}{L^2}+\frac{n^2}{B^2}\right)}H\right)} \tag{4.30}$$

where $m,n=0,1,2,\cdots$ and $m\cdot n\neq 0$. Here, it should be noted that the subscript m and n correspond to the directions along the length and width side of the 3D rectangular tank, respectively. For example, ω_{30} denotes the third smallest natural frequency in the x direction, and ω_{02} is the second smallest natural frequency in the y direction. In this chapter, unless specific statements are made, the results will be nondimensionalised by $(x,y,z,\eta)\to(x,y,z,\eta)H$, $t\to\tau\sqrt{H/g}$, $\omega\to\omega\cdot\sqrt{g/H}$ and $\varphi\to\varphi\cdot H\sqrt{gH}$. Here, the displacement of the tank is set as $x_c(\tau)=A_x\sin(\omega_x\tau)$, $y_c=0$ and $z_c=0$, where A_x is the amplitude and ω_x is the frequency. Note that the tank is only undergoing a surge excitation. The parameters are set as $L=2$, $B=0.4$, $A_x=0.01$ and $\omega_x=\omega_{10}$.

Firstly, the convergence with the mesh is studied. For the surface mesh, M_1, M_2 and M_3 are used to denote the numbers of segments along the length, width and depth edge of the tank, respectively. Mesh-1 with $(M_1 \times M_2 \times M_3) = (20 \times 3 \times 6)$ and Mesh-2 with $(M_1 \times M_2 \times M_3) = (40 \times 6 \times 12)$ are adopted for comparison. The temporal step Δt is fixed as $1/100$ of the excitation period $T = 2\pi / \omega_x$. The upper subfigure of Fig.4.3 shows the wave elevation history along the left tank wall, while the lower subfigure shows the spatial distribution of the wave elevation in the x direction at an instant $\tau = 10.37$. To show the comparison details clearly, the history of the wave elevation is stretched and only the first 8 periods are shown in Fig.4.3. Fig. 4.3 shows that the corresponding curves are graphically identical for this scale under consideration. Since Mesh-2 is a refinement of Mesh-1 in each of the three dimensions, it is reasonable to think that further refining Mesh-1 to Mesh-2 does not affect the simulation results much. In other words, Mesh-1 can guarantee the mesh convergence. For the cases in this thesis, 20 segments along the wave propagation direction could generally guarantee the mesh convergence. In the following simulations, meshes of $(M_1 \times M_2) = (20 \times 3)$ and $(M_1 \times M_2) = (20 \times 20)$ are adopted for 2D and 3D cases, respectively. The value of M_3 may vary from 4 to 10 depending on the water depth. Fig.4.4 shows two examples of the mesh models.

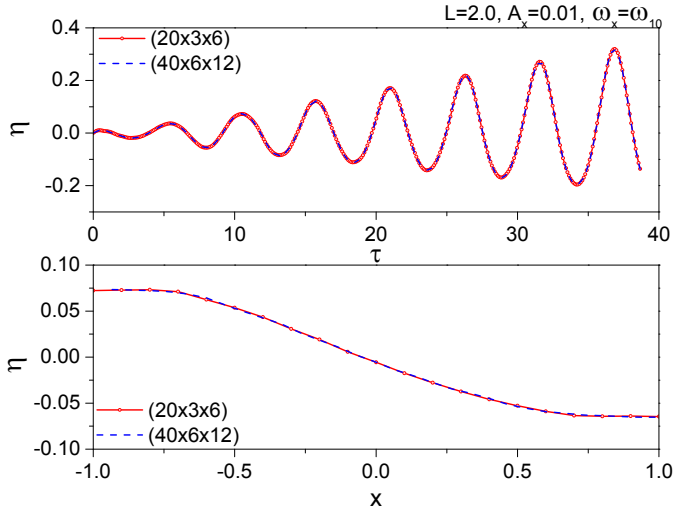

Fig. 4.3 Wave elevation history and free-surface profile for mesh convergence study

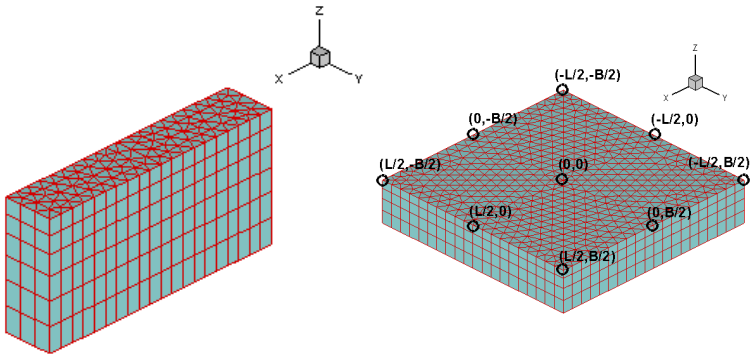

(a) (b)

Fig. 4.4 Mesh models for (a) 2D and (b) 3D simulations

Then, the temporal convergence is studied. The results when $\Delta t = T/50$ and $\Delta t = T/100$ are compared. Fig.4.5 shows the free-surface elevation history at the left tank wall. These two lines are also coincident with each other. To save the computation resources, $\Delta t = T/50$ is selected for future simulations. This time step can guarantee the Courant number $C_r = \bar{v}\Delta t/\Delta l \le 0.5$, where $\bar{v}$ is the average linear velocity at a mesh node and Δl is the local dimension of the mesh element.

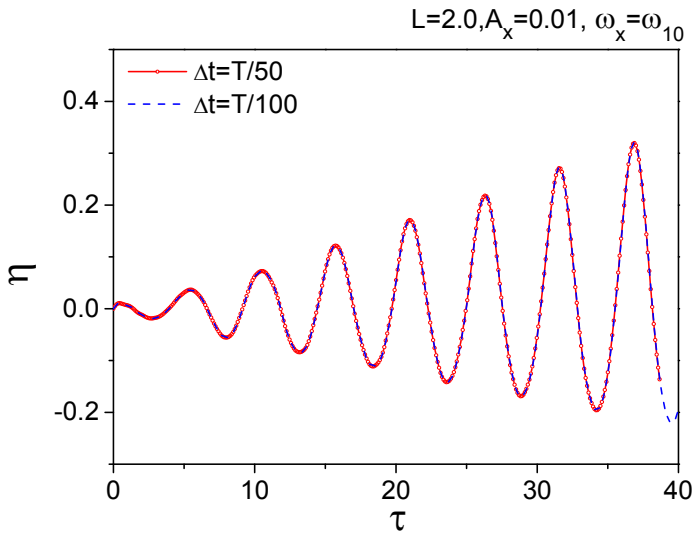

Fig. 4.5 Wave elevation history for temporal convergence study

The effectiveness of the parallel computation procedure should also be studied. The simulations would be carried out on the PC with Intel(R) Core(TM) i7-3770 CPU, using Intel(R) Visual Fortran Compiler XE 2013 as the compiler of the Fortran codes. The parallel procedure is applied to the

most time-consuming module of the BEM solver, i.e. the matrix calculation module. There are 8 CPU cores in maximum that could be assigned for the parallelism. Consider the mesh model with 1898 boundary elements and 1391 mesh nodes. Fig.4.6(a) compares the consumed CPU time for calculating the BEM matrix when a different number of cores are involved. It is observed that, as the number of cores increases from 1 to 5, the CPU time reduces dramatically. After that, the parallel acceleration slows down. When 8 cores are applied, the CPU time has reached nearly a quarter of that of the single-core calculation. After the calculation and construction of the BEM matrix, a system of equations could be obtained. The number of unknowns of the equation system is the same as the number of mesh nodes (i.e. 1391 in the present model). Note that the generated matrix of the system of equations is fully populated and unsymmetrical. So the generalised minimal residual (GMRES) equation solver is preferred, as an efficient iterative approach for an unsymmetric system of linear equations. Due to the limited scale of the present model, preconditioners that might be used to quicken the convergence of the GMRES solver are not needed. The iteration error is set to be 10^{-9}, and it takes about 4.5 seconds for each solution with less than 100 iterations. Fig.4.6(b) shows the efficiency comparison between paralleled (using 8 cores) and unparalleled codes for other mesh models. It is observed that, for the same problem, the paralleled code is nearly 4 times faster than the unparalleled one. Comparing with the matrix construction, the CPU time for solving the equations is much less. So, the paralleled procedure is not involved in the equation solving module. It is noted that the CPU time is sensitive to the concerned problem. The value of the CPU time in Fig.4.6 does not have to be the same for a different problem with the same number of elements.

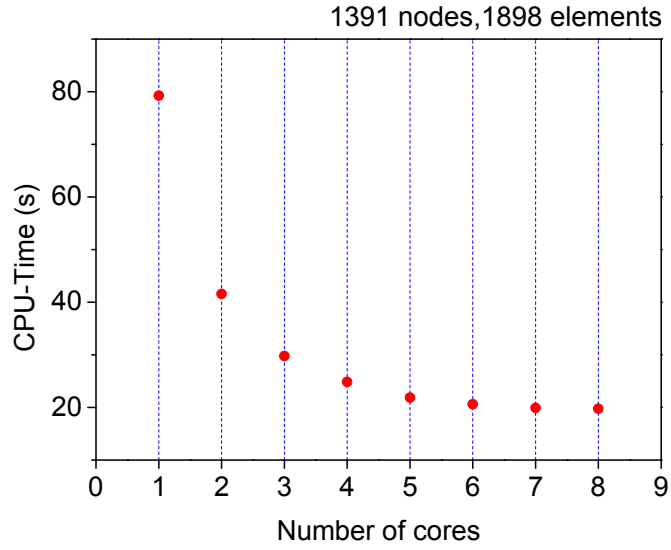

(a)

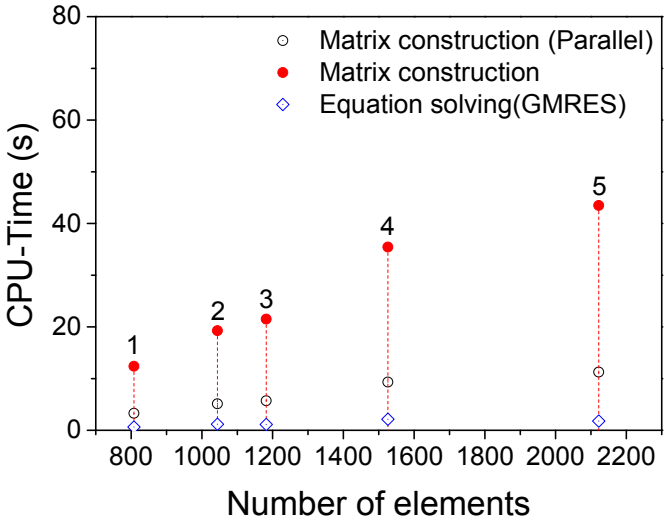

(b)

Fig. 4.6 Comparisons of CPU time consumption

4.4 Accuracy study and validation

In this section, the present numerical scheme is to be verified and validated through a series of case studies. The verification is to make sure that the numerical solutions are consistent with the governing equation together with boundary conditions. It could be achieved by testing (1) the temporal and spatial convergence as in Section 4.3 and (2) the conservation of the liquid mass, momentum and energy. Comparisons should be made with analytical methods such as the linear potential-flow theory. The validation is to

check the mathematical model of the numerical scheme by comparing with experiments.

4.4.1 Free sloshing in stationary tank

The free sloshing in a stationary tank is considered. The inside liquid has an initial free-surface profile. During the sloshing, the liquid motion is only driven by the gravity, and no extra energy is input into the system. In the first case, the fluid has a cosine-type initial surface profile, i.e. $\eta_{\text{ini}} = A\cos\left[2\pi\left(x+L/2\right)/L\right]$. The analytical solution of the wave elevation can be found in Wu and Eatock Taylor (1994) based on the perturbation approach. The first and second-order nonlinear wave elevations at the centre of the free surface are

$$\eta^{(1)}(0,0,t) = A\cos\omega_2 t\cos\left(\frac{1}{2}k_2 L\right) \tag{4.31}$$

$$\eta^{(2)}(0,0,t) = \frac{1}{8g}\begin{pmatrix} 2(\omega_2 A)^2\cos 2\omega_2 t + \dfrac{A^2}{\omega_2^2}(k_2^2 g^2 + \omega_2^4) \\ -\dfrac{A^2}{\omega_2^2}(k_2^2 g^2 + 3\omega_2^4)\cos\omega_4 t \end{pmatrix} \tag{4.32}$$

where A is the initial wave amplitude, $k_n = n\pi / L$ and $\omega_n = \sqrt{k_n g\tanh\left(k_n H\right)}$.

For the tank with $L = 2$, the wave elevation history at the centre of the free surface is given in Fig.4.7. Effects of various initial wave amplitudes are tested. In Fig.4.7(a-1) when the initial amplitude is as small as $A = 0.01$, the linear, second-order and obtained nonlinear numerical results are in a good agreement. Having increased A to the value 0.05, the distinction between the linear and numerical solutions can be observed, although the second-order solution still agrees well with the numerical one (Fig.4.7(b-1)). In the case of $A = 0.1$, Fig.4.7(c-1) shows that the agreement between the second-order and numerical solution is not as good as the previous two cases. In this case, the wave nonlinearities such as sharper crests, flatter troughs and longer periods have become evident. These observations are consistent with those in Greaves et al (1997) and Wu et al (1998) using FEM. The conservation of the fluid volume, momentum and energy are checked in

Figs.4.7 (a-2), (b-2) and (c-2). During the whole simulation, the maximum percentage of volume error is less that 0.03%, the fluid momentum is in good agreement with the impulse for the z-direction, and the kinetic energy of the fluid is coincident with the work done by the gravity.

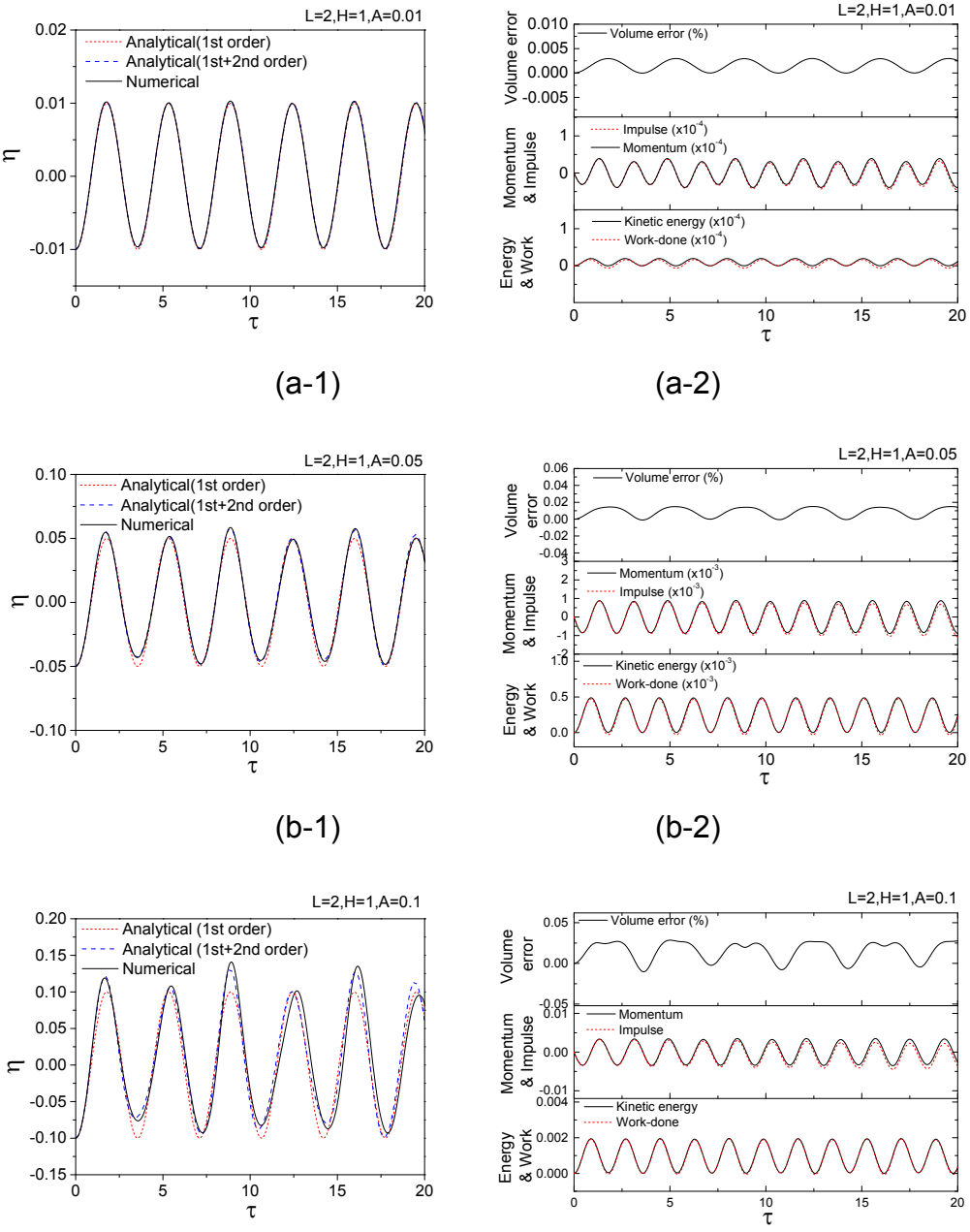

Fig. 4.7 Wave elevation history and conservation check for free sloshing with cosine-type symmetric initial surface profile

Further, consider the case when the initial free surface is asymmetric. Assuming an inclined free surface of $\eta_{ini} = (2A/L)x$, the first-order analytical

solution derived by Wu and Eatock Taylor (1994) has the expression

$$\eta(x,t)=\frac{2A}{L^2}\sum_{n=1}^{\infty}\frac{a_n}{k_n^2}\cos(\omega_n t)\cos\left(k_n(x+L/2)\right) \tag{4.33}$$

where $a_n=-2+2\cos(k_nL)+k_nL\sin(k_nL)$. For the tank of $L=2$, the wave elevation histories at the left tank wall are obtained. For the case of $A=0.01$ in Fig.4.8(a-1), the numerical solution shows a good agreement with the analytical one. After increasing A to 0.1, the nonlinear effects become more evident as in Fig.4.8(b-1). The conservation of the fluid volume, momentum and energy in Figs.4.8(a-2) and (b-2) confirm the accuracy of this numerical scheme.

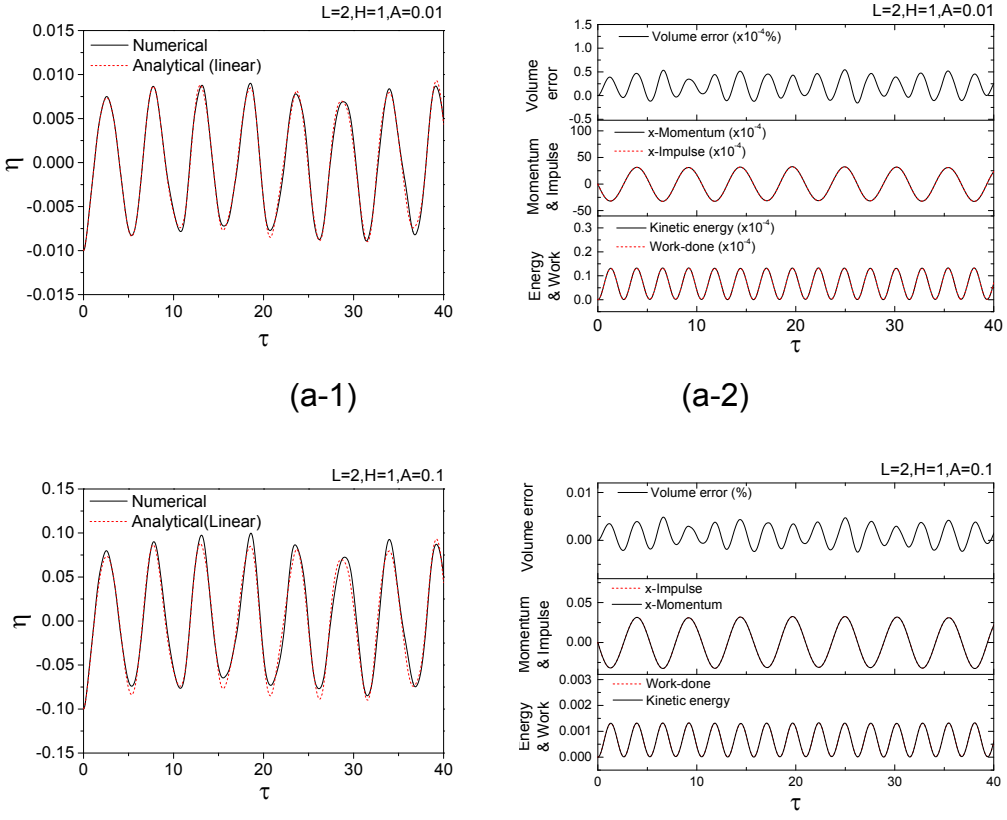

Fig. 4.8 Wave elevation history and conservation check for free sloshing with asymmetric initial surface profile

4.4.2 Forced sloshing due to horizontal excitation

For the forced sloshing, the liquid motion is excited by the tank undergoing a prescribed oscillation. Comparing with the previous free

sloshing, the tank motion will be taken into account. In this subsection, the sloshing due to the surge excitation is simulated. The free surface is ensured to be stationary before the excitation is started.

In the first case, the situation when the tank is undergoing a small amplitude excitation is considered, so that the obtained numerical results could be compared with analytical solutions derived in Faltinsen (1978). When the tank is undergoing the motion of $x_c(\tau) = A_x \sin(\omega_x \tau)$, the analytical wave elevation has the form

$$\begin{aligned}\eta(x,y,t) = &\frac{A}{g}\left(x\omega^2 + \sum_{n=0}^{\infty} C_n \omega \sin k_n' x \right) \sin \omega t \\ &- \frac{A}{g} \sum_{n=0}^{\infty} \omega_n' \left(C_n + \frac{H_n}{\omega^2} \right) \sin k_n' x \sin \omega_n' t\end{aligned} \tag{4.34}$$

where $k_n' = \pi(2n+1)/L$, $\omega_n' = \sqrt{g k_n' \tanh(k_n' H)}$, $H_n = 4\omega^3 (-1)^n / (L k_n'^2)$ and $C_n = H_n / (\omega_n'^2 - \omega^2)$. Parameters are set as $L = 2$ and $A_x = 0.001$. Two frequencies $\omega_x = 0.9\omega_{10}$ and $\omega_x = \omega_{10} = 1.20$ are considered. The wave elevation histories on the left tank wall are given in Fig.4.9 (a-1) and (b-1), which shows that the numerical and analytical solutions are nearly coincident with each other. From Fig.4.9 (a-2) and (b-2), the corresponding conservation results are also satisfactory.

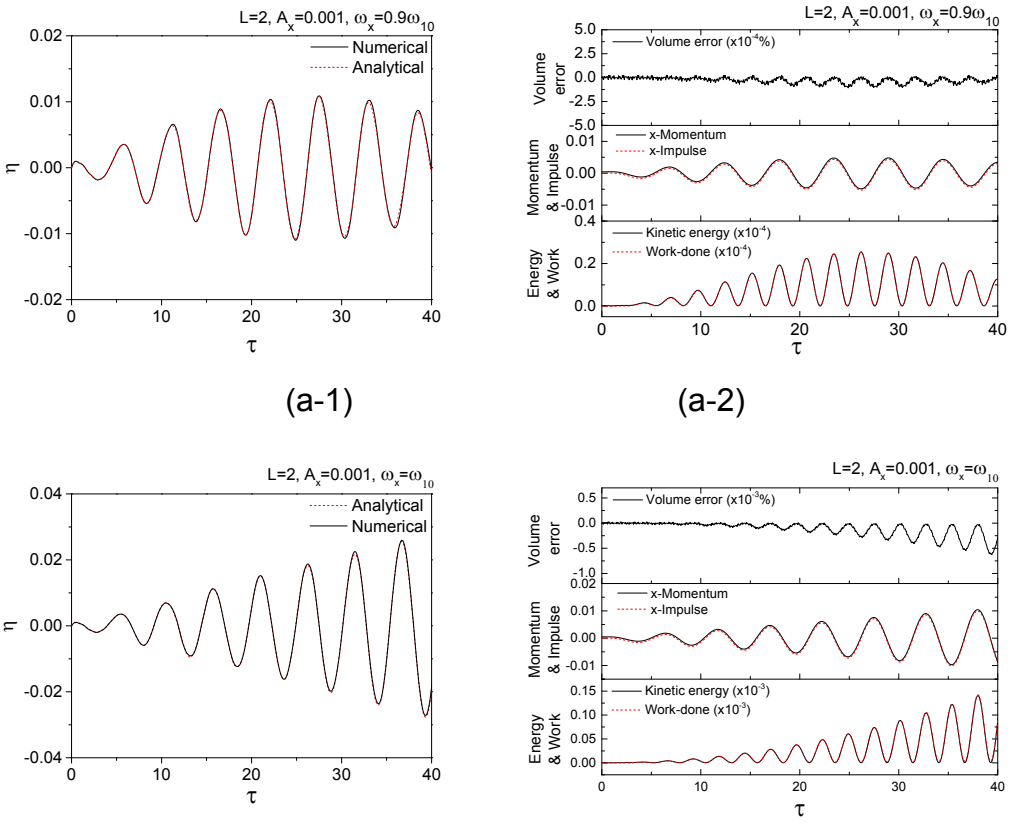

Fig. 4.9 Wave elevation history and conservation check for forced sloshing due to surge excitation

In the second case, the sloshing with a larger amplitude is considered. The numerical results are compared with the experimental data (Liu and Lin 2008) and linear analytical solutions. It should be noted that, in this thesis, dimensional values are used when a comparison with experimental data or some literature is needed. A special statement will be made for each case using dimensional parameters. For this case, dimensional parameters are adopted as $L=0.57m$, $H=0.15m$, $x_c=-A_x\sin(\omega_x t)$, $y_c=0$, $z_c=0$, $A_x=0.005m$ and $\omega_x=6.0578\,rad/s$. From the linear analytical theory, it is known that the first-order resonance occurs in this situation. Fig.4.10 shows the free-surface elevation histories measured at the right tank wall and the free-surface centre. Comparing with analytical solutions, the numerical results have demonstrated evident nonlinear effects such as sharper crests and flatter troughs. The numerical results have a good agreement with the experimental data, which

has not only verified the numerical accuracy but also validated the mathematical model.

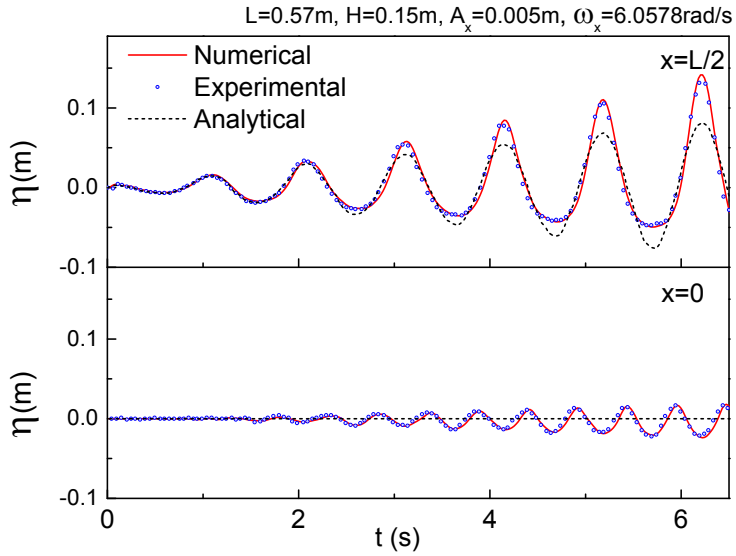

Fig. 4.10 Wave elevation history for forced sloshing due to surge excitation

The third case aims to check the simulation of wave profiles. The sloshing experiment in Gao (2011) is reproduced by the numerical scheme. Dimensional parameters are also adopted. The tank has length $L=0.6m$ and initial filling depth $H=0.3m$. A wave probe is placed $0.02m$ from the right wall to measure the free surface elevation. The tank undergoes a cosine-type surge excitation. The amplitude and frequency of the excitation are set as $A=0.005m$ and $\omega=6.85rad/s$, respectively. The time history of the free-surface elevation is plotted in Fig.4.11 for comparison. Excellent agreement between the numerical and experimental results is observed. The free-surface profiles at different time instants ($t=0.00s$, $2.10s$, $4.35s$ and $5.775s$) are shown in Fig.4.12. The sub-figures (a-i) are the numerical results, in which the mesh on the tank wall at $y=-B/2$ is shown to indicate the free-surface profile. Sub-figures (b-i) are experimental photographs at the corresponding time instant. There is a fairly good agreement between the numerical and experimental free-surface profiles.

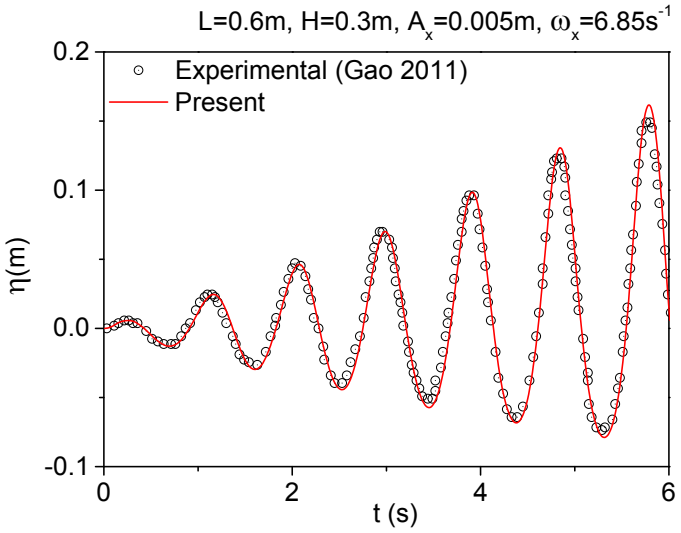

Fig. 4.11 Wave elevation history for $L=0.6m$, $H=0.3m$, $A_x=0.005m$ and $\omega_x=6.85rad/s$

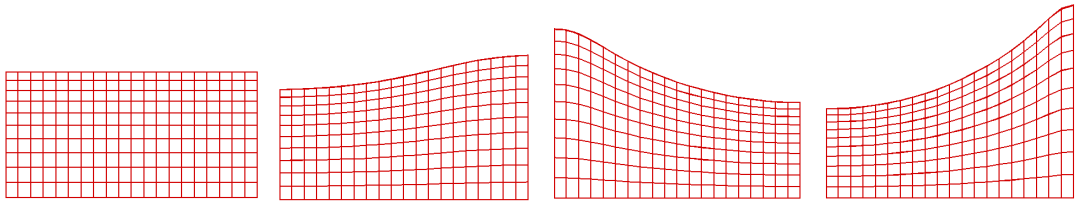

(a-1) (a-2) (a-3) (a-4)

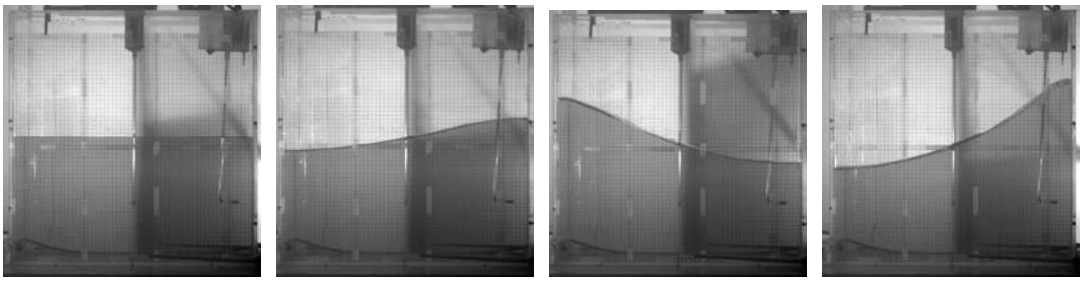

(b-1) (b-2) (b-3) (b-4)

Fig. 4.12 Snapshots of sloshing waves at $t=0.00s, 2.10s, 4.35s$ and $5.775s$ for $L=0.6m$, $H=0.3m$, $\theta=0$, $A=0.005m$ and $\omega=6.85rad/s$: (a-i) present results (b-i) experiments by Gao (2011)

In the fourth case, the situation when the tank is undergoing a large amplitude excitation as in Xue and Lin (2011) is considered. The tank has a length of $L=0.57m$ and water depth of $H=0.18m$. The surge displacement also follows a cosine function $x=-A_x\cos(\omega_x t)$ with $A_x=0.1m$ and

$\omega_x = 3.5317\,rad/s$. Wave gauges are placed at $\Delta x = \pm 0.275m$ away from the tank centre. It is observed that the tank sloshing, in this case, is very complex and irregular. Yet, as shown in Fig.4.13, the agreement between free-surface elevations from the present numerical scheme, experimental data and VOF solver is still satisfactory.

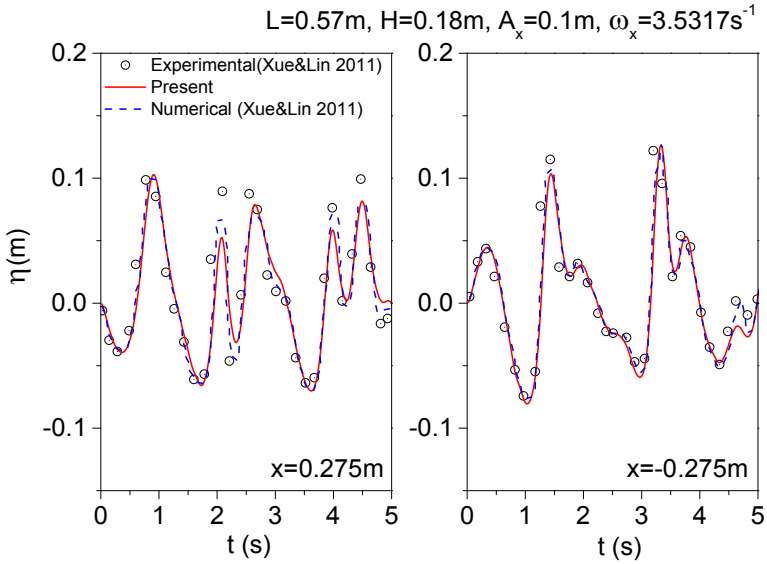

Fig. 4.13 Wave elevation history for $L = 0.57m$, $H = 0.18m$, $A_x = 0.1m$ and $\omega_x = 3.5317\,rad/s$

The fifth case further considers the 3D sloshing when the tank is undergoing a coupled surge and sway oscillation. The numerical results are compared with Wu et al (1998) which simulated this nonlinear sloshing problem based on FEM. The displacement of the tank is governed by $x_c = A_x \sin(\omega_x \tau)$, $y_c = A_y \sin(\omega_y \tau)$ and $z_c = 0$. Fig.4.14 presents the free-surface elevation histories at four tank corners, with the parameters of $L = 8$, $B = 4$, $A_x = 0.0372$, $A_y = 0.0186$, $\omega_x = 0.3831$ and $\omega_y = 0.7177$. Fig.4.15 compares histories of the dynamic pressure at two corners of the tank bottom, for $L = B = 4$, $A_x = A_y = 0.0372$, $\omega_x = \omega_{10} = 0.7177$ and $\omega_y = \omega_{01} = 0.7177$. It could be seen that present BEM results agree well with the corresponding FEM results in Wu et al (1998).

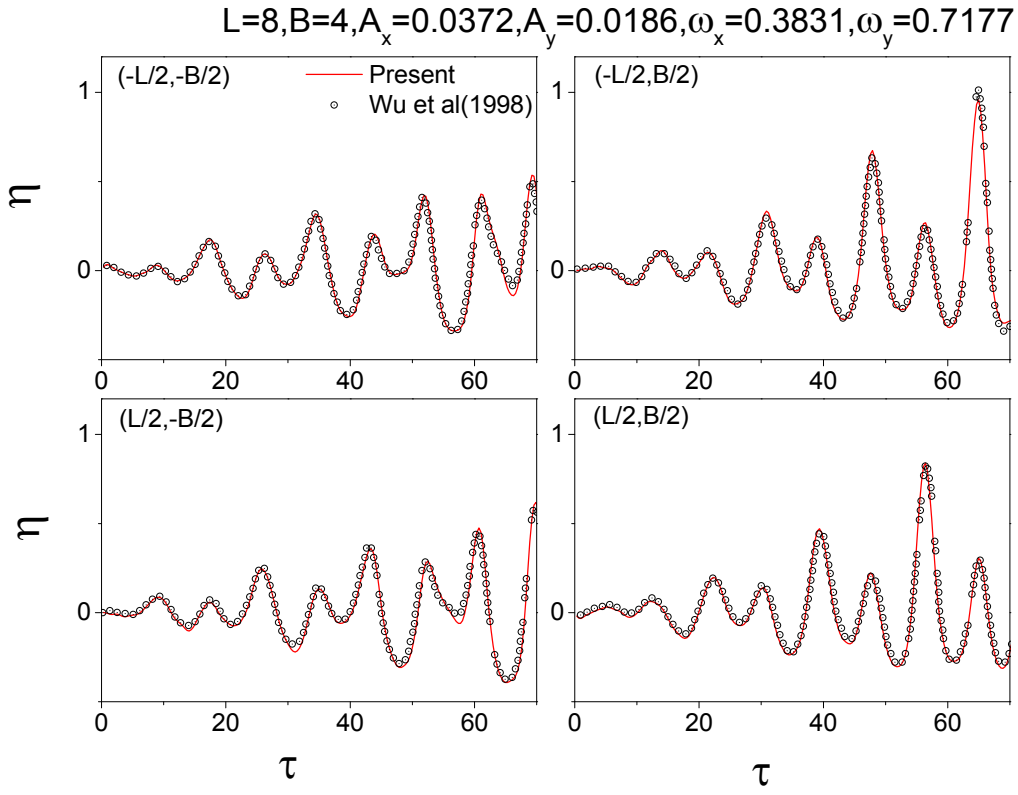

Fig. 4.14 Wave elevation histories for forced sloshing due to coupled-surge-sway excitation

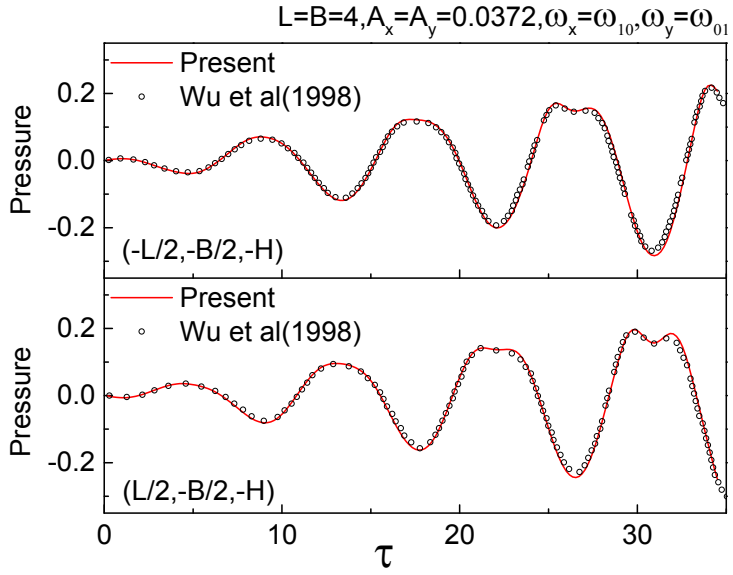

Fig. 4.15 Dynamic pressure histories at two corners of the tank bottom

4.4.3 Forced sloshing due to vertical excitation

Then the situation when the vertical oscillation is involved is considered. If a tank with an undisturbed initial free surface is accelerated vertically, ideally,

the interface would keep flat and the entire fluid moves like a rigid body. However, there exists the unstable state, under which even a tiny disturbance to the fluid could lead to a violent sloshing. Waves induced by vertical oscillations, as a consequence of the hydrodynamic instability, are the famous Faraday waves (Faraday 1831). Properties of Faraday waves would be further discussed in Chapter 8. This subsection only focuses on the verification of this numerical scheme.

One unstable case mentioned in Nakayama and Washizu (1981) is firstly simulated. The free surface has an initial profile $\eta_{ini} = A \cdot \cos(2\pi x/L)$ with $L = 2H$ and $A = 0.01L$ to generate a disturbance. The motion parameters are set as $z_c = -A_z \cdot \sin(\omega_z t)$, $A_z = 0.01L$ and $\omega_z = 5.0\sqrt{g/L}$. Comparisons of the wave elevation history along the right wall and at the tank centre are shown in Fig.4.16. Present numerical results have a good agreement with the FEM results in Nakayama and Washizu (1981).

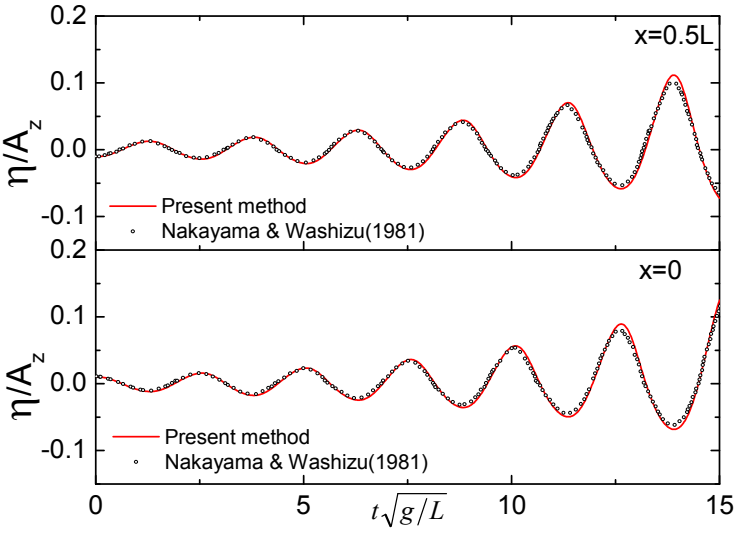

Fig. 4.16 Wave elevation history for forced sloshing due to heave excitation

Two more unstable cases mentioned in Frandsen (2004) are also simulated. Parameters are set as $\eta_{ini} = A \cdot \cos(k_n \cdot (x + L/2))$, $z_c = A_z \cdot \cos(\omega_z t)$ and $L = 2H$. Other parameters are set as $\omega_z = 2\omega_{10}$, $A_z = 0.3g/\omega_z^2$ and $A = 0.0014g/\omega_{10}^2$ in one case and $\omega_z = 2\omega_{30}$, $A_z = 0.2g/\omega_z^2$ and $A = 0.0014g/\omega_{30}^2$ in the other. As explained in Section 4.3, the subscript m

and n of ω_{mn} in Eq.(4.30) indicate two dimensions. So, ω_{10} and ω_{30} in this case denote the first and third smallest natural frequency in the x direction, respectively. Wave elevation histories along the left wall, obtained from the present method and FDM in the literature, are compared in Fig.4.17. It can be seen that, for either case, two results agree well with each other.

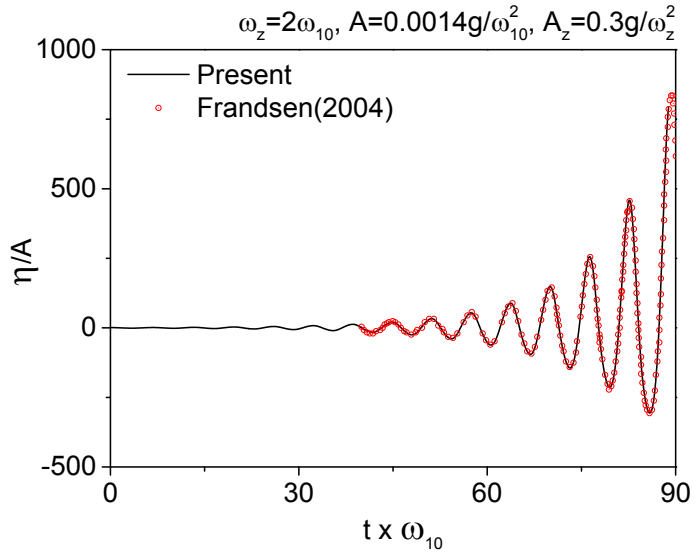

(a)

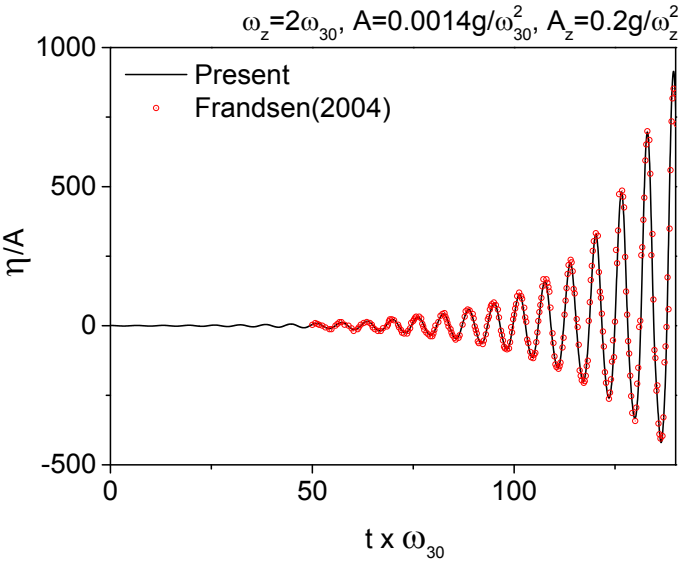

(b)

Fig. 4.17 Wave elevation history for forced sloshing due to heave excitation

Further the case when the liquid tank is undergoing surge and heave motions at the same time is considered. The free surface is initially flat.

Parameters given in Frandsen (2004) are adopted, i.e. $x_c = A_x \cdot \cos(\omega_x t)$, $z_c = A_z \cdot \cos(\omega_z t)$, $L = 2H$, $\omega_z = \omega_{10}/1.253$, $A_z = 0.5g/\omega_z^2$, $\omega_x = 0.98\omega_{10}$ and $A_x = 0.0014g/\omega_x^2$. Referring to Fig.4.18, the obtained wave elevation history along the left wall has also shown a good agreement with that from FDM in Frandsen (2004).

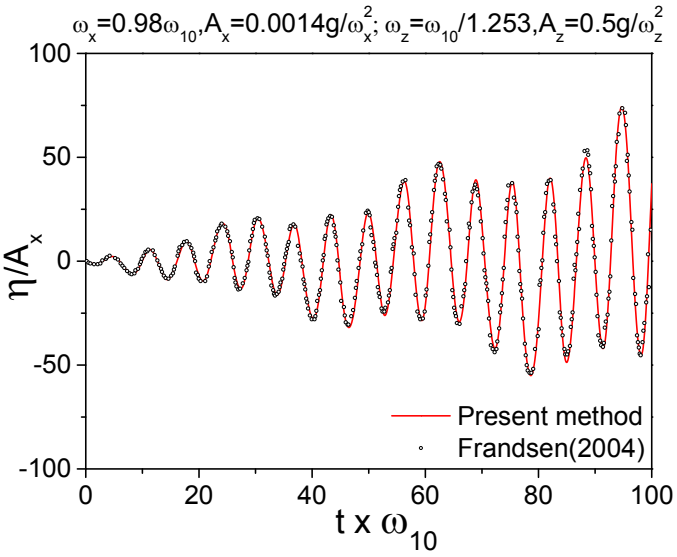

Fig. 4.18 Wave elevation history for forced sloshing due to coupled-surge-heave excitation

4.4.4 Forced sloshing due to rotational excitation

This subsection takes the tank rotation into account. The tank is doing a rotational oscillation, the pitch motion. Incline the tank at an angle Θ with the free surface on horizontal, as in Fig. 4.1(a). In the body-fixed system, the free-surface profile can be written as $\eta_{ini} = x\tan\Theta$. Then, the tank is forced to pitch harmonically about the origin as $\theta(t) = \Theta\cos\omega t$. Dimensional parameters are chosen the same as those in Nakayama and Washizu (1980) for the comparison purpose, i.e. $L = 0.9m$, $H = 0.6m$, $e = e_1 = 0$, $\Theta = 0.8^o$ and $\omega = 5.5\text{rad/s}$. The obtained wave elevation history on the right tank wall is given in Fig.4.19, which shows that the present result from BEM has a good agreement with that from FEM in Nakayama and Washizu (1980).

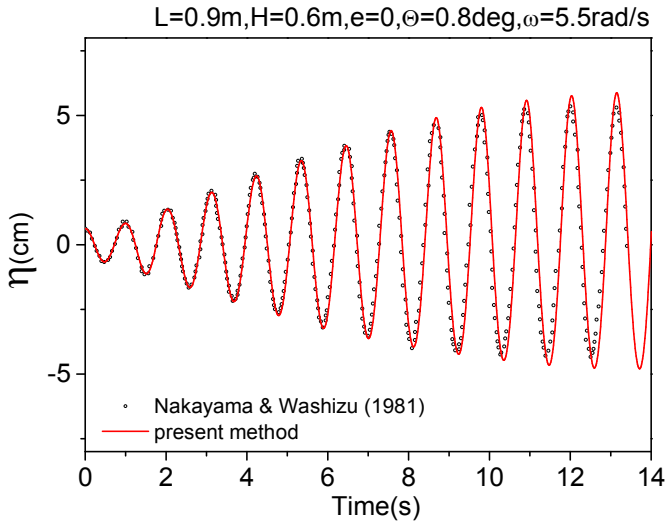

Fig. 4.19 Wave elevation history for forced sloshing due to pitch excitation

4.5 Summary

In this chapter, the methodology for the nonlinear sloshing simulation in 3D wall-sided tanks is described. Case studies are performed based on 3D rectangular tanks. The sloshing problems in either fixed or forced oscillating tanks have been considered. The present BEM results are compared with the analytical solution, experimental data or published results from other numerical methods (e.g. FEM, FDM and two-phase solvers). In all cases, the comparisons have shown a good agreement. Thus, the mathematical model of the numerical scheme has been validated, and the numerical accuracy has been verified. Although the sloshing in wall-sided tanks has been studied for so many years, there are still many gaps to be filled, because the sloshing is such a complex nonlinear problem. In the following chapter, the developed numerical scheme is applied to study a distinct resonance phenomenon (i.e. the 'second-order resonance'), as an attempt to help fill a gap.

Chapter 5 Second-order resonance in 3D rectangular tanks

5.1 Introduction

Associated with the sloshing phenomenon, the resonance is of major concern. When the resonance occurs, the wave amplitude in the tank would grow to a large value rapidly. The resulted violent sloshing might damage the tank structures and affect the motion behaviour of the vessel. Thus, a good understanding of the resonance mechanism and conditions that could trigger the resonance is important.

From previous linear analyses, it is known that a classical resonance could occur when the tank is laterally excited at one of the 'natural sloshing frequencies' (Faltinsen 1987). The natural sloshing frequencies here are non-trivial solutions of the free sloshing in a stationary tank. However, Wu (2007) mathematically predicted that, in a 2D rectangular tank, the resonant sloshing does not have to occur near a natural frequency. This distinct type of resonance is called the 'second-order resonance'. The second-order resonance can be explained by analysing the nonlinear solution up to the second order. Through the perturbation analysis within the potential-flow theory, the solution (e.g. the wave elevation) of the sloshing is expressed as the summation of the linear, second-order and higher-order terms. Then, the classical resonance is when the amplitude of the linear term grows with time, and the second-order resonance is when the amplitude of the second-order term grows with time.

Later, the second-order resonance is observed in some 2D applications. For example, Firouz-Abadi et al (2011) investigated the second-order sloshing effects in tanks with complex bottom geometry. Wang and Wu (2008) observed a similar phenomenon in the confined water between two floating bodies. However, these studies are still based on the weakly-nonlinear assumption, which is theoretically limited to the small-wave-amplitude case. Some other works further involve the full nonlinear free-surface boundary conditions. For example, Ning et al (2012) and Chern et al (2012) developed

numerical methods to simulate the second-order resonance in rectangular tanks. Wang et al (2011) investigated the second-order effects of liquid motion between two floating bodies.

When it comes to 3D cases, the sloshing phenomenon becomes more complex. From a similar perturbation analysis, Zhang et al (2014) further derived the second-order solution in 3D rectangular tanks. From the solution, the second-order resonance in the 3D tank is predicted, although this prediction has not been verified numerically in open literature yet.

In this chapter, the second-order resonance in 3D rectangular tanks is to be investigated based on the numerical scheme developed in Chapter 4. Section 5.2 would briefly explain the mathematics behind the sloshing resonance. In Section 5.3, a series of 2D and 3D case studies on the second-order resonance will be performed. The occurrence of the second-order resonance is investigated by a spectral analysis of the free-surface elevation time histories. Conclusions are drawn in Section 5.4.

5.2 Mathematical interpretation

This section would briefly interpret the sloshing resonance from a mathematical point of view. Based on the standard perturbation theory, the solution of the boundary value problem in Chapter 4 could be approximated as the summation $\varphi = \varphi^{(1)} + \varphi^{(2)} + \cdots$. Here, $\varphi^{(1)}$ and $\varphi^{(2)}$ are the first- and second-order terms of the solution, respectively. According to the superposition principle, the first-order term can be decomposed as $\varphi^{(1)}\left(x,y,z,t\right) = \varphi_L^{(1)}\left(x,z,t\right) + \varphi_B^{(1)}\left(y,z,t\right)$. The subscript L or B refers to the solution of the 2D case when the tank is excited only in the length or width direction, respectively. The second-order term could be decomposed as $\varphi^{(2)}\left(x,y,z,t\right) = \varphi_L^{(2)}\left(x,z,t\right) + \varphi_B^{(2)}\left(y,z,t\right) + \varphi_C^{(2)}\left(x,y,z,t\right)$, where $\varphi_C^{(2)}\left(x,y,z,t\right)$ denotes the interaction of two orthogonal plane waves in length and width directions.

The solutions of $\varphi_L^{(1)}$ and $\varphi_L^{(2)}$ can be obtained referring to Wu (2007) as

$$\varphi_L^{(1)}(x,z,t)=Q_0(t)+\sum_{n=1}^{\infty}Q_n(t)\frac{\cosh\left[k_n(z+H)\right]}{\cosh\left[k_nH\right]}\cos\left[k_n(x+L/2)\right]$$
$$=\sum_{n=1}^{\infty}P_n(t)\frac{\cosh\left[k_n(z+H)\right]}{\cosh\left[k_nH\right]}\cos\left[k_n(x+L/2)\right] \tag{5.1}$$

$$\varphi_L^{(2)}(x,z,t)=K_0(t)+\sum_{n=1}^{\infty}K_n(t)\frac{\cosh\left[k_n(z+H)\right]}{\cosh\left[k_nH\right]}\cos\left[k_n(x+L/2)\right] \tag{5.2}$$

where

$$P_n(t)=-\omega_n\frac{(-1)^n-1}{k_n^2\cdot L/2}\cdot\int_0^t v_{cx}(\tau)\sin\omega_n(t-\tau)\,\mathrm{d}\tau;\quad Q_n(t)=\frac{1}{\omega^2}\frac{\mathrm{d}^2P_n(t)}{\mathrm{d}t^2} \tag{5.3}$$

$$K_n(t)=\int_0^t M_n(\tau)\sin\omega_n(t-\tau)\,\mathrm{d}\tau \tag{5.4}$$

$$k_n=n\pi/L;\quad \omega_n=\sqrt{gk_n\tanh(k_nH)} \tag{5.5}$$

The $M_n(t)$ is a linear superposition of terms such as $\left[dP_m(t)/dt\right]Q_{m-n}(t)$, $P_m(t)\left[d\mathrm{Q}_{m-n}(t)/dt\right]$, $\left[dP_m(t)/dt\right]P_{m-n}(t)$ and so on with $m\geq n+1$. Replacing L with B and x with y leads to the solution of $\varphi_B^{(1)}$ and $\varphi_B^{(2)}$.

The solution of $\varphi_C^{(2)}(x,y,z,t)$ could be found in Zhang et al (2014)

$$\varphi_C^{(2)}(x,y,z,t)=\sum_{m=1}^{\infty}\sum_{n=1}^{\infty}R_{mn}(t)\frac{\cosh k_{mn}(z+H)}{\cosh k_{mn}H}\cos\left[k_m(x+L/2)\right]\cos\left[\tilde{k}_n(y+B/2)\right] \tag{5.6}$$

$$R_{mn}(t)=\frac{1}{\omega_{mn}}\int_0^t f_{mn}(t)\sin\omega_{mn}(t-\tau)\,\mathrm{d}\tau \tag{5.7}$$

with $k_{mn}=\pi\sqrt{(m/L)^2+(n/B)^2}$. The $f_{mn}(t)$ is the linear superposition of terms such as $\left[dP_m(t)/dt\right]\tilde{P}_n(t)$, $P_m(t)\left[d\tilde{P}_n(t)/dt\right]$, $\left[dP_m(t)/dt\right]\left[d^2\tilde{P}_n(t)/dt^2\right]$, $\left[d^2P_m(t)/dt^2\right]\left[d\tilde{P}_n(t)/dt\right]$ and so on. The tilde symbol means the corresponding function in the width direction, e.g. $\tilde{P}_n(t)=-2\tilde{\omega}_n\left[\left((-1)^n-1\right)\Big/\left(\tilde{k}_n^2B\right)\right]\int_0^t v_{cy}(\tau)\sin\tilde{\omega}_n(t-\tau)\,\mathrm{d}\tau$ with $\tilde{k}_n=n\pi/B$ and $\tilde{\omega}_n=\sqrt{g\tilde{k}_n\tanh\left(\tilde{k}_nH\right)}$.

If the tank velocity $v_{cx}(t)$ or $v_{cy}(t)$ is harmonic (e.g. $v_{cx}\sin\omega t$ or $v_{cx}\cos\omega t$), the $P_n(t)$, $\tilde{P}_n(t)$, $K_n(t)$, $\tilde{K}_n(t)$ and $R_{mn}(t)$ would contain convolution terms. It is known that the convolution has the character

$$\lim_{\omega\to\omega_n}\int_0^t \sin\omega(\tau)\sin\omega_n(t-\tau)\,\mathrm{d}\tau = \lim_{\omega\to\omega_n}\left(\frac{\omega_n\sin\omega t-\omega\sin\omega_n t}{\omega_n^2-\omega^2}\right) = \frac{1}{2\omega}\cdot\sin\omega_n t - t\cdot\frac{\omega_n}{2\omega}\cdot\cos\omega t \tag{5.8}$$

or

$$\lim_{\omega\to\omega_n}\int_0^t \cos\omega(\tau)\sin\omega_n(t-\tau)\,\mathrm{d}\tau = \lim_{\omega\to\omega_n}\left(\frac{\omega_n\cos\omega t-\omega_n\cos\omega_n t}{\omega_n^2-\omega^2}\right) = \frac{1}{2}t\cdot\sin\omega_n t \tag{5.9}$$

where the amplitude of the convolution is growing with time. If this type of convolution exists in $P_n(t)$ or $\tilde{P}_n(t)$, the first-order resonance or classical resonance occurs. If it exists in $K_n(t)$, $\tilde{K}_n(t)$ or $R_{mn}(t)$, the second-order resonance occurs. This could be a mathematical interpretation of the resonance phenomenon.

5.3 Numerical results and discussion

The following numerical simulations are based on the mesh model of $(M_1\times M_2\times M_3)=(20\times 20\times 6)$ and time step as $1/50$ of the excitation period. The results in this chapter will be nondimensionalised according to $(x,y,z,\eta)\to(x,y,z,\eta)H$, $t\to\tau\sqrt{H/g}$, $\omega\to\omega\cdot\sqrt{g/H}$ and $\varphi\to\varphi\cdot H\sqrt{gH}$.

5.3.1 First-order resonance

In this subsection, the first-order sloshing resonance is firstly simulated. The tank is undergoing a surge motion as $x_c(\tau)=A_x\sin(\omega_x\tau)$, $y_c(\tau)=0$ and $z_c(\tau)=0$. Parameters are set as $L=2.0$ and $A_x=0.001$. Referring to Eq. (5.3), the convolution of P_1 in the case of $\omega_x=\omega_{10}$ has the same form as Eq. (5.9), which satisfies the condition of the first-order resonance. Fig.5.1(a) presents the free-surface elevation history along the left tank wall and the

corresponding spectral analysis. The wave amplitude has a clearly increasing trend, which is a feature of the first-order resonance. From the power spectrum of the elevation history, it is evident that only one frequency component is dominant. However, for the case of $\omega_x = \omega_{20}$, it has $P_2 = 0$ due to the coefficient of $\left[(-1)^n - 1\right]$ and the first-order resonance could not be observed. This is confirmed by the observation in Fig.5.1(b). The wave elevation history has an irregular form and multiple dominant frequency components coexist. The case of $\omega_x = \omega_{30}$ is further considered in Fig.5.1(c), when the first-order resonance also occurs.

For a 3D case with $L = B = 10$, $A_x = A_y = 0.001$, $\omega_x = \omega_{10}$ and $\omega_y = \omega_{01}$, wave elevation histories at four tank corners are shown in Fig.5.2. It is evident that the elevation at diagonal corners $(-L/2, -B/2)$ and $(L/2, B/2)$ could rapidly reach a large amplitude, even though the excitation is very small. These wave elevation histories have a very sharp crest and flat trough, which suggests the non-negligible effect of the nonlinearity. Furthermore, the wave elevations at two diagonal corners are much more violent than those at the other sub-diagonal corners. For the illustration purpose, Fig.5.3 shows snapshots of wave profiles at a series of time steps $\tau = 353.23$, 354.86, 356.49, 358.11, 359.74 and 361.36, in which the diagonal-type waves can be observed evidently.

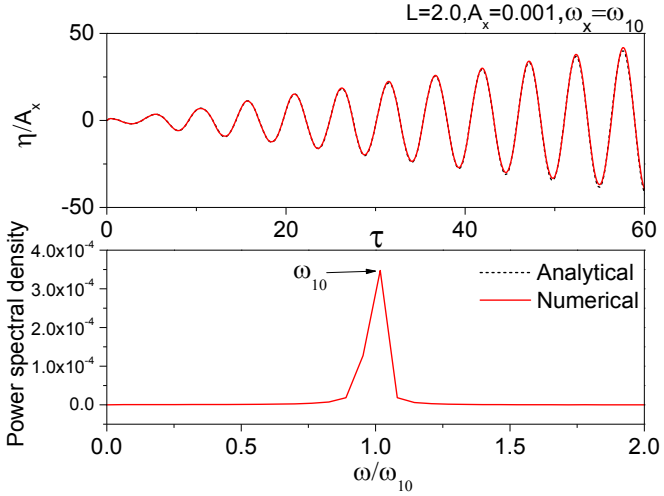

(a)

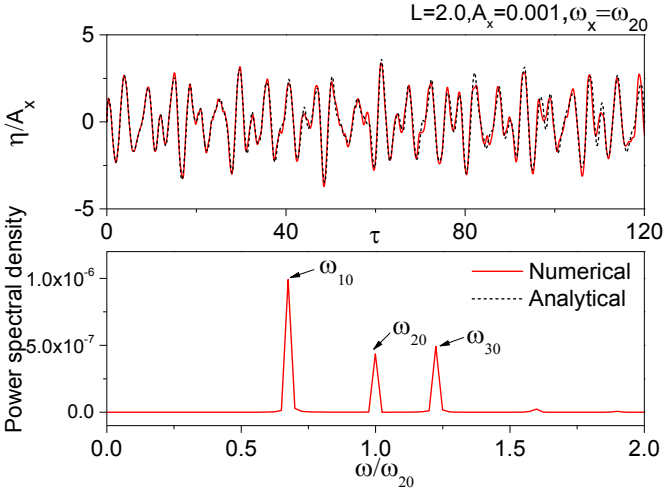

(b)

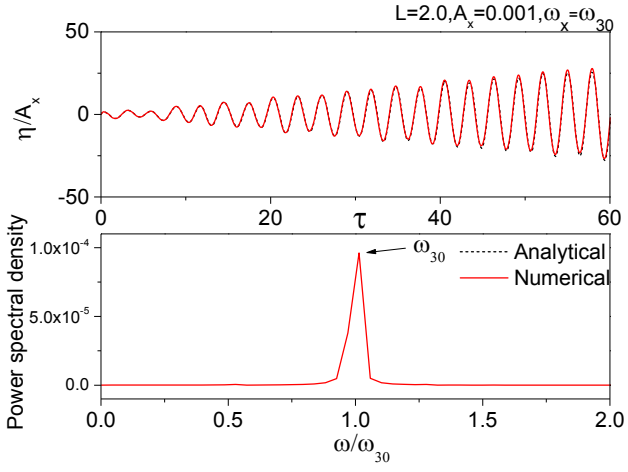

(c)

Fig. 5.1 Wave elevation history and spectrum along left tank wall for $L = 2$, $A_x = 0.001$ and (a) $\omega_x = \omega_{10}$; (b) $\omega_x = \omega_{20}$; (c) $\omega_x = \omega_{30}$

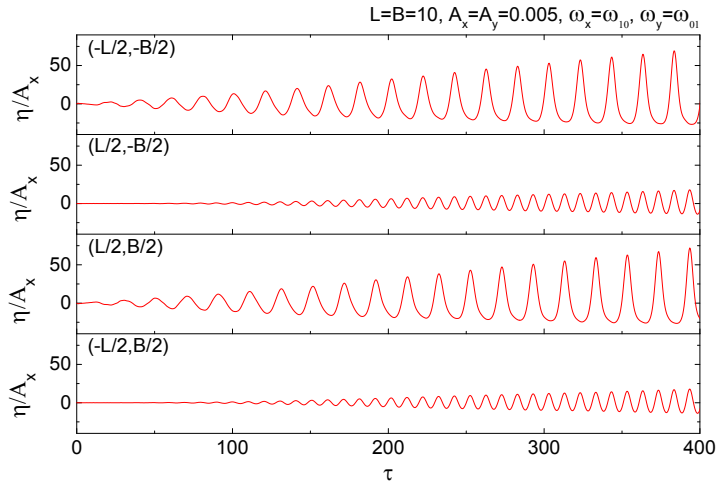

Fig. 5.2 Wave elevation history at tank corners

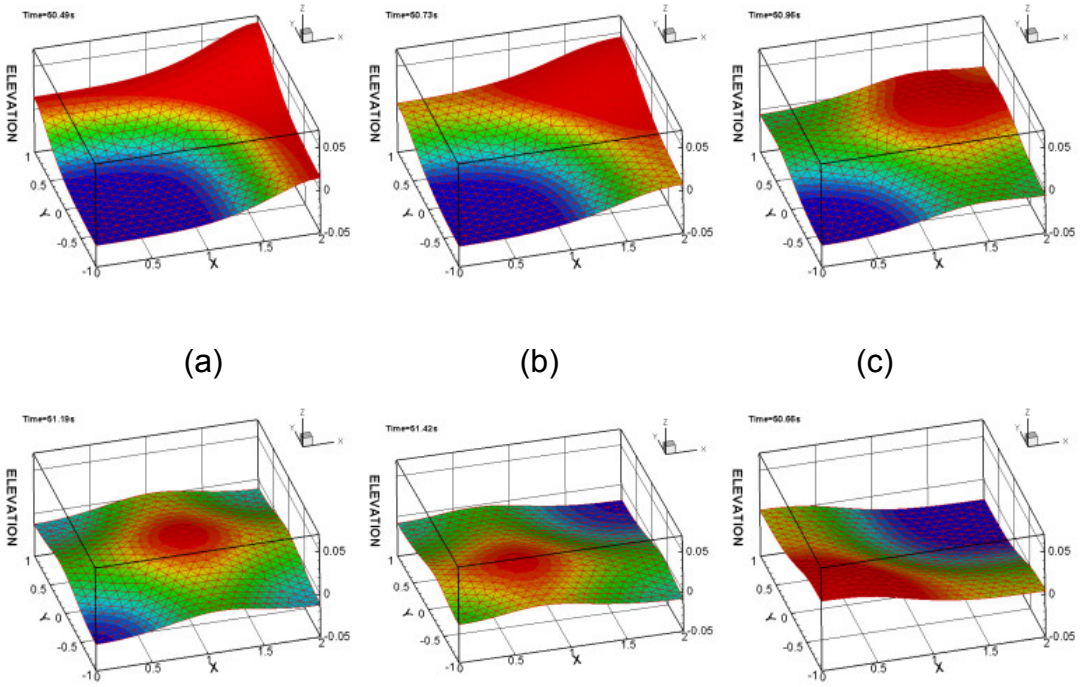

Fig. 5.3 Snapshots of resonant sloshing in 3D rectangular tank

5.3.2 Second-order resonance in 2D cases

This subsection would focus on the second-order resonance in 2D sloshing cases. Consider the second-order solution in Eqs. (5.2)-(5.5). When the tank is excited harmonically as $x_c(\tau) = A_x \sin(\omega_x \tau)$, $y_c(\tau) = 0$ and $z_c(\tau) = 0$. The M_n contains harmonic components such as $\sin(2\omega_x \tau)$ and

$\sin\left[\left(\omega_x \pm \omega_{m0}\right)\tau\right]$ ($m = 1,3,5,\cdots$). According to Eqs. (5.8) and (5.9), the amplitude of K_n is expected to increase with time for $2\omega_x = \omega_{n0}$ and $\omega_x \pm \omega_{m0} = \omega_{n0}$. Here, $n = 2,4,6,\cdots$ and $m = 1,3,5,\cdots$. These are typical conditions of the second-order resonance in 2D sloshing cases.

Firstly the situation of $\omega_x = 0.5\omega_{20}$ is considered. Three tank models with different lengths as $L = 10$, $L = 5$ and $L = 2$ are introduced for comparison. The excitation amplitude is set to be $A_x = 0.005$. For $L = 10$, the obtained wave elevation history along the left tank wall is shown in Fig.5.4(a). Then, the spectral analysis is performed at three different instants of the elevation history as in Fig.5.4(b). It is found that three frequency components, the excitation frequency $0.5\omega_{20}$, the natural sloshing frequency ω_{10} and the frequency ω_{20}, are dominant in the sloshing system. According to Section 5.2, the frequency component ω_{20} is a feature of the second-order effect in this situation. The increase of the peak amplitude of ω_{20} with time suggests the occurrence of the second-order resonance.

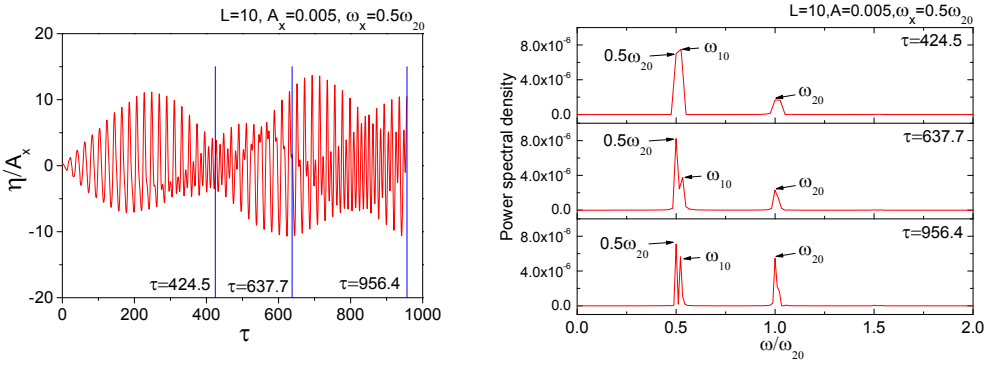

(a) (b)

Fig. 5.4 Wave elevation history along the left tank wall and corresponding power spectrum for $L = 10$, $A_x = 0.005$ and $\omega_x = 0.5\omega_{20}$

For the case of $L = 5$, the wave elevation history and its power spectrum are given in Fig.5.5(a-1) and (a-2). It is found that although the ω_{20} component exists and its power spectral density increases with time, it is not as dominant as $0.5\omega_{20}$ and ω_{10} in the sloshing system. Also, these two dominant frequencies lead to an evident beating behaviour in Fig.5.5(a-1). To

observe an evident second-order resonance, A_x is amplified by ten times. This is due to the fact that K_n is proportional to A_x^2 unlike P_n to A_x. Amplifying the excitation amplitude by n times could magnify the second-order amplitude by n^2 times. In Fig.5.5(b-1) and (b-2), the wave elevation history and the corresponding power spectrum are represented. This time, the amplitude of the wave elevation has an evident general trend of increase. Meanwhile, the ω_{20} component has increased to be dominant within a short period.

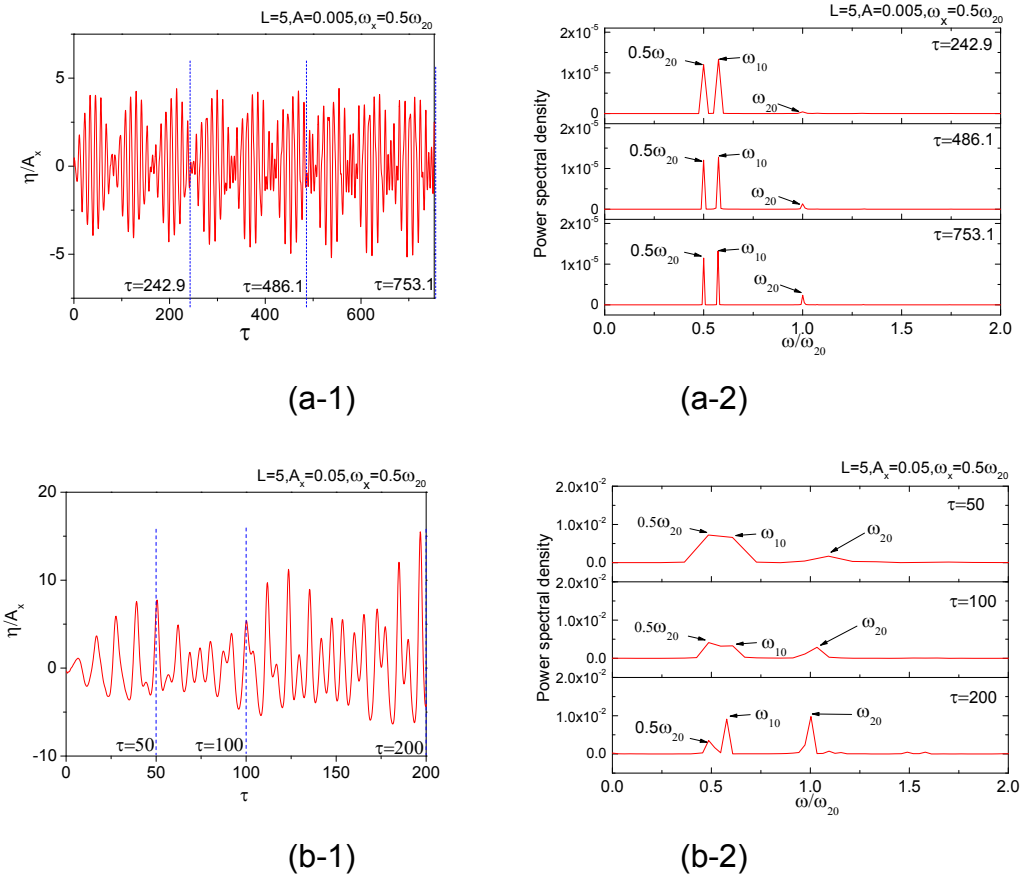

(a-1) (a-2)

(b-1) (b-2)

Fig. 5.5 Wave elevation histories along left tank wall and corresponding power spectrum for $L=5$, $\omega_x=0.5\omega_{20}$ and $A_x=0.005\,\&\,0.05$

Fig.5.6 gives the results of the case $L=2$. The observations are similar to those in the case of $L=5$. When the excitation amplitude is as small as $A_x=0.005$, the wave elevation is irregular but steady. Also, the power spectral density value of the ω_{20} component is tiny. After increasing the excitation amplitude to $A_x=0.05$, the amplitude of the wave elevation shows a general

trend to grow with time. The frequency component ω_{20} has become dominant by the end of the simulation. Its power spectral density also grows with time. It is also noticed that the second-order effect in the case of $L=10$ is more evident than that in the case of $L=5$ and $L=2$. This is because the value of $\omega_x=0.5\omega_{20}$ is more close to ω_{10} in the tank of $L=10$, which leads to a larger wave amplitude. The second-order effect is more evident for larger amplitude sloshing waves.

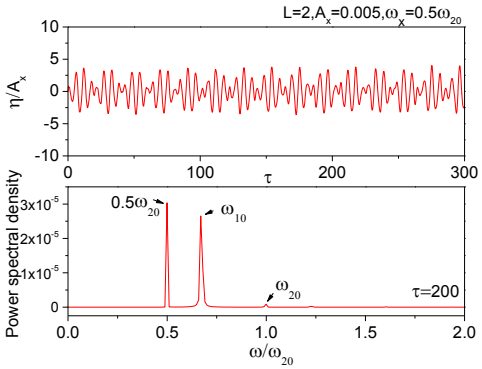

(a)

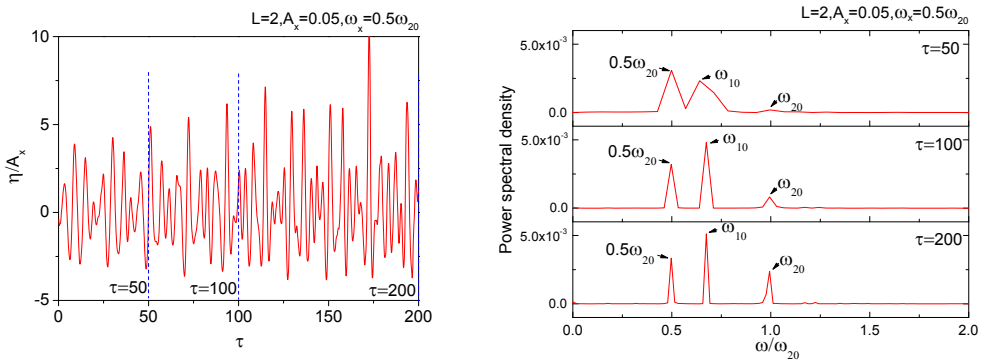

(b-1) (b-2)

Fig. 5.6 Wave elevation history along left tank wall and corresponding power spectrum for $L=2$, $\omega_x=0.5\omega_{20}$ and $A_x=0.005\,\&\,0.05$

From the computational point of view, there would be a compromising choice for the excitation amplitude and simulation time length. On the one hand, it is desired to observe the second-order effects early, which could be helped by increasing the excitation amplitude. On the other hand, the increasing process of the second-order term is detected based on the spectral analysis of the time history. The accuracy of the spectral analysis is determined by the number of simulation periods. Thus, in the following cases,

the excitation amplitude is restricted to make sure that: (a) the simulation could run for a sufficiently long time (at least 20 periods for each spectral analysis); and (b) the second-order frequency could be observed during this time length.

In the next situation, the tank is excited at the frequency $\omega_x = \omega_{20} - \omega_{10}$. Parameters are set as $L = 10$ and $A_x = 0.005$. The wave elevation history is shown in Fig.5.7(a). Several envelopes could be observed. It is evident that the amplitude of the envelopes is growing with time. From the power spectrum in Fig.5.7(b), it is found that the ω_{20} plays a dominant role by the end of the simulation and its weight in the sloshing system is increasing with time, which is a feature of the second-order resonance.

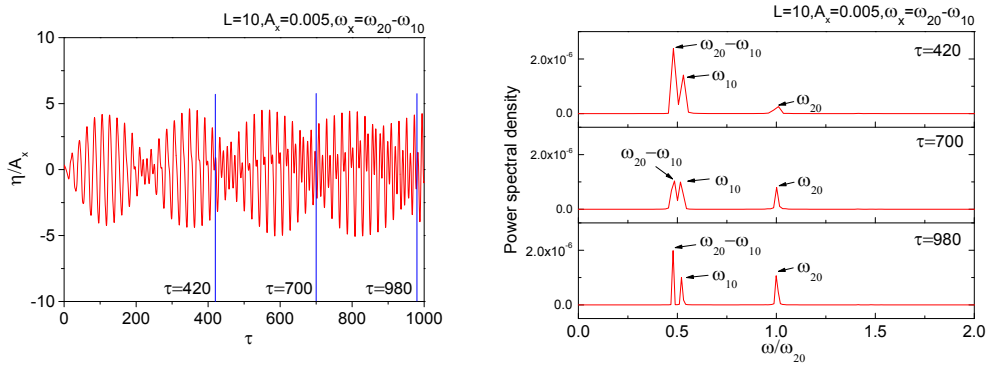

(a) (b)

Fig. 5.7 Wave elevation history along left tank wall and corresponding power spectrum for $L = 10$, $A_x = 0.005$ and $\omega_x = \omega_{20} - \omega_{10}$

Further, consider $x_c(\tau) = A\sin(\omega_a \tau) + A\sin(\omega_b \tau)$. It is obvious that the harmonic components $\omega_a \pm \omega_b$ would exist in the nonlinear sloshing system. According to Eqs. (5.8) and (5.9), the second-order resonance could also be triggered when $\omega_a \pm \omega_b = \omega_{20}$. Thus, in the third situation, parameters are set as $L = 10$, $A = 0.05$, $\omega_a = 0.4\omega_{20}$ and $\omega_b = 0.6\omega_{20}$. Before moving forward, two cases with $x_c(\tau) = A\sin(\omega_a \tau)$ and $x_c(\tau) = A\sin(\omega_b \tau)$ are tested. The results are shown in Fig.5.8(a) and (b), respectively. In both cases, the wave elevation histories are steady. No obvious combination effects between the excitation and natural frequencies exist. Then, the tank is excited as

$x_c(\tau) = A\sin(\omega_a \tau) + A\sin(\omega_b \tau)$ and give the results in Fig.5.8(c). It is obvious that the elevation history in Fig.5.8(c) is not a simple superposition of those in sub-figure (a) and (b). The amplitude of the wave elevation has an increasing trend. The frequency component ω_{20} as a symbol of the second-order resonance has grown to be dominant within a short time.

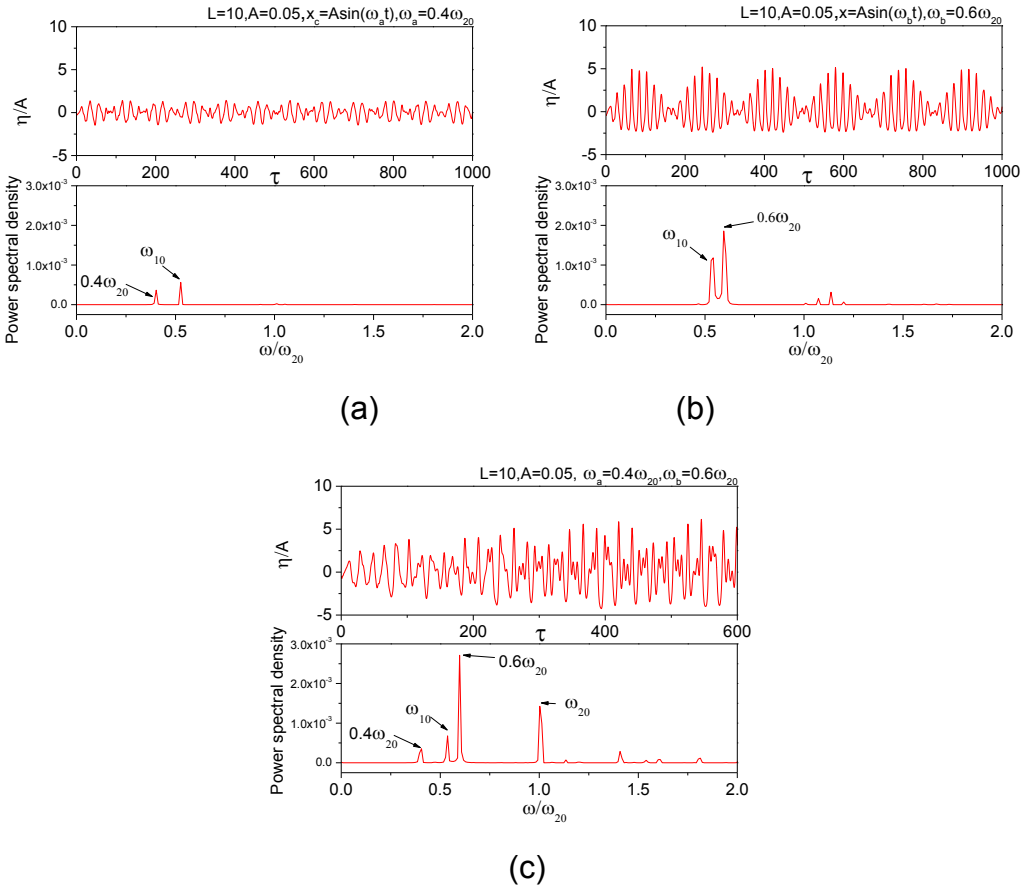

Fig. 5.8 Wave elevation histories along left tank wall and corresponding power spectrum for $L = 10$, $A_x = 0.05$, $\omega_a = 0.4\omega_{20}$ and $\omega_b = 0.6\omega_{20}$

5.3.3 Second-order resonance in 3D cases

In this subsection, the 3D sloshing cases are further considered. The displacement of the tank is governed by $x_c(\tau) = A_x \sin(\omega_x \tau)$, $y_c(\tau) = A_y \sin(\omega_y \tau)$ and $z_c(\tau) = 0$. Here, the $A_{x(y)}$ and $\omega_{x(y)}$ are amplitudes and frequencies of the surge (or sway) motion, respectively. To describe the 3D effects in detail, the wave elevation histories are recorded at four corners, midpoints of four sides and the centre of the tank. These nine test points are marked in Fig.4.4(b).

Firstly, $L = B = 10.0$, $A_x = A_y = 0.001$ and $\omega_x = \omega_y = 0.5\omega_{20} = 0.5\omega_{02}$ are set. In this situation, both the tank geometry and external excitation are symmetrical about the vertical plane joining the corner $(-L/2, -B/2)$ and $(L/2, B/2)$. As a result, the free-surface motion inside the tank is also diagonally symmetrical. Thus, only six test points can be considered. Fig.5.9 presents the wave elevation histories at these six test points. It is found that the elevation histories at diagonal corners $(-L/2, -B/2)$ and $(L/2, B/2)$ are quite similar to those in 2D cases in Fig.5.4(a). High-frequency oscillations are especially evident during periods $\tau = 300 \sim 500$ and $\tau = 700 \sim 900$. However, at the middle point of tank sides $(L/2, 0)$ and $(0, -B/2)$, the high-frequency oscillations are not evident in wave elevation histories. At the sub-diagonal corner $(L/2, -B/2)$ and tank centre $(0, 0)$, the elevation histories have clear envelopes. The envelope amplitude grows with time, which suggests a type of resonance.

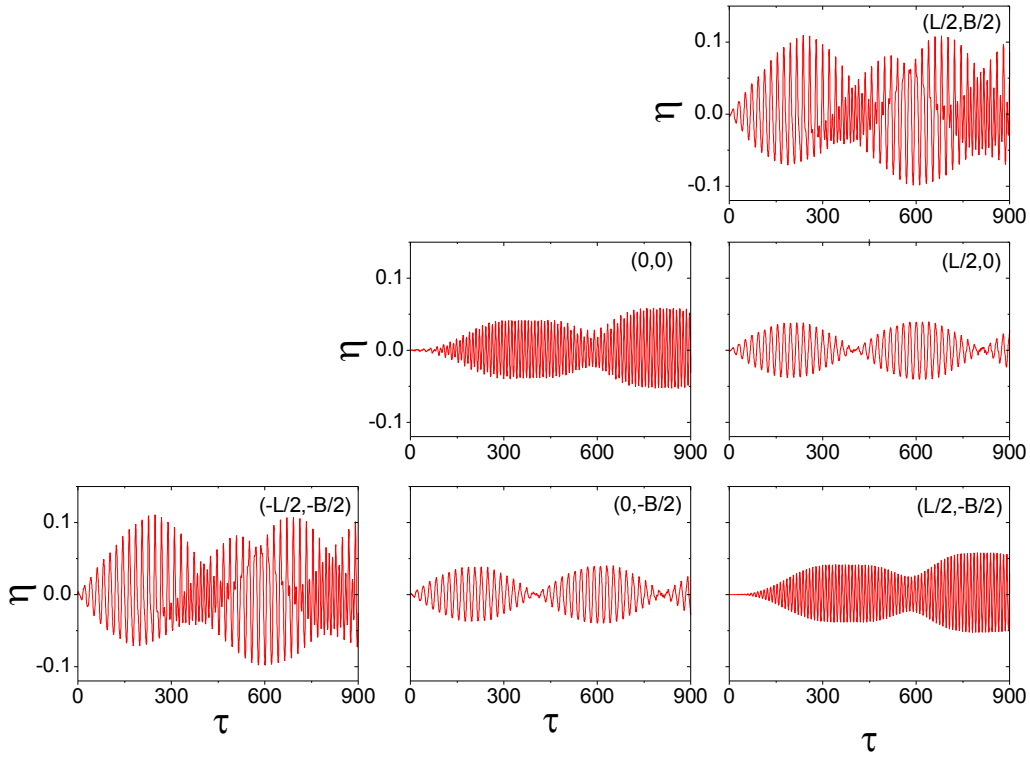

Fig. 5.9 Wave elevation histories at the test points for $L = B = 10$, $A_x = A_y = 0.001$, $\omega_x = 0.5\omega_{20}$ and $\omega_y = 0.5\omega_{02}$

The spectral analysis is performed on these wave elevation histories. In Fig.5.10(a) and (b), corresponding power spectra at $(-L/2,-B/2)$ and $(L/2,B/2)$ are given. Three main frequency components (i.e. the excitation frequency $0.5\omega_{20}$, natural sloshing frequency ω_{10} and the frequency ω_{20} as a symbol of the second-order effect) exist. At three different instants, it is found that the spectral density value of ω_{20} increases with time, which suggests a second-order resonance phenomenon. The power spectrum of wave elevation histories at $(L/2,0)$ and $(0,-B/2)$ is given in Fig.5.10(c) and (d), where the second-order component ω_{20} is not dominant. Fig.5.10(e) and (f) give the power spectrum of elevation histories at $(L/2,-B/2)$ and $(0,0)$. The ω_{20} is found to be the primary frequency. Its power spectral density also increases with time, indicating the occurrence of the second-order sloshing resonance.

To make the second-order resonance clearer in this 3D case, the excitation amplitude is amplified by 10 times, i.e. $A_x = A_y = 0.01$. The wave elevation histories at six positions are given in Fig.5.11. Compared with Fig.5.9, at $(-L/2,-B/2)$ and $(L/2,B/2)$, high-frequency oscillations emerge earlier at about $\tau = 200$ and are always evident since their emergence. At $(L/2,0)$ and $(0,-B/2)$, some high-frequency perturbations are observed at the elevation histories, although the perturbation amplitudes are still small. At $(L/2,-B/2)$ and $(0,0)$, the second envelope of the elevation history also forms earlier than that in Fig.5.9. For all the sub-figures in Fig.5.11, the increasing trend of the envelope amplitude is more obvious.

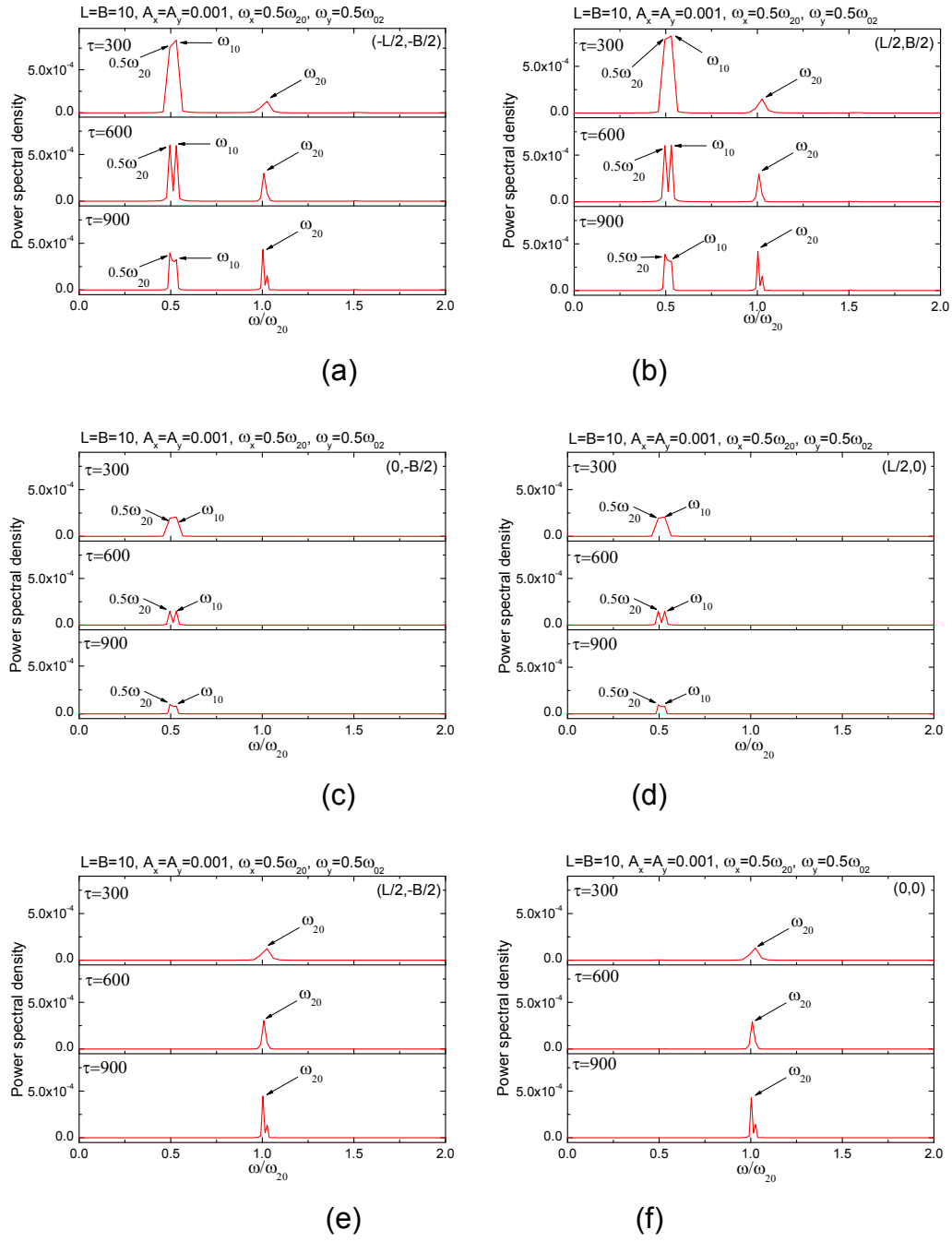

Fig. 5.10 Power spectrum of wave elevation histories at the test points for $L = B = 10$, $A_x = A_y = 0.001$, $\omega_x = 0.5\omega_{20}$ and $\omega_y = 0.5\omega_{02}$

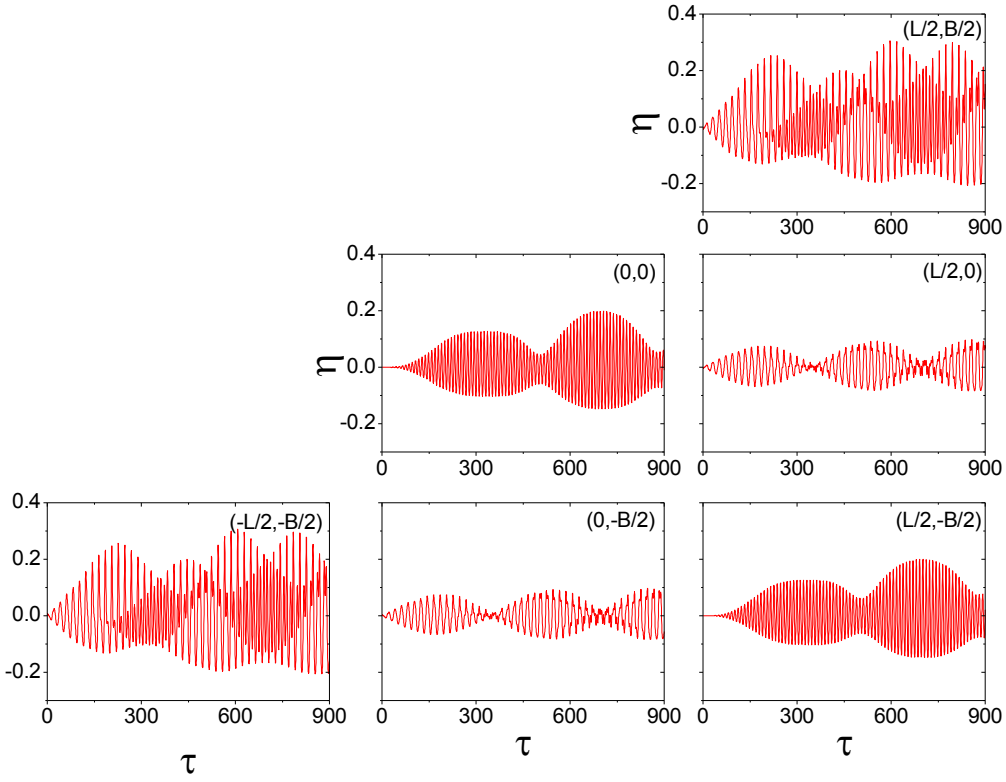

Fig. 5.11 Wave elevation histories at the test points for $L = B = 10$, $A_x = A_y = 0.01$, $\omega_x = 0.5\omega_{20}$ and $\omega_y = 0.5\omega_{02}$

Fig.5.12 shows the corresponding power spectrum. Compared with Fig.5.10(a) and (b), the weight of the component ω_{20} grows faster in Fig.5.12(a) and (b). Specifically, by $\tau = 600$, the power spectral density of ω_{20} has become comparable with that of the $0.5\omega_{20}$ and ω_{10}. At $\tau = 900$, the ω_{20} becomes the most dominant frequency component. From Fig.5.12(c) and (d), it is known that the second-order effects are still small at test point $(L/2, 0)$ and $(0, -B/2)$. In Fig.5.12(e) and (f), the ω_{20} is also the primary frequency component of elevation histories at $(L/2, -B/2)$ and $(0,0)$. The increase of its spectral density value suggests the occurrence of the second-order resonance.

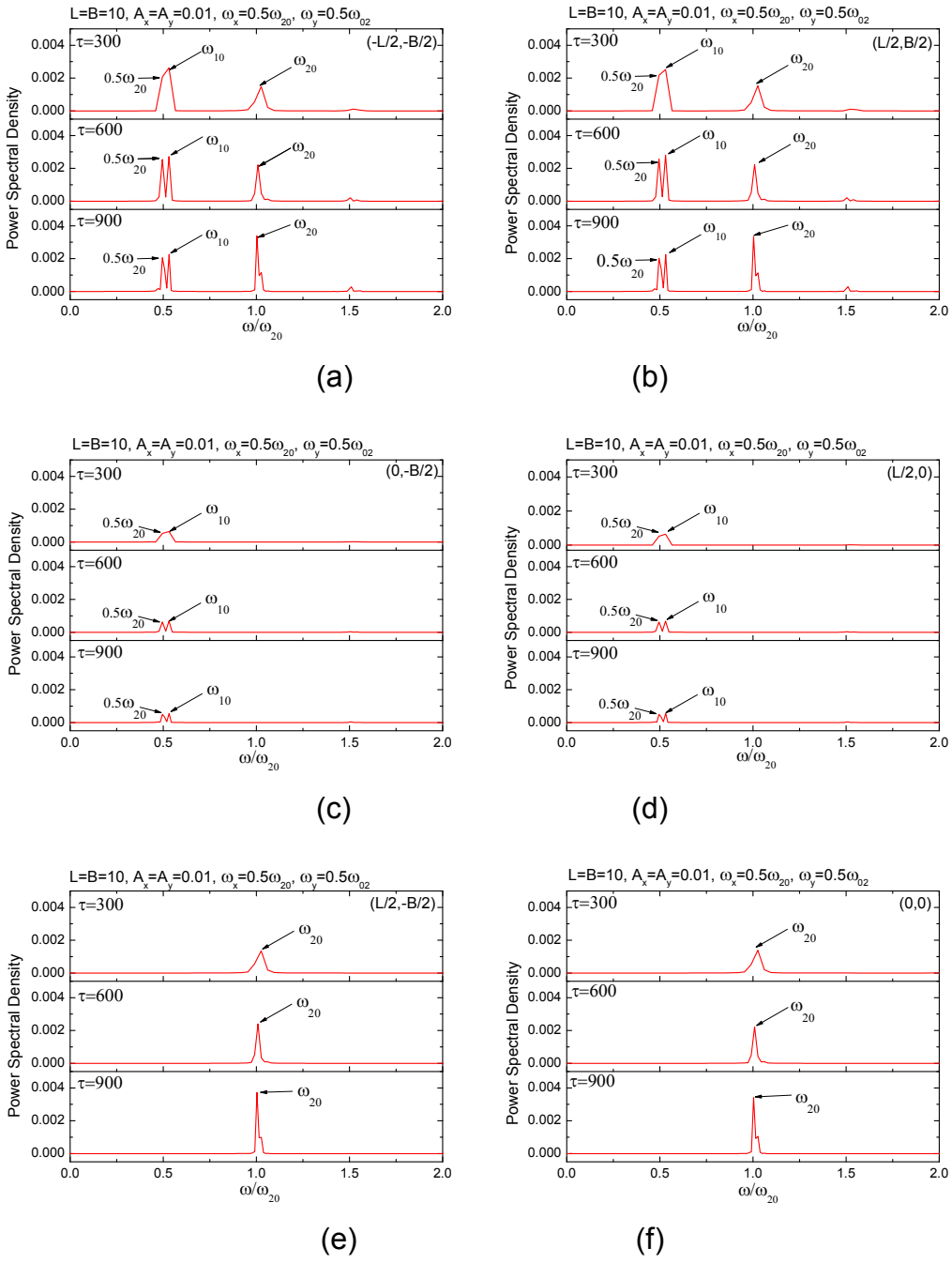

Fig. 5.12 Power spectrum of wave elevation histories at the test points for $L = B = 10$, $A_x = A_y = 0.01$, $\omega_x = 0.5\omega_{20}$ and $\omega_y = 0.5\omega_{02}$

This thesis also illustrates the time variation of the 3D free-surface profiles. Fig.5.13 shows the wave profiles at six instants from $\tau = 102.82$ to $\tau = 111.32$. During this period, the second-order resonance has not occurred yet. It is observed that the quasi-standing waves are dominant. Fig.5.14 gives the free-surface profiles between $\tau = 596.10$ and $\tau = 606.30$ when the

second-order effects become dominant. An evident travelling wave between two diagonal corners is evident. The second-order sloshing resonance is accompanied by travelling waves.

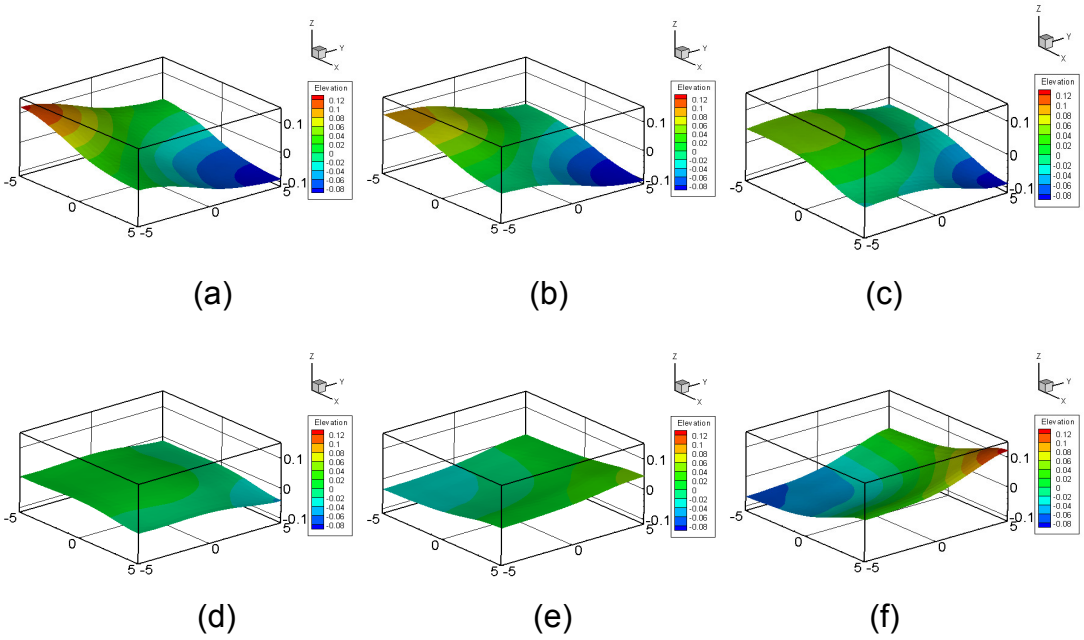

(a) (b) (c)

(d) (e) (f)

Fig. 5.13 Free-surface profiles at $\tau = 102.82$, 104.52, 106.22, 107.92, 109.62 and 111.32

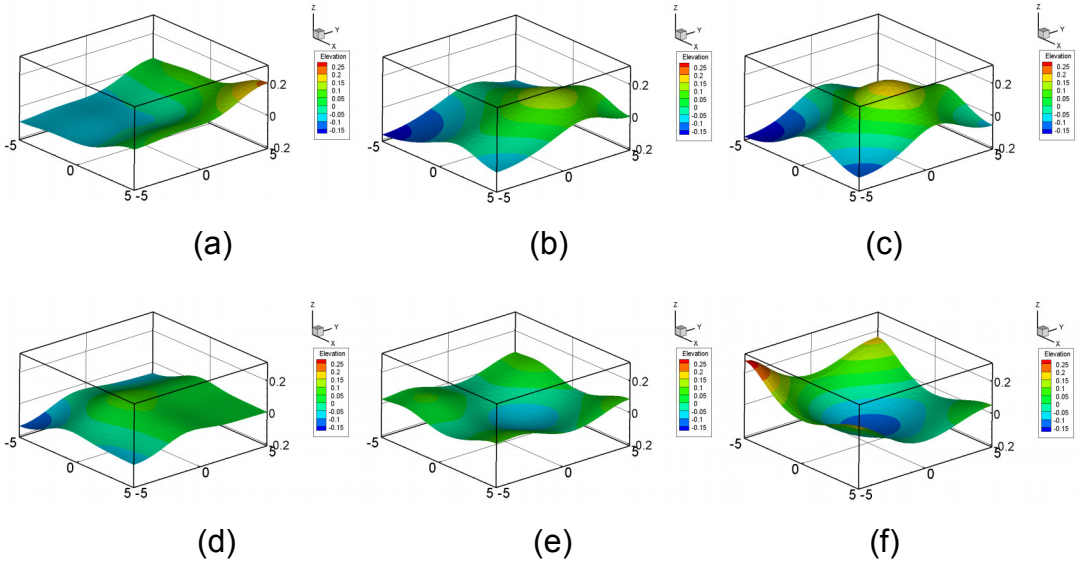

(a) (b) (c)

(d) (e) (f)

Fig. 5.14 Free-surface profiles at $\tau = 597.80$, 599.50, 601.20, 602.90, 604.60 and 606.30

Focusing on the coupling term $\varphi_C^{(2)}(x,y,z,t)$ in Eqs. (5.6) and (5.7), it is found that the value of $f_{mn}(t)$ is nonzero only when $m,n = 1,3,\cdots$. The

second-order resonance might emerge when $\omega_x + \omega_y = \omega_{11}$. The frequency component ω_{11} represents the 3D second-order effect. Parameters are set as $L = B = 10.0$, $A_x = A_y = 0.1$ and $\omega_x = \omega_y = 0.5\omega_{11}$. The wave elevation histories at six test points are given in Fig.5.15. In all sub-figures, the elevation histories are irregular. At corner $(-L/2, -B/2)$, $(L/2, B/2)$ and $(L/2, -B/2)$, the general trend of the maximum wave amplitude is denoted by the dashed line. It shows that the maximum wave amplitude has an increasing trend as time going on. Through a power spectral analysis in Fig.5.16(a), (b) and (e), it is found that the weight of ω_{11} grows with time. This suggests an occurrence of the second-order resonance. However, at the rest test points, the wave elevation amplitude does not show an increasing trend evidently, and the ω_{11} is not dominant in the corresponding spectrum, either.

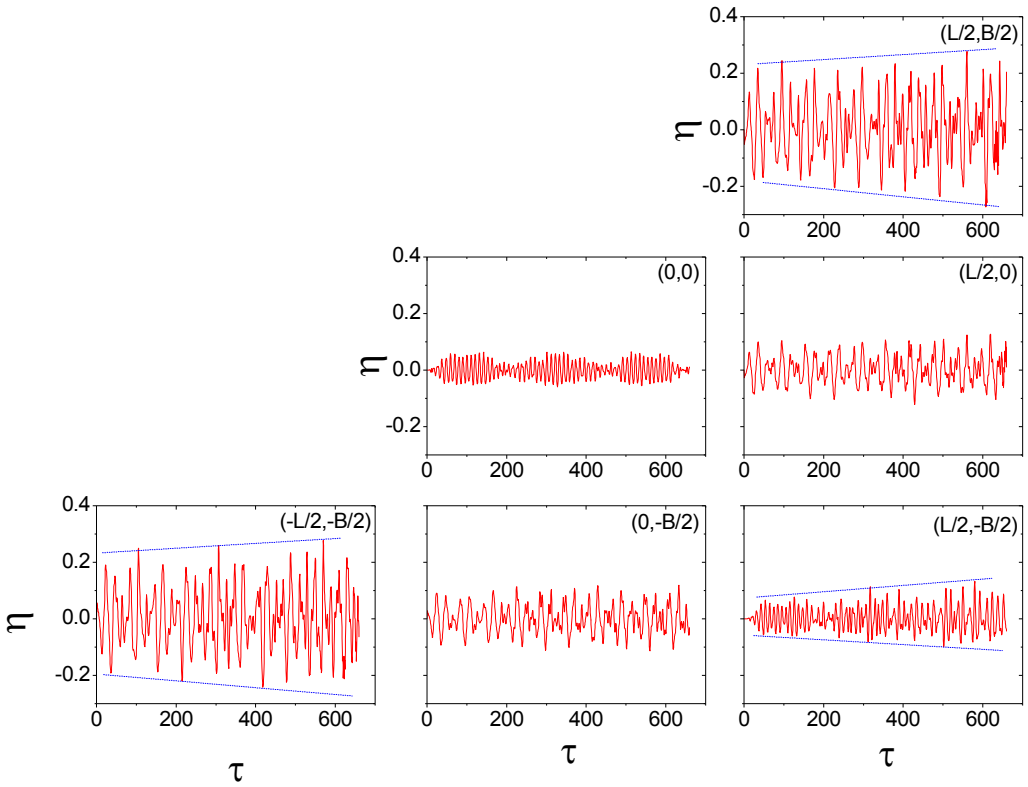

Fig. 5.15 Wave elevation histories at the test points for $L = B = 10$, $A_x = A_y = 0.1$ and $\omega_x = \omega_y = 0.5\omega_{11}$

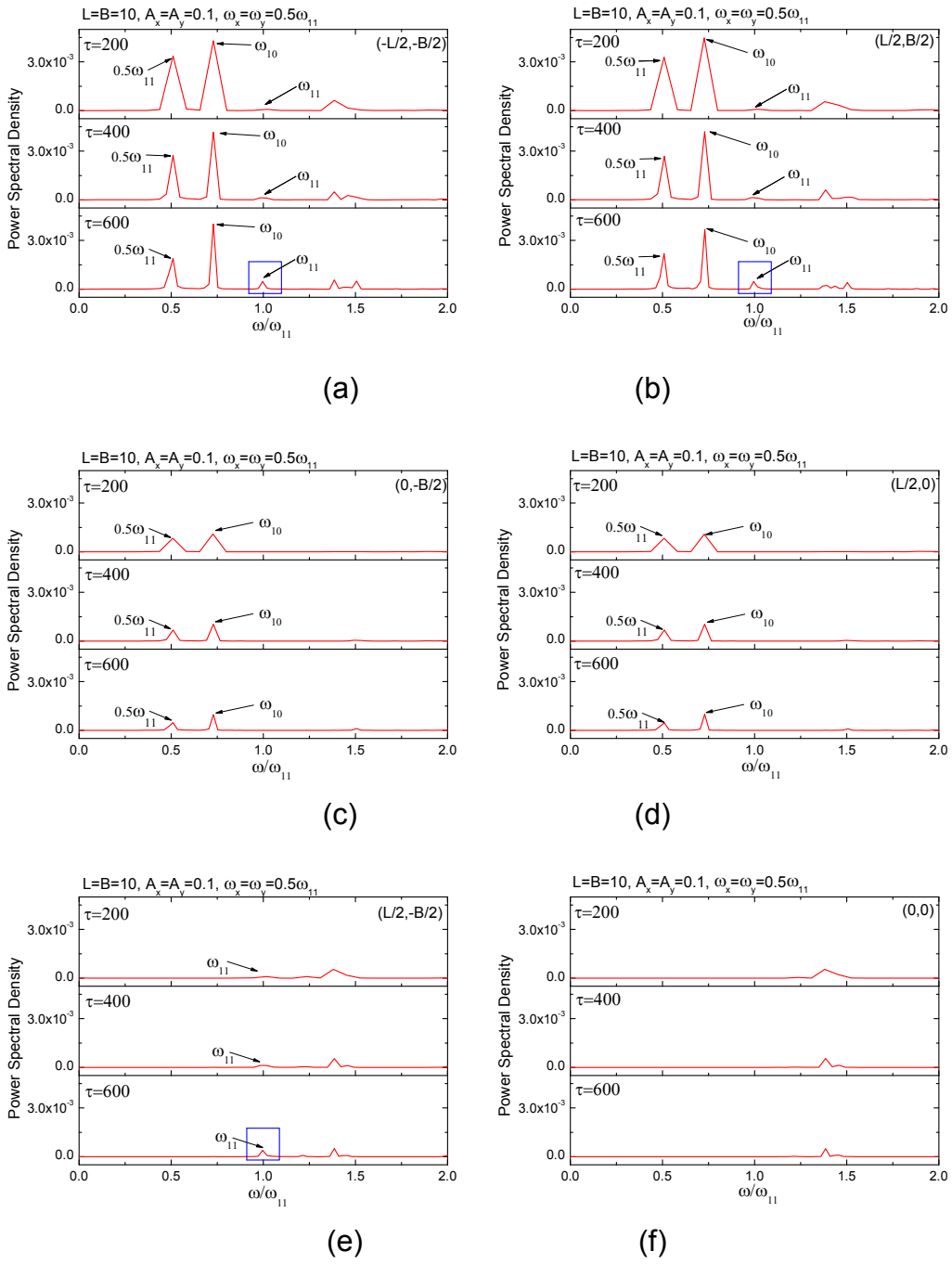

Fig. 5.16 Power spectrum of wave elevation histories at the test points for $L = B = 10$, $A_x = A_y = 0.1$ and $\omega_x = \omega_y = 0.5\omega_{11}$

The situation when $L \neq B$ is further considered. The generated sloshing waves are no longer diagonally symmetric and the sloshing waves would be more complex. Parameters are set as $L = 10.0$, $B = 8.0$, $A_x = A_y = 0.1$ and $\omega_x = \omega_y = 0.5\omega_{11}$. Fig.5.17 shows the wave elevation histories at nine test points. Fig.5.18 gives the corresponding spectrum. It is found that the wave

elevation amplitude at four tank corners has a growing trend in general. In their corresponding spectrum as Fig.5.18(a) to (d), the ω_{11} is also growing to be dominant, which is an evidence of the second-order resonance. At the rest test points, the ω_{11} does not play an important role. Meanwhile, it is interesting to find in Fig.5.18(e) and (f) that at the middle point of the width side, i.e. $(-L/2,0)$ and $(L/2,0)$, the dominant wave frequency besides the excitation frequency $0.5\omega_{11}$ is the natural frequency ω_{10} in the length direction of the tank. From Fig.5.18(g) and (h), at the middle point of the length side, i.e. $(0,-B/2)$ and $(0,B/2)$, the dominant frequency component besides $0.5\omega_{11}$ is the natural sloshing frequency ω_{01} in the width direction.

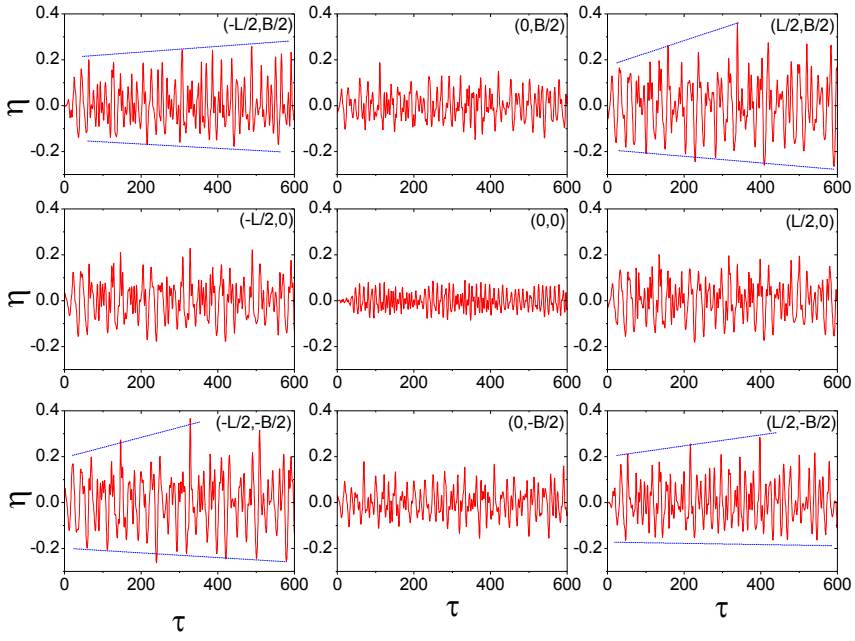

Fig. 5.17 Wave elevation histories at the test points for $L=10$, $B=8$, $A_x=A_y=0.1$ and $\omega_x=\omega_y=0.5\omega_{11}$

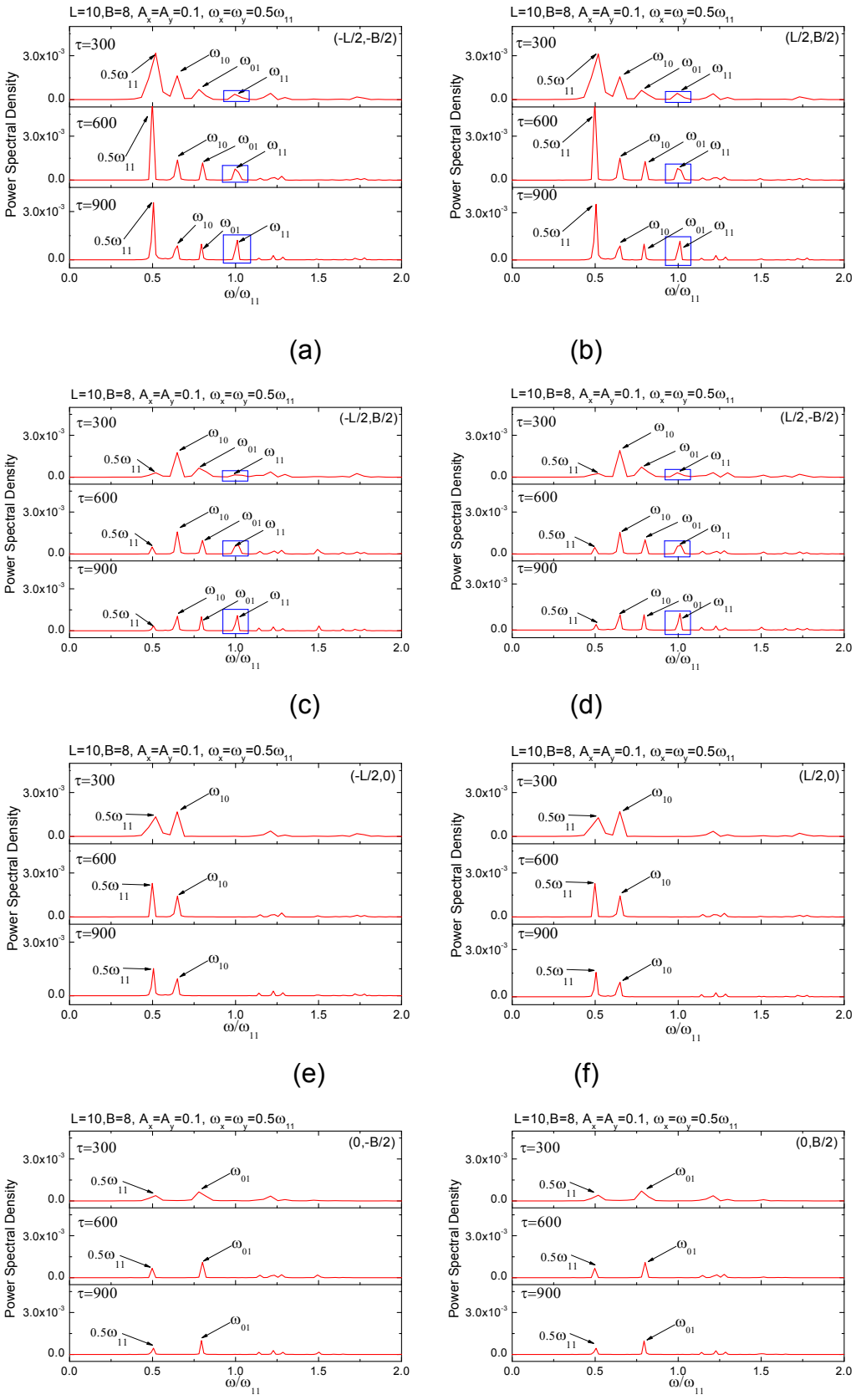

Fig. 5.18 Power spectrum of wave elevation histories at the test points for $L=10$, $B=8$, $A_x=A_y=0.1$ and $\omega_x=\omega_y=0.5\omega_{11}$

From the observations in above 2D and 3D studies, it is found that the second-order resonance does not increase as fast as the fundamental resonance in Fig.5.1(a). This seems to be reasonable from the perturbation theory. The solution (e.g. the wave elevation) is expressed as the summation of the linear, second-order and even higher-order terms. Theoretically, the amplitude of the second-order term is at least one order smaller than that of the linear term. Since the second-order resonance is a resonance of the second-order term, it might take some time to become apparent. Thus, in order to explicitly show the increasing process of the second-order term, the spectral analysis is performed on the wave elevation history at different instants. From the growing weight of the second-order frequency component, the increasing of the second-order term can be observed.

5.4 Conclusions

Associated with the sloshing phenomenon, the resonance is of major concern. From the perturbation analysis, the nonlinear sloshing solution could be expressed as the summation of the first, second and higher-order terms. No matter the first- or second-order term, it contains the convolution. The convolution has this mathematical property, that at certain conditions its amplitude could increase with time. It is well known that, when the tank oscillation frequency is equal to the natural sloshing frequency, the wave amplitude in the tank could grow with time, leading to the classical resonance. Under this condition, the first-order term grows with time. So, the classical resonance is essentially the ‘first-order’ resonance. However, the second-order term also has this convolution. Under certain conditions, the second-order term can also grow with time, leading to a different resonance. This type of resonance is called the ‘second-order resonance’.

The second-order resonance conditions for 2D sloshing tanks was firstly predicted in Wu (2007), followed by a few numerical studies in literature. Then, Zhang et al (2014) further derived the second-order resonance conditions for 3D tanks. This chapter, for the first time, numerically verifies the existence and observes the behaviour of the second-order sloshing resonance in 3D

rectangular tanks. It is found that the second-order resonance can become as dominant as the classical resonance. Its effects become more evident for larger amplitude sloshing waves. The existence of the second-order resonance has practical meanings. For example, people conventionally consider that the classical resonance condition at the natural sloshing frequencies is the most dangerous situation for a liquid cargo vessel. Now this chapter may further suggest that the second-order resonance conditions should also be tested in a vessel design stage.

However, it should also be pointed out that, the evidence of the second-order resonance is dependent on the time. After a sufficiently long time (e.g. hundreds of excitation periods), the dissipation factors in the tank might become important. Then, the second-order resonance effects might not always be so evident in reality.

In Part I (Chapter 3, 4 and 5), the sloshing problems in wall-sided tanks have been discussed. Next in Part II (Chapter 6, 7 and 8), a new FLNG vessel with wedged tanks will be proposed, and sloshing problems in wedged tanks will be focused on.

Part II (Ch 6, 7 & 8) Sloshing in non-wall-sided tanks

Chapter 6 Model analysis with numerical approach

6.1 Introduction

As described in Chapter 1, on the FLNG vessel, there are several wall-sided LNG tanks with clear internal surfaces. These tanks normally have similar dimensions and are filled to similar levels for the load balance, which suggests that the liquid in each tank has similar natural sloshing frequencies. According to the linear potential-flow theory, the resonance occurs when the tank is excited at certain natural sloshing frequencies (Faltinsen 1978). So, under certain ocean-wave excitations, the sloshing resonance could occur simultaneously in all tanks, which would be one of the most dangerous situations in practice.

This thesis would introduce a new design of the FLNG vessel, in order to avoid this dangerous situation. The vertical walls between neighbour tanks are replaced with inclined or curved ones, to make sure that different tanks have different natural sloshing frequencies. Thus, even though the resonant sloshing occurs in one tank, the liquid motion in the remaining tanks might still be gentle. This would potentially minimise the resultant sloshing effects on the vessel motions. Considering the construction complexity, the wedged LNG tanks as in Fig. 6.1 are adopted, without changing the internal capacity of the vessel hull. Before a systematic verification of this design, the mechanism of the sloshing in wedged tanks has to be understood. However, unlike expensive studies for sloshing in wall-sided tanks, such wedged tanks have rarely been considered in the open literature. So, Chapter 6 to 8 aim to help fill this gap.

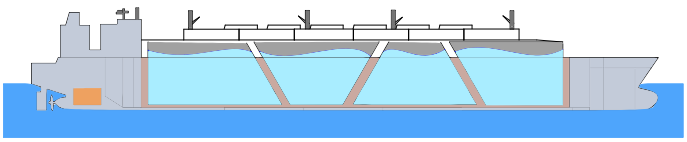

Fig. 6.1 Design of FLNG vessel with wedged tanks

This chapter would firstly calculate the natural sloshing frequencies/modes of the tank through the modal analysis. At present, natural frequencies/modes in non-wall-sided tanks could be obtained based on the

analytical, approximation, numerical or spectral method. Using the analytical method, a proper coordinate system should be selected. The mean fluid boundaries (including the free surface and tank walls) must coincide with coordinate iso-surfaces. Through a conformal mapping, the sloshing problem is transformed to a mathematical problem in the rectangular or cylindrical coordinate system. For cases when such a coordinate system cannot be found, the solution is sometimes possible by dividing the fluid domain into sub-domains, constructing analytical solutions for each sub-domain and then matching solutions on the interfaces. Typical analytical works are as follows. McIver (1989) determined the natural sloshing frequencies in the spherical and horizontal cylindrical tanks using the toroidal and bipolar coordinates, respectively. Lukovsky and Timokha (2002) developed an analytically-oriented modal approach to calculate natural modes of a circular conical tank based on a curvilinear coordinate system. Gavrilyuk et al (2008) further extended the modal approach to find natural frequencies of the truncated conical tank. Hasheminejad and Mostafa Aghabeigi (2011) performed the conformal mapping and analysed the sloshing in half-full horizontal elliptical tanks. The natural sloshing frequencies of a tank could also be predicted by an approximation method based on existing solutions of similar geometries. An estimation of the upper and lower bounds is usually given. For example in Faltinsen and Timokha (2001), the lowest natural sloshing frequency of a prismatic tank was estimated based on the solution of rectangular tanks. Unlike the above two methods, the numerical method is capable of dealing with sloshing in general tanks. Discretizing the boundary value problem for linear potential flows leads to an eigenvalue problem whose nontrivial solutions correspond to the natural frequencies and modes. For example, Firouz-Abadi et al (2009) developed a numerical modal approach for 3D sloshing analyses. Natural frequencies and mode patterns of the sloshing in different tanks (e.g. off-centre annular cylindrical tank and U-shape tank) were calculated. Additionally, the natural frequencies could be obtained through the Fourier spectral analysis from a statistical perspective. For example, Damattya et al (2005) tested the fundamental natural sloshing frequency of conical tanks using the spectral analysis method.

In this chapter, a numerical approach with the help of BEM would be developed to calculate natural sloshing frequencies and corresponding modes of a general tank. A series of case studies are performed focusing on wedged tanks. The effects of the wall incline angle and liquid fill depth on natural frequencies/modes are studied. Furthermore, the vessel is set in different excitation situations and the linear behaviour of sloshing waves in each tank is investigated.

6.2 Mathematical formulation

6.2.1 Problem description

The governing equation and boundary conditions of the sloshing problem are expressed by Eqs. (2.29)-(2.33) in the body-fixed system $O-xyz$. The origin O is set at the rotational centre of the tank. Assume that the sloshing amplitude is small relative to the characteristic tank dimension. Then, the boundary value problem could be linearized about the averaged fluid domain $\overline{V}$, mean wetted tank surface $\overline{S}_B$ and mean free surface $\overline{S}_F$ as

$$\nabla^2\varphi = 0 \text{, in } \overline{V} \tag{6.1}$$

$$\frac{\partial\varphi}{\partial n} = \sum_{j=1}^{6} v_j n_j \text{, on } \overline{S}_B \tag{6.2}$$

$$\frac{\partial\varphi}{\partial z} = \frac{\partial\eta}{\partial t} + \sum_{j=1}^{6} v_j n_j \text{, on } \overline{S}_F \tag{6.3}$$

$$\eta = -\frac{1}{g}\frac{\partial\varphi}{\partial t} - z_c + \alpha_2 x - \alpha_1 y \text{, on } \overline{S}_F \tag{6.4}$$

where α_1 and α_2 are Euler angles described in Chapter 2, $\mathbf{v}_c = \{v_1, v_2, v_3\} = d\mathbf{r}_c/dt$ is the velocity of O, $\mathbf{\Omega} = \{v_4, v_5, v_6\}$ is the angular velocity of $O-xyz$, and $\mathbf{n} = \{n_1, n_2, n_3\}$ is the unit normal vector pointing out of $\overline{V}$. The expression $(\mathbf{r}\times\mathbf{n}) = \{n_4, n_5, n_6\}$ is adopted for convenience, with $\mathbf{r} = \{x, y, z\}$ as the position vector of a point on $\overline{S}_B$. Tank motions corresponding to v_1, v_2, v_3, $v_4 = d\alpha_1/dt$, $v_5 = d\alpha_2/dt$ and $v_6 = d\alpha_3/dt$ are called surge, sway, heave, roll, pitch and yaw, respectively.

Assume that the fluid motion starts from stationary. The initial position of the free surface is $z=\bar{z}$ in $O-xyz$. Thus, the initial conditions can be set as

$$\varphi = 0 \text{ and } \frac{\partial \varphi}{\partial t} = 0, \text{ for } t = 0 \text{ and } z=\bar{z} \tag{6.5}$$

To isolate the terms related to tank motions, the velocity potential is decomposed as

$$\varphi(x,y,z,t) = \phi(x,y,z,t) + \sum_{j=1}^{6} v_j(t)\phi_j'(x,y,z) \tag{6.6}$$

Here, the spatial function $\phi_i'(x,y,z)$ is determined by the Neumann-type boundary value problem

$$\nabla^2 \phi_j' = 0, \text{ in } \overline{V} \tag{6.7}$$

$$\frac{\partial \phi_j'}{\partial n} = n_j, \text{ on } \overline{S}_B \text{ and } \overline{S}_F \tag{6.8}$$

It is obvious that $\phi_1' = x$, $\phi_2' = y$ and $\phi_3' = z$. The BEM could be used to calculated ϕ_4', ϕ_5' and ϕ_6'. Substituting Eq. (6.6) into Eqs. (6.1)-(6.4) leads to the boundary value problem of $\phi(x,y,z,t)$

$$\nabla^2 \phi = 0, \text{ in } \overline{V} \tag{6.9}$$

$$\frac{\partial \phi}{\partial n} = 0, \text{ on } \overline{S}_B \tag{6.10}$$

$$\frac{\partial \eta}{\partial t} = \frac{\partial \phi}{\partial z}, \text{ on } \overline{S}_F \tag{6.11}$$

$$\frac{\partial \phi}{\partial t} + g\eta = -\sum_{j=1}^{6} \dot{v}_j(t)\phi_j'(x,y,\bar{z}) - gz_c + g(\alpha_2 x - \alpha_1 y), \text{ on } \overline{S}_F \tag{6.12}$$

The solution ϕ of this non-homogeneous problem can be expanded in a series form

$$\phi(x,y,z,t) = \sum_{i=1}^{\infty} \xi_i(t)\overline{\phi}_i(x,y,z) \tag{6.13}$$

where $\xi_i(t)$ are the time-dependent coefficients and $\overline{\phi}_i$ are ‘natural modes’.

From a physical point of view, $\overline{\phi}_i$ are non-trivial solutions of steady freestanding waves in a stationary tank. Each natural mode corresponds to a natural frequency. To obtain the natural frequencies and modes, the steady (periodic) sloshing should be considered. In a steady state, the free-surface problem has the time-periodic solution $\phi(x,y,z,t)=\sum_{i=1}^{\infty}\cos(\omega_i t)\overline{\phi}_i(x,y,z)$. Substituting the periodic expression into the linear sloshing problem yields the following boundary value problem

$$\nabla^2\overline{\phi}_i=0 \text{, in } \overline{V} \tag{6.14}$$

$$\partial\overline{\phi}_i/\partial n=0 \text{, on } \overline{S}_B \tag{6.15}$$

$$\frac{\partial\overline{\phi}_i}{\partial z}=\frac{\omega_i^2}{g}\overline{\phi}_i \text{, on } \overline{S}_F \tag{6.16}$$

The ω_i that give non-trivial solutions for above equations are natural frequencies while the corresponding non-trivial solutions $\overline{\phi}_i$ are natural modes. Since the sloshing liquid satisfies the conservation of volume, the following equations are also guaranteed

$$\int_{\overline{S}_F}\eta dxdy=0 \quad \text{or} \quad \int_{\overline{S}_F}\overline{\phi}_i dxdy=0 \tag{6.17}$$

6.2.2 BEM solution

A BEM based approach is applied to calculate ω_i and $\overline{\phi}_i$. In this section, the subscript i is omitted for convenience. Firstly, the governing Laplace's equation of $\overline{\phi}$ is transformed into a boundary integral equation (BIE) over the whole fluid boundary S using the Green's third identity

$$c(\mathbf{x}_p)\overline{\phi}(\mathbf{x}_p)=\iint_S\left[G(\mathbf{x}_p,\mathbf{x})\frac{\partial\overline{\phi}(\mathbf{x})}{\partial n}-\overline{\phi}(\mathbf{x})\frac{\partial G(\mathbf{x}_p,\mathbf{x})}{\partial n}\right]dS \tag{6.18}$$

where the index p denotes a collocation point on S, $c(\mathbf{x}_p)$ is the solid angle and $G(\mathbf{x}_p,\mathbf{x})$ denotes the Green's function

$$G(\mathbf{x}_p,\mathbf{x})=\left[(x-x_p)^2+(y-y_p)^2+(z-z_p)^2\right]^{-1/2} \tag{6.19}$$

Then, the BIE is numerically expressed by discretizing the boundary surface into triangular or rectangular flat elements. The velocity potential and its normal derivative on each element are assumed to be constant, which is different from the BEM in Chapter 4 with quantities linearly distributed on each element. Then, Eq. (6.18) becomes

$$2\pi\bar{\phi}_i + \sum_{e=1}^{N_e}\bar{\phi}_e H_{ie} = \sum_{e=1}^{N_e}\left(\frac{\partial\bar{\phi}}{\partial n}\right)_e G_{ie} \ , \quad i=1,2,\cdots,N_e \tag{6.20}$$

$$H_{ie} = \iint_{S_e}\left[\frac{\partial G(\mathbf{x}_i,\mathbf{x})}{\partial n}\right]dS \ , \quad G_{ie} = \iint_{S_e}\left[G(\mathbf{x}_i,\mathbf{x})\right]dS \tag{6.21}$$

Here, N_e is the total number of elements, S_e denotes the e-th element and $\mathbf{x}_i$ denotes the centre of the i-th element with $c(\mathbf{x}_i)=2\pi$.

Assume that the free surface is covered by the first N_a elements, while the tank surface is covered by the remaining $N_b = N_e - N_a$ elements. The Eq. (6.20) could be expressed in the compact form as

$$\begin{pmatrix}[H_{aa}] & [H_{ab}]\\ [H_{ba}] & [H_{bb}]\end{pmatrix}\begin{pmatrix}\{\bar{\phi}\}_a\\ \{\bar{\phi}\}_b\end{pmatrix} = \begin{pmatrix}[G_{aa}] & [G_{ab}]\\ [G_{ba}] & [G_{bb}]\end{pmatrix}\begin{pmatrix}\{\bar{\phi}_n\}_a\\ \{\bar{\phi}_n\}_b\end{pmatrix} \tag{6.22}$$

where $\{\ \}_a$ and $\{\ \}_b$ denote variables on the free-surface and tank-wall elements, respectively. Substituting boundary conditions Eqs. (6.15) and (6.16) into Eq. (6.22) yields

$$\begin{cases}[H_{aa}]\{\bar{\phi}\}_a + [H_{ab}]\{\bar{\phi}\}_b = \dfrac{\omega^2}{g}[G_{aa}]\{\bar{\phi}\}_a\\ [H_{ba}]\{\bar{\phi}\}_a + [H_{bb}]\{\bar{\phi}\}_b = \dfrac{\omega^2}{g}[G_{ba}]\{\bar{\phi}\}_a\end{cases} \tag{6.23}$$

Eliminating the $\{\bar{\phi}\}_b$ leads to

$$\left([G_{aa}]-[H_{ab}][H_{bb}]^{-1}[G_{ba}]\right)^{-1}\left([H_{aa}]-[H_{ab}][H_{bb}]^{-1}[H_{ba}]\right)\{\bar{\phi}\}_a = \frac{\omega^2}{g}\{\bar{\phi}\}_a \tag{6.24}$$

This is a standard eigenvalue problem with eigenvalues ω_i^2/g $(i=1,2,\cdots,N_a)$ and eigenfunctions $\bar{\phi}_i$. The ω_i are natural sloshing

frequencies and $\overline{\phi}_i$ are corresponding natural modes. Although the number of natural frequencies is infinite in reality, only the lowest N_a natural frequencies could be obtained from the numerical solution, with $0 < \omega_1 \le \omega_2 \le \cdots \le \omega_{N_a}$. The equalities suggest that different modes may correspond to natural frequencies of the same value. Take the 3D rectangular tank with a squared base for example. Natural frequencies for two modes in the length and width direction may have the same value. It should be noted that the obtained natural modes are a set of linearly independent eigenfunctions after orthogonalization. The orthogonal property is expressed as

$$\int_{S_F} \overline{\phi}_i \overline{\phi}_j = 0 \text{, for } i \neq j \tag{6.25}$$

6.2.3 Linear free-surface elevation

Since Eq. (6.13) automatically satisfies the Laplace's governing equation and the boundary condition on $\overline{S}_B$, the $\xi_i(t)$ is only determined by the free-surface conditions on $\overline{S}_F$. Substituting Eq. (6.13) to Eq. (6.11) yields

$$\sum_{i=1}^{\infty} \xi_i(t) \frac{\omega_i^2}{g} \overline{\phi}_i = \frac{\partial \eta}{\partial t} \text{, on } \overline{S}_F \tag{6.26}$$

So, it can be constructed as

$$\eta(x, y, t) = \sum_{i=1}^{\infty} \varsigma_i(t) \overline{\phi}_i(x, y, \overline{z}) \tag{6.27}$$

According to the orthogonality, the following relation is guaranteed

$$\dot{\varsigma}_i(t) = \frac{\omega_i^2}{g} \xi_i(t) \tag{6.28}$$

The general solution of the BVP with the non-homogeneous condition can be expanded by orthogonal natural modes. Substituting Eq. (6.13) into Eq. (6.12) leads to

$$\sum_{i=1}^{\infty} \left[\dot{\xi}_i(t) + g\varsigma_i(t) \right] \overline{\phi}_i(x, y, \overline{z}) = -\sum_{j=1}^{6} \dot{v}_j(t) \phi_j'(x, y, \overline{z}) - g z_c + g(\alpha_2 x - \alpha_1 y), \quad \text{on } \overline{S}_F \tag{6.29}$$

or

$$\sum_{i=1}^{\infty}\left[\frac{1}{\omega_i^{\,2}}\ddot{\varsigma}_i(t)+\varsigma_i(t)\right]\bar{\phi}_i(x,y,\bar{z})=-\frac{1}{g}\sum_{j=1}^{6}\dot{v}_j(t)\phi_j'(x,y,\bar{z})-z_c+(\alpha_2 x-\alpha_1 y),\quad \text{on } \bar{S}_F \tag{6.30}$$

Based on the orthogonality of $\bar{\phi}_i$, the linear differential equations could be obtained

$$\begin{aligned}&\left(\int_{\bar{S}_F}\bar{\phi}_i\bar{\phi}_i dS\right)\left(\frac{1}{\omega_i^{\,2}}\ddot{\varsigma}_i(t)+\varsigma_i(t)\right)=-\frac{1}{g}\sum_{j=1}^{6}\dot{v}_j(t)\left(\int_{\bar{S}_F}\phi_j'\bar{\phi}_i dS\right)\\&-z_c\left(\int_{\bar{S}_F}\bar{\phi}_i dS\right)+\alpha_2(t)\left(\int_{\bar{S}_F}x\bar{\phi}_i dS\right)-\alpha_1(t)\left(\int_{\bar{S}_F}y\bar{\phi}_i dS\right)\end{aligned},\ \text{for } i=1,2,\cdots,\infty \tag{6.31}$$

Eq. (6.31) could be rewritten in a neater form

$$\ddot{\varsigma}_i(t)+\omega_i^2\varsigma_i(t)=\frac{\omega_i^{\,2}}{g\mu_i}K_i(t);\quad K_i(t)=-\sum_{j=1}^{6}\dot{v}_j(t)\lambda_{ij}+g\alpha_2(t)\lambda_{i1}-g\alpha_1(t)\lambda_{i2},\quad \text{for } i=1,2,\cdots,\infty \tag{6.32}$$

with

$$\mu_i=\int_{\bar{S}_F}\bar{\phi}_i\bar{\phi}_i dS;\quad \lambda_{i1}=\int_{\bar{S}_F}x\bar{\phi}_i dS;\quad \lambda_{i2}=\int_{\bar{S}_F}y\bar{\phi}_i dS;\quad \lambda_{i3}=-z_c\int_{\bar{S}_F}\bar{\phi}_i dS=0;$$
$$\lambda_{ij}=\int_{\bar{S}_F}\left(\phi_j'\bar{\phi}_i\right)dxdy\quad \text{for } j=4\sim 6 \tag{6.33}$$

Above all, once the spatial functions ϕ_j' and natural modes $\bar{\phi}_i$ are obtained, hydrodynamic coefficients μ_i and λ_{ij} could be known from the integration. Then, the time-dependent coefficients $\varsigma_i(t)$ could be solved by standard time stepping procedure (e.g. Euler's method, or Runge-Kutta method). Finally, the velocity potential $\varphi(x,y,z,t)$ and other variables could be obtained. For a special case when $K_i(t)\equiv 0$, it has $\varsigma_i(t)\equiv 0$ and the i-th mode $\bar{\phi}_i$ can be inactive.

It should be mentioned that, although the BEM could solve Eqs. (6.9)~(6.12) directly in the time domain, the modal analysis method in this chapter has several evident advantages. (1) It resolves the modal components of any complex sloshing. (2) The contribution (coefficients) of different modes to the sloshing solution could be told explicitly. (3) During the

time marching, the matrix size is the truncation number (20 is chosen here), instead of the large boundary element number.

6.3 Numerical verification

In this section, the 3D rectangular tank is considered for the numerical verification. The tank has the length L and width B. The height between the bottom and ceiling of the tank is expressed by H_t. The averaged depth of the liquid in the tank is denoted by H. The analytical solution of natural sloshing frequencies ω_{mn} can be obtained from Eq. (4.30) for comparison. In this chapter, variables are nondimensionalized as $\underbrace{(x,y,z,L,B,H)}_{\text{dimensional}} \rightarrow \underbrace{(x,y,z,L,B,H)}_{\text{nondimensional}} H_t$, $\underset{\text{dimensional}}{\omega} \rightarrow \underset{\text{nondimensional}}{\omega} \sqrt{g/H_t}$ and $\underset{\text{dimensional}}{\varphi} \rightarrow \underset{\text{nondimensional}}{\varphi} H_t\sqrt{gH_t}$. The tank dimensions are set as $L=4/3$, $B=1$ and $H=2/3$.

Firstly the mesh convergence of the numerical scheme is tested. This thesis discretises the free surface using triangular elements, and the tank bottom and walls using quadrilateral ones. These boundary elements have constructed a surface mesh from a geometry point of view. M_1, M_2 and M_3 are used to denote the number of segments along the length, width and depth edge of the tank, respectively. On the side walls of the tank, mesh nodes are distributed rationally from the free surface to the bottom.

In the beginning, $(M_1 \times M_2)=(20\times 20)$ is set and the effect of M_3 is tested. Fig. 6.2(a) shows the lowest twelve natural sloshing frequencies. Here, the analytical solution of ω_n is obtained by sorting ω_{mn} in an ascending order. It is found that numerical results are converging to the analytical ones as M_3 increases. Solutions for the case of $M_3=12$ and $M_3=24$ are graphically indistinguishable. Then, a fixed value $M_3=12$ is set and the case of $(M_1 \times M_2)=(40\times 40)$ is considered. As shown in Fig. 6.2(b), the corresponding numerical results are nearly coincident with each other. To sum up, for the case under investigation, $(M_1 \times M_2 \times M_3)=(20\times 20\times 12)$ with 2378 elements could guarantee mesh convergence. The mesh model is shown in Fig. 6.3. Patterns of the lowest three natural modes are given in Fig.

6.4 for illustration. The contour indicates the amplitude difference of the free-surface elevation under this mode. The modes in terms of ω_{01} and ω_{10} are fundamental modes, which are primarily concerned by marine engineering applications.

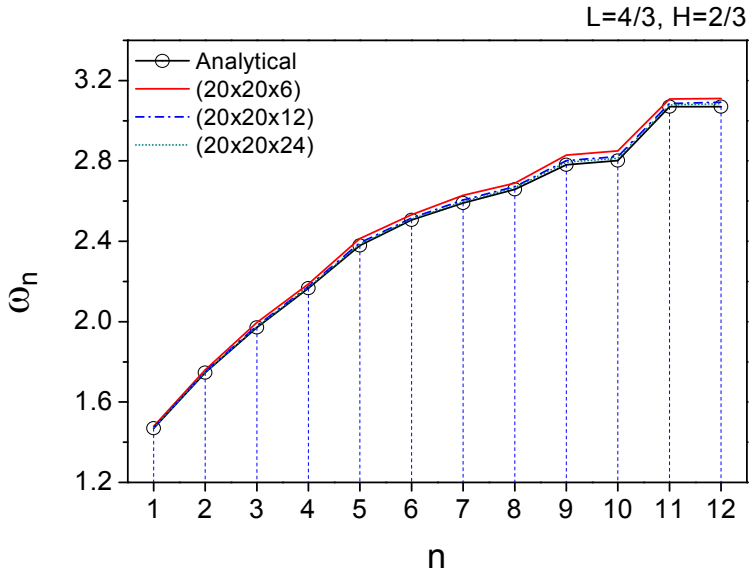

(a)

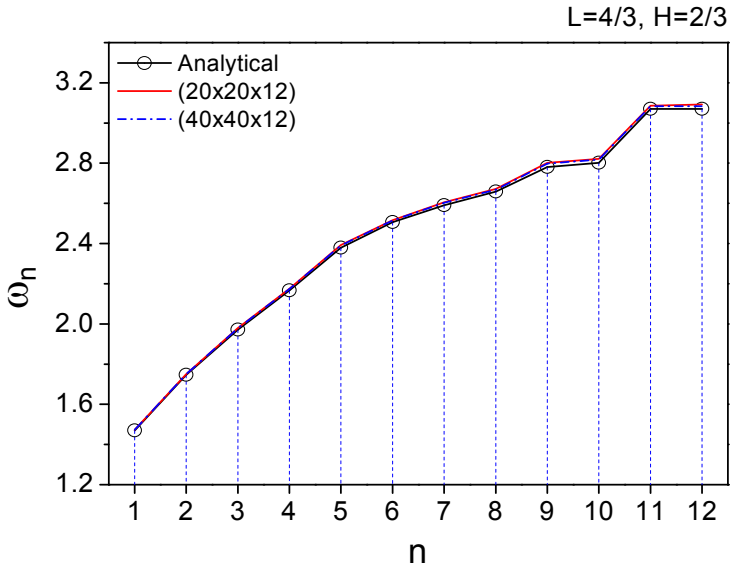

(b)

Fig. 6.2 Natural sloshing frequencies of 3D rectangular tank for $L = 4/3$, $B = 1$ and $H = 2/3$

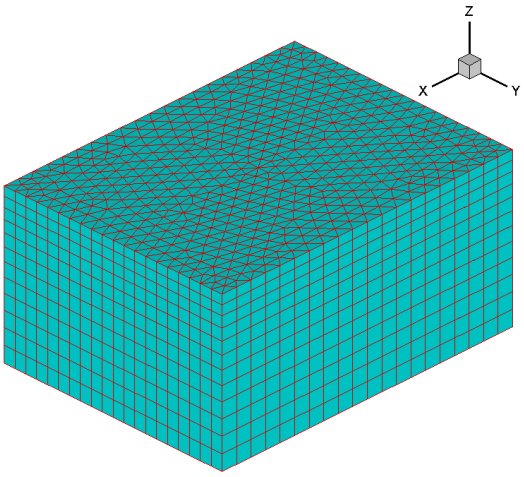

Fig. 6.3 Mesh model for BEM

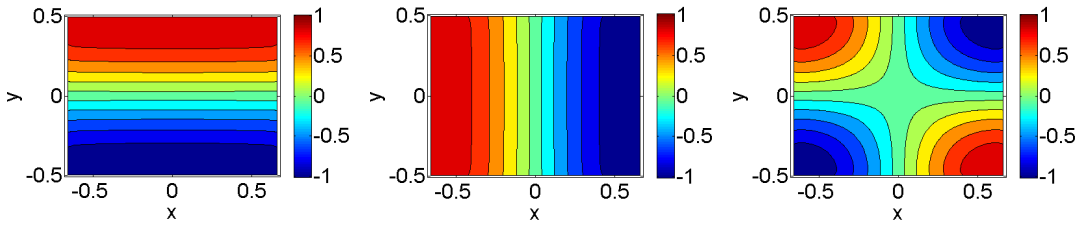

(a) (b) (c)

Fig. 6.4 Patterns of lowest three modes, (a) ω_{01}, (b) ω_{10} and (c) ω_{11}

Further, the numerical scheme for the wave elevation calculation is verified. The tank is undergoing a surge oscillation $x_c(\tau) = A\sin\omega\tau$. The obtained wave elevation histories are compared with the analytical solutions of Eq. (4.34). The excitation amplitude A is set to be 0.001 and two frequencies $\omega = 0.9\omega_{10}$ and $\omega = \omega_{10}$ are considered. The wave elevation histories at a point $x = -0.63$ near the left tank wall are given in Fig. 6.5. It is clear that the numerical results agree well with the corresponding analytical ones. This has verified the present numerical scheme for wave elevation calculations.

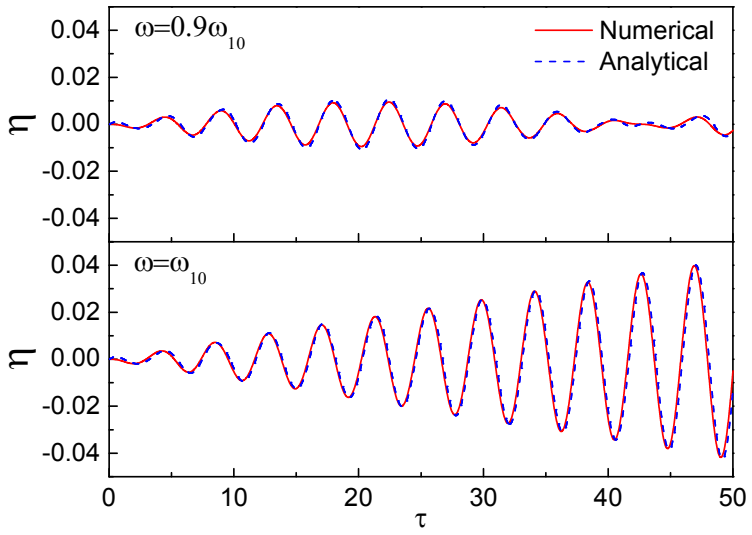

Fig. 6.5 Wave elevation history at a point $x=-0.63$ in rectangular tank for $L=4/3$, $B=1$, $H=2/3$ and $A=0.001$

6.4 Results and discussion

6.4.1 Natural sloshing frequencies and modes

In this section, the FLNG vessel with four wedged tanks is considered. The design of these tanks is illustrated in Fig. 6.6. Each tank has a trapezoidal cross-section with one or two walls inclined and the rest walls vertical. The incline angle is θ about the axis at $z=0.5H_t$, and all tanks have the same maximum storage. To be convenient, Tank-II and Tank-IV are called the 'converging tank', since the tank ceiling area is smaller than the bottom area. Conversely, the Tank-I and Tank-III are called the 'diverging tank'. The tank dimensions are chosen to be $L=B=1$. Six incline angles $\theta=k\pi/24\ (k=0,1,\cdots,5)$ and four fill levels 10%, 30%, 50% and 70% would be considered. The BEM meshes are obtained by scaling the mesh in Fig. 6.3. Fig. 6.7 shows examples of mesh models for the case of $H=50\%$ and $\theta=5\pi/24$.

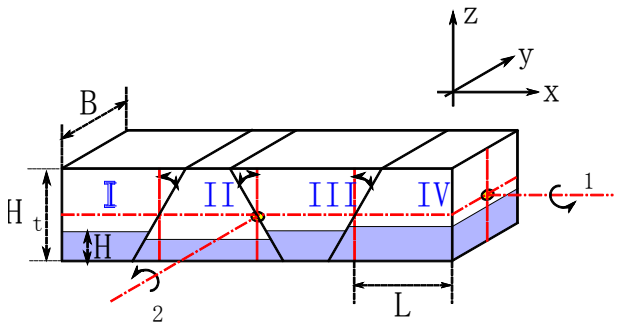

Fig. 6.6 Designed tanks on FLNG vessel

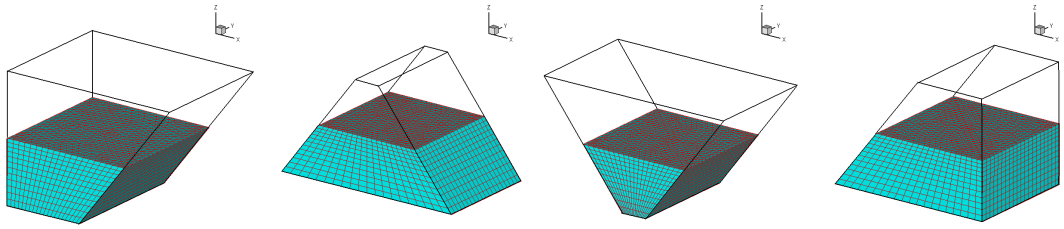

(a) (b) (c) (d)

Fig. 6.7 Mesh models of wedged tanks, (a) Tank-I, (b) Tank-II, (c) Tank-III, and (d) Tank-IV

Natural modes for a wedged tank could be considered as a variation of those in the rectangular tank. Fig. 6.8 to Fig. 6.11 show the pattern of natural modes corresponding to ω_{01} for Tank-I to Tank-IV, respectively. The tanks are filled to $H = 50\%$. In all cases, the mode patterns are asymmetric about the x-axis, which means that integrations in λ_{i1} and λ_{i5} are zero. At this mode, the maximum wave amplitude emerges at corners near the inclined wall in Tank-I, the middle of vertical walls in Tank-II, four corners in Tank-III, and corners of vertical walls in Tank-IV, respectively. For all tanks, the wave peaks become even sharper as the incline angle increases.

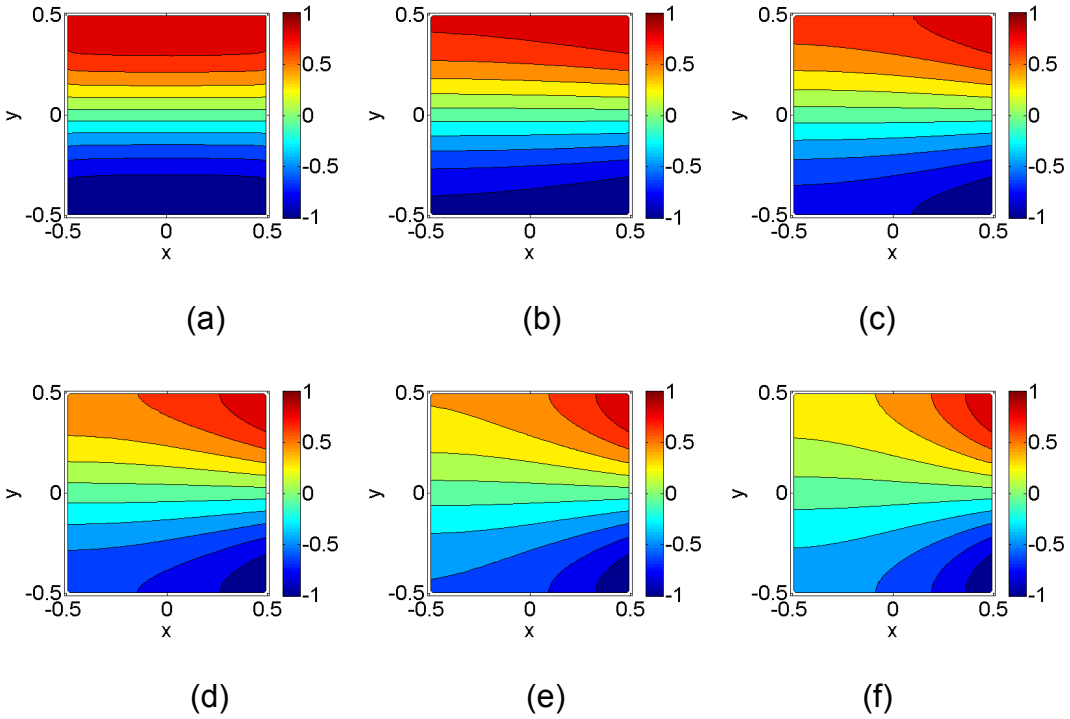

Fig. 6.8 Mode patterns corresponding to ω_{01} in Tank-I, (a) $\theta = 0$, (b) $\theta = \pi/24$, (c) $\theta = 2\pi/24$, (d) $\theta = 3\pi/24$, (e) $\theta = 4\pi/24$, and (f) $\theta = 5\pi/24$

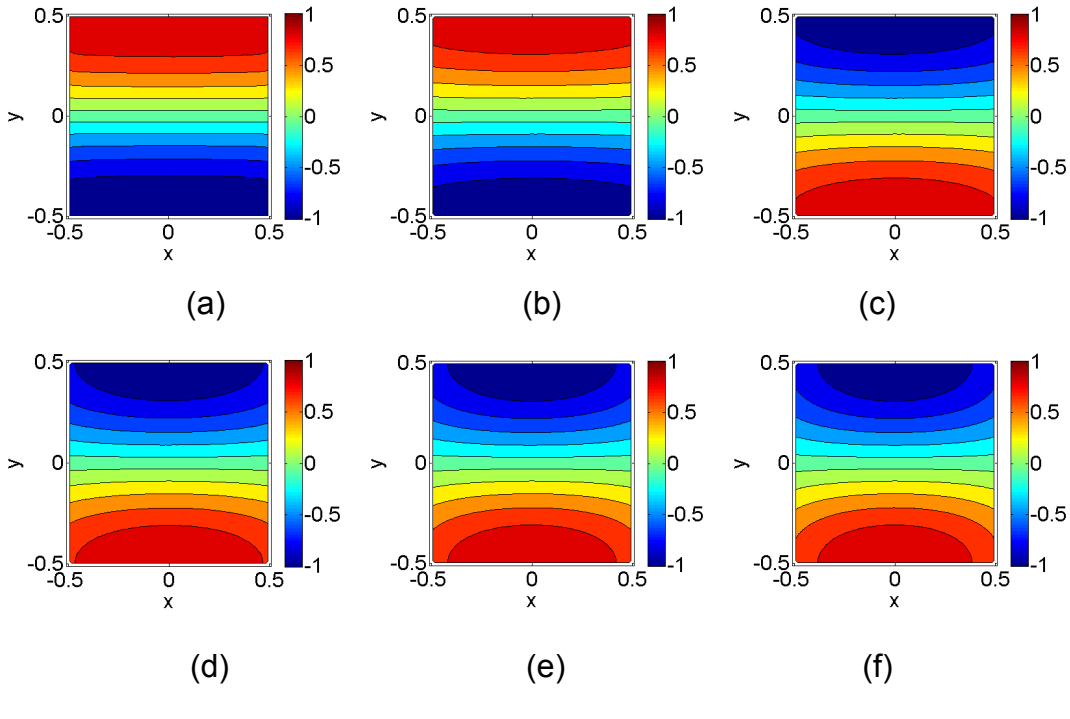

Fig. 6.9 Mode patterns corresponding to ω_{01} in Tank-II, (a) $\theta = 0$, (b) $\theta = \pi/24$, (c) $\theta = 2\pi/24$, (d) $\theta = 3\pi/24$, (e) $\theta = 4\pi/24$, and (f) $\theta = 5\pi/24$

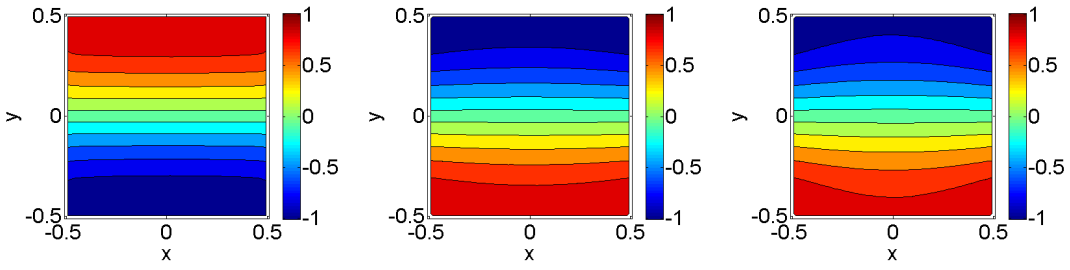

(a) (b) (c)

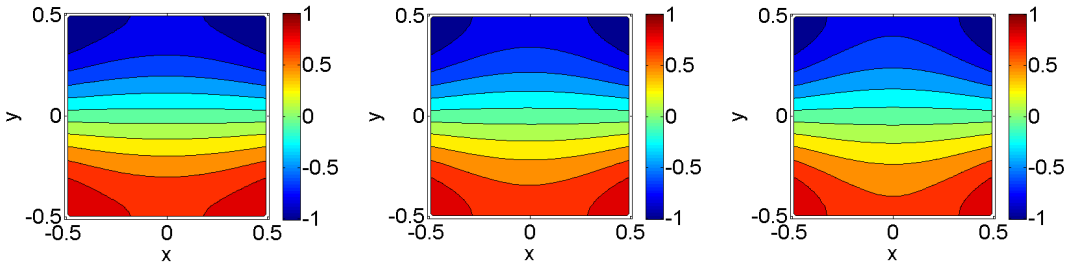

(d) (e) (f)

Fig. 6.10 Mode patterns corresponding to ω_{01} in Tank-III, (a) $\theta = 0$, (b) $\theta = \pi/24$, (c) $\theta = 2\pi/24$, (d) $\theta = 3\pi/24$, (e) $\theta = 4\pi/24$, and (f) $\theta = 5\pi/24$

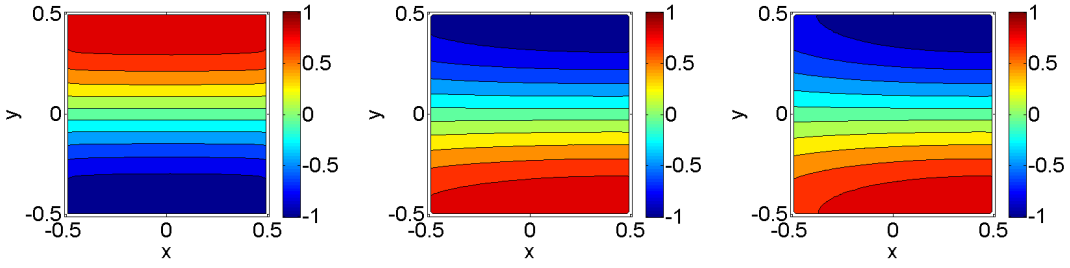

(a) (b) (c)

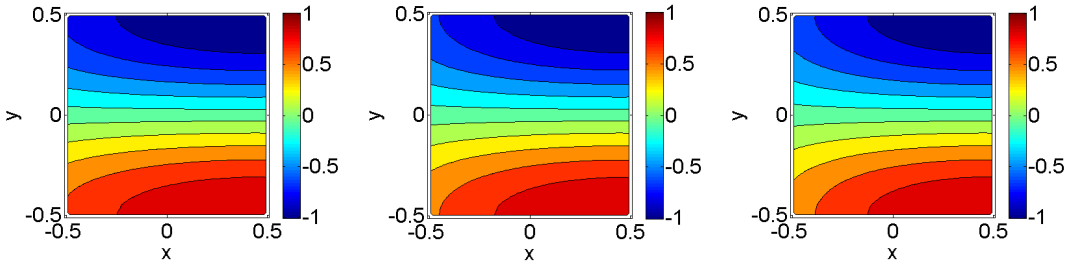

(d) (e) (f)

Fig. 6.11 Mode patterns corresponding to ω_{01} in Tank-IV, (a) $\theta = 0$, (b) $\theta = \pi/24$, (c) $\theta = 2\pi/24$, (d) $\theta = 3\pi/24$, (e) $\theta = 4\pi/24$, and (f) $\theta = 5\pi/24$

Then the natural sloshing frequency ω_{01} of the four tanks is plotted in

Fig. 6.12. From Fig. 6.12(a), the following observations are obtained. (1) As the incline angle grows from $\theta = \pi/24$ to $\theta = 5\pi/24$, the value of ω_{01} decreases in diverging tanks (Tank I and Tank III) but increases in converging tanks (Tank II and Tank IV). So the value of ω_{01} in four tanks becomes more dispersed as θ grows. (2) The value of ω_{01} in the four tanks becomes more dispersed, as the fill level increases. (3) The changing rate of ω_{01} in diverging tanks is greater than that in converging tanks, as θ grows. (4)The value of ω_{01} for tanks with two inclined walls (Tank II and Tank III) changes greater than that with only one inclined wall (Tank I and Tank IV). Fig. 6.12(b) is used to investigate whether four tanks filled at different levels could have the same natural frequency ω_{01}. Fig. 6.12(b) describes the data in Fig.6.12(a) from a different perspective. It should firstly be noted that, in practice, all tanks should be filled at a similar level for the load balance on vessel structures. Then, if all tanks are filled at a low level (e.g. $H < 30\%$), these tanks may have the same ω_{01}, but the liquid mass is not expected to be large enough to greatly affect the vessel motion. Otherwise, four tanks could not have the same ω_{01} within the permitted filling differences.

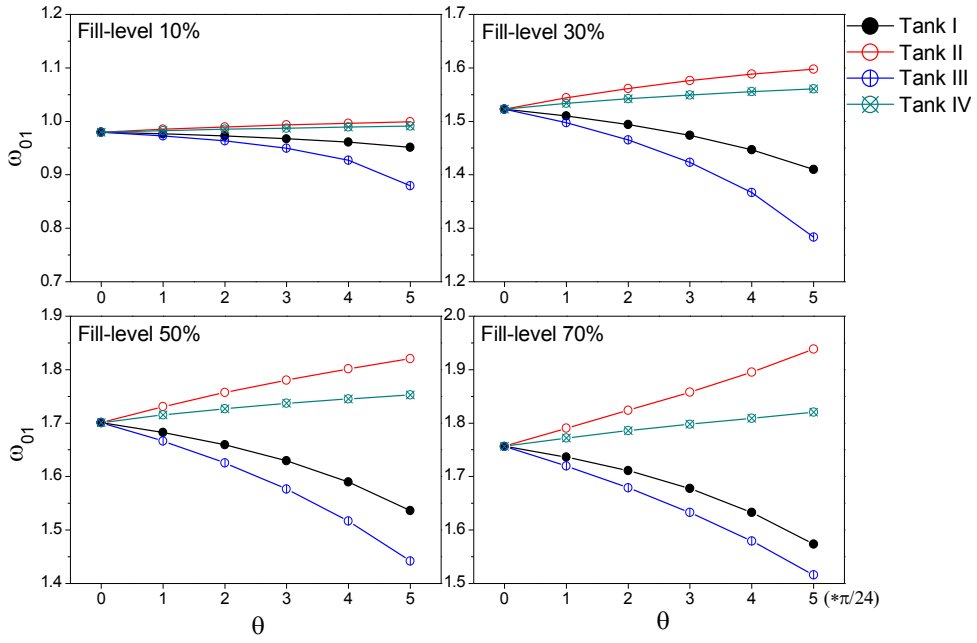

(a)

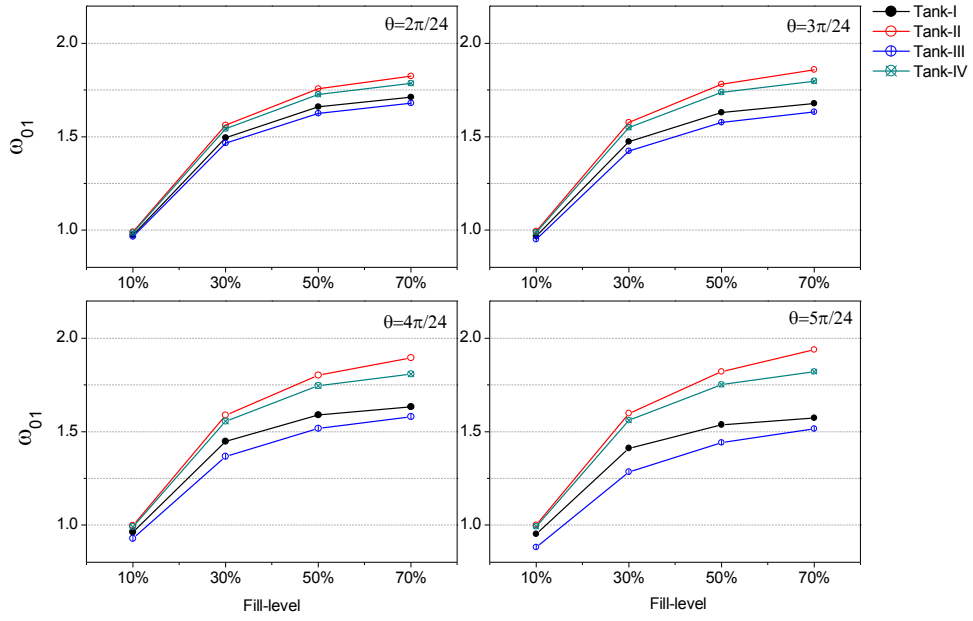

(b)

Fig. 6.12 Natural sloshing frequency ω_{01} for $L = B = 1$

Then the natural modes corresponding to ω_{10} are considered. Fig. 6.13

to Fig. 6.16 show patterns of the natural mode in Tank-I to Tank-IV, respectively. These mode patterns are symmetric about the x-axis. From Eqs. (6.32) and (6.33), it is known that this natural mode could be triggered by the surge or pitch excitation. At this mode, as the incline angle increases, the wave peak in diverging tanks would become sharper near the inclined wall. For converging tanks, a flatter peak or trough tends to emerge near the inclined wall.

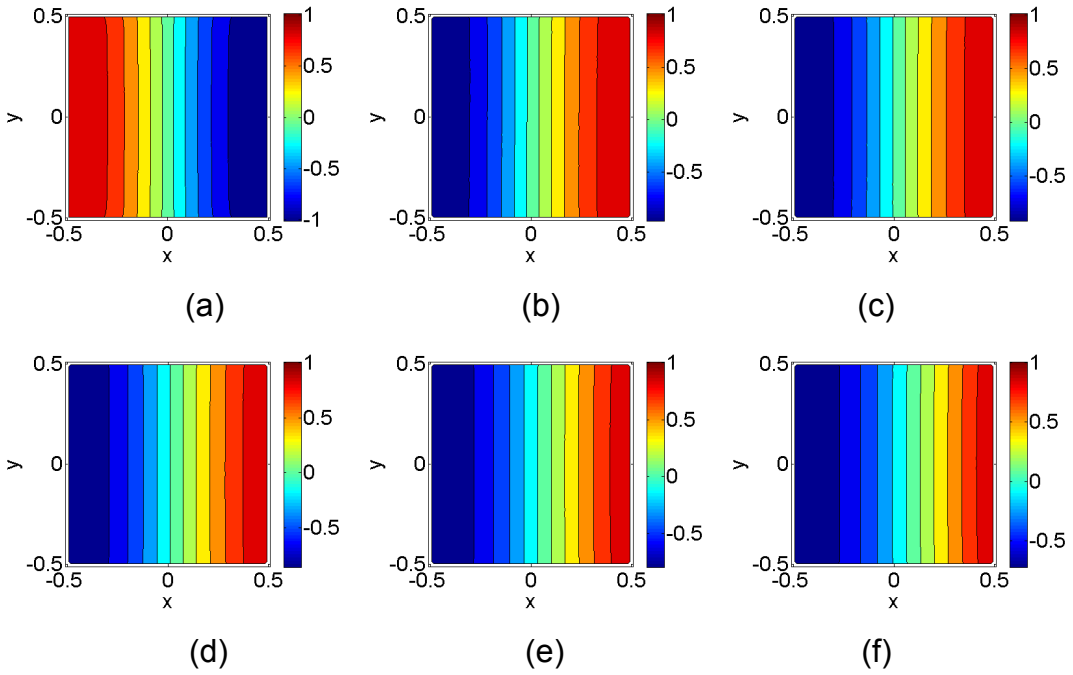

Fig. 6.13 Mode patterns corresponding to ω_{10} in Tank-I, (a) $\theta = 0$, (b) $\theta = \pi/24$, (c) $\theta = 2\pi/24$, (d) $\theta = 3\pi/24$, (e) $\theta = 4\pi/24$, and (f) $\theta = 5\pi/24$

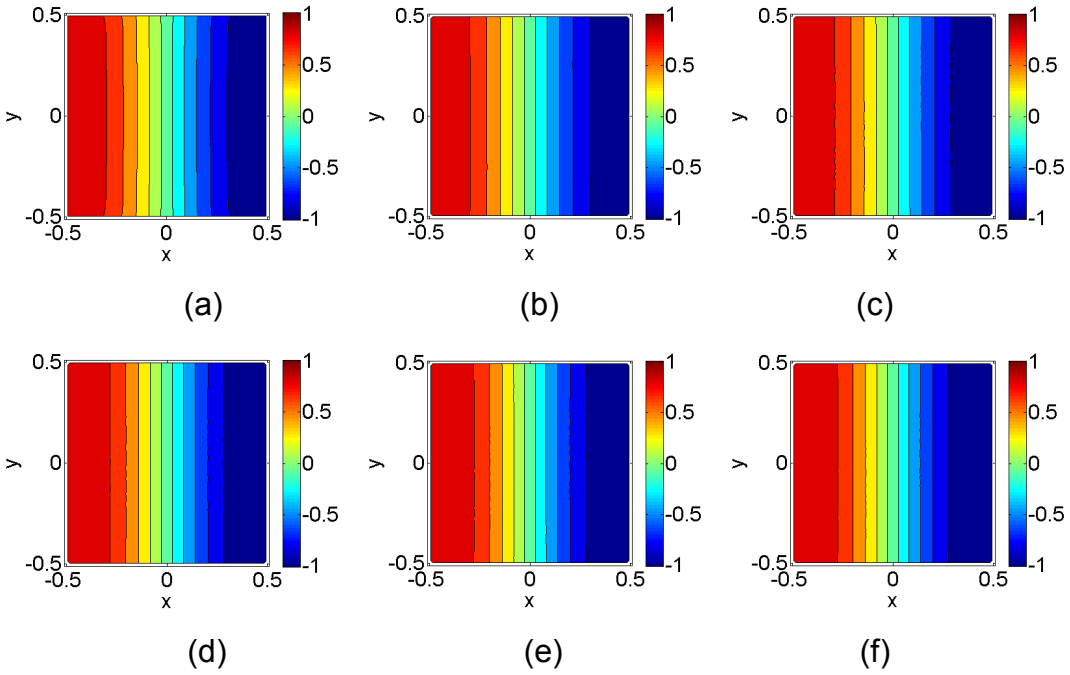

Fig. 6.14 Mode patterns corresponding to ω_{10} in Tank-II, (a) $\theta = 0$, (b) $\theta = \pi/24$, (c) $\theta = 2\pi/24$, (d) $\theta = 3\pi/24$, (e) $\theta = 4\pi/24$, and (f) $\theta = 5\pi/24$

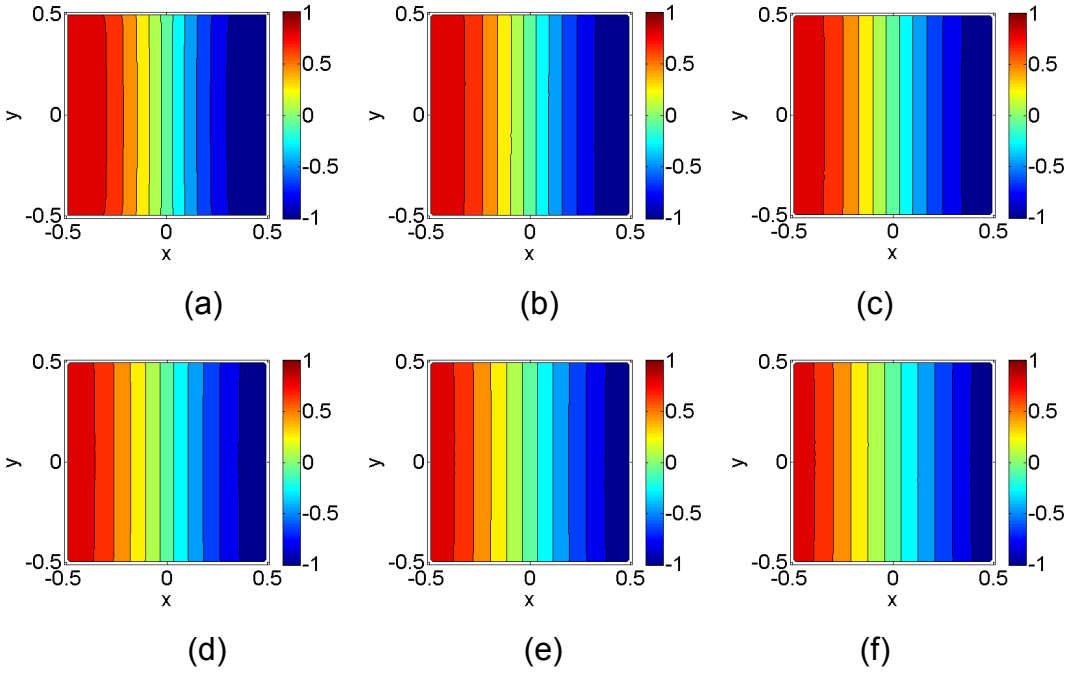

Fig. 6.15 Mode patterns corresponding to ω_{10} in Tank-III, (a) $\theta = 0$, (b) $\theta = \pi/24$, (c) $\theta = 2\pi/24$, (d) $\theta = 3\pi/24$, (e) $\theta = 4\pi/24$, and (f) $\theta = 5\pi/24$

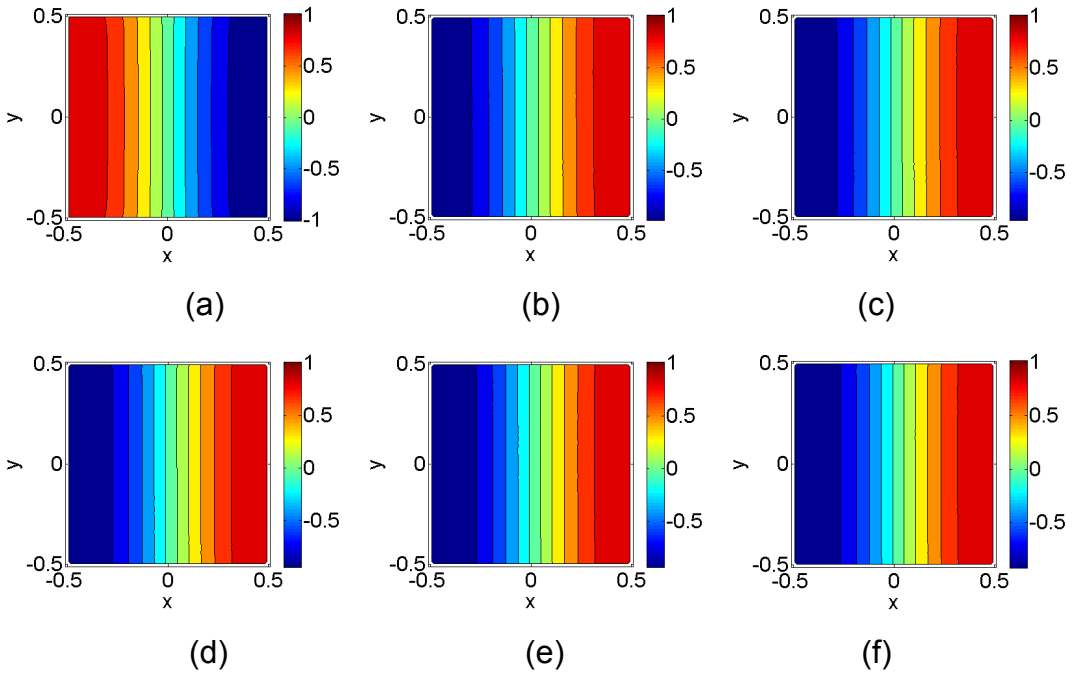

Fig. 6.16 Mode patterns corresponding to ω_{10} in Tank-IV, (a) $\theta = 0$, (b) $\theta = \pi/24$, (c) $\theta = 2\pi/24$, (d) $\theta = 3\pi/24$, (e) $\theta = 4\pi/24$, and (f) $\theta = 5\pi/24$

The values of ω_{10} in the four tanks with different fill levels are given in Fig. 6.17. Fig. 6.17(a) shows that at a certain fill level, the value of ω_{10} in each tank generally becomes more dispersed as the incline angle increases. Also, the value of ω_{10} for tanks with two inclined walls (i.e. Tank-II and Tank-III) changes faster than that with only one inclined wall (i.e. Tank-I and Tank-IV), as θ increases. However, it seems that there might exist a critical fill level between 30% and 50%. Below this level, the value of ω_{10} in diverging tanks grows with θ; but above this level, ω_{10} decreases. The ω_{10} in converging tanks has opposite trend. Fig. 6.17(b) describes the data in Fig. 6.17(a) from a different perspective. Consider fill levels above 30%. The value of ω_{10} in converging tanks increases with the fill level while a decreasing trend is found in diverging tanks. It is interesting to find that the natural frequencies ω_{10} in four tanks filled at about 45% are nearly the same. Besides this critical situation, four tanks could not have the same natural frequency ω_{10} at a similar fill level.

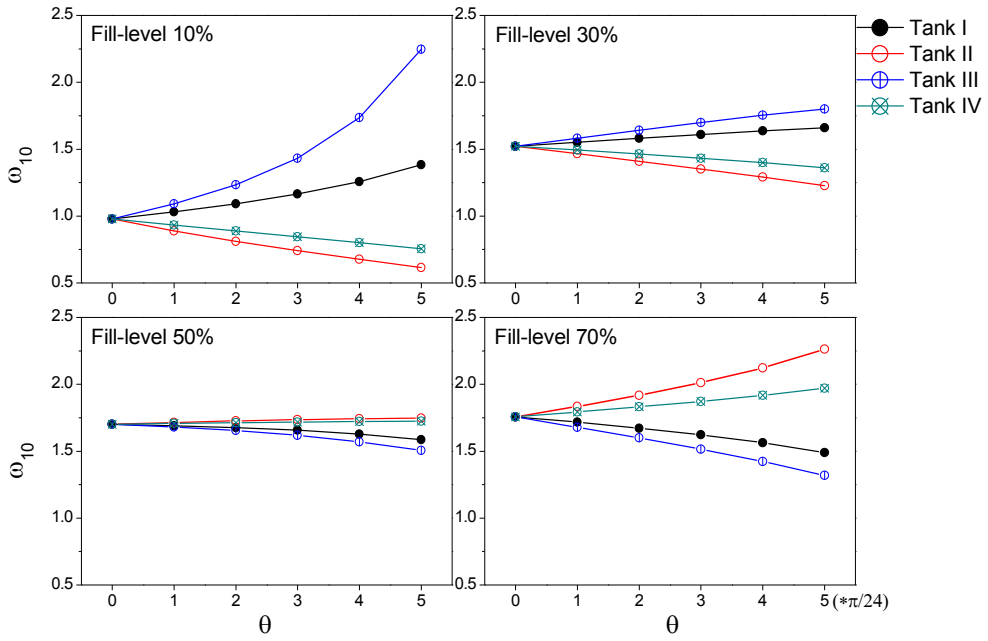

(a)

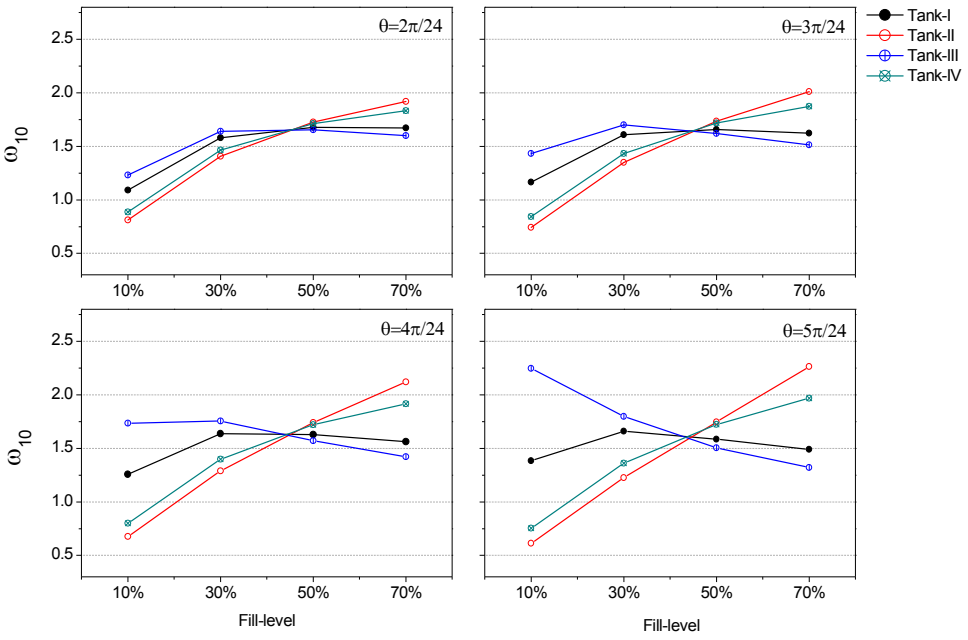

(b)

Fig. 6.17 Natural sloshing frequency ω_{10} for $L = B = 1$

6.4.2 Sloshing under resonance conditions

In this subsection, the vessel is excited by sway, roll, surge and pitch motions at the resonance condition of each sloshing tank, and study the linear sloshing behaviour in these wedged tanks. The situation of $\theta = 5\pi/24$ and $H = 50\%$ is taken as an example. The first 20 modes of Eq. (6.27) are truncated.

Firstly the sway excitation $y_c(t) = A\sin(\omega\tau)$ with $A = 0.001$ is considered. The amplitude is set to be small in order to keep the problem within the linear range. From the above modal analysis, it is known that the first active mode triggered by the sway excitation corresponds to the natural frequency ω_{01}. According to the linear theory, when ω equals to ω_{01}, the resonant sloshing would occur. For Tank-I, II, III and IV, the natural sloshing frequency ω_{01} are represented using $\omega_{01}^{(I)}$, $\omega_{01}^{(II)}$, $\omega_{01}^{(III)}$ and $\omega_{01}^{(IV)}$, respectively. Fig. 6.18 (a)-(d) show the wave elevation histories in four tanks, when the vessel is forced to sway at $\omega = \omega_{01}^{(I)}$, $\omega_{01}^{(II)}$, $\omega_{01}^{(III)}$ and $\omega_{01}^{(IV)}$, respectively. Here, each elevation history is measured where the maximum wave amplitude occurs on the free surface. From Fig. 6.18 (a) to (d), it is clear that when the vessel sways at $\omega = \omega_{01}^{(I)}$, $\omega_{01}^{(II)}$, $\omega_{01}^{(III)}$ and $\omega_{01}^{(IV)}$, the sloshing resonance occurs in Tank-I, II, III and IV, respectively. Meanwhile, the sloshing in the rest of the tanks remains gentle.

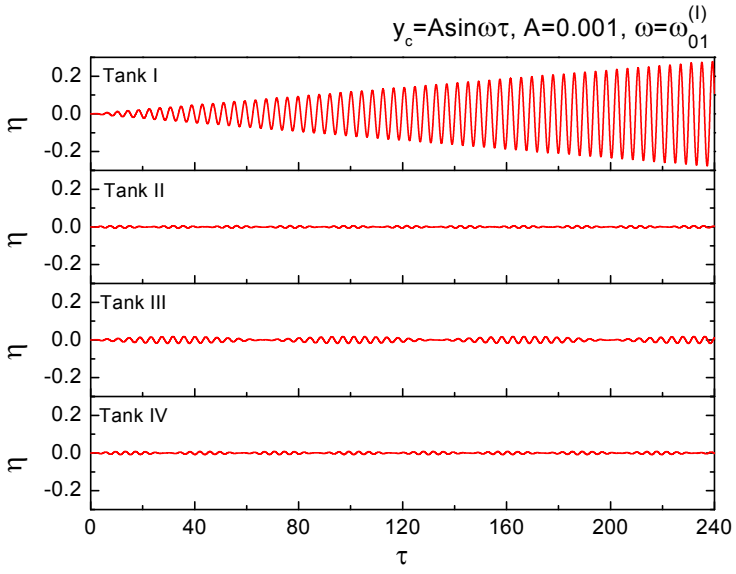
y_c=Asinωτ, A=0.001, ω=$\omega_{01}^{(I)}$
Tank I
Tank II
Tank III
Tank IV
η
0.2
0.0
-0.2
0
40
80
120
160
200
240
τ

(a)

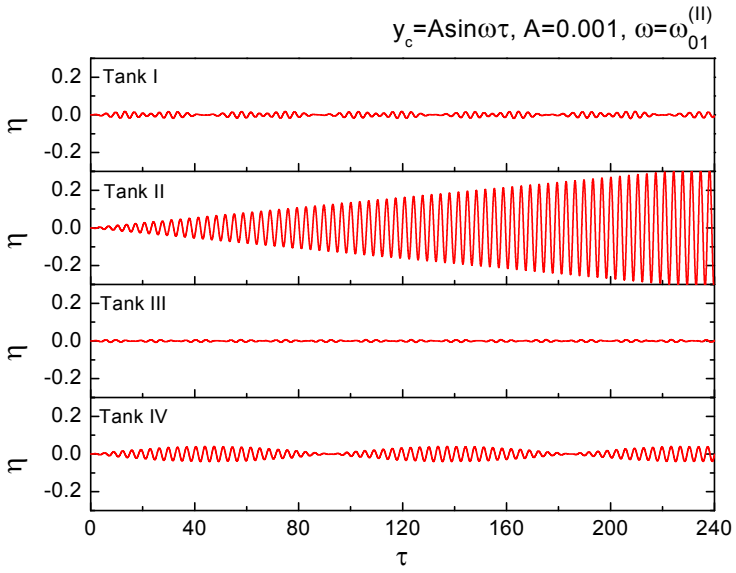
y_c=Asinωτ, A=0.001, ω=$\omega_{01}^{(II)}$
Tank I
Tank II
Tank III
Tank IV
η
0.2
0.0
-0.2
0
40
80
120
160
200
240
τ

(b)

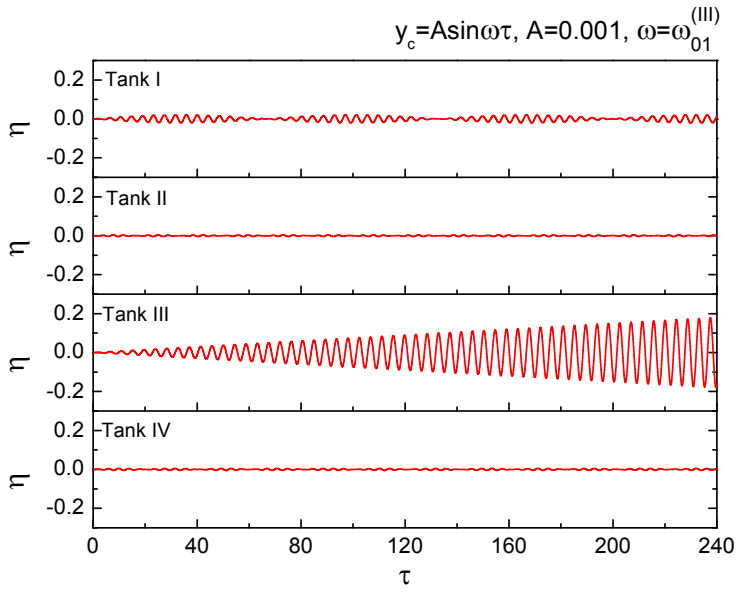

(c)

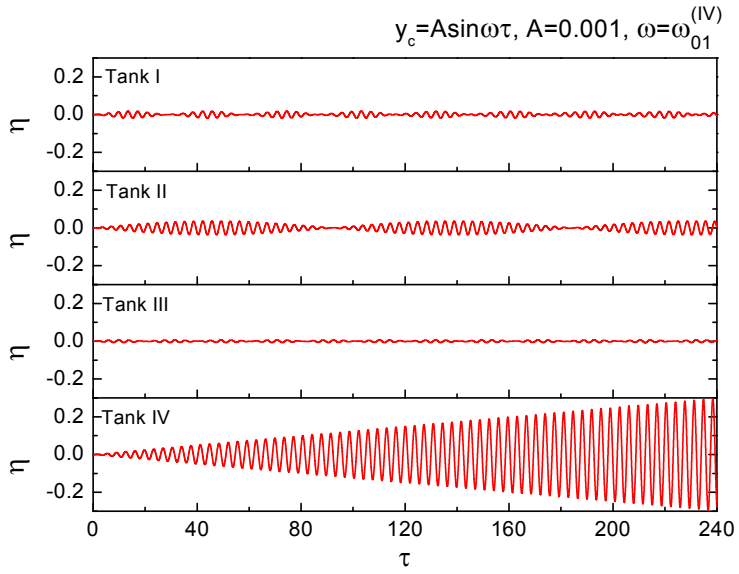

(d)

Fig. 6.18 Wave elevation history in tanks due to sway excitation for $L=B=1$, $H=0.5$, $\theta=5\pi/24$, $A=0.001$, and $\omega=$(a) $\omega_{01}^{(I)}$; (b) $\omega_{01}^{(II)}$; (c) $\omega_{01}^{(III)}$; (d) $\omega_{01}^{(IV)}$

Secondly, the roll excitation of $\alpha_1(t)=A\sin(\omega\tau)$ is considered. Similar to the sway cases, the fundamental natural sloshing mode triggered by the roll excitation also corresponds to the natural frequency ω_{01}. The roll amplitude is set to be $A=\pi/360$. The excitation frequency is set as $\omega=\omega_{01}^{(I)}$, $\omega_{01}^{(II)}$, $\omega_{01}^{(III)}$ and $\omega_{01}^{(IV)}$, respectively. The corresponding wave elevation histories in four tanks are given in Fig. 6.19. It is also observed that in any case, the resonant

sloshing does not occur simultaneously in all tanks.

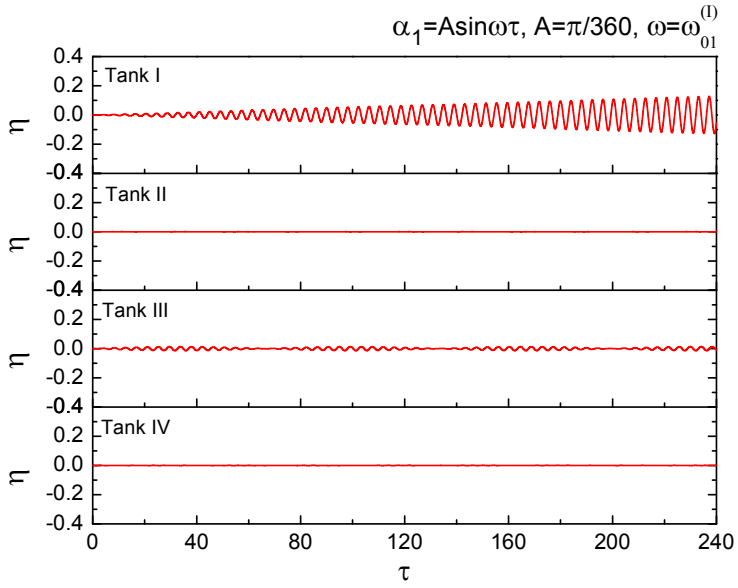

(a)

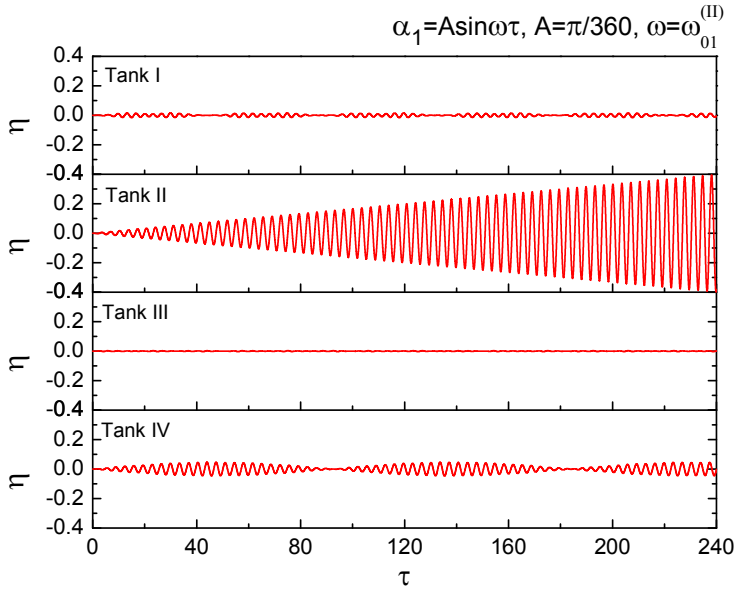

(b)

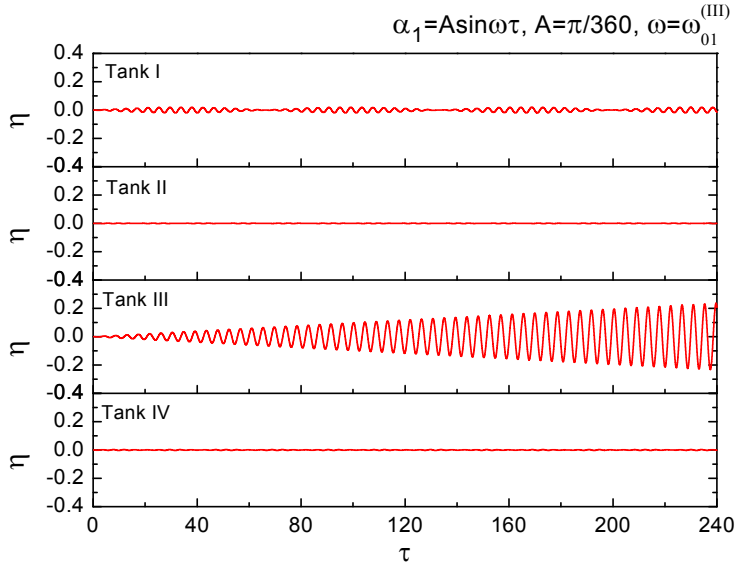

(c)

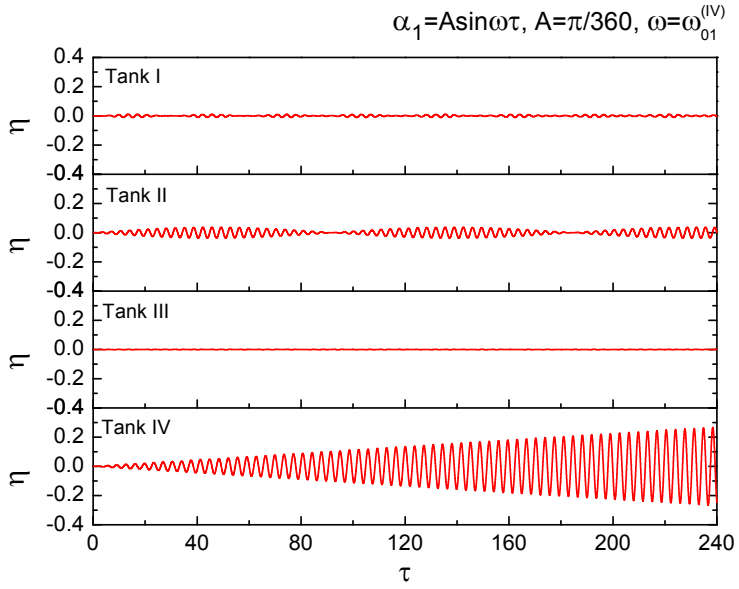

(d)

Fig. 6.19 Wave elevation history in tanks due to roll excitation for $L = B = 1$, $H = 0.5$, $\theta = 5\pi/24$, $A = \pi/360$, and $\omega =$ (a) $\omega_{01}^{(I)}$; (b) $\omega_{01}^{(II)}$; (c) $\omega_{01}^{(III)}$; (d) $\omega_{01}^{(IV)}$

Thirdly, the vessel is surged as $x_c(t) = A\sin(\omega\tau)$ with $A = 0.001$. From Eqs. (6.32) and (6.33), it is known that the first active mode triggered by the surge excitation corresponds to natural frequency ω_{10}. For Tank-I, II, III and IV, the natural sloshing frequency ω_{10} is expressed as $\omega_{10}^{(I)}$, $\omega_{10}^{(II)}$, $\omega_{10}^{(III)}$ and $\omega_{10}^{(IV)}$, respectively. Fig. 6.20 shows the wave elevation histories in the

four tanks under these surge frequencies. When the resonance occurs in either of the diverging tanks, the liquid motion in converging tanks would be gentle, and vice versa. However, when the resonance occurs in one converging tank, the wave amplitude in the other would also be evident, referring to Fig. 6.20 (b) and (d). This could be explained by Fig. 6.17 that at the present fill level 50%, the difference of the ω_{10} in converging tanks is small.

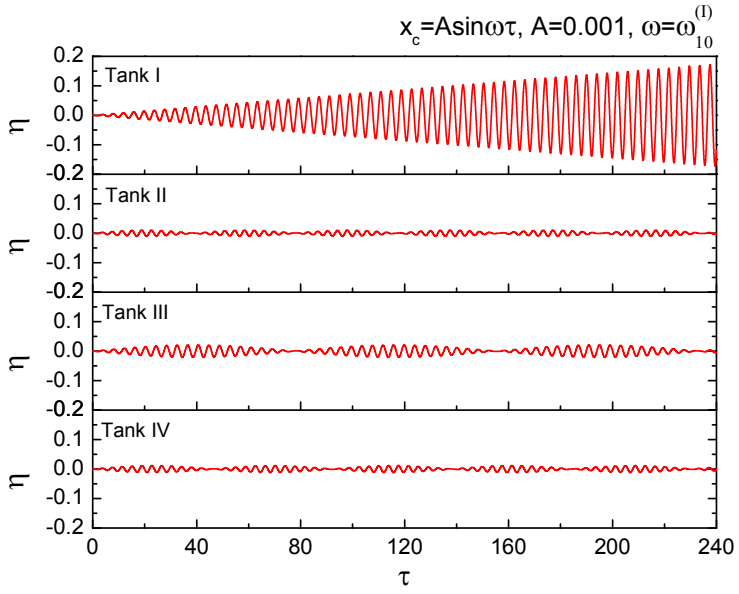

(a)

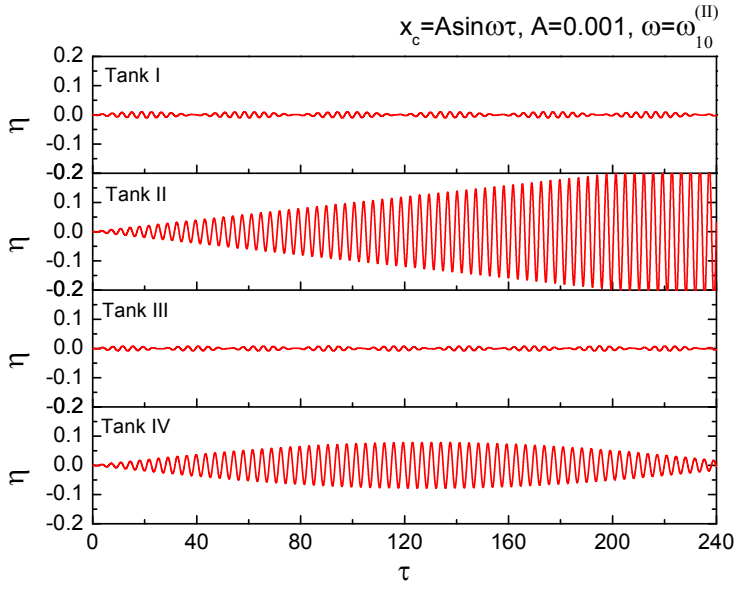

(b)

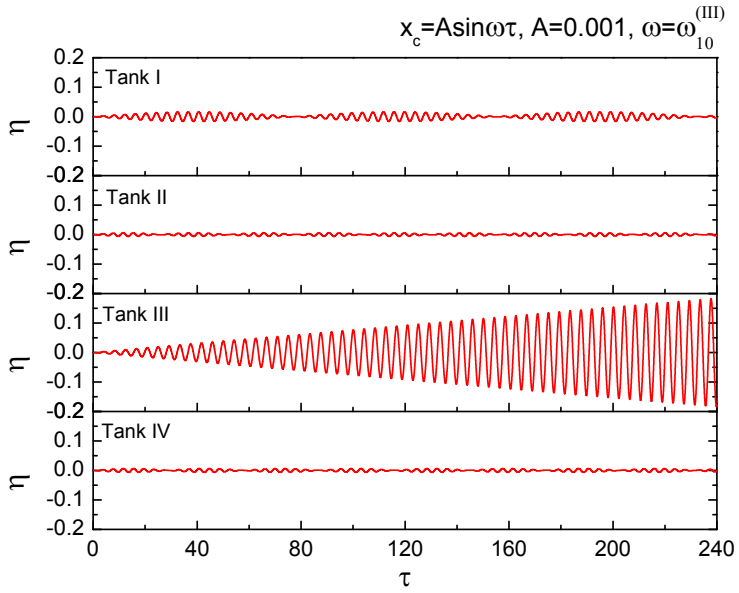

(c)

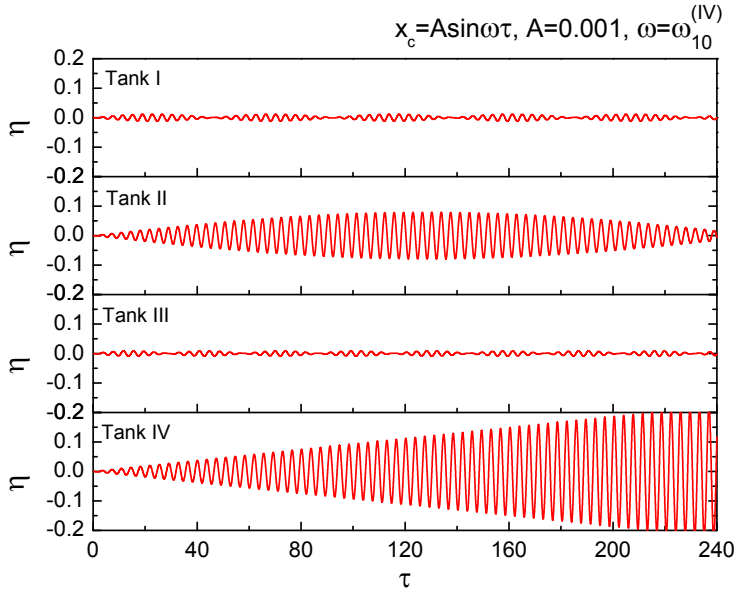

(d)

Fig. 6.20 Wave elevation history in tanks due to surge excitation for $L=B=1$, $H=0.5$, $\theta=5\pi/24$, $A=0.001$, and $\omega=$ (a) $\omega_{10}^{(I)}$; (b) $\omega_{10}^{(II)}$; (c) $\omega_{10}^{(III)}$; (d) $\omega_{10}^{(IV)}$

Finally, the pitch excitation as $\alpha_2(t)=A\sin(\omega\tau)$ with $A=\pi/360$ is considered. The rotational axis is the intersection of the plane $x=0$ and $z=0$ as shown in Fig. 6.6. The pitch frequency is set as $\omega=\omega_{10}^{(I)}$, $\omega_{10}^{(II)}$, $\omega_{10}^{(III)}$ and $\omega_{10}^{(IV)}$, respectively, to trigger the sloshing mode. The wave elevation histories are shown in Fig. 6.21. It is found that in all cases the wave

elevation at Tank-I and IV has evident amplitudes. This is due to the fact that the sloshing response is related to the vessel's acceleration. Although all tanks have the same angular acceleration, two tanks at the vessel ends have larger accelerations than the rest of the tanks. For Tank-I in Fig.6.21 (a) and Tank-IV in Fig.6.21(d), the wave amplitudes grow to a large value in a short time. After that, the linear assumption adopted by the present method is not valid any more, and the elevation histories are not plotted in the figure. In Fig. 6.21 (b) and (c), the wave amplitudes in Tank-II and -III grow with time, respectively, as a resonance phenomenon. In Fig. 6.21 (b), the wave amplitude in Tank-IV is also high, but its amplitude does not keep increasing with time. For Tank-I and -III in Fig.6.21 (b) and Tank-I, -II and –IV in Fig. 6.21 (c), the wave amplitudes are limited.

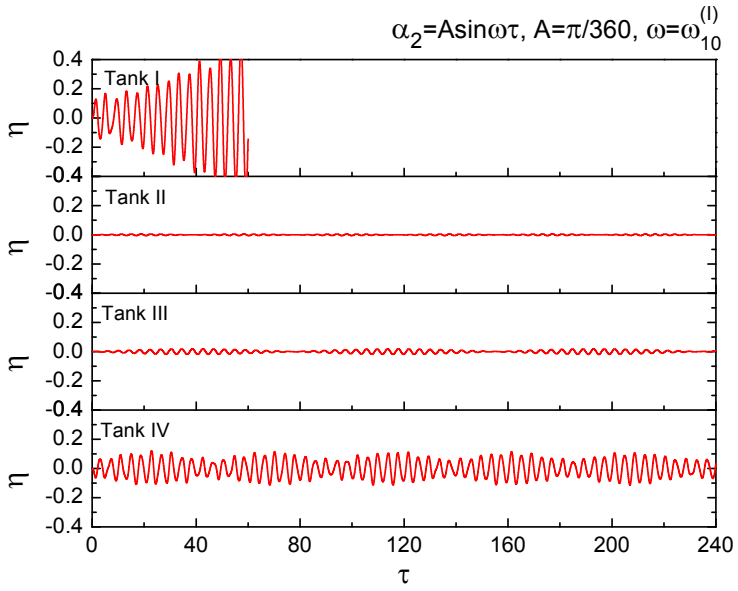
α_2=Asin$\omega\tau$, A=π/360, $\omega=\omega_{10}^{(I)}$
Tank I
Tank II
Tank III
Tank IV
η
τ
0.4
0.2
0.0
-0.2
-0.4
0
40
80
120
160
200
240

(a)

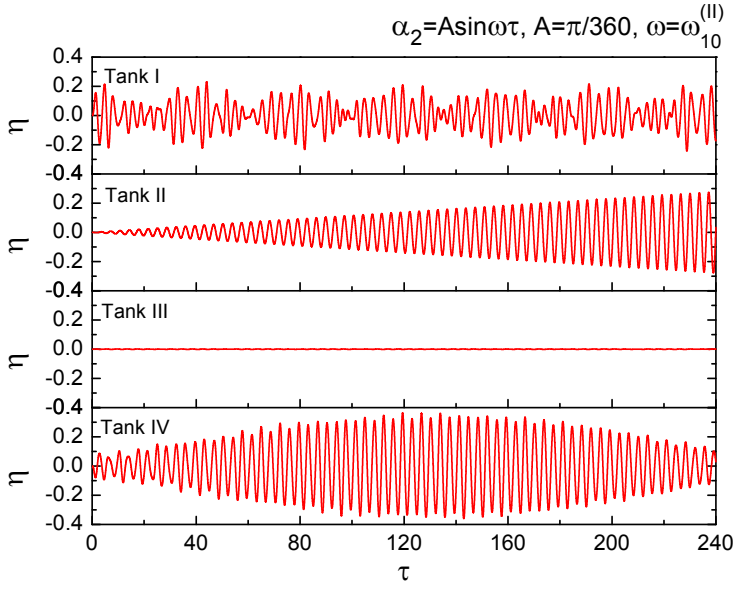
α_2=Asin$\omega\tau$, A=π/360, $\omega=\omega_{10}^{(II)}$
Tank I
Tank II
Tank III
Tank IV
η
τ
0.4
0.2
0.0
-0.2
-0.4
0
40
80
120
160
200
240

(b)

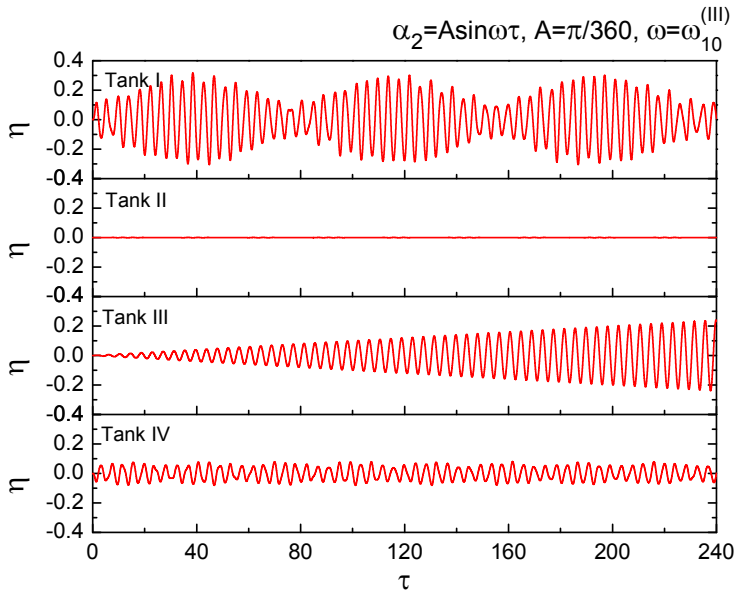

(c)

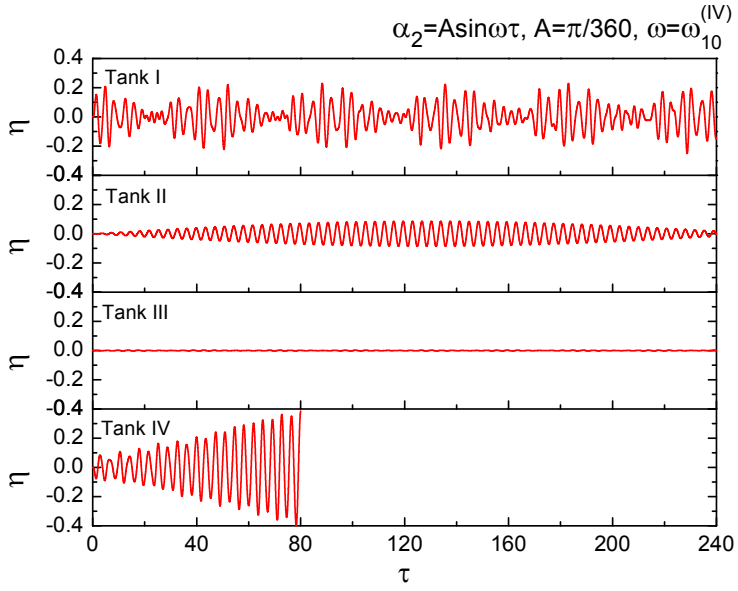

(d)

Fig. 6.21 Wave elevation history in tanks due to pitch excitation for $L = B = 1$, $H = 0.5$, $\theta = 5\pi/24$, $A = \pi/360$, and $\omega =$ (a) $\omega_{10}^{(I)}$; (b) $\omega_{10}^{(II)}$; (c) $\omega_{10}^{(III)}$; (d) $\omega_{10}^{(IV)}$

From Fig. 6.18 to Fig.6.21, it is confirmed that the distinction of natural frequencies in the four tanks is sufficiently large to guarantee that the resonant sloshing could not occur simultaneously in all tanks. Since the violent liquid sloshing indicates large forces and moments acting on the vessel, it is expected that this design of the FLNG vessel with wedged tanks could restrict the sloshing dynamic effects on the vessel motion.

6.5 Conclusions

In this chapter, the design of the FLNG vessel with wedged tanks was considered. A numerical approach with the help of BEM is developed to calculate the natural sloshing frequencies and corresponding modes for these wedged tanks. The effects of the inclined tank wall on natural sloshing frequencies/modes are identified. It is found that, in general, the fundamental natural frequencies of four tanks become more dispersed as the wall incline angle increases. The natural frequencies of diverging tanks are more sensitive to the incline angle than those of converging tanks. Further the vessel is excited by sway, roll, surge and pitch motions at the resonance condition of each wedged tank. The linear sloshing behaviours in these tanks are studied. The observations suggest that using this design, even though the resonance occurs in one tank, the sloshing in remaining tanks could still be gentle. This is expected to minimise the sloshing effect on the vessel motion. Thus, the effectiveness of this new design is preliminarily verified.

Chapter 7 An improved semi-Lagrangian free-surface updating procedure

7.1 Introduction

In the subsequent two chapters, the nonlinear sloshing behaviour in wedged tanks will be investigated. As shown in Chapter 5, two key modules are required for the nonlinear sloshing simulation. One is the BEM solver for the boundary value problem (BVP) of the velocity potential, and the other is the free-surface updating procedure. For the sloshing problem in wall-sided tanks, a semi-Lagrangian (SL) procedure has been applied to update the free surface. Using the SL procedure, the mesh nodes on the free surface are only allowed to move freely in the vertical direction to represent the free-surface deformation. The position of each node and velocity potential on it are updated according to the SL type free-surface boundary conditions. However, the SL procedure is only available to deal with the free-surface motion near vertical walls (Fig.7.1(a)). For more general situations that consider the free-surface updating near inclined or curved walls, the SL procedure would fail (e.g. Fig.7.1(b)).

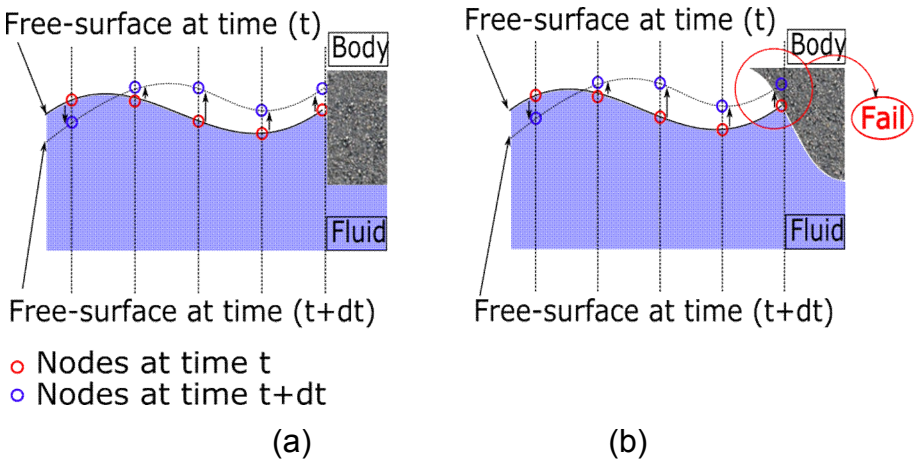

Fig. 7.1 Semi-Lagrangian free-surface updating procedure

One possible solution for the free-surface updating near non-vertical walls is the mixed-Euler-Lagrange (MEL) procedure. For the MEL procedure, the free-surface mesh nodes are regarded as Lagrangian particles on the free surface. At any instant, the fluid velocity and material derivative of the velocity

potential on each individual node can be found by solving the BVP in the Eulerian frame. Then, the free-surface position and velocity potential on the free surface can be updated to the next time step by following the particles. The foundation of this procedure was built by Longuet-Higgins and Cokelet (1976) for modelling 2D steep waves. Because of its flexibility, it was further extended to study 3D nonlinear surface waves and wave-body interactions, such as those in Dommermuth and Yue (1987), Wu and Eatock Taylor (1994), Ferrant (1997), Tanizawa (2000), Celebi (2000), Xue et al (2001), Koo (2003), Guyenne and Grilli (2006), Ma and Yan (2008), Bai and Eatock Taylor (2009) and Wang and Wu (2010). Over a long period, the MEL has been the most popular option for the simulation of nonlinear surface waves. However, although theoretically simple, the MEL does have some major drawbacks. Firstly, it is troublesome when tracing the intersection line between the body and free surface. Since by following the Lagrangian particles the predicted water line usually moves apart from the body (Fig.7.2(a)), people have to artificially drag it back to the exact body surface. Secondly, to avoid the mesh distortion, the interpolation and mesh regeneration process should be used frequently during the simulation as in Fig.7.2(b) (Wang and Wu 2010). Additionally, the ‘saw-tooth’ numerical instabilities are usually observed during the time marching of the free-surface conditions (Longuet-Higgins and Cokelet 1976). This is due to the fact that the Lagrangian particles tend to concentrate in the region with high gradients which inevitably results in a violation of the Courant stability condition after a certain number of time steps (Dommermuth and Yue 1987). An artificial smoothing technique has to be used in order to mask the instabilities. Above all, all the artificial interventions involved in MEL can cause a loss of the fluid volume. For the sloshing problem which is sensitive to the fluid volume, the MEL procedure does not seem to be an ideal option for long time simulations.

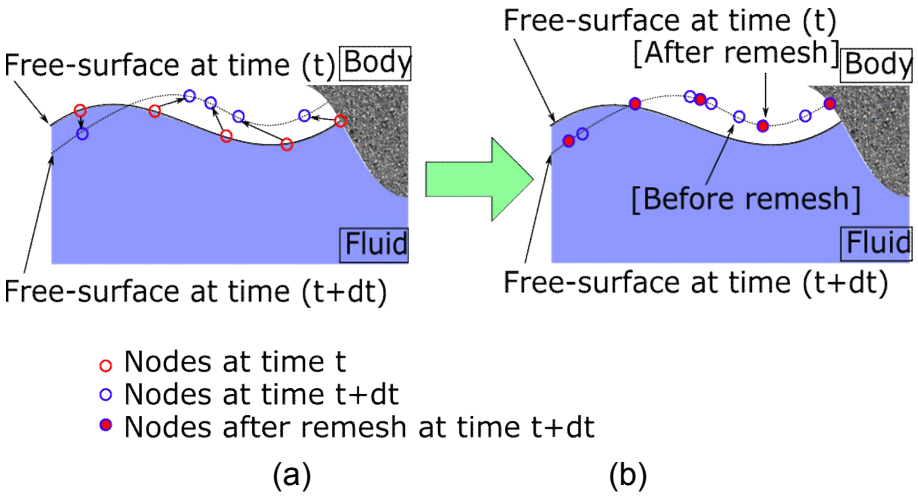

Fig. 7.2 Mixed Eulerian-Lagrangian free-surface updating procedure

Thus, this chapter will develop a new procedure to update the free surface near non-vertical walls, in order to complete the simulation methodology for nonlinear sloshing in non-wall-sided tanks. The procedure is named an 'improved semi-Lagrangian procedure' which has avoided the 'vertical-wall' limitation of the SL procedure. The essential idea is shown in Fig.7.3. A guide path through each free-surface mesh node is defined. The mesh nodes may slide along their paths to represent the free-surface deformation. The path of a waterline node is set to be a 'body-fitted path' clinging to the body surface, so that the mesh nodes on the waterline are always on the body surface. Over the rest of the free surface, the path changes gradually to be vertical as the node position becomes far away from the waterline. Corresponding free-surface boundary conditions are derived to predict the position of each node and velocity potential on it for the next time step. During the simulation, the mesh at a new instant could be formed as the mesh nodes move along the paths.

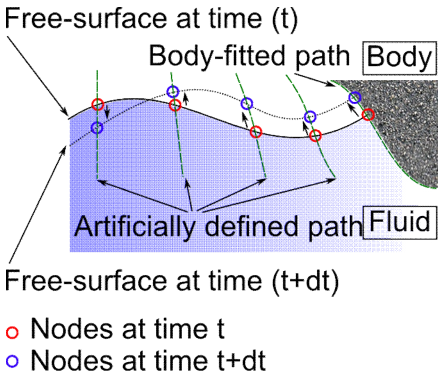

Fig. 7.3 Improved semi-Lagrangian free-surface updating procedure

It is obvious that this procedure is essentially the same as the SL procedure if all paths are set to be vertical. The improved SL procedure has not only inherited the advantages of the SL procedure that the mesh quality at any instant can be guaranteed and extra artificial interventions such as dragging mesh nodes and smoothing are not needed, but also avoided the 'vertical-wall' limitation. It should be noted that the paths can be dynamically adjusted at any instant during the simulation, although they only need to be defined once in some simple cases.

The organisation of this chapter is as follows. In Sections 7.2, the mathematical equations and numerical notes of the improved SL free-surface updating procedure are given. In Section 7.3, the improved SL procedure together with the BEM solver is applied to simulate the nonlinear sloshing problem in wedged tanks. The accuracy of this numerical scheme is verified through the result comparison with the open source CFD software OpenFOAM.

7.2 Improved semi-Lagrangian procedure

The sloshing problem is expressed in the body-fixed coordinate system $O-xyz$. The governing equation and body-surface boundary condition are the same as those in Chapter 5. However, free-surface boundary conditions should be reformulated according to the idea of the improved SL procedure.

Firstly consider the kinematic free-surface boundary condition which assumes that a fluid particle on the free surface S_F will always stay on the free surface. If the free-surface profile has an implicit definition $Z(x,y,z,t)=0$ in $O-xyz$, the material derivative of Z should always be zero

$$\left(\frac{dZ}{dt}\right)_o=\left(\frac{\partial Z}{\partial t}\right)_o+\nabla_o\varphi\cdot\nabla_o Z=\frac{\partial Z}{\partial t}-(\mathbf{v}_c+\boldsymbol{\omega}\times\mathbf{r})\cdot\nabla Z+\nabla\varphi\cdot\nabla Z=0 \tag{7.1}$$

As is mentioned in Section 7.1, the body-fitted paths are clinging to the body surface and other paths are given artificially. A local coordinate system $O'-x'y'z'$ is introduced for each path. As illustrated in Fig.7.4, the origin O' is set on the free surface and $O'z'$ is parallel to the tangent of the corresponding path. Note that at a different instant when the free surface has

changed, the $O'-x'y'z'$ could be different. In the local system, the free-surface profile can be expressed as

$$Z(x,y,z,t)=Z(x',y',z',t)=z'-\eta'(x',y',t) \tag{7.2}$$

Comparing with $O-xyz$, the $O'-x'y'z'$ only changes the perspective of viewing the free surface. So, the temporal derivation $\partial/\partial t$ and vector dot product are the invariant from $O-xyz$ to $O'-x'y'z'$. The spatial derivative becomes

$$\nabla Z(x',y',z',t)=-\left(\frac{\partial\eta'}{\partial x'}\mathbf{i}'+\frac{\partial\eta'}{\partial y'}\mathbf{j}'-\mathbf{k}'\right) \tag{7.3}$$

where $\mathbf{i}'$, $\mathbf{j}'$ and $\mathbf{k}'$ are the unit vectors of three axes. Substituting Eqs. (7.2) and (7.3) into Eq. (7.1) yields the kinematic free-surface boundary condition

$$\frac{\partial\eta'}{\partial t}=\left(\mathbf{v}_c+\boldsymbol{\omega}\times\mathbf{r}-\nabla\varphi\right)\cdot\left(\frac{\partial\eta'}{\partial x'}\mathbf{i}'+\frac{\partial\eta'}{\partial y'}\mathbf{j}'-\mathbf{k}'\right) \tag{7.4}$$

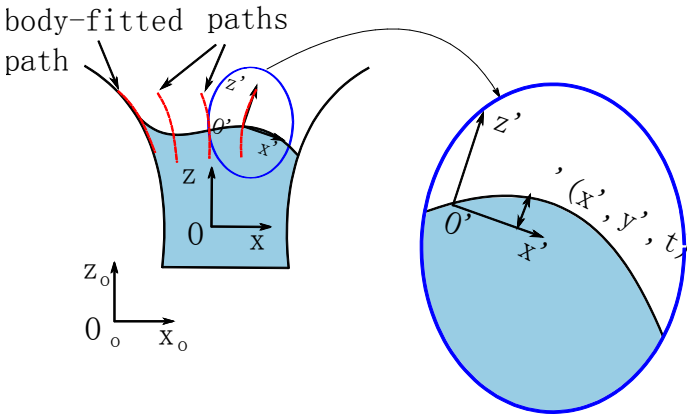

Fig. 7.4 Local coordinate system on free surface

The dynamic free-surface boundary condition can be obtained by letting the pressure on the free surface equal to the constant atmospheric pressure $p_o=0$. In $O-xyz$, it has the form

$$\frac{\partial\varphi}{\partial t}-\left(\mathbf{v}_c+\boldsymbol{\Omega}\times\mathbf{r}\right)\cdot\nabla\varphi+\frac{1}{2}\nabla\varphi\cdot\nabla\varphi+gz_o=0 \tag{7.5}$$

The notation $\delta/\delta t=\partial/\partial t+\left(\partial\eta'/\partial t\right)\partial/\partial z'$ is introduced into Eq. (7.5) and rewrite the dynamic free-surface condition in the following form

$$\frac{\delta\varphi}{\delta t}=\frac{\partial\eta'}{\partial t}\frac{\partial\varphi}{\partial z'}+\left(\mathbf{v}_c+\boldsymbol{\Omega}\times\mathbf{r}\right)\cdot\nabla\varphi-\frac{1}{2}\nabla\varphi\cdot\nabla\varphi-gz_o \tag{7.6}$$

where $\delta/\delta t$ denotes the time variation of a variable detected by the node moving along the $O'z'$ axis. Both kinematic and dynamic free-surface boundary conditions are satisfied on the instantaneous free surface. The kinematic condition is used to predict the free-surface position for the next instance while the dynamic one is for updating the velocity potential.

The tangential derivatives of η' could be obtained using the techniques in Section 4.2.2. In $O'-x'y'z'$, the η' at a free-surface node $\mathbf{x}_0$ can be approximated as

$$\eta^h\left(\mathbf{x},\mathbf{x}_0\right)=\sum_{j=1}^{m}p_j\left(\mathbf{x}\right)a_j\left(\mathbf{x}_0\right) \tag{7.7}$$

where $\eta^h\left(\mathbf{x},\mathbf{x}_0\right)$ is the fitting function, $p_j\left(\mathbf{x}\right)$ are the base functions and $a_j\left(\mathbf{x}_0\right)$ are the coefficients. The $p_j\left(\mathbf{x}\right)$ can be chosen as polynomial functions. This gives the linear set $\left\{p_1,p_2,p_3\right\}=\left\{1,x',y'\right\}$ with $m=3$ and the quadratic set $\left\{p_1,p_2,\cdots,p_6\right\}=\left\{1,x',y',x'^2,x'y',y'^2\right\}$ with $m=6$. To obtain the coefficients $a_j\left(\mathbf{x}_0\right)$, the weighted least-square method is used among $\mathbf{x}_0$ and its neighbour nodes. After that, the derivatives $\partial\eta'/\partial x'$ and $\partial\eta'/\partial y'$ can be obtained from a direct differentiation of Eq. (7.7). The derivatives could be transferred to $O_o-x_oy_oz_o$ or $O-xyz$ as needed.

7.3 Numerical verification

The effectiveness of the numerical scheme with this improved SL procedure is to be verified in wedged tanks. The wedged tank has been described in Chapter 6. Its geometry is a variation of the rectangular one, as shown in Fig.7.5(a). The tank has the height H_t, width B and length L at half of its height. The θ is used to denote the incline angle of the side wall as in Fig.7.5(a). To be convenient, the wedged tank is called ‘diverging tank’ for $\theta>0$ and ‘converging tank’ for $\theta<0$. Initially, the liquid has the free-surface length L_l and depth H. Paths are chosen to be straight lines through the

free-surface mesh nodes as in Fig.7.5(b). The path is on the $O-xz$ plane and it has an incline angle $\theta'=(2r/L)\theta$ with the Oz axis.

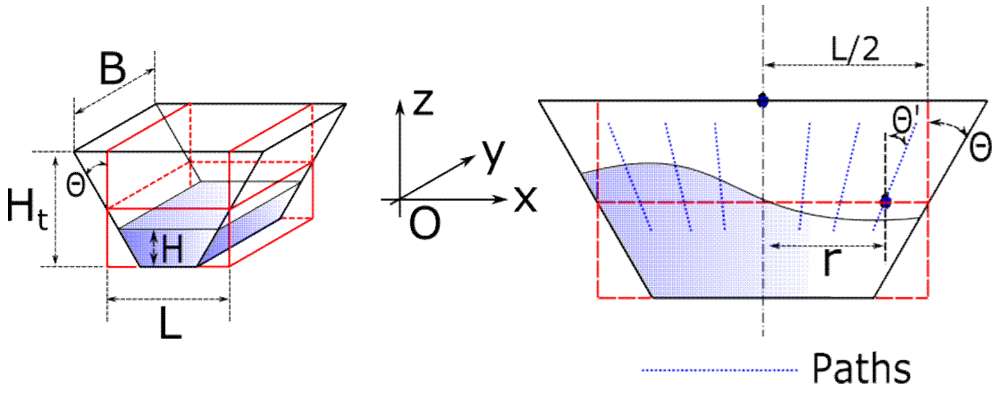

(a) (b)

Fig. 7.5 Sketch of the wedged tank with the height H_t, width B, length L at half of its height, liquid depth H, incline angle θ of the tank wall and incline angle θ' of the path

Since sloshing in wedged tanks has rarely been studied in the open literature, proper publications could not be found for comparison. So results from the present numerical scheme and the open source CFD software OpenFOAM are compared. The OpenFOAM solver InterDyMFoam, which is specially developed for sloshing problems, is selected. Compared with the present numerical method, the InterDyMFoam primarily has the following distinctions. (1) It deals with the viscous flows whose governing equations are the Navier-Stokes equations. (2) The numerical discretization of governing equations is based on the finite volume method (FVM). (3) The model of two-phase flows is used. (4) The free surface is represented implicitly by a colour function through the volume of fluid (VOF) algorithm. The VOF treats the interface between two phases as a transition region within which the density and viscosity vary smoothly.

Firstly, the accuracy of the OpenFoam results for the sloshing problem is tested for the rectangular tank (i.e. $\theta=0$). The experimental data in Liu and Lin (2008) are adopted for comparison. Dimensional parameters are set as $L_l=0.57m$, $H=0.15m$, $x_c=-A\sin(\omega t)$, $y_c=0$, $z_c=0$, $A=0.005m$ and $\omega=6.0578rad/s$. In the OpenFOAM set-up, the tank contains two fluid phases.

The lower phase is the water with density $\rho = 10^3 kg/m^3$ and kinematic viscosity $\nu = 10^{-6} m^2 s^{-1}$ while the upper phase is the gas with density $\rho_a = 1 kg/m^3$. The fluid domain is discretised into a structured mesh with 49848 cells, referring to the mesh convergence tests (Gui and Jiang 2014). The time step is adaptive in order to guarantee the Courant number $C_r = \bar{v}\Delta t/\Delta l \leq 0.5$, where $\bar{v}$ is the average linear velocity at a location, Δt is the maximum time step and Δl is the local dimension of the cell. Fig.7.6 gives the history of the free-surface elevation along the right wall of the rectangular tank. Note that, the η is used to denote the vertical displacement of the free surface motion in the tank. Results of the OpenFOAM are compared with those of the present method, published experiments and linear analytical solutions. It is found that both numerical methods could provide reliable results that match the experimental data. This also suggests that the liquid viscosity does not affect the free-surface elevations in this case. On the other hand, the analytical method could not approximate this sloshing problem well. Comparing with the analytical solution, the numerical results demonstrate evident nonlinear effects such as sharper crests and flatter troughs. In Fig.7.7, the snapshots of sloshing waves at three instants from $t = 5.70s$ to $5.91s$ are further demonstrated. Sub-figures (a-1) to (a-3) denote the geometry of the fluid domain at three instants, as results from the present numerical method. Sub-figures (b-1) to (b-3) are those generated by OpenFOAM. Sub-figures (a-i) and (b-i) correspond to the same instant, and they are put in pairs for a qualitative result comparison. From Fig.7.7, it can be seen that, at each instant, two corresponding wave profiles fit well with each other. With respect to above comparisons, it is reasonable to further verify the accuracy of the present numerical scheme in wedged tanks using OpenFOAM.

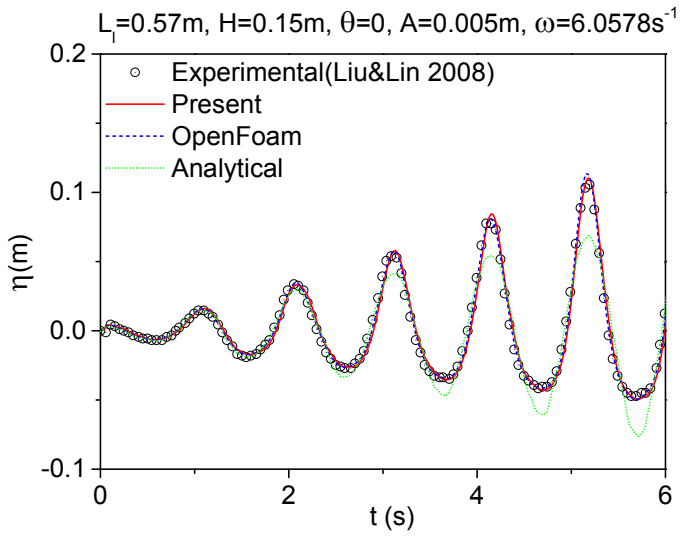

Fig. 7.6 Wave elevation history along right tank wall for $L_l = 0.57m$, $H = 0.15m$, $\theta = 0$, $A = 0.005m$ and $\omega = 6.0578 rad/s$

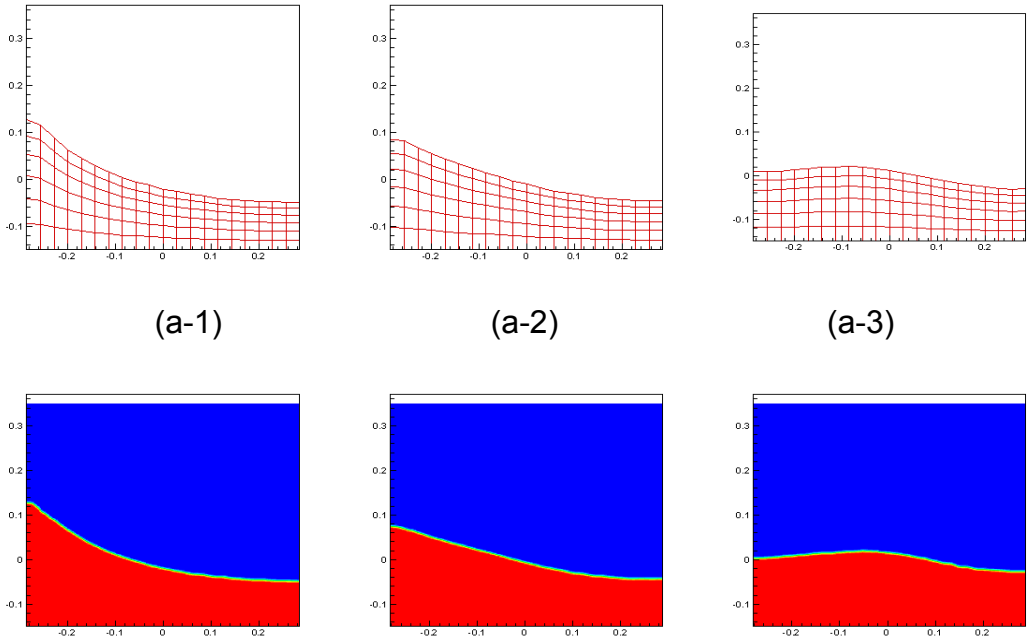

(a-1) (a-2) (a-3)

(b-1) (b-2) (b-3)

Fig. 7.7 Snapshots of sloshing waves at $t = 5.70s$, 5.80s and 5.91s for $L_l = 0.57m$, $H = 0.15m$, $\theta = 0$, $A = 0.005m$ and $\omega = 6.0578 rad/s$

Subsequently, the sloshing in a tank with $\theta = \pi/6$ is simulated. Parameters of the excitation, initial free-surface length and liquid depth are the same as those in the previous case. The free-surface elevation histories along the left and right tank walls are shown in Fig.7.8. It is found that the

OpenFOAM results exhibit a small disturbance in the beginning of the simulation, which is different from the present smooth result curve. This is because the interface capturing algorithm VOF of OpenFOAM treats the free surface implicitly as a transition region, unlike the explicit free-surface definition in the present method. Thus, the capture of small free-surface motions might lack accuracy especially when the free surface has a small intersection angle with the tank wall. However, as the free-surface amplitude grows larger, the perturbations in the OpenFOAM result gradually vanish, and results from two numerical methods come to an excellent agreement. Snapshots of the fluid domain at six instants between $t = 5.83s$ and $6.33s$ can be seen in Fig.7.9. It is observed that sub-figure (a-i) from the present numerical method fits well with sub-figure (b-i) from the OpenFOAM at the corresponding instant.

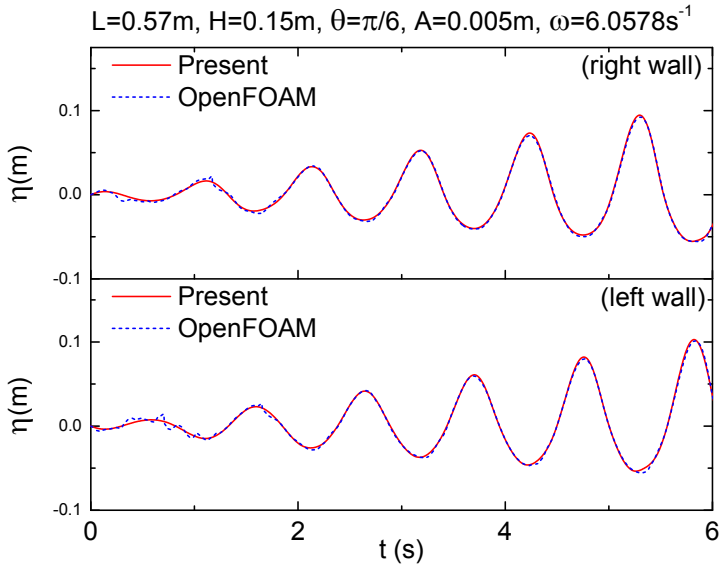

Fig. 7.8 Wave elevation history along tank walls for $L_l = 0.57m$, $H = 0.15m$, $\theta = \pi/6$, $A = 0.005m$ and $\omega = 6.0578\,rad/s$

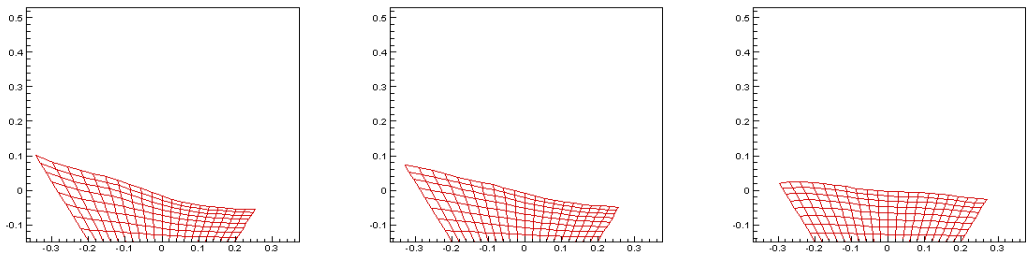

(a-1) (a-2) (a-3)

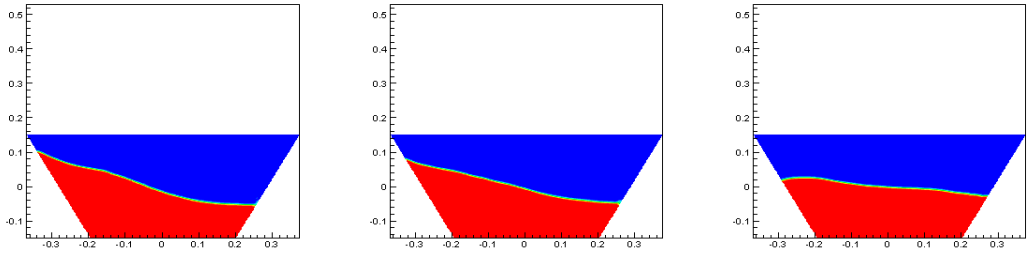

(b-1) (b-2) (b-3)

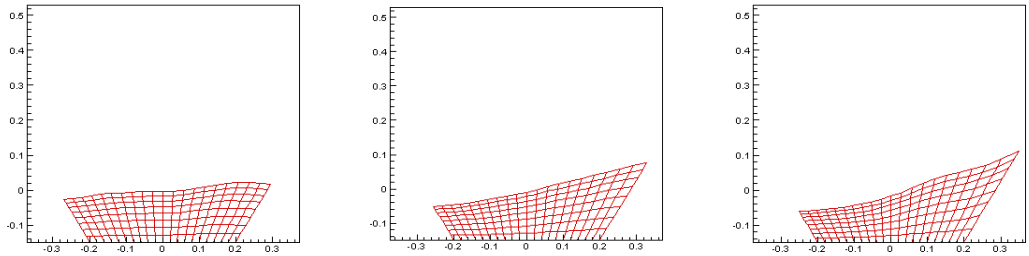

(a-4) (a-5) (a-6)

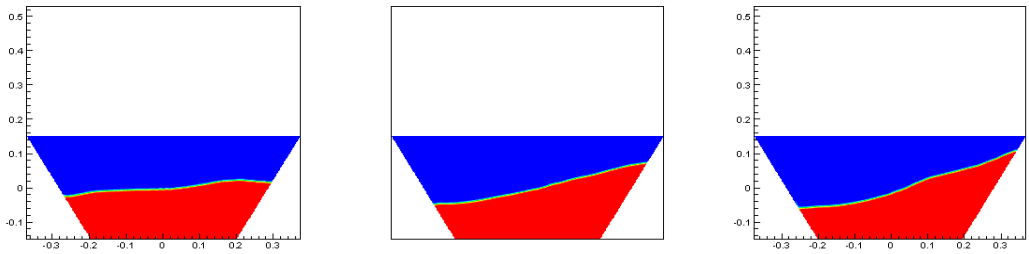

(b-4) (b-5) (b-6)

Fig. 7.9 Snapshots of sloshing waves at $t = 5.83$s, 5.93s, 6.03s, 6.13s, 6.23s and 6.33s for $L_l = 0.57m$, $H = 0.15m$, $\theta = \pi/6$, $A = 0.005m$ and $\omega = 6.0578\,rad/s$

Further, the incline angle of the tank wall is changed to $\theta = \pi/4$. The free-surface elevation histories along the left and right tank walls are shown in Fig.7.10. Like the previous case, the OpenFOAM results have perturbations within the first two periods. After that, the disturbances vanish as the wave amplitude grows, and the OpenFOAM results have a good agreement with the present numerical results. In Fig.7.11, the snapshots of the fluid domain at six instants between $t = 7.63s$ and $8.08s$ are given. At each instant, the wave profile given by the present numerical scheme (sub-figure (a-i)) is visually identical to that given by OpenFOAM (sub-figure(b-i)).

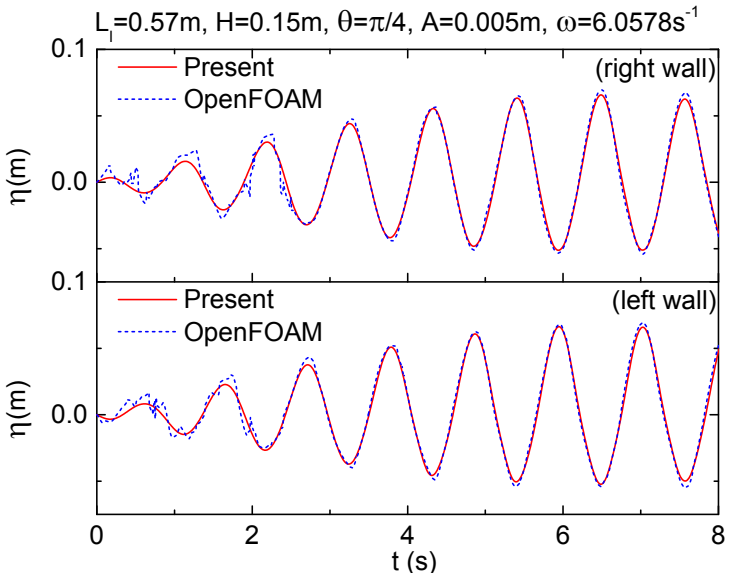

Fig. 7.10 Wave elevation history along tank walls for $L_l = 0.57m$, $H = 0.15m$, $\theta = \pi/4$, $A = 0.005m$ and $\omega = 6.0578\,rad/s$

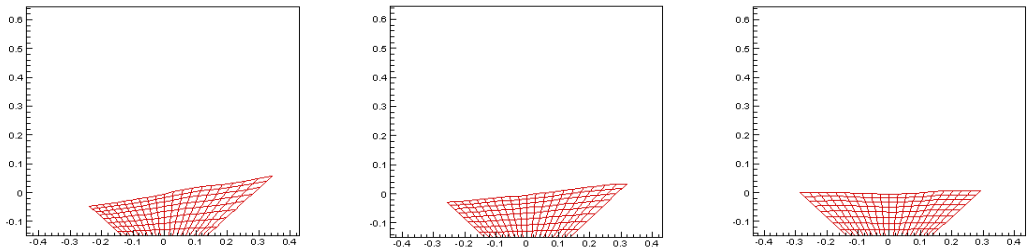

(a-1) (a-2) (a-3)

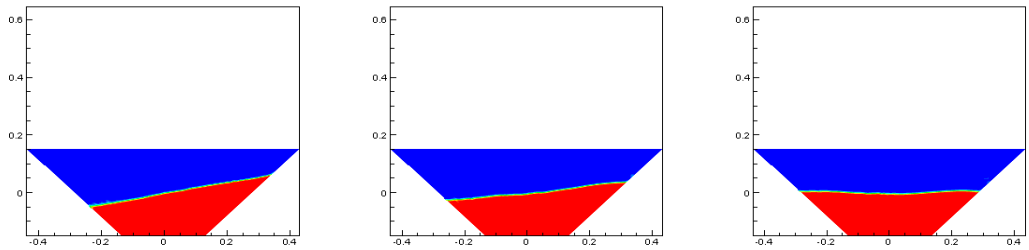

(b-1) (b-2) (b-3)

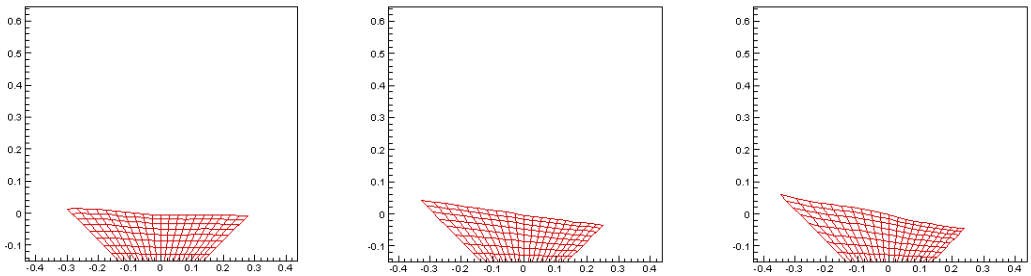

(a-4) (a-5) (a-6)

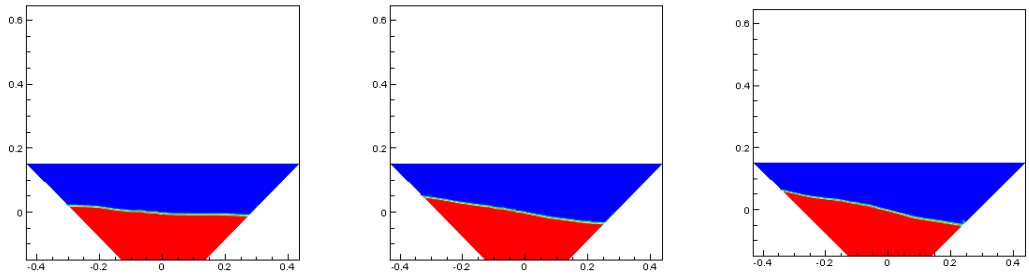

(b-4) (b-5) (b-6)

Fig. 7.11 Snapshots of sloshing waves at $t = 7.63$s, 7.73s, 7.83s, 7.88s, 7.98s and 8.08s for $L_l = 0.57m$, $H = 0.15m$, $\theta = \pi/4$, $A = 0.005m$ and $\omega = 6.0578\,rad/s$

Having performed the above comparisons, it is fair to say that the improved SL procedure together with the BEM solver could provide reliable and accurate results. Then, more case studies for the sloshing in wedged tanks could be carried out.

7.4 Conclusions

In this chapter, an improved semi-Lagrangian procedure is developed for the free-surface updating, which avoids the 'vertical-wall' limitation of the conventional semi-Lagrangian procedure. The improved semi-Lagrangian procedure together with the BEM solver is applied to simulate the nonlinear sloshing in wedged tanks, whose reliability and accuracy have been verified through the comparison with the OpenFOAM CFD software. From the comparison, it is found that the viscous influence on the results is not important. This is reasonable, considering the fact that the low-viscous water is chosen as the sloshing liquid. In terms of the computational time, the OpenFOAM does not take much longer time than the present method for 2D cases. However, for 3D simulations, the OpenFOAM requires much larger computing resources and much longer CPU time (often beyond the capability of a PC). In the next chapter, the technique developed in this chapter will be used to study the resonant sloshing in wedged tanks.

Chapter 8 Simulation of resonant sloshing in wedged tanks

8.1 Introduction

Aiming at the sloshing in wedged tanks, Chapter 6 has given the resonance conditions and Chapter 7 has provided the simulation methodology. Further in this chapter, the wedged tank is further excited at resonance conditions and the resonant sloshing behavior is investigated numerically.

At present, the sloshing behaviour in non-wall-sided tanks has been studied in literature. For example, Mitra et al (2008) concerned the linear sloshing in 2D trapezoidal and horizontal circular cylindrical tanks using FEM. Hasheminejad and Mostafa-Aghabeigi (2011) developed a semi-analytical linear model for the half-full elliptical tank excited laterally. Ramaswamy (1990) studied the oscillation of viscous liquids in non-wall-sided tanks with varying depth, based on an arbitrary-Lagrangian-Eulerian (ALE) method. Behr and Abraham (2002) simulated the viscous liquid sloshing in a 2D trapezoidal tank based on FEM. Gavrilyuk et al (2005) and Gavrilyuk et al (2013) derived weakly nonlinear modal equations to describe the liquid sloshing in the truncated conical tank. Dai and Xu (2006) developed a potential-flow FDM to simulate the sloshing in 3D horizontal cylindrical tanks. Modaressi-Tehrani et al (2007) modelled the transient liquid motion in a horizontal cylindrical tank with baffles using the FLUENT software. Zhou et al (2008) extended the techniques developed by Behr and Abraham (2002) for free-surface motions in 2D circular tanks. Marsh et al (2011) studied the sloshing effects in TLDs with different geometries using the particle method. From the above review, it is found that the 3D wedged tank is not widely considered.

In this chapter, two types of resonance in 3D wedged tanks will be considered. The first type is the classical resonance, which occurs due to a lateral tank oscillation at certain resonance frequencies. The second type is the Faraday waves, which is observed in the unstable status during the tank heave motion.

The tank model has been shown in Fig.7.5. In this chapter, all results are nondimensionalised The g and H_t are chosen as bases of the nondimensionalisation, so that the dimensionless parameters can be obtained according to $(x,y,z,L,B,H,\eta)\to(x,y,z,L,B,H,\eta)H_t$, $t\to\tau\sqrt{H_t/g}$, $\omega\to\omega\sqrt{g/H_t}$ and $\varphi\to\varphi H_t\sqrt{gH_t}$. In this chapter, the tank with $L=B=1$ and $H=0.5$ is mainly considered. The incline angle may vary from $\theta=-5\pi/24$ to $\theta=5\pi/24$. Mesh models in Fig. 6.7 are adopted for the BEM simulation.

8.2 Resonance due to surge excitation

Consider the tank undergoing the motion of $x_c(\tau)=A_x\sin(\omega_x\tau)$, $y_c(\tau)=0$ and $z_c(\tau)=0$. When the oscillation frequency ω_x is set as the natural sloshing frequency ω_{10} in the length direction of the tank, the resonant sloshing might occur. The value of ω_{10} calculated in Chapter 6 is adopted. Patterns of the natural mode corresponding to ω_{10} for diverging, rectangular and converging tanks are given in Fig. 8.1 for illustration. From a physical point of view, they could be considered as wave patterns during the resonance. The contour variation denotes the distribution of the free-surface amplitude.

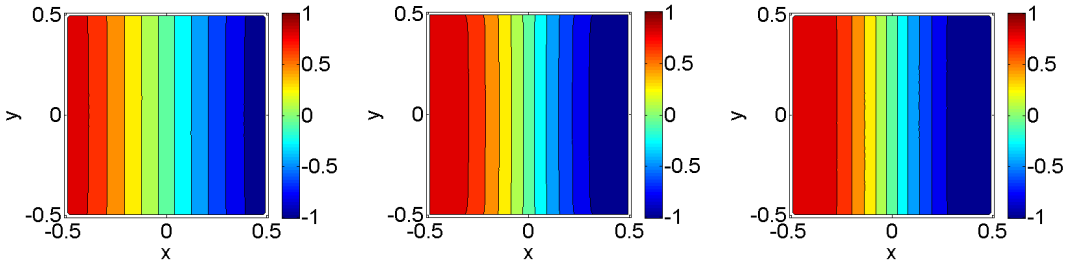

(a) (b) (c)

Fig. 8.1 Mode patterns corresponding to ω_{10}, for (a) $\theta=5\pi/24$; (b) $\theta=0$; (c) $\theta=-5\pi/24$

The excitation amplitude is firstly set as $A_x=0.001$. The earlier periods of the wave elevation histories along the right tank wall are shown in Fig. 8.2(a).

It is clear that, in all tanks, the wave amplitude grows with time, which confirms the occurrence of the resonance. Linear solutions from Chapter 6 are also shown for comparison. It is observed that, within the first ten periods, there is a good agreement between the linear and nonlinear solutions. However, after that, as the wave amplitude increases with time, the phase shift between two curves grows. For diverging tanks as well as the rectangular tank, the nonlinear result tends to have a phase delay compared with the linear solution. As the incline angle decreases to negative, the phase delay is getting smaller. When it comes to $\theta = -5\pi/24$, the nonlinear result even has a phase advance of the linear solution. Fig. 8.2(b) are spectral analyses of nonlinear solutions in Fig. 8.2(a). It is evident that only one frequency dominates each resonant sloshing. Also, the value of ω_{10} decreases as the incline angle varies from negative to positive.

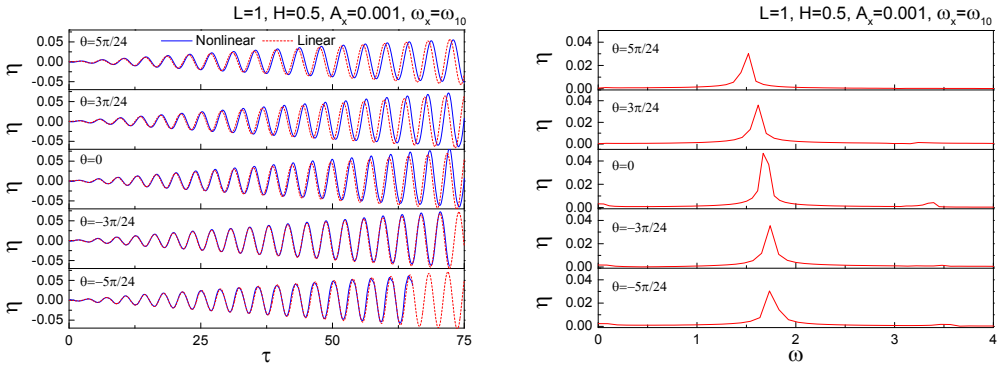

(a) (b)

Fig. 8.2 (a) Time history and (b) corresponding spectrum of wave elevations, for $A_x = 0.001$ and $\omega_x = \omega_{10}$:

The case of $\theta = 0$ and $\theta = 5\pi/24$ is further simulated for a much longer time. The obtained wave elevation histories are shown in Fig. 8.3. It is observed that neither of the nonlinear wave histories grows to infinity as linear solutions do. From the beginning to around $\tau = 100$, the wave amplitudes in both tanks keep increasing almost linearly. Then, the increasing slows down and the amplitude reaches a peak at approximately $\tau = 150$. After that, the wave amplitude starts to drop rapidly. This is due to the nonlinear effects during the sloshing. For the rectangular tank, at a large wave amplitude, the actual natural sloshing frequency has changed due to the free-surface

nonlinearity. As the natural sloshing frequency grows to be distinct from the excitation frequency, the condition that maintains the resonance has changed. Thus, the wave amplitude stops growing and the sloshing becomes less violent. For the wedged tank, the geometric nonlinearity caused by inclined tank walls further accelerates the variation of the natural sloshing frequency. The maximum wave peak in the diverging tank is much lower than that in the rectangular one. The diverging tanks have shown the possibility to reduce wave amplitudes. From Fig. 8.3(b), it can be seen that, as the wave amplitude decreases to a small value, a rapid increase of the wave amplitude has re-started from about $\tau = 300$. The envelope of the wave amplitude becomes evident. One may wonder whether this envelope is due to an inaccurate prediction of ω_{10}. Because, if the tank is excited at a frequency not exactly at but close to ω_{10}, the liquid oscillations would be dominated by two frequencies, leading to the beating behaviour. However, for the envelope produced by the beating of the difference of two frequencies, the amplitude increasing and decreasing stages of the wave elevation history are symmetric. But clearly in Fig. 8.3(b), the envelopes are asymmetric about the peak of the wave amplitude. Thus, the envelope in this case is not caused by an inaccurate prediction of ω_{10}, but by nonlinearities.

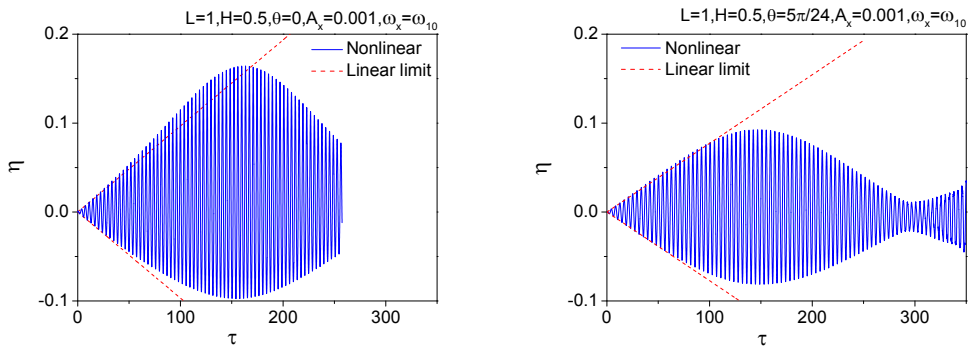

(a) (b)

Fig. 8.3 Time history of wave elevations, for $A_x = 0.001$, $\omega_x = \omega_{10}$, and: (a) $\theta = 0$; (b) $\theta = 5\pi/24$

Then, the excitation amplitude is amplified by ten times, i.e. $A_x = 0.01$. For the tank of $\theta = 5\pi/24$, the wave run-ups along the tank wall within the

amplitude increasing stage are shown in Fig. 8.4(a). It can be seen that, when the tank is excited at the larger amplitude, nonlinear effects have played a more evident role. The corresponding phase plane, which is used for analysing vibration systems, is plotted in Fig. 8.4(b). The coordinates of the plane are defined by the wave elevation and its time derivative. As time progresses, a trajectory could be drawn, whose direction is indicated by the arrow. From Fig. 8.4(b), it can be seen that both trajectories of this resonance situation are outgoing spirals. Compared with the stable vibration system whose trajectory is a closed curve, the spiral trajectory here suggests that the sloshing behaviour is unstable at this stage. Specifically for the small amplitude case, the trajectory has a regular spiral pattern. This means that the free-surface oscillation has a nearly periodic property except for the increasing amplitude. However, for the large amplitude case, the spiral trajectory gradually deforms as time progresses. The averaged trajectory centre moves to the right, which suggests that the averaged free-surface elevation along the tank wall is above the stationary liquid surface. In Fig. 8.4(c), the spectral analysis is further performed on the nonlinear wave elevation histories. For the small amplitude case, the dominant sloshing frequency is coincident with ω_{10}. For the large amplitude case, the spectrum has a more broad bound due to the limited number of wave periods. But it is still clear that the dominant sloshing frequency shifts away and becomes slightly lower than ω_{10}. This is consistent with the observation in Fig. 8.4(a). The wave profiles (from $\tau = 33.85$ to 35.92) are shown in Fig. 8.5. From the wave profiles, it is noticed that, when the wave runs up along the inclined tank wall to its highest, a bump normally protrudes on the free surface away from the tank wall. The streamlines describing the flow directions are plotted to show the formation of the surface bump.

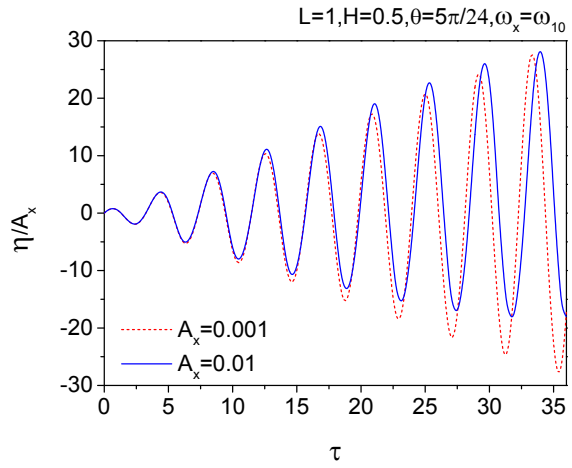

(a)

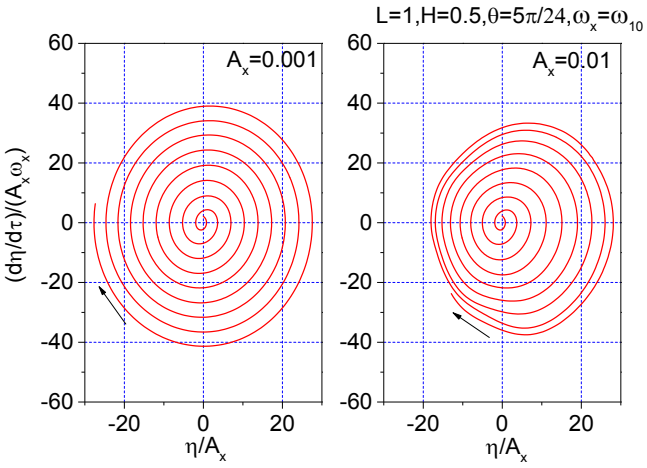

(b)

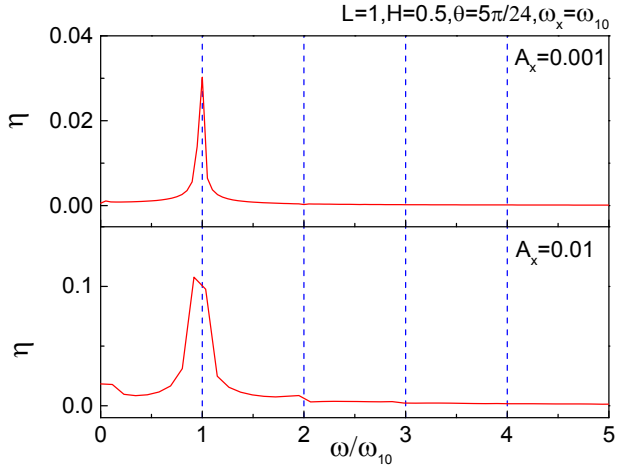

(c)

Fig. 8.4 (a) Time history, (b) corresponding phase plane and (c) spectrum of wave elevations, for $\omega_x = \omega_{10}$ and $\theta = 5\pi/24$

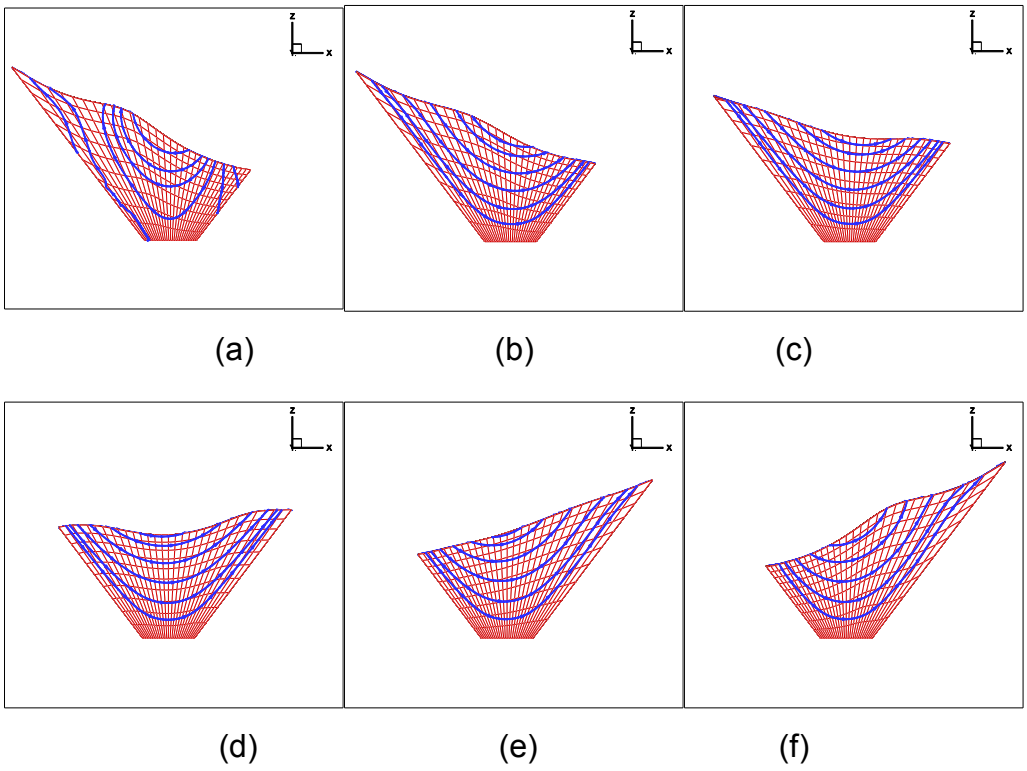

Fig. 8.5 Snapshots of sloshing waves in wedged tank, for $A_x = 0.01$, $\omega_x = \omega_{10}$ and $\theta = 5\pi/24$, from $\tau =$ (a) 33.85; (b) 34.27; (c) 34.68; (d) 35.09; (e) 35.51; (f) 35.92

For the tank of $\theta = -5\pi/24$, wave elevation histories along the tank wall and at the tank centre are shown in Fig. 8.6. It can be seen that waves due to a large excitation have sharper peaks along the tank wall and more evident oscillations at the tank centre. However, it should be noted that the simulation for the large-amplitude case here could only stably run for around four excitation periods. This can be explained from the wave profiles. Fig. 8.7 gives the time variation of the water line along the vertical tank wall. Fig. 8.8 shows the wave profile on the vertical tank wall at $\tau =$ 8.96, 9.32, 9.68, 10.04, 10.38 and 10.74. Profiles in Fig.8.8 are the sections of Fig.8.7 along the time axis. It is observed that, as the wave amplitude increases, the maximum wave height no longer emerges along the tank wall. Instead, the highest wave peaks could be found on a free-surface region near the inclined walls. This process is also clear from the flow streamlines in Fig. 8.8. This is different from the resonant sloshing in diverging and rectangular tanks whose largest

wave height occurs along the tank wall. Also, it is noticed that the wave slope at the inner side of a sharp wave peak is steeper than the side near the tank wall. As the wave amplitude continues growing, the wave peak has an evident trend to overturn, which could lead to a break down the present numerical scheme. This is likely to be the reason why the present simulation becomes unstable after that. However, the fact that the converging tank promotes the overturning of sloshing waves might not be a bad news for a practical FLNG vessel. Because the energy dissipation of sloshing waves is mainly from three sources: the wave breaking, viscous damp along the tank wall and wave impact on either the ceiling or walls of a tank. Unlike the wave impact that might lead to structural damages and the viscous damping that requires a sufficiently long time, the wave breaking seems to be a better option to dissipate the sloshing energy.

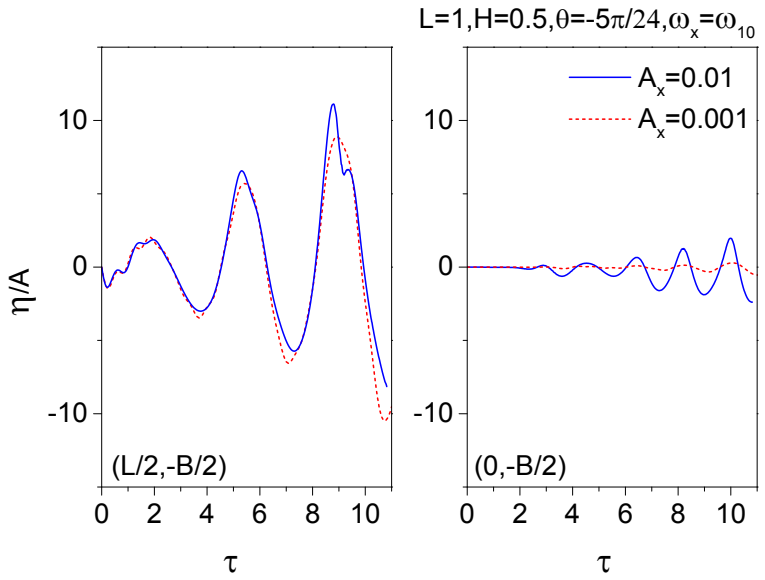

Fig. 8.6 Wave elevation along the tank wall (left subfigure) and at the tank centre (right subfigure), for $L=1$, $H=0.5$, $\theta=-5\pi/24$ and $\omega_x=\omega_{10}$

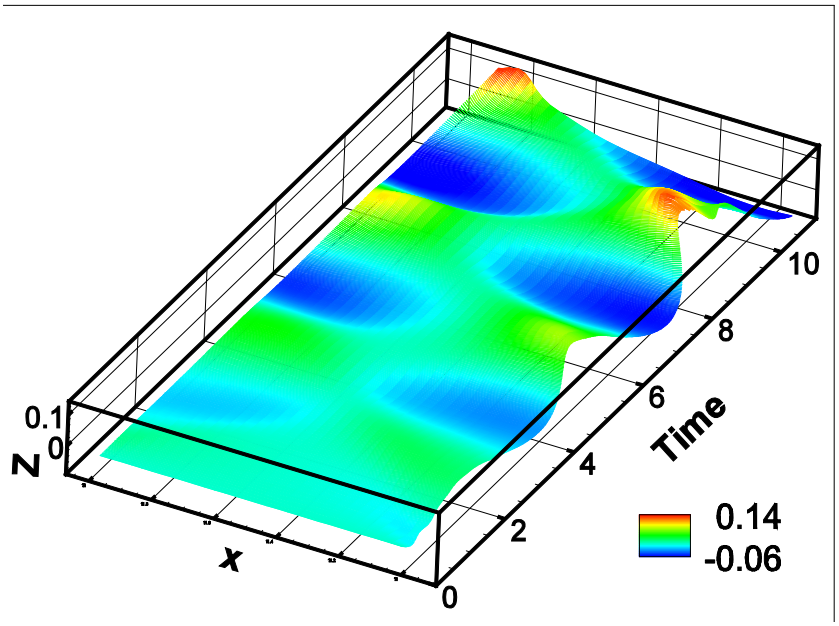

Fig. 8.7 History of wave profiles along vertical wall at $y=-B/2$ for $A_x=0.01$, $\omega_x=\omega_{10}$ and $\theta=-5\pi/24$

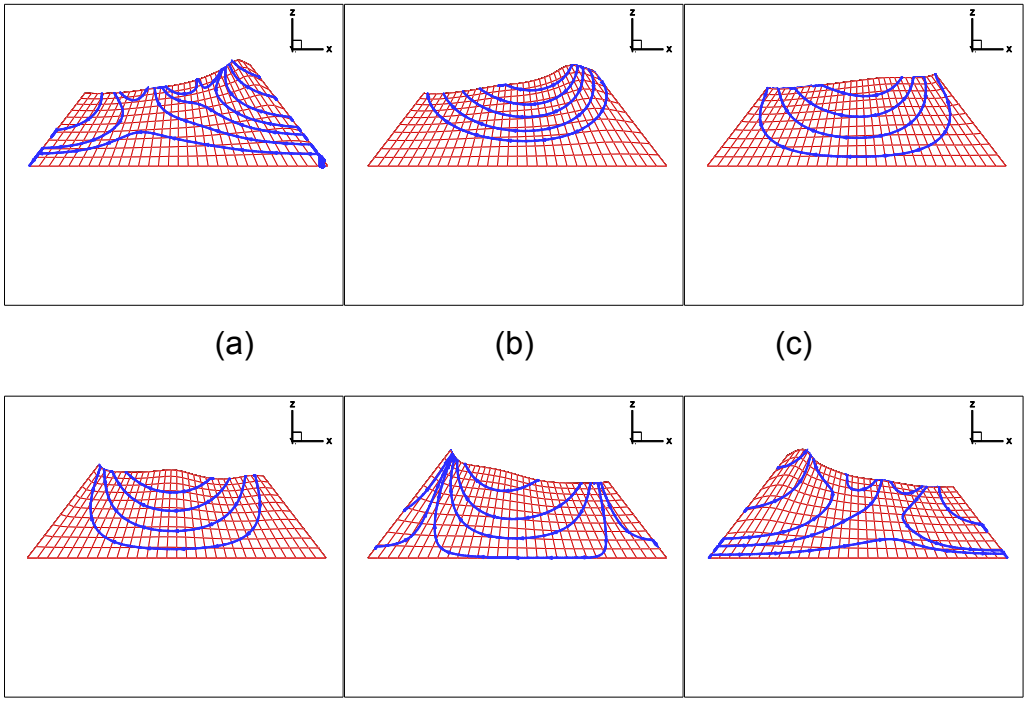

(a) (b) (c)

(d) (e) (f)

Fig. 8.8 Snapshots of sloshing waves in wedged tank, for $A_x=0.01$, $\omega_x=\omega_{10}$ and $\theta=-5\pi/24$, at $\tau=$ (a) 8.96; (b) 9.32; (c) 9.68; (d) 10.04; (e) 10.38; (f) 10.74

The resonant sloshing in tanks with different fillings is further considered.

The diverging tank with $\theta = 5\pi/24$ is considered. Three filling levels 50%, 30% and 10% are considered. The tank is still excited at $\omega_x = \omega_{10}$ and $A_x = 0.01$. Note that the value of ω_{10} for the same tank with different fillings is different. Fig. 8.9 gives the wave elevation history along the inclined tank wall. The time axis has been normalised by the excitation period T_x. It is interesting to find that wave elevations during each period have similar amplitudes. However, for this large amplitude excitation, the wave amplitude grows rapidly at the resonance state. In this case, only after two excitation periods, the wave height in the low filling tank with $H = 10\%$ has become greater than the liquid depth. The large wave amplitude leads to a large distortion of the computational mesh on the free surface. So the calculation becomes unstable after about two excitation periods. In Fig. 8.10, wave profiles at the end of each excitation period are shown. It is found that the tank with a higher filling level tends to have a flatter free surface.

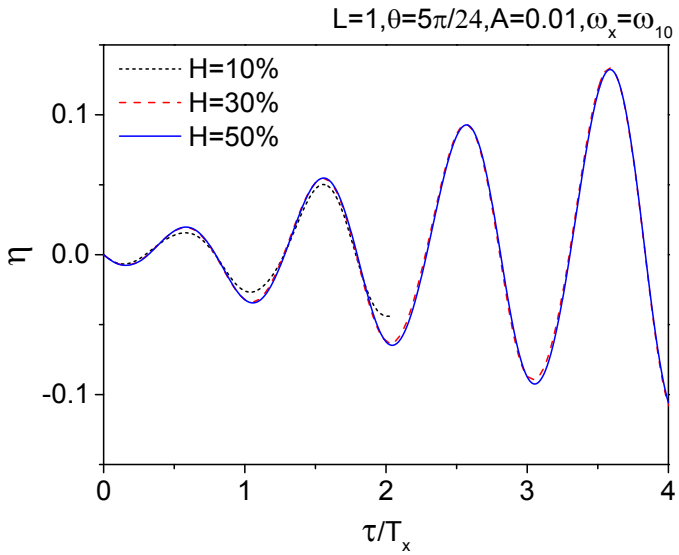

Fig. 8.9 Wave elevation along tank wall

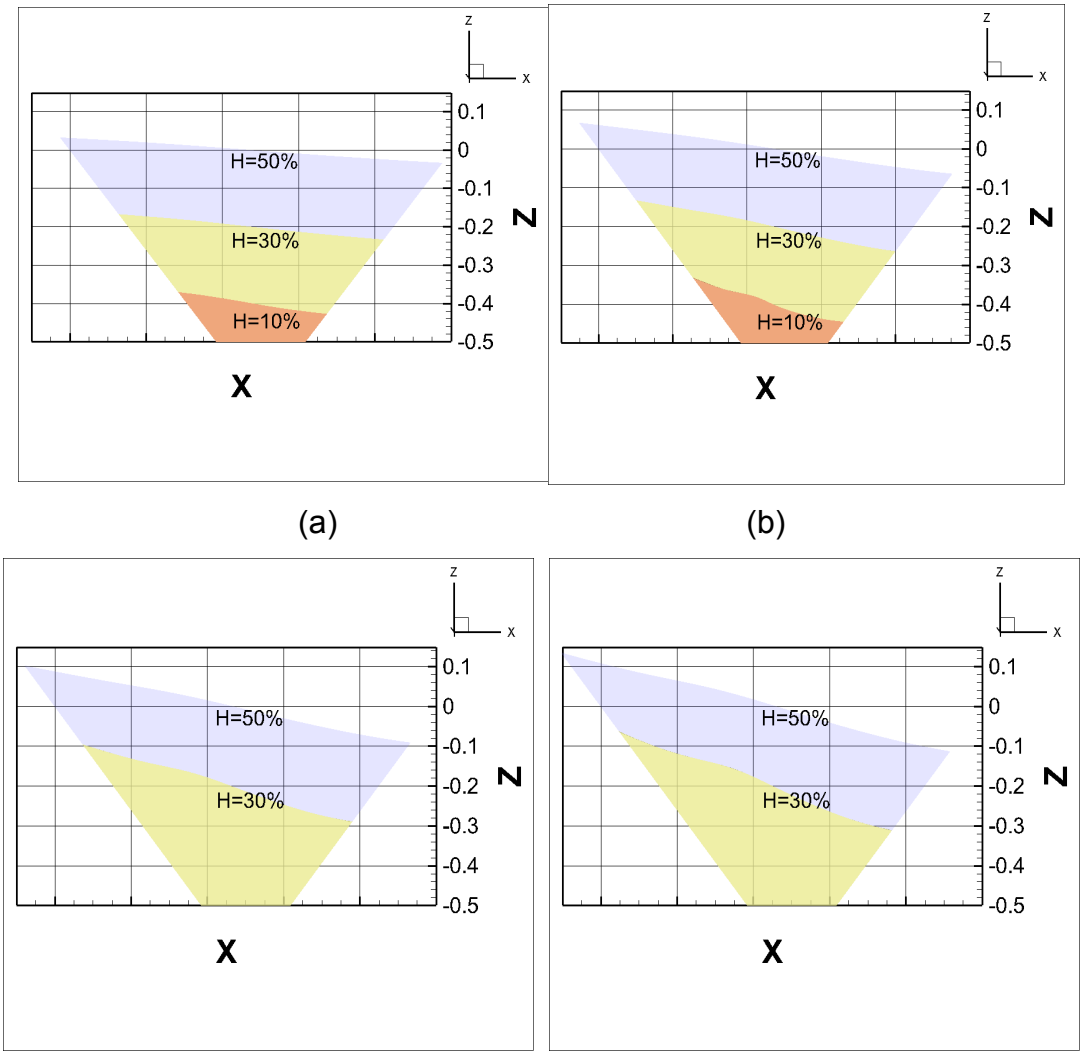

Fig. 8.10 Snapshots of sloshing waves in wedged tank at $\tau = T_x$, $2T_x$, $3T_x$ and $4T_x$

8.3 Resonance due to sway excitation

In this subsection, the resonant sloshing caused by the sway excitation is considered. The tank motion is defined as $x_c(\tau) = 0$, $y_c(\tau) = A_y \sin(\omega_y \tau)$ and $z_c(\tau) = 0$ with $A_y = 0.001$ and $\omega_y = \omega_{01}$. The ω_{01} is the fundamental natural sloshing frequency in the width direction of the tank. Theoretically, the resonant sloshing in the width direction of the tank would occur in this situation. The mode patterns corresponding to ω_{01} for diverging, rectangular and converging tanks are shown in Fig. 8.11.

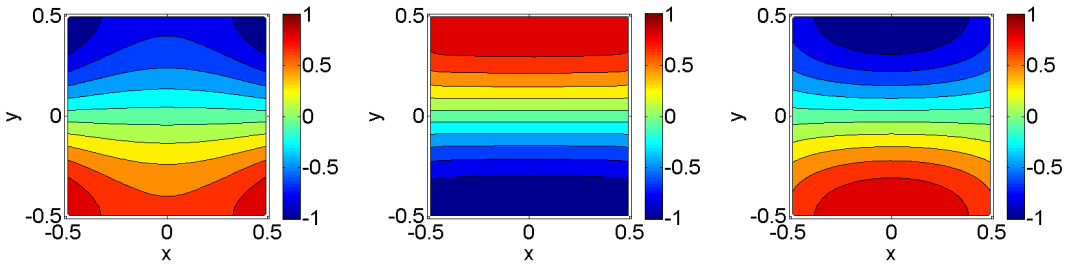

(a) (b) (c)

Fig. 8.11 Mode patterns corresponding to ω_{01}, for (a) $\theta = 5\pi/24$; (b) $\theta = 0$; (c) $\theta = -5\pi/24$

Wave elevations at three positions, the tank corner $(-L/2, -B/2)$, mid-point of the vertical wall $(0, -B/2)$ and tank centre $(0,0)$, are considered. For the diverging tank of $\theta = 5\pi/24$, the obtained elevation histories are shown in Fig. 8.12(a). It is clear that the wave amplitude at all these three positions has a nearly linear increasing trend within the first 20 periods. Then, the increasing slows down and the amplitude gradually reaches the peak at about $\tau = 200$. After that, the wave amplitude gradually decreases. During the periods under consideration, the wave height at $(0, -B/2)$ and $(0,0)$ is always smaller than that at the corner. The envelope of the wave elevation history for the rectangular tank (e.g. Fig. 8.3(a)) is also marked in Fig. 8.12(a). It can be seen that the maximum wave amplitude and the amplitude increasing rate in the diverging tank are much lower than those in the rectangular one. The corresponding spectra of wave elevations are given in Fig. 8.12(b). At $(-L/2, -B/2)$ and $(0, -B/2)$ of the tank end, the dominant wave frequency is ω_{01}, which is to be expected. Meanwhile, the additional frequency $2\omega_{01}$ due to the nonlinear mode to mode interaction could be observed. The geometric nonlinearity due to the wall slope of the wedged tank has promoted the mode to mode interactions. At tank centre $(0,0)$, the free-surface amplitude is not zero, and the wave oscillation is solely governed by the nonlinear effect. In Fig. 8.13, a series of free-surface profiles within one period is plotted. It can be seen that the form of the standing wave is still clear, although its pattern has evidently changed compared with the natural mode in

Fig. 8.11(a).

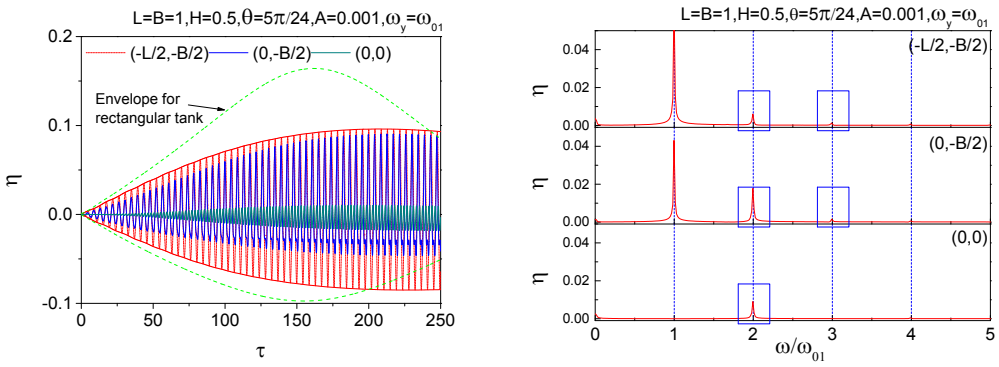

(a) (b)

Fig. 8.12 (a) Time history and (b) corresponding spectrum of wave elevations in diverging tank, for $A_x = 0.001$, $\omega_x = \omega_{01}$ and $\theta = 5\pi/24$

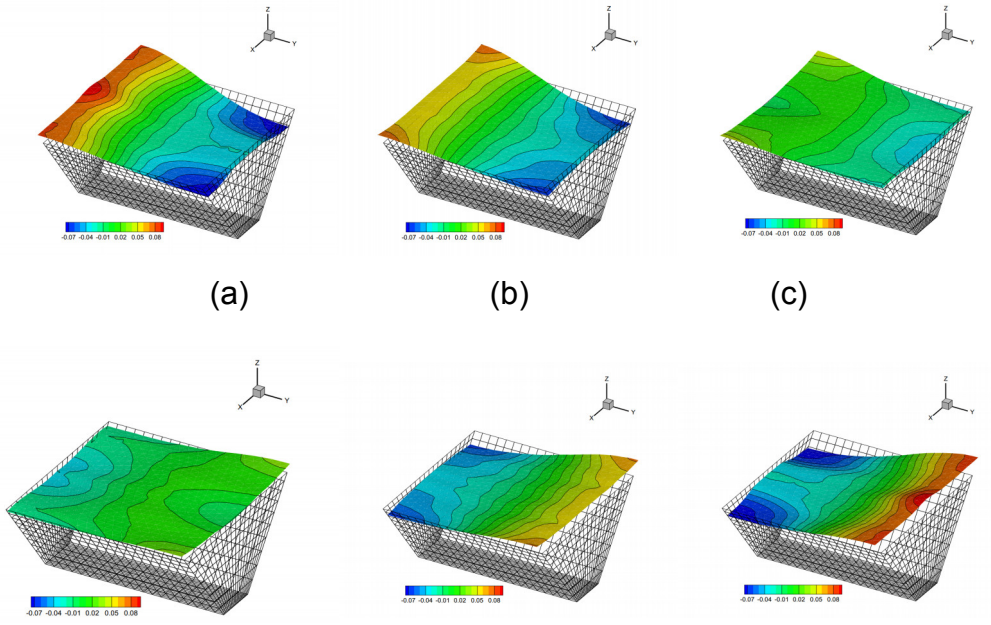

(a) (b) (c)

(d) (e) (f)

Fig. 8.13 Snapshots of 3D sloshing waves in wedged tank, for $A_x = 0.001$, $\omega_x = \omega_{01}$ and $\theta = 5\pi/24$, at $\tau =$ (a) 130.31; (b)130.75; (c)131.18; (d)131.61; (e)132.05; (f)132.48

Further, the converging tank with $\theta = -5\pi/24$ is considered. Fig. 8.14(a) shows the wave elevation histories at three test positions. It is found that the wave amplitude at corner $(-L/2, -B/2)$ is always lower than that at $(0, -B/2)$ over the same period. Also, the maximum wave amplitude in this

converging tank is much lower than that in the corresponding rectangular one. Fig. 8.14(b) gives the associated spectra. The frequency $2\omega_{01}$ which is induced by the nonlinearity is also evident. Especially at the tank centre $(0,0)$, the wave elevation is solely caused by the nonlinearity. The nonlinear wave components have changed the wave patterns compared with the natural modes. This could be observed from wave profiles within one sloshing period in Fig. 8.15.

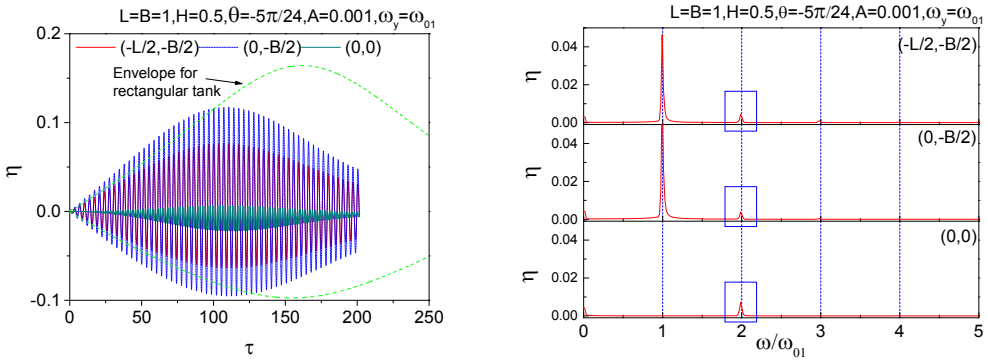

(a) (b)

Fig. 8.14 (a) Time history and (b) corresponding spectrum of wave elevations in converging tank, for $A_x = 0.001$, $\omega_x = \omega_{01}$ and $\theta = -5\pi/24$

Thus, due to the geometric nonlinearity caused by inclined tank walls, the actual natural sloshing frequency keeps changing as waves running up. So, the amplitude of the resonant waves may increase to a peak and then start to drop. During the resonance induced by surge excitation, the maximum wave amplitude in the diverging tank is generally smaller than that in the corresponding rectangular tank in the same condition. For converging tanks, the wave peak has an evident trend to overturn as the wave amplitude grows. In practice, the resulted wave breaking is expected to dissipate the energy and reduce the sloshing violence. During the resonance induced by sway excitation, for both diverging and converging tanks, the maximum wave amplitude is generally smaller than that in the corresponding rectangular tank in the same condition. In summary, the wedged tanks have shown the potential to reduce the sloshing violence during the resonance.'

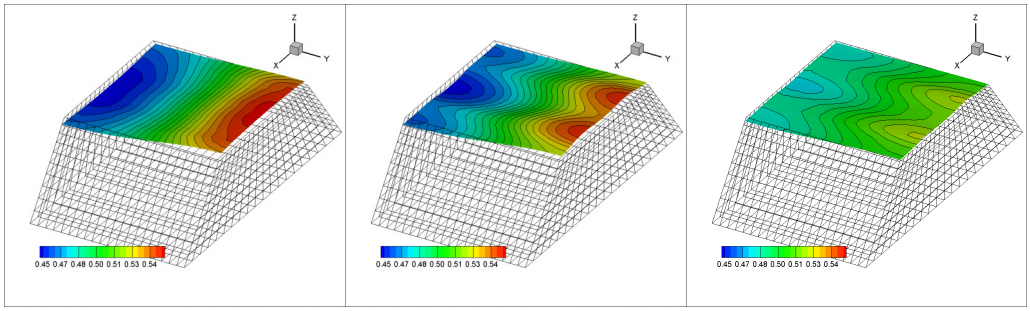

(a) (b) (c)

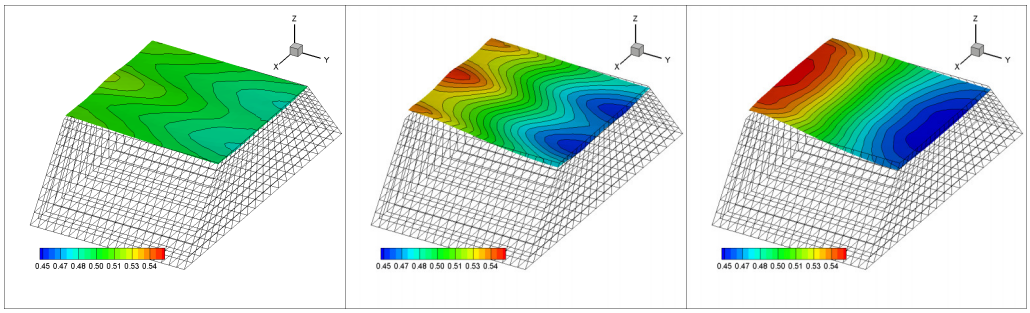

(d) (e) (f)

Fig. 8.15 Snapshots of 3D sloshing waves in converging tank, for $A_x = 0.001$, $\omega_x = \omega_{01}$ and $\theta = -5\pi/24$, at $\tau =$ (a) 39.61; (b) 39.96; (c) 40.30; (d) 40.65; (e) 40.99; (f) 41.33

8.4 Resonance due to heave excitation

In this subsection, the sloshing induced by the heave excitation is considered. When a liquid tank is accelerated vertically with an undisturbed initial free surface, ideally, the free surface is always flat and the entire fluid moves like a rigid body. However, Faraday (1831) observed in his experiment that, under a certain state, even a tiny disturbance on the free surface could finally lead to violent surface waves. He also found that the frequency of the sloshing waves was half that of the imposed excitation. But later, Matthiessen (1868) in his experiments found that the fluid oscillations were synchronous. So, Rayleigh (1883) made further experiments with the improved equipment, whose observation supported Faraday's findings. In 1954, Benjamin and Ursell transformed the sloshing problem to a decoupled system of Mathieu's equations and explained this discrepancy mathematically. After that, Faraday standing waves in both rectangular and cylindrical tanks have been widely studied based on theoretical, experimental or numerical approaches (as

reviewed in Ibriham (2015)). Typical numerical studies could be found in Wu et al (1998), Wright et al (2000), Murakami and Chikano (2001) and Frandsen (2004). For wedged tanks, it is expected that the geometric nonlinearity might affect the sloshing characteristics as the free-surface amplitude increases.

The theory developed by Benjamin and Ursell (1954) for 2D rectangular tanks could be generalised to 3D wedged tanks. When the tank is only undergoing the heave motion, from the linear solution in Section 6.2.3, it could be seen that the vertical excitation could not trigger the sloshing. However, by further including the nonlinear term $\dot{v}_3\eta$, the occurrence of Faraday waves could be explained. Eq. (6.30) could be rewritten as

$$\sum_{i=1}^{\infty}\left[\frac{1}{\omega_i^2}\ddot{\zeta}_i(t)+\zeta_i(t)\right]\bar{\phi}_i\left(x,y,\bar{z}\right)=-\frac{1}{g}\dot{v}_3(t)\eta(x,y,t)-z_c \tag{8.1}$$

Then, the following relationship is obtained

$$\sum_{i=1}^{\infty}\left[\ddot{\zeta}_i(t)+\omega_i^2\left(1+\dot{v}_3(t)/g\right)\zeta_i(t)\right]\bar{\phi}_i\left(x,y,\bar{z}\right)=-z_c \tag{8.2}$$

Taking advantage of the orthogonality property of the $\bar{\phi}_i$ set leads to

$$\ddot{\zeta}_i(t)+\omega_i^2\left(1+\dot{v}_3(t)/g\right)\zeta_i(t)=0\text{, for } i=1,2,\cdots \tag{8.3}$$

If the tank undergoes a cosine-type heave oscillation, i.e. $\dot{v}_3(t)=-A_z\omega_z^2\cos(\omega_z t)$, Eq. (8.3) could be expressed in the standard form of Mathieu's equations

$$\frac{\partial^2\zeta_i}{\partial T^2}+\left[p_i-2q_i\cos(2T)\right]\zeta_i=0\text{, for } i=1,2,\cdots \tag{8.4}$$

where $T=\omega_z t/2$, $p_i=4\left(\omega_i/\omega_z\right)^2$ and $q_i=2A_z\omega_i^2/g$. Note that, once the gravitational acceleration g and natural frequencies ω_i are fixed, p_i and q_i would only depend on the oscillation frequency and amplitude. It is known that for different p_i and q_i, the solution of the Mathieu's equation may be either stable or unstable (Abramowitz and Stegun 1964). The stability chart of the solution is shown in Fig. 8.16(a), in which the unstable regions have been

shaded. If the parameter pair (p_i, q_i) lies in a stable region, the solution is bounded (either periodic or not). Otherwise, in unstable regions, the solution grows exponentially (Abramowitz and Stegun 1964) and Faraday waves would occur. Back to the different experimental observations by Faraday and Matthiessen, the discrepancy is due to the fact that the parameter pair (p_i, q_i) lies in different unstable regions. For a better expression, the diagram of (p_i, q_i) could be transformed to that of $(a_z, \omega_i/\omega_z)$ i.e. $\left(2q_i/p_i, \sqrt{p_i}/2\right)$ in Fig. 8.16(b) (Frandsen 2004). Here, $a_z = A_z\omega_z^2/g$ is the non-dimensionalized amplitude of the heave acceleration.

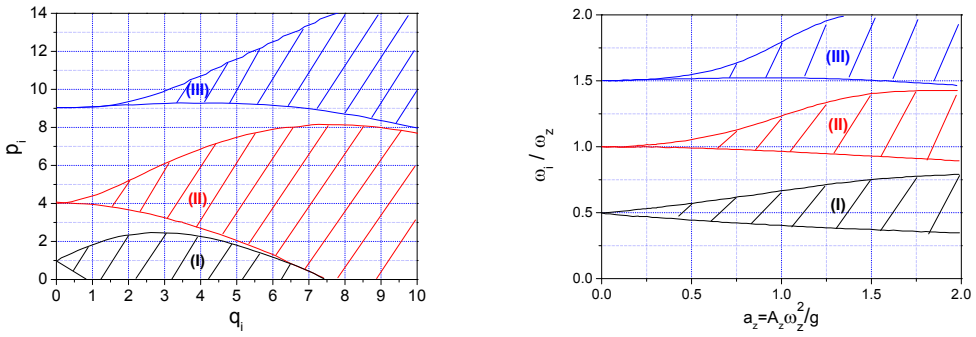

(a) (b)

Fig. 8.16 Stability diagram for solutions of Mathieu's equation: (a) diagram of (p_i, q_i); (b) diagram of $(a_z, \omega_i/\omega_z)$

Faraday waves in the tank of $\theta = 5\pi/24$ would be compared with that of $\theta = 0$. The tanks are firstly excited for a short time $\tau_{disturb}$ to give the liquid an initial disturbance. Then, the tanks are forced to heave at 7 conditions marked by C1 to C7 in Table 8.1. These conditions are reorganised into three groups. Group-1 involves C1 to C3, where the tank heaves at the same frequency but different amplitudes. Group-2 including C2, C4 and C5 concerns the situation when the heave excitation has different frequencies but the same acceleration amplitude. Group-3 aims to compare the wave behaviour in different regions. C3, C6 and C7 are located in the unstable region (I), stable region and unstable region (II), respectively. The general tank motion could be described as

$$\begin{cases} x_c = A_x \sin(\omega_x \tau); y_c = A_y \sin(\omega_y \tau); z_c = 0 & \text{for } \tau \le \tau_{disturb} \\ x_c = 0; y_c = 0; z_c = A_z \sin(\omega_z \tau). & \text{for } \tau > \tau_{disturb} \end{cases} \tag{8.5}$$

where $\tau_{disturb}$ is the time duration of the initial disturbance.

Table 8.1 Parameters for study of Faraday waves

	C1	C2	C3	C4	C5	C6	C7
a_z	0.083	0.15	0.5	0.15	0.15	0.5	0.5
ω_i / ω_z	0.5	0.5	0.5	0.51	0.49	0.61	1.0
Group-1	X	X	X				
Group-2		X		X	X		
Group-3			X			X	X

Firstly, the initial free-surface disturbance is caused by a surge excitation. Initial disturbance parameters are set as $A_x = 0.001$, $\omega_x = \omega_{10}$, $A_y = 0$, $\omega_y = \omega_{01}$ and $\tau_{disturb} = 10$. Then, the tank heaves according to the parameters in Table 8.1. Consider the single case of C1. Fig. 8.17(a) shows the wave elevation histories along the right walls of the rectangular and wedged tank. Unlike the prediction by the Mathieu's equation, the nonlinear wave elevation in both tanks has not exponentially grown to the infinity as time progresses. Instead, the wave amplitude increases rapidly to a peak value from $\tau = 10$ to approximately $\tau = 170$, and then it drops evidently. This is due to the nonlinear effects which have been observed in Fig. 8.3. At a large wave amplitude, the actual natural sloshing frequency has been changed, which further affects the wave behaviour. As the wave amplitude decreases to a small value, a rapid increasing trend of the wave amplitude returns. Comparing the wave elevation histories in the rectangular and wedged tank, It can be seen that the maximum wave peak in the wedged tank is much lower than that in the rectangular one. Also, the amplitude increase and decrease stage in the wedged tank are less steep than those in the rectangular tank. This difference could be attributed to the geometric nonlinearity caused by inclined tank walls. Fig. 8.17(b) gives the spectra of the elevation histories. It is clear that, even though the tanks are excited at $2\omega_{10}$, the dominant

sloshing frequency in either tank is still around ω_{10}. For the rectangular tank, the wave elevation shows a higher-order frequency component near $2\omega_{10}$. The phase planes associated with the wave elevations are drawn in Fig. 8.17(c) and (d). It could be seen that, at the growing stage of the wave amplitude, the trajectories are outgoing spirals. Then, after the wave elevation reaches the peak amplitude, spiral trajectories begin to go inwards. For the wedged tank, the trajectory has a nearly regular spiral pattern. But the trajectory pattern for the rectangular tank has an evident deformation as time progresses.

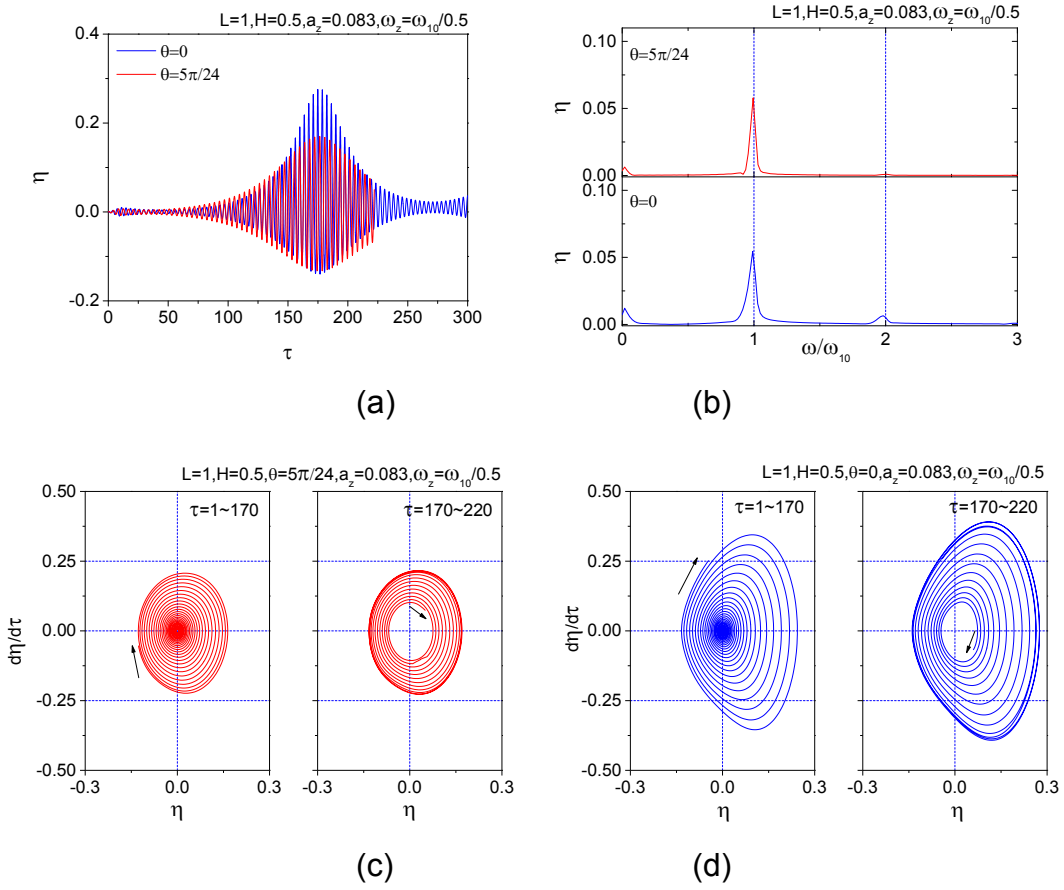

Fig. 8.17 Wave elevations, for $a_z = 0.0083$ and $\omega_z = \omega_{10}/0.5$: (a) time history; (b) spectral analysis; (c) phase plane for wedged tank; (d) phase plane for rectangular tank

Before performing systematic studies from Group-1 to 3, the disturbance amplitude is increased by ten times and the effect of the initial disturbance is tested. Parameters of the heave excitation are the same as C1. Fig. 8.18 shows the wave elevation histories along the tank wall. Referring to Fig.

8.17(a), it is clear that the initial disturbance does have effects on the behaviour of Faraday waves. For the rectangular tank, the wave amplitude increases rapidly to a very large value within twenty periods, which leads to a breakdown of the simulation. However, for the wedged tank, the wave amplitude does not increase continuously. Like the previous small-disturbance case, the wave amplitude begins to drop after reaching the peak. Also, the maximum wave amplitude in the wedged tank due to either small- or large-disturbance does not change much. This might reflect one advantage of the wedged tank geometry.

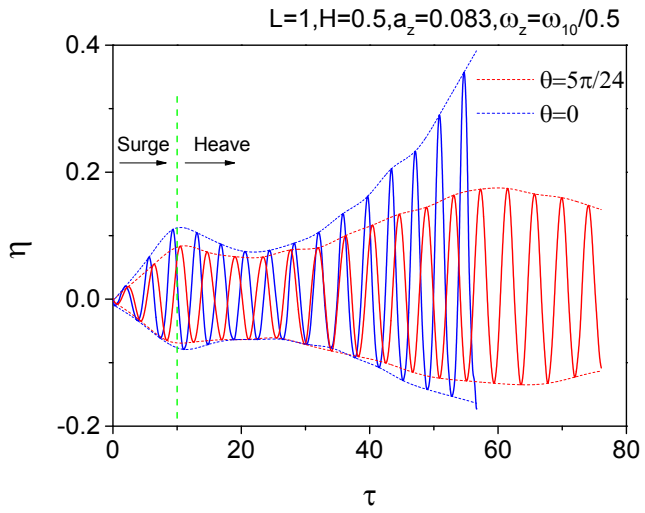

Fig. 8.18 Time history of wave elevations, for $a_z = 0.0083$ and $\omega_z = \omega_{10}/0.5$

Subsequently, cases in Group-1 are considered. For C2, the heave frequency remains the same, but the amplitude has been amplified by about two times. The small-disturbance condition is still adopted in this and subsequent simulations. Fig. 8.19(a) compares the wave elevations along the wall of rectangular and wedged tanks. Similar to Fig. 8.17(a), the wave amplitude of each tank is still bounded and the maximum amplitude in the wedged tank is smaller than that in the rectangular one. From the associated spectra in Fig. 8.19(b), it is clear that the dominant sloshing frequency in both tanks is still near ω_{10}. However, strictly speaking, the value of the dominant frequency at the peak is slightly lower than ω_{10}. This reflects the nonlinear effects as the wave amplitude has increased. Fig. 8.20 compares the wave elevation histories in Group-1. It can be seen that, for a larger acceleration

amplitude, the peak of the wave amplitude not only emerges earlier but also has a larger value. For the case of C3 where the heaving acceleration reaches half of the gravitational acceleration, the wave amplitude grows sharply to a very large value. This reaches the limit of the computation, so that the amplitude peak does not have the chance to emerge. These observations apply to both the rectangular and wedged tank. From Fig. 8.20, it can also be seen that, at the same excitation condition, the maximum wave amplitude in the wedged tank is always smaller than that in a corresponding rectangular tank.

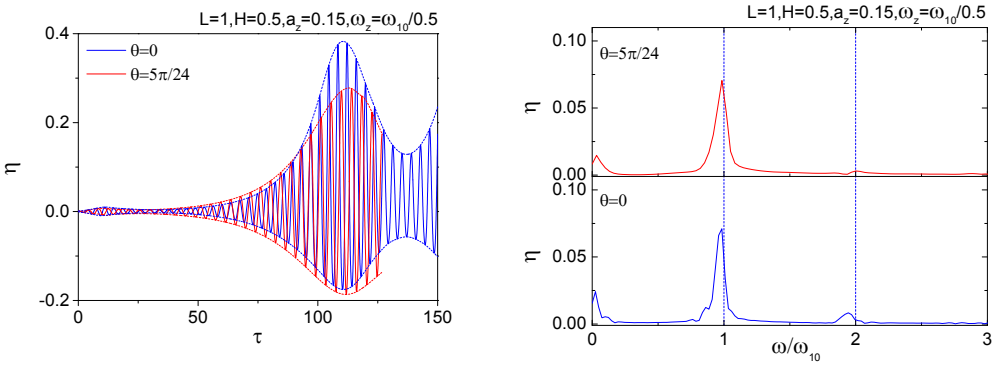

(a) (b)

Fig. 8.19 (a) Time history and (b) corresponding spectrum of wave elevations, for $a_z = 0.15$ and $\omega_z = \omega_{10}/0.5$

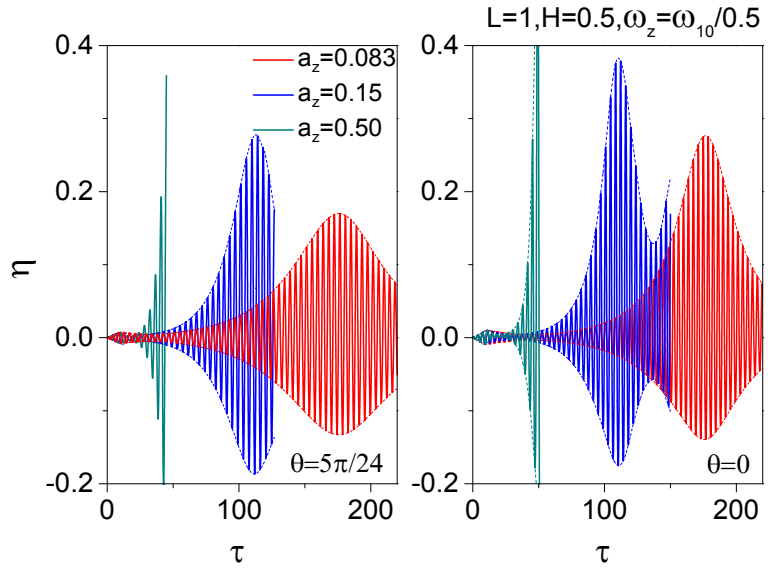

Fig. 8.20 Effect of the acceleration amplitude ($a_z = 0.083$ in green, $a_z = 0.15$ in blue, and $a_z = 0.50$ in red) on wave elevation histories, for $\omega_z = \omega_{10}/0.5$

Further, Group-2 is considered, focusing on effects of the excitation frequency. The cases of C2, C4 and C5 all exist in the unstable region (I). At C4, the excitation frequency is slightly lower than that at C2. For this excitation case, Fig. 8.21 (a) compares the elevation history along the wall of the rectangular and wedged tank. It is evident that the wave amplitude in the rectangular tank continuously increases until it reaches the computational limitation. However, in the wedged tank, the wave amplitude has an extreme value. Unlike C4, the case of C5 requires the excitation frequency to be slightly higher than that at C2. The wave elevation histories in the wedged and rectangular tanks are shown in Fig. 8.21 (b). In this case, the amplitude peak could be found in both curves. The maximum wave amplitude in the wedged tank is still smaller than that in the rectangular one. Also, the amplitude peak emerges earlier in the rectangular tank. In practice when the dissipation effects are involved, a later occurrence of the amplitude peak means a longer time for the energy to dissipate. Further, the wave elevation histories in the wedged tank are extracted from Fig. 8.21(a), Fig. 8.19(a) and Fig. 8.21(b), and are compared in Fig. 8.22. It is evident that the maximum value of the wave amplitude decreases as excitation frequency grows. In other words, when the tank heaves at a fixed acceleration within the same unstable region, a lower excitation frequency tends to lead to a larger amplitude extreme.

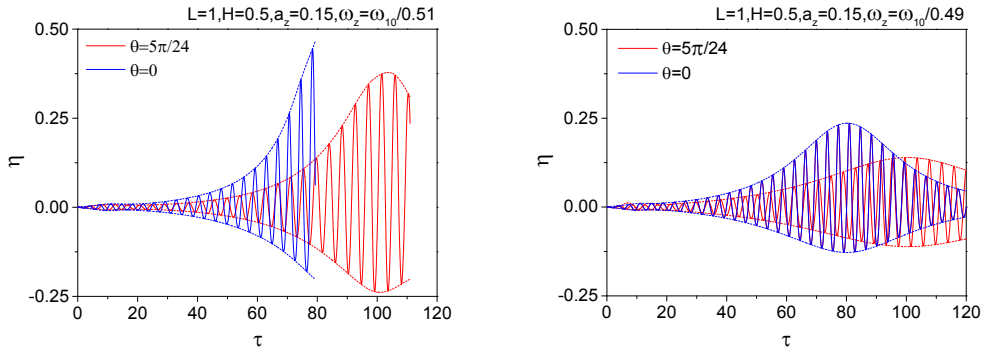

(a) (b)

Fig. 8.21 Effect of the heave frequency on wave elevation histories, for $a_z = 0.15$ and: (a) $\omega_z = \omega_{10}/0.51$ (b) $\omega_z = \omega_{10}/0.49$

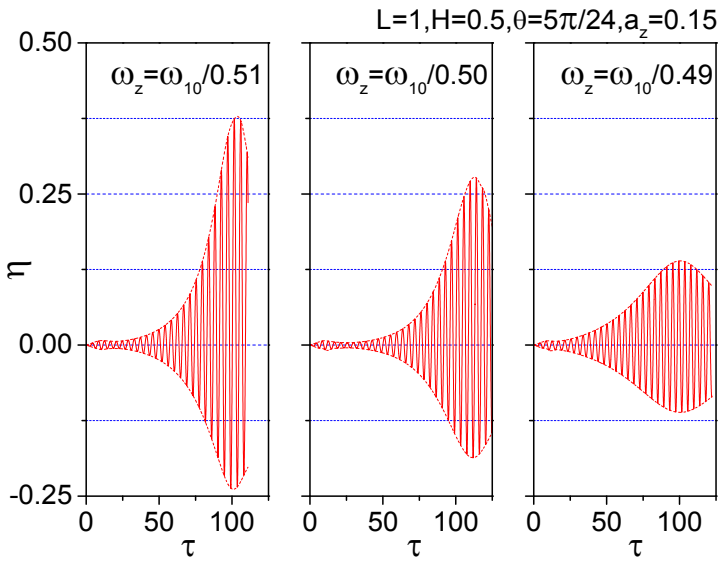

Fig. 8.22 Effect of the heave frequency on wave elevation histories, for $a_z = 0.15$

In Group-3, the heave acceleration is fixed at a large amplitude $a_z = 0.5$. The excitation frequency decreases from C3 of the unstable region (I) to C6 of the stable region and C7 of the unstable region (II). Wave elevation histories along the tank wall are compared in Fig. 8.23(a). In the case of C6, it is obvious that the wave elevation remains stable with a small amplitude during the long simulation, even though the position of C6 is just outside the unstable region (I) in Fig. 8.16(b). At C3 and C7, typical Faraday waves could be observed. It can be seen that the amplitude in the unstable region (I) grows much more rapidly than that in the unstable region (II). Fig. 8.23(b) gives the spectra of the wave elevation histories for the case of C3 and C7. It is found that the dominant sloshing frequency in both cases remains ω_{10}.

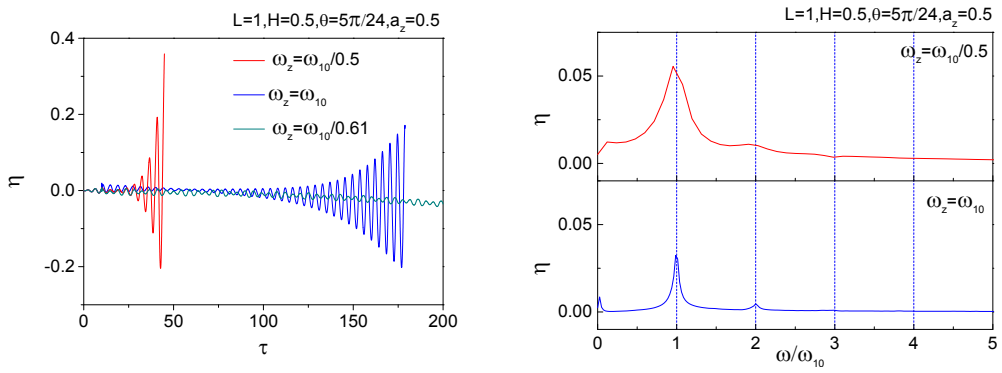

(a) (b)

Fig. 8.23 (a) Time history and (b) corresponding spectrum of wave elevations, for $a_z = 0.15$

Further, the situation when the free surface is initially disturbed by a sway excitation is considered. Parameters could be set as $A_x = 0$, $A_y = 0.001$, $\omega_y = \omega_{01}$ and $\tau_{disturb} = 10$. Fig. 8.24 shows the wave elevation histories for three cases in Group-3. It is found that Faraday waves in the case of C3 and C7 could also occur under this initial disturbance. Also, under the same acceleration amplitude of the heave excitation, the resonant waves in the condition of the unstable region (I) emerge much earlier than those of the unstable region (II). This is evidently reflected in the corresponding phase plane diagrams in Fig. 8.25, where the spiral radius for the case of C3 increases much more rapidly. For C6 in the stable region, the Faraday waves could not be observed. These observations are similar to those in Fig. 8.23. However, from the spectrum in Fig. 8.26, it is found that the dominant wave frequency is ω_{01} instead of the ω_{10} in previous cases. This is because the liquid in a tank undergoing the heave excitation intrinsically has natural modes corresponding to both ω_{10} and ω_{01}. However, the initial disturbance could determine which modes could become active. In addition, the wave profile of C3 at $\tau = 44.57$ is given for illustration purpose. From Fig. 8.27, it could be seen that the surface mesh is still smooth under this large free-surface deformation, which reflects the capability of the present numerical scheme.

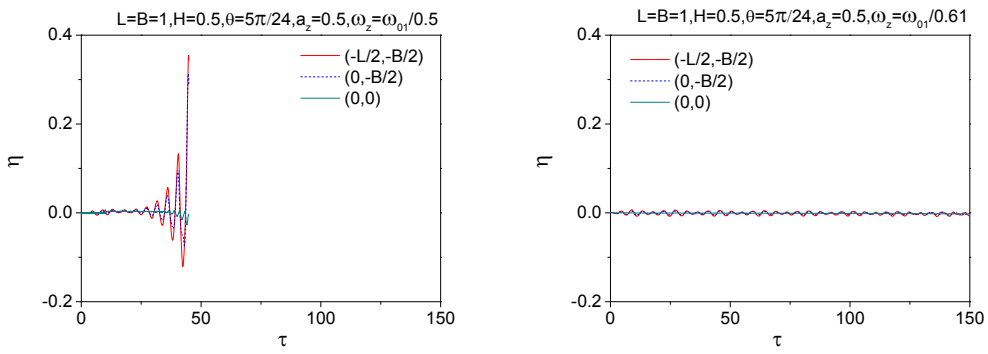

(a) (b)

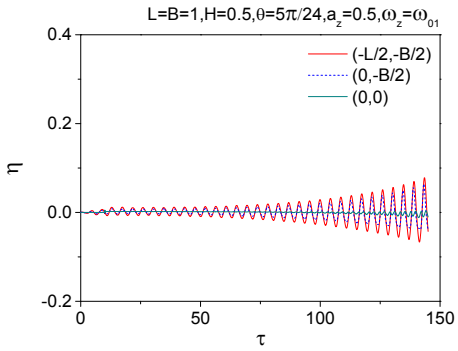

(c)

Fig. 8.24 Time history of wave elevations, for $a_z = 0.15$, $\theta = 5\pi/24$ and: (a) $\omega_z = \omega_{01}/0.5$; (b) $\omega_z = \omega_{01}/0.61$; (c) $\omega_z = \omega_{01}$

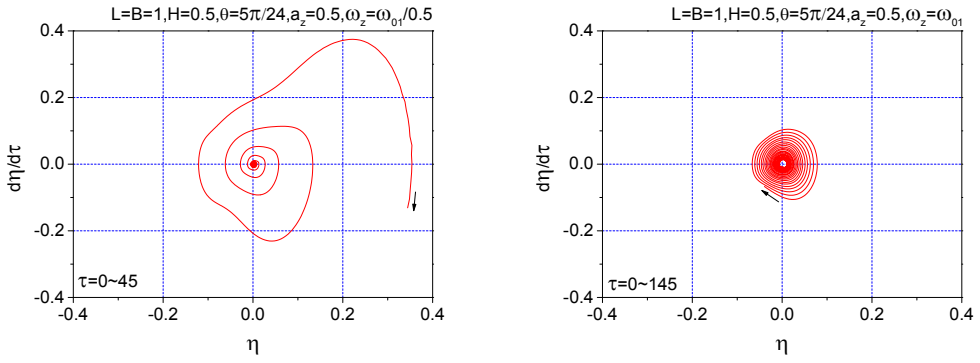

(a) (b)

Fig. 8.25 Phase plane of wave elevations, for $a_z = 0.15$, $\theta = 5\pi/24$ and: (a) $\omega_z = \omega_{01}/0.5$; (b) $\omega_z = \omega_{01}/0.61$; (c) $\omega_z = \omega_{01}$

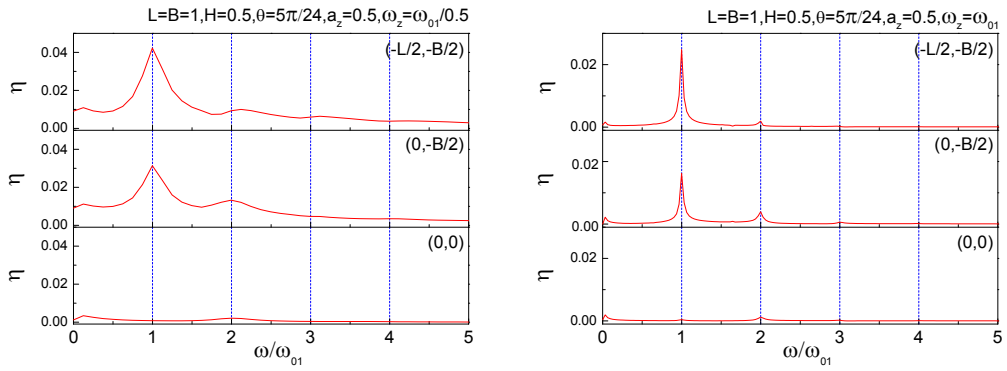

(a) (b)

Fig. 8.26 Spectrum of wave elevations, for $a_z = 0.15$, $\theta = 5\pi/24$ and: (a) $\omega_z = \omega_{01}/0.5$; (b) $\omega_z = \omega_{01}/0.61$; (c) $\omega_z = \omega_{01}$

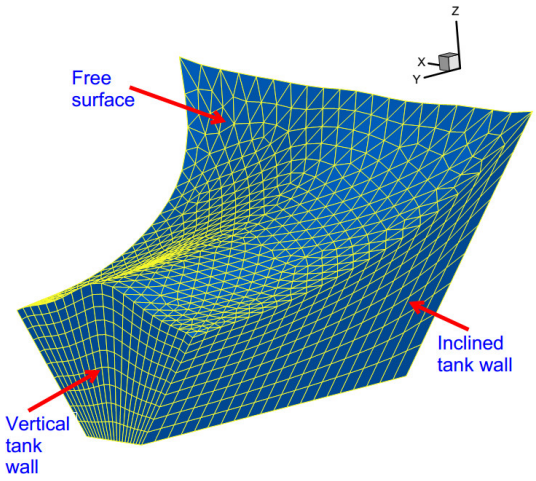

Fig. 8.27 Wave profile at $\tau = 44.57$ for C3 with sway disturbance

8.5 Conclusions

The resonant sloshing problems in 3D wedged tanks are simulated based on the improved SL free-surface updating procedure together with the BEM solver. Two types of resonance, the classical resonance and Faraday waves, are mainly investigated.

The classical resonance is induced by a lateral tank oscillation at the lowest natural sloshing frequency in the length or width direction of the tank. For the resonant sloshing due to either surge or sway excitation, the wave amplitude in rectangular and diverging tanks may increase to a peak and then start to drop, due to the nonlinear effects of the sloshing system. The inclined walls of the diverging tank cause geometric nonlinearities, which accelerates the variation of the natural sloshing frequency during waves running up. As a

result, the maximum wave amplitude in the diverging wedged tank is much lower than that in the rectangular one. For the resonant sloshing in converging tanks, the maximum wave height may not emerge along the inclined tank wall, and the wave peak has an evident trend to overturn at a large wave amplitude. In practice, the resulted wave breaking is expected to dissipate the energy and reduce the sloshing violence.

For Faraday waves, the tanks are firstly forced to surge or sway to give the liquid an initial disturbance and then forced to oscillate perpendicular to the undisturbed free surface plane. The following phenomena are observed. At the same heave frequency, the tank with a larger acceleration has the larger maximum wave amplitude. When the tank heaves at a fixed acceleration within the same unstable region, a lower excitation frequency tends to lead to a larger maximum wave amplitude. With the same heave acceleration in different unstable regions, the resonant waves in the unstable region (I) emerge much earlier than those in the unstable region (II). The initial disturbance could affect the dominant natural mode of the Faraday waves. At the same excitation, the maximum wave amplitude in the diverging wedged tank is generally smaller than that in the rectangular one.

Part III (Ch 9, 10 & 11) Coupling of sloshing and vessel motion

Chapter 9 Analytical study of coupling between vessel motion and sloshing in multiple tanks

9.1 Introduction

In previous chapters, the sloshing in tanks undergoing pre-described motions has been studied. From this chapter on, the coupling between the liquid sloshing and vessel motions will be taken into account.

For the FLNG vessel, during the offloading operation, the liquid sloshing inside an LNG tank could have non-negligible effects on the vessel motion (Zhao et al 2011). Meanwhile, the vessel motions would further excite the liquid sloshing in return. Thus, the interaction between the liquid sloshing and vessel motions forms a coupling problem. What makes the coupling more complicated is that the vessel motion itself is also coupled with the complex external environment such as ocean waves at the same time. Moreover, each vessel may have multiple liquid tanks, so that the liquid motion in each tank could have an interaction with the vessel motion.

At present, simulations on this coupling problem could be found in a few works such as Rognebakke & Faltinsen (2001), Molin et al (2002), Malenica et al (2003), Newman (2005), Kim et al (2007), Mitra et al (2012) and Zhao et al (2014). However, due to the complexity of the problem, a systematic understanding of the complete coupling system is still far behind. The complexity is mainly from the inclusion of too many influencing factors (i.e. the external environment, vessel motion and liquid sloshing in any of the tanks). Thus, to help understand the complete problem, it is necessary to firstly isolate the influencing factors and make clear the coupling mechanism between different pairs of them. The present chapter would focus on the coupling pair of the liquid sloshing and vessel motions.

The coupling of vessel motion and liquid sloshing in a single tank has been studied in literature by some researchers. Cooker (1994) ever introduces a typical model, which is a single-tank vessel suspended as a bifilar pendulum. Initially, the vessel with still water is dragged away from the

equilibrium position, before it is released from rest. During the swing motion, the vessel remains horizontal. The swing amplitude, liquid depth and wave amplitude are all assumed to be small, so that the vertical vessel displacement is neglected and the sloshing could be analysed using the linear shallow-water theory. It is found that the presence of the sloshing fluid could evidently change the natural oscillation frequency of the suspended system. In recent years, Cooker's model has received attention. Alemi Ardakani and Bridges (2010) extended Cooker's theory by including the nonlinear terms in shallow water equations, although the vessel motion was still restricted in a linear sense. They developed a numerical algorithm to solve the coupling problem. Their nonlinear results have shown distinctions from the linear ones in the near resonance situation. Yu (2010) applied the linear finite-depth water wave theory to Cooker's model. It is found that the shallow-water theory, which assumes the pressure acting on tank walls to be hydrostatic, does not give satisfactory results for cases of shorter suspension length and larger water depth where non-hydrostatic pressure becomes significant. Then, Herczynski and Weidman (2012) performed a related experiment to measure the horizontal oscillation of a vessel solely driven by the liquid sloshing inside. The linear finite-depth solutions were validated by the experiment. Alemi Ardakani et al (2012) further used a weakly-nonlinear finite-depth water wave theory for Cooker's model. The resonance, when the natural frequency of the system coincides with that of sloshing modes, is identified. Later, Turner and Bridges (2013) investigated the subtle energy transfer from the liquid sloshing to vessel motions through the nonlinearity. Turner et al (2015) further allowed the pivoting of the vessel with a sloshing tank, which is also different from the model considered in this chapter.

Another model in dealing with the vessel-liquid-coupling problem is the TLD. The TLD model is simplified as a liquid vessel constrained by springs and allowed to move freely only in the horizontal direction, which is essentially a mass-spring-damper system. The TLD and Cooker's bifilar pendulum have equivalent governing equations after linearization, but different characteristics in the nonlinear mathematical form. Ikeda and Nakagawa (1997) harmonically excited the TLD model from rest by an electromagnetic exciter. The free

surface is weakly-nonlinear. Stability analyses for the nonlinear vibration were performed. Frandsen (2005) studied a similar vibration system. A FDM solver based on the nonlinear potential-flow theory is developed for the sloshing simulation. The coupling of the sloshing and vessel motions in a time-varying force field was investigated. Gavrilyuk et al (2011) derived linear modal equations for the mechanical system carrying a tapered-conical liquid tank. Harmonic external forces were also applied.

The existing literature has mainly considered the single-tank vessel restrained by suspensions or springs, or even placed in time-varying force fields. Studies on the 'purely' free motion of a multiple-tank vessel seem to be rare. The term 'purely' here indicates that external factors (e.g. restoring forces from springs or suspension structures) are not involved. The vessel with liquid tanks itself is an oscillation system, whose natural frequency can be changed by extra suspensions or springs. On the vessel with 'multiple' tanks, two related works are those of Weidman (2005) and Turner et al (2013). In their study, the Cooker's experiment with a multi-tank vessel was examined. Turner et al (2013) also give the characteristic equation for natural frequencies of the coupling problem. However, like most of the aforementioned literature, the coupling system without external constraints is not considered either.

To help fill this gap, the present chapter investigates the coupling between the vessel motion and liquid sloshing in multiple tanks. The vessel is only excited by the liquid sloshing in tanks without external factors that could disturb characteristics of the oscillation system. The vessel motion is initially driven by the free-surface deformation in tanks. Based on the potential-flow theory, the analytical solution of the coupling problem is derived and an approach to determine the natural frequencies of the system is introduced. Firstly the dynamic properties of the coupling system with a single sloshing tank are investigated. Subsequently, multiple sloshing tanks will be considered. Effects of factors such as the vessel mass, number of tanks and tank configuration will be studied.

9.2 Theoretical analyses

9.2.1 Problem description

Consider a vessel with N liquid tanks as shown in Fig. 9.1. The tanks are numbered from Tank-1 to Tank-N in sequence. The fluid domain, free surface and wetted wall in Tank-k ($k=1\sim N$) are denoted by V^k, S_F^k and S_B^k, respectively. To analyse the liquid sloshing in Tank-k, a tank-fixed coordinate system $O^k-x^k y^k z^k$ is set, with the origin O^k at the centre of the mean free surface and $O^k z^k$ axis pointing upward. The earth-fixed coordinate system $O_o-x_o y_o z_o$ is also set, which coincides with the initial position of $O^1-x^1 y^1 z^1$. The vessel is undergoing a free motion in the $O_o x_o$ direction on the horizontal ground without friction.

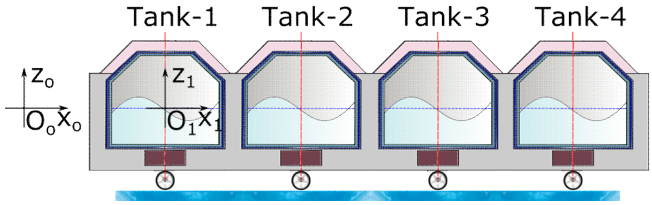

Fig. 9.1 Sketch of vessel with multiple rectangular sloshing tanks

The motion of the vessel is determined by the Newton's Second Law

$$m\dot{\mathbf{v}}_c=\sum_{k=1}^{N}\mathbf{F}^k \tag{9.1}$$

where m is the vessel mass without liquid, $\dot{\mathbf{v}}_c=\{\dot{v}_1,0,0\}=\{\ddot{x}_c,0,0\}$ is the transversal acceleration of the vessel and $\mathbf{F}^k=\{F_1^k,0,0\}$ is the sloshing-induced force from the domain V^k. Hereafter, a dot over a variable represents a time derivative, and the superscript k indicates a variable from the fluid domain in Tank-k.

The value of $\mathbf{F}^k$ is from the integration of the pressure over the wetted tank wall S_B^k, while the pressure could be calculated based on the potential-flow theory. The velocity potential in Tank-k is expressed by $\varphi^k\left(x^k,y^k,z^k,t\right)$. For convenience sake, the superscript k of variables in Tank-k is omitted, before calculating the resultant hydrodynamic force. The

small-amplitude assumption is further adopted, which requires the amplitude of the liquid and vessel motions to be small relative to the characteristic tank dimension. Then, the velocity potential could be determined from the linearized boundary value problem in Eqs. (6.1)-(6.4). Initial conditions should be further supplemented as

$$\varphi(x,y,z,t)=0\ ;\ \ \eta(x,y,t)=\overline{\eta}(x,y)\text{, for }\ t\le 0 \tag{9.2}$$

to give the free surface an initial profile. The fluid pressure p is obtained from the linearized Bernoulli's equation as

$$p=-\rho\frac{\partial\varphi}{\partial t}-\rho gz+C(t) \tag{9.3}$$

where ρ is the fluid density and $C(t)$ is a spatial-independent function. By redefining φ appropriately, $C(t)$ could be set as zero without affecting the velocity field.

9.2.2 General solutions

This subsection aims to derive the solution of the linearized vessel-liquid coupling problem. Firstly, consider the sloshing problem in each tank. The velocity potential and free-surface elevation are constructed as follows:

$$\varphi(x,y,z,t)=v_1(t)\,x+\sum_{i=1}^{\infty}\xi_i(t)\,\overline{\phi}_i(x,y,z) \tag{9.4}$$

$$\eta(x,y,t)=\sum_{i=1}^{\infty}\zeta_i(t)\,\overline{\phi}_i(x,y,0) \tag{9.5}$$

Following the derivations in Section 6.2.3, the following linear differential equations can be obtained according to Eq. (6.32)

$$\ddot{\zeta}_i(t)+\omega_i^{\,2}\zeta_i(t)=-\left(\frac{\omega_i^{\,2}}{g}\right)\left(\frac{\lambda_{i1}}{\mu_i}\right)\dot{v}_1\text{, for }\ i=1,2,\cdots,\infty \tag{9.6}$$

with

$$\mu_i=\int_{\overline{S}_F}\left(\overline{\phi}_i\overline{\phi}_i\right)dS\ ;\ \ \lambda_{i1}=\int_{\overline{S}_F}\left(x\overline{\phi}_i\right)dS \tag{9.7}$$

Thus, the first relationship between the $\zeta_i(t)$ and $\dot{v}_1$ is found.

The second relationship lies in the motion equation of the vessel. The hydrodynamic force generated from Tank-k is

$$\begin{aligned} F_1 &= \rho\int_{\bar{S}_B} pn_1 dS = -\rho\int_{\bar{S}_B}\left(\frac{\partial\varphi}{\partial t}+gz\right)n_1 dS = -\rho\int_{\bar{S}_B}\left(\sum_{j=1}^{\infty}\dot{\xi}_j(t)\bar{\phi}_j+\dot{v}_1(t)x+gz\right)n_1 dS \\ &= -\rho\sum_{j=1}^{\infty}\dot{\xi}_j(t)\left(\int_{\bar{S}_B}\bar{\phi}_j n_1 dS\right)-\rho\dot{v}_1(t)\left(\int_{\bar{S}_B}xn_1 dS\right)-\rho g\left(\int_{\bar{S}_B}zn_1 dS\right) \\ &= -\rho g\sum_{j=1}^{\infty}\frac{\ddot{\zeta}_j(t)}{\omega_j^{\,2}}\left(\int_{\bar{S}_B}\bar{\phi}_j n_1 dS\right)-\rho\dot{v}_1(t)\left(\int_{\bar{S}_B}xn_1 dS\right)-\rho g\left(\int_{\bar{S}_B}zn_1 dS\right) \\ &= -\rho g\sum_{j=1}^{\infty}\left(\frac{\gamma_{j1}}{\omega_j^{\,2}}\right)\ddot{\zeta}_j(t)-m_l\dot{v}_1(t)-m_z g \end{aligned} \tag{9.8}$$

with

$$\gamma_{j1}=\int_{\bar{S}_B}\bar{\phi}_j n_1 dS\,;\quad m_l=\rho\left(\int_{\bar{S}_B}xn_1 dS\right);\quad m_z=\rho\left(\int_{\bar{S}_B}zn_1 dS\right) \tag{9.9}$$

Substituting F_1^k into Eq. (9.1) leads to

$$-\rho g\sum_{k=1}^{N}\left[\sum_{j=1}^{\infty}\left(\frac{\gamma_{j1}^{\ k}}{\left(\omega_j^{\,k}\right)^2}\right)\ddot{\zeta}_j^{\,k}(t)\right]-g\sum_{k=1}^{N}m_z^{\,k}=\left(m+\sum_{k=1}^{N}m_l^{\,k}\right)\dot{v}_1(t) \tag{9.10}$$

The superscript k indicates a variable from Tank-k.

Combine Eqs. (9.6) and (9.10) by eliminating the vessel motion term $\dot{v}_1$. A series of second-order ordinary differential equations could be obtained as

$$\begin{aligned} &\ddot{\zeta}_i^{\,p}(t)-\frac{\rho\left(\omega_i^{\,p}\right)^2}{\left(m+\sum_{k=1}^{N}m_l^{\,k}\right)}\left(\frac{\lambda_{i1}^{\ p}}{\mu_i^{\,p}}\right)\sum_{k=1}^{N}\left[\sum_{j=1}^{\infty}\left(\frac{\gamma_{j1}^{\ k}}{\left(\omega_j^{\,k}\right)^2}\right)\ddot{\zeta}_j^{\,k}(t)\right]+\left(\omega_i^{\,p}\right)^2\zeta_i^{\,p}(t) \\ &=\frac{\left(\sum_{k=1}^{N}m_z^{\,k}\right)}{\left(m+\sum_{k=1}^{N}m_l^{\,k}\right)}\left(\omega_i^{\,p}\right)^2\left(\frac{\lambda_{i1}^{\ p}}{\mu_i^{\,p}}\right) \end{aligned} \quad\text{, for} \tag{9.11}$$

$$i=1,2,\cdots,\infty \quad\text{and}\quad p=1,2,\cdots,N$$

or

$$\ddot{\zeta}_i^{\,p}(t)-A_i^p\sum_{k=1}^{N}\left[\sum_{j=1}^{\infty}B_j^k\ddot{\zeta}_j^{\,k}(t)\right]+C_i^p\zeta_i^{\,p}(t)=\left(\sum_{k=1}^{N}m_z^{\,k}\right)A_i^p/\rho\,; \tag{9.12}$$

$$m_L=\sum_{k=1}^{N}m_l{}^k\ ;\ \ A_i^p=\frac{\rho\left(\omega_i{}^p\right)^2}{\left(m+m_L\right)}\left(\frac{\lambda_{i1}{}^p}{\mu_i{}^p}\right);\ \ B_j^k=\left(\frac{\gamma_{j1}{}^k}{\left(\omega_j{}^k\right)^2}\right);\ \ C_i^p=\left(\omega_i{}^p\right)^2,$$

$$\text{for}\ \ i=1,2,\cdots,\infty\ \ \text{and}\ \ p=1,2,\cdots,N$$

The $\zeta_j(t)$ could be solved numerically using time-stepping methods. Then, the vessel motions could be calculated based on Eq. (9.10).

Further, consider the mechanical energy of the oscillation system. The kinetic energy of the vessel is defined as

$$E_K{}^0(t)=\frac{1}{2}mv_1{}^2 \tag{9.13}$$

The potential energy $E_P{}^k$ and kinetic energy $E_K{}^k$ of the liquid in Tank-k have the expressions

$$\begin{aligned}E_K{}^k(t)&=\frac{\rho}{2}\iiint_{\bar{V}^k}\left(\nabla\varphi^k\cdot\nabla\varphi^k\right)dV=\frac{\rho}{2}\iint_{\bar{S}_F^k+\bar{S}_B^k}\varphi^k\nabla\varphi^k\cdot\mathbf{n}dS\\&=\frac{\rho}{2}\iint_{\bar{S}_F^k+\bar{S}_B^k}\varphi^k\varphi_n{}^k dS\end{aligned} \tag{9.14}$$

$$E_P{}^k(t)=\frac{\rho g}{2}\iint_{\bar{S}_F^k}\left(\eta^k\right)^2dS \tag{9.15}$$

9.2.3 Solutions for rectangular tanks

For the vessel with rectangular tanks, natural frequencies and corresponding modes for the sloshing in Tank-k have the explicit form

$$\omega_j{}^k=\sqrt{gk_j{}^k\tanh\left[k_j{}^kH^k\right]}\text{, with }\ k_j{}^k=j\pi/L^k \tag{9.16}$$

$$\begin{aligned}\bar{\phi}_j{}^k\left(x^k,y^k,z^k\right)&=\frac{\cosh\left[k_j{}^k\left(z^k+H^k\right)\right]}{\cosh\left[k_j{}^kH^k\right]}\cos\left[k_j{}^k\left(x^k+L^k/2\right)\right];\\\bar{\phi}_j{}^k\left(x^k,y^k,0\right)&=\cos\left[k_j{}^k\left(x^k+L^k/2\right)\right]\end{aligned} \tag{9.17}$$

where L^k and H^k are the length and averaged liquid depth of Tank-k .Then, integrations in Eq. (9.12) can be calculated analytically

$$\mu_i{}^k=L^k/2\ ;\ \ \lambda_{i1}{}^k=\left[\cos(i\pi)-1\right]\Big/\left(k_i^k\right)^2=\left[(-1)^i-1\right]\Big/\left(k_i^k\right)^2; \tag{9.18}$$

$$m_l^{\,k} = \rho L^k H^k ; \;\; m_z^{\,k} = 0 ;$$

$$\gamma_{j1}^{\,k} = \frac{\cos(j\pi)-1}{k_j^{\,k}} \tanh\left[k_j^{\,k} H^k\right] = \frac{(-1)^j - 1}{k_j^{\,k}} \tanh\left[k_j^{\,k} H^k\right]$$

So that Eq. (9.12) could be written as

$$\ddot{\zeta}_i^{\,p}(t) - A_i^p \sum_{k=1}^{N}\left[\sum_{j=1}^{\infty} B_j^k \ddot{\zeta}_j^{\,k}(t)\right] + C_i^p \zeta_i^{\,p}(t) = 0 ;$$

$$A_i^p = \frac{2\rho\left[(-1)^i - 1\right]}{L^p\left(m + m_L\right)}\left(\frac{\omega_i^{\,p}}{k_i^p}\right)^2 ; \;\; B_j^k = \left(\frac{1}{k_j^{\,k}}\right)^2\left(\frac{(-1)^j - 1}{g}\right) ; \;\; C_i^p = \left(\omega_i^{\,p}\right)^2 , \tag{9.19}$$

$$\text{for } \; i = 1,2,\cdots,\infty \;\; \text{and} \;\; p = 1,2,\cdots,N$$

Since $\zeta_i^{\,k}(t) \equiv 0$ for $i = 2,4,6,\cdots$, Eq. (9.19) could be further simplified as

$$A_i^p \sum_{k=1}^{N}\left[\sum_{j=1}^{\infty} B_j^k \ddot{\zeta}_j^{\,k}(t)\right] - \ddot{\zeta}_i^{\,p}(t) = C_i^p \zeta_i^{\,p}(t) , \text{ for } \; i = 1,3,5,7,\cdots,\infty , \tag{9.20}$$

$$j = 1,3,5,7,\cdots,\infty \;\; \text{and} \;\; p = 1,2,\cdots,N$$

with

$$A_i^p = -\left(\frac{4\rho}{L^p}\right)\frac{1}{\left(m + m_L\right)}\left(\frac{\omega_i^{\,p}}{k_i^p}\right)^2 ; \;\; B_j^k = -\left(\frac{2}{g}\right)\left(\frac{1}{k_j^{\,k}}\right)^2 ; \;\; C_i^p = \left(\omega_i^{\,p}\right)^2 \tag{9.21}$$

For the purpose of calculation, finite terms in Eq. (9.20) should be chosen. Here is an example. If the three-tank vessel (i.e. $N = 3$) is considered and the first two active modes (i.e. $i = 1,3$ and $j = 1,3$) are taken into account, the second-order ordinary differential equations could be expressed in the following matrix form

$$\begin{bmatrix}
A_1^1 B_1^1 - 1 & A_1^1 B_2^1 & A_1^1 B_1^2 & A_1^1 B_2^2 & A_1^1 B_1^3 & A_1^1 B_2^3 \\
A_2^1 B_1^1 & A_2^1 B_2^1 - 1 & A_2^1 B_1^2 & A_2^1 B_2^2 & A_2^1 B_1^3 & A_2^1 B_2^3 \\
A_1^2 B_1^1 & A_1^2 B_2^1 & A_1^2 B_1^2 - 1 & A_1^2 B_2^2 & A_1^2 B_1^3 & A_1^2 B_2^3 \\
A_2^2 B_1^1 & A_2^2 B_2^1 & A_2^2 B_1^2 & A_2^2 B_2^2 - 1 & A_2^2 B_1^3 & A_2^2 B_2^3 \\
A_1^3 B_1^1 & A_1^3 B_2^1 & A_1^3 B_1^2 & A_1^3 B_2^2 & A_1^3 B_1^3 - 1 & A_1^3 B_2^3 \\
A_2^3 B_1^1 & A_2^3 B_2^1 & A_2^3 B_1^2 & A_2^3 B_2^2 & A_2^3 B_1^3 & A_2^3 B_2^3 - 1
\end{bmatrix}
\begin{Bmatrix}
\ddot{\zeta}_1^{\,1} \\ \ddot{\zeta}_3^{\,1} \\ \ddot{\zeta}_1^{\,2} \\ \ddot{\zeta}_3^{\,2} \\ \ddot{\zeta}_1^{\,3} \\ \ddot{\zeta}_3^{\,3}
\end{Bmatrix} =
\begin{Bmatrix}
C_1^1 \zeta_1^1 \\ C_3^1 \zeta_3^1 \\ C_1^2 \zeta_1^2 \\ C_3^2 \zeta_3^2 \\ C_1^3 \zeta_1^3 \\ C_3^3 \zeta_3^3
\end{Bmatrix} \tag{9.22}$$

Knowing $\ddot{\zeta}_j^{\,k}$, the acceleration of the vessel could be calculated by

$$\dot{v}_1(t) = -\frac{\rho g}{(m+m_L)} \sum_{k=1}^{N} \left[\sum_{j=1}^{\infty} B_j^k \ddot{\xi}_j^k(t) \right], \text{ for } j = 1,3,5,7,\cdots,\infty \tag{9.23}$$

Note that m is the vessel mass without liquid and m_L is the total mass of the liquid in all tanks. The velocity and displacement of the vessel could be further calculated based on time-stepping methods.

9.2.4 Natural frequencies of coupling system

For the coupling system under consideration, there might be a situation, where the vessel and liquid in all tanks oscillate with the same frequency ω. Then, the ω would be the natural frequency of the coupling system. It is noted that Turner et al (2013) investigated the Cooker's experiment with a multi-compartment vessel and gave the characteristic equation with respect to the vessel oscillation frequencies. In a limit case when the suspended string length is infinite, their solution could be applied to the present problem. This subsection will provide an alternative derivation for the natural frequencies, based on the cosine-type expansions as in Eq. (9.17).

Consider the steady state when the vessel oscillates freely at a frequency ω. Unlike the wave radiation problem for a floating body, this problem does not contain imaginary terms in boundary conditions. So, the sloshing response in tanks would have no phase shift with the vessel oscillation, and it may be set as $\zeta_i^k(t) = \overline{\zeta}_i^k \sin(\omega t)$. Eq. (9.20) can be reformulated as

$$-\omega^2 \sin(\omega t) A_i^p \sum_{k=1}^{N} \left[\sum_{j=1}^{\infty} B_j^k \overline{\zeta}_j^k \right] + \overline{\zeta}_i^p \omega^2 \sin(\omega t) = C_i^p \overline{\zeta}_i^p \sin(\omega t), \text{ for } i = 1,3,5,7,\cdots,\infty, \quad j = 1,3,5,7,\cdots,\infty \text{ and } p = 1,2,\cdots,N \tag{9.24}$$

i.e.

$$-\omega^2 A_i^p \sum_{k=1}^{N} \left[\sum_{j=1}^{\infty} B_j^k \overline{\zeta}_j^k \right] + \left(\omega^2 - C_i^p\right) \overline{\zeta}_i^p = 0, \text{ for } i = 1,3,5,7,\cdots,\infty, \quad j = 1,3,5,7,\cdots,\infty \text{ and } p = 1,2,\cdots,N \tag{9.25}$$

Accordingly, the matrix form in Eq. (9.22) could be expressed as

$$\left[M(\omega)\right]\left\{\overline{\zeta}_1^{\,1},\overline{\zeta}_3^{\,1},\overline{\zeta}_1^{\,2},\overline{\zeta}_3^{\,2},\overline{\zeta}_1^{\,3},\overline{\zeta}_3^{\,3}\right\}^T=0 \tag{9.26}$$

$$\begin{aligned}\left[M(\omega)\right]=\omega^2&\begin{bmatrix} A_1^{\,1}B_1^{\,1}-1 & A_1^{\,1}B_2^{\,1} & A_1^{\,1}B_1^{\,2} & A_1^{\,1}B_2^{\,2} & A_1^{\,1}B_1^{\,3} & A_1^{\,1}B_2^{\,3} \\ A_2^{\,1}B_1^{\,1} & A_2^{\,1}B_2^{\,1}-1 & A_2^{\,1}B_1^{\,2} & A_2^{\,1}B_2^{\,2} & A_2^{\,1}B_1^{\,3} & A_2^{\,1}B_2^{\,3} \\ A_1^{\,2}B_1^{\,1} & A_1^{\,2}B_2^{\,1} & A_1^{\,2}B_1^{\,2}-1 & A_1^{\,2}B_2^{\,2} & A_1^{\,2}B_1^{\,3} & A_1^{\,2}B_2^{\,3} \\ A_2^{\,2}B_1^{\,1} & A_2^{\,2}B_2^{\,1} & A_2^{\,2}B_1^{\,2} & A_2^{\,2}B_2^{\,2}-1 & A_2^{\,2}B_1^{\,3} & A_2^{\,2}B_2^{\,3} \\ A_1^{\,3}B_1^{\,1} & A_1^{\,3}B_2^{\,1} & A_1^{\,3}B_1^{\,2} & A_1^{\,3}B_2^{\,2} & A_1^{\,3}B_1^{\,3}-1 & A_1^{\,3}B_2^{\,3} \\ A_2^{\,3}B_1^{\,1} & A_2^{\,3}B_2^{\,1} & A_2^{\,3}B_1^{\,2} & A_2^{\,3}B_2^{\,2} & A_2^{\,3}B_1^{\,3} & A_2^{\,3}B_2^{\,3}-1 \end{bmatrix} \\ &+\begin{bmatrix} C_1^{\,1} & & & & & 0 \\ & C_3^{\,1} & & & & \\ & & C_1^{\,2} & & & \\ & & & C_3^{\,2} & & \\ & & & & C_1^{\,3} & \\ 0 & & & & & C_3^{\,3} \end{bmatrix}\end{aligned} \tag{9.27}$$

For the homogeneous system in Eq. (9.26), it is known that non-zero solutions exist only if the determinant of the matrix $\left[M(\omega)\right]$ is zero, i.e.

$$\det\left[M(\omega)\right]=0 \tag{9.28}$$

All solutions of ω that could satisfy Eq. (9.28) are natural frequencies of the coupling system. The root of Eq. (9.28) could be determined from the diagram of the determinant of $M(\omega)$ with respective to ω.

Then, the acceleration of the vessel has the form

$$\dot{v}_1(t)=\frac{\rho g\omega^2}{(m+m_L)}\sum_{k=1}^{N}\left(\sum_{j=1}^{\infty}B_j^k\overline{\zeta}_i^{\,k}\right)\sin(\omega t),\ \text{for}\ \ j=1,3,5,7,\cdots,\infty \tag{9.29}$$

from which the amplitude of the vessel motion could be known.

9.3 Accuracy comparison

The experimental case in Herczynski and Weidman (2012) is adopted to validate the present derivations. The physical model is a vessel with a rectangular liquid tank on the horizontal frictionless ground. The tank has length $L=0.2474m$ and width $B=0.08255m$, and the vessel with the tank empty has weight $m=0.8865kg$. In order to achieve the low-friction situation in the experiment, the vessel is outfitted with four knife-edge wheels which would rotate freely on high-quality ball bearings. Firstly, the vessel is manually

oscillated in the length direction, so that the free-surface profile of the first or second anti-symmetric mode (i.e. $j=1$ or $j=3$ in Eq. (9.17)) is obtained. Then, the vessel is set free.

The analytical solution of this problem could be obtained by setting the initial conditions as

$$\zeta_j(0)=A;\ \ \dot{\zeta}_j(0)=0;\ \ x_c(0)=0;\ \ \dot{x}_c(0)=0 \tag{9.30}$$

which means that the vessel is initially stationary and the free surface has a cosine-type initial profile

$$\eta(x,y,0)=A\cos\left[k_j\left(x+L/2\right)\right] \tag{9.31}$$

The first and second anti-symmetric free-surface modes are represented by 'Mode-1' with $j=1$ and 'Mode-2' with $j=3$, respectively. Truncating 20 terms in the expansion of Eq. (9.5) could provide a sufficient convergence of the result, which would be seen later in Fig. 9.5. When set free, the vessel would undergo an oscillation solely excited by sloshing pressure forces inside the tank.

Dominant frequencies of the vessel oscillation, obtained through the FFT on the time histories, are compared with theoretical solutions and experimental data in Herczynski and Weidman (2012). In Fig. 9.2, the ω_v denotes the dominant vessel oscillation frequency and ω_R is a reference frequency computed in the literature for normalisation. The liquid mass m_L varies by adjusting the liquid depth H. It is observed that the present results have a good agreement with the theoretical and experimental results from the literature, which has validated the present derivation. Additionally, it is found that the vessel oscillation frequency generally increases with the liquid depth. The oscillation frequency of the vessel with a deep-liquid tank does not change much for the case of Mode-2.

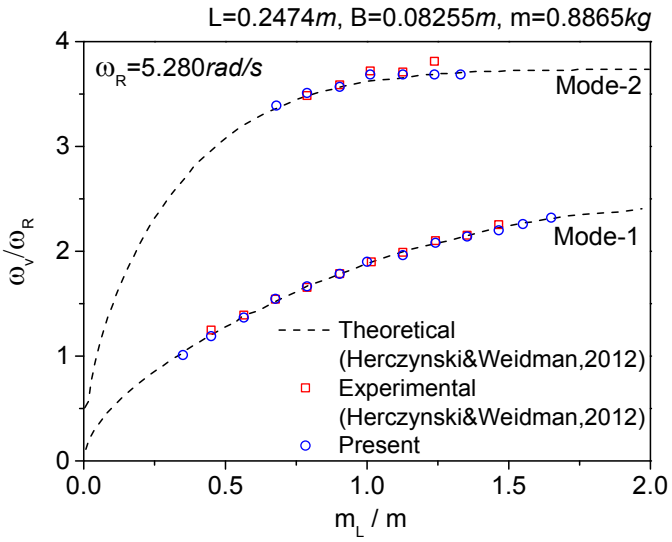

Fig. 9.2 Oscillation frequency of single-tank vessel, with initial free-surface deformation of Mode-1 and Mode-2

The vessel with multiple tanks is also considered. Assume that all tanks on the vessel have the same height H_t and width B, with $B = H_t$. The tank height H_t, as well as the gravity acceleration g and liquid density ρ, are used as bases of the nondimensionalization, as in Chapter 6. Initially, a single-tank vessel is used. The tank has the length $L = 1$ and mean liquid depth $H = 0.5$. The vessel mass equals the liquid mass. Then, non-porous baffles are inserted into the tank, leading to multiple uniform 'sub-tanks'. Here, 6 sub-tanks maximum are considered. The vessel motion is initially excited by the free-surface deformation of Mode-1 in a sub-tank. The theoretical solution derived by Turner et al (2013) could be applied to verify the present results. In Fig. 9.3, the vessel motion frequencies obtained from the present method and the literature are compared. Corresponding results have shown fairly good agreement. Thus, the derivation for the multiple-tank vessel is verified.

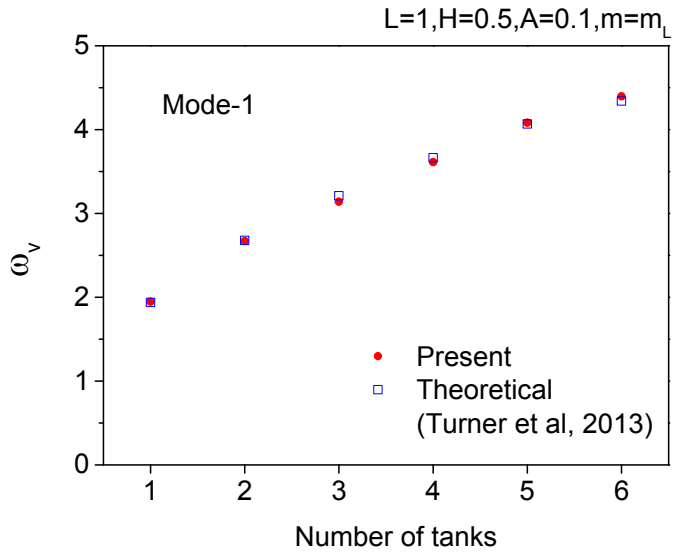

Fig. 9.3 Oscillation frequency of multiple-tank vessel, with initial free-surface deformation of Mode-1 in Tank-1

In the following sections, an initial deformation of the free surface as Eq. (9.30) is used to drive the vessel motion.

9.4 Free motion of a single-tank vessel

9.4.1 An initial case study

In this subsection, the free motion of a single-tank vessel is considered. The first case aims to give an intuitive description of the vessel-fluid coupling effects before a systematic analysis. The vessel carries a tank of dimensions $L = B = 1$ and averaged liquid depth $H = 0.5$. The free surface has an initial deformation of Mode-1 with the amplitude $A = 0.1$. Note that, for the linear problem, the amplitude A could not affect the oscillation frequencies of the solution. Let $m = m_L$. The vessel positions and free-surface profiles in the tank within the first period are shown in Fig. 9.4. It is clear that the initial tank motion is motivated by the asymmetric distribution of the static pressure on side walls. As the vessel moves left to an extreme position, the waterline along the right tank wall rises to the maximum. Thus, the vessel motion and liquid sloshing in the situation are in an 'antiphase' status, according to Cooker (1994). This antiphase character is different from that of Cooker's suspended system. For the suspended system, the restoring force could be in concert with or in opposition to the hydrodynamic force, so that both inphase

and antiphase oscillations can occur. When the suspension length tends to infinity as in this case, only the antiphase mode becomes dominant.

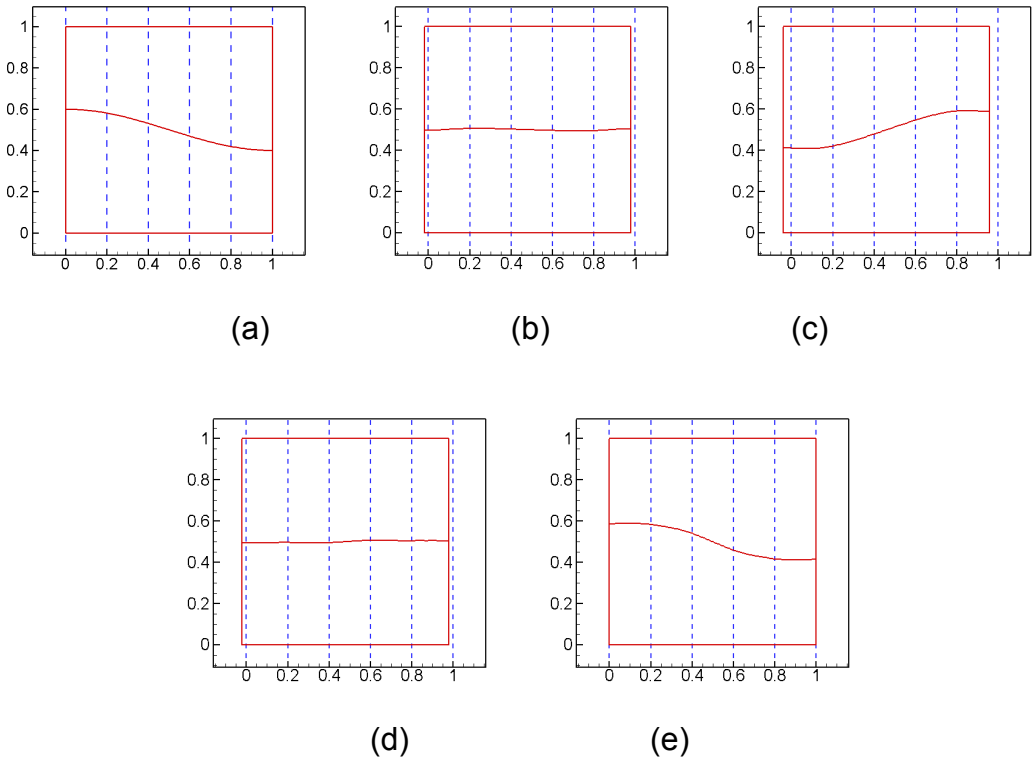

Fig. 9.4 Position and free-surface profiles for single-tank vessel, with initial free-surface deformation of Mode-1 at: (a) $\tau = 0$; (b) $\tau = 0.8$; (c) $\tau = 1.6$; (d) $\tau = 2.4$; (e) $\tau = 3.2$

Fig. 9.5 gives time histories of the vessel displacement and wave elevation along the right tank wall. The first 20 and 40 terms in the expansion of Eq. (9.5) are adopted, respectively. For either the vessel displacement or the wave elevation, results from these two truncation options coincide graphically. This indicates that the 20-term truncation could provide a sufficient convergence of the result. Fig. 9.6(a) shows the corresponding spectra of both time histories. It is clear that the frequency dominating both the wave and vessel motions is ω_{v1}. However, in the spectrum of the wave elevation history, higher frequencies ω_{v2}, ω_{v3} and ω_{v4} could also be observed. Fig. 9.6(b) is the diagram of $\det\left[M(\omega)\right]$ for this system, from which it can be told that ω_{v1} to ω_{v4} are natural frequencies of the coupling system. The occurrence of these higher-order frequencies in this linear

system is due to the initial conditions. It is known that Eq. (9.30) gives the exact form of a free-surface mode for the stationary sloshing tank. Thus, when set free, the free surface in a stationary tank would oscillate periodically with an constant amplitude. However, when the tank is allowed to move freely, the sloshing mode in a freely moving vessel is expected to be different from that in the stationary tank. The initial free-surface deformation in Eq. (9.30) could be further expanded to a summation of the 'true' free-surface modes corresponding to each ω_v. Then, more than one frequency components could be observed in the spectrum of the time history.

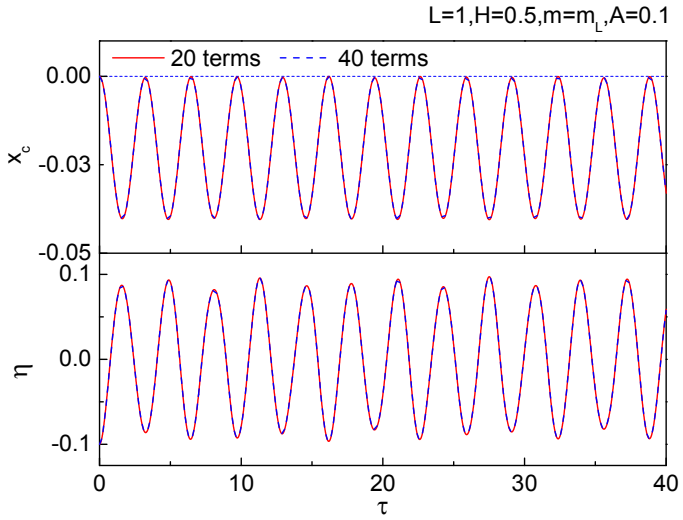

Fig. 9.5 Displacement of single-tank vessel and wave elevation along the right tank wall, with initial free-surface deformation of Mode-1

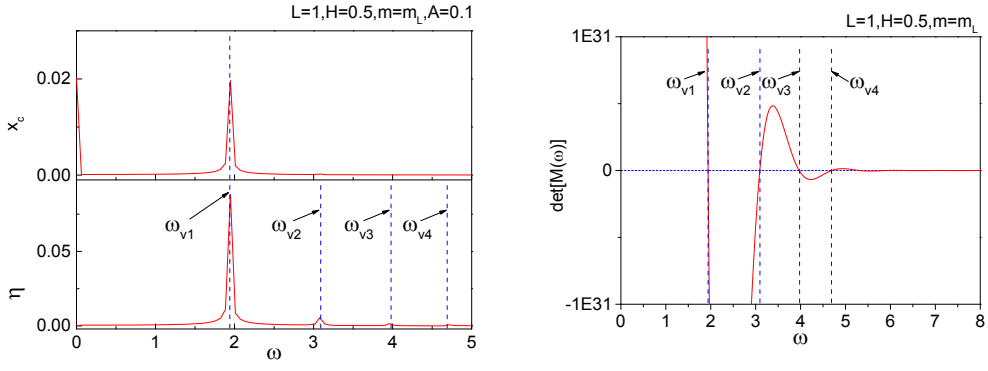

(a) (b)

Fig. 9.6 Frequency analysis for single-tank vessel, with initial free-surface deformation of Mode-1: (a) spectrum of vessel displacement and wave elevation along the right tank wall, with $A = 0.1$; (b) diagram of $\det\left[M\left(\omega\right)\right]$

Fig. 9.7 shows the mechanical energy components of the system. The proportion of the vessel's kinetic energy E_K^0, fluid's kinetic energy E_K and fluid's potential energy E_P varies with time. Since this is an isolated system which is only subject to conservative forces, the conservation of the mechanical energy is satisfied. From Fig. 9.7, it is observed that the summation of E_K^0, E_K and E_P is nearly constant. Strictly speaking, the calculated summation has a slight shake as time progresses. This is because the integration calculation for E_K is performed on the mean fluid boundary instead of the exact one, under the linear approximation. It is observed that the kinetic and potential energy are always antiphase, which is expected. Also, the oscillation frequency of the kinetic/potential energy is two times that of the vessel motion. This is because the potential energy could reach a maximum value at both the left and right extreme of the vessel position. It is also interesting to find that the kinetic energy of the vessel and fluid are inphase. This suggests that as the potential energy reaches the maximum, both the vessel and fluid could be stationary at the same time.

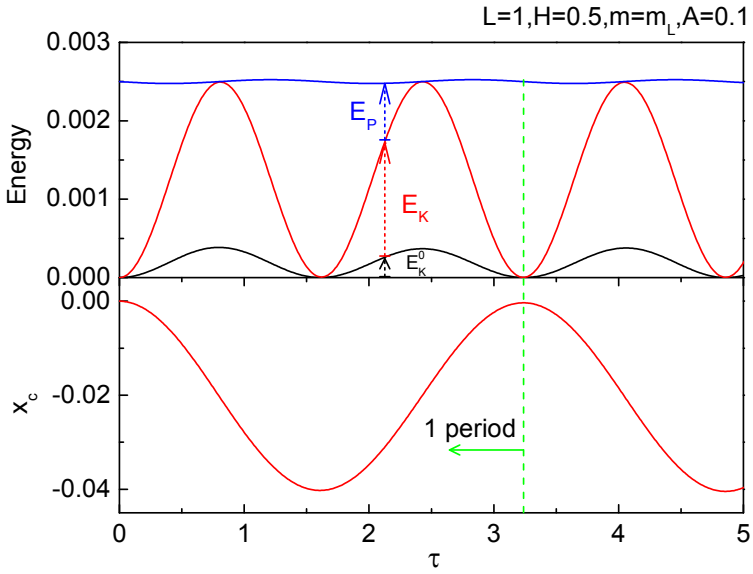

Fig. 9.7 Energy analysis for single-tank vessel, with initial free-surface deformation of Mode-1

9.4.2 Effect of vessel mass

In this subsection, effects of the vessel mass are considered. The free surface in the tank still has the initial deformation of Mode-1, with $A = 0.1$. Fig.

9.8 shows the obtained dominant frequency ω and averaged amplitude A_c of the vessel oscillation. The vessel mass varies from $m = 0.01m_l$ to $m = 20m_l$. As the vessel mass increases, it is found that the vessel motion amplitude decreases and gradually approaches zero. Also, the rate of this amplitude decrease slows down evidently. This could be explained from Eq. (9.29). The motion amplitude and vessel mass have a near reciprocal relationship. Further, it is found that the oscillation frequency of the free vessel is always higher than the fundamental natural sloshing frequency ω_1 in the stationary tank. As the mass ratio grows, the motion frequency has a decreasing trend. At $m = 20m_l$, the ω has become very close to ω_1. On this point, the vessel-liquid system has a similarity with the mass-spring system whose natural oscillation frequency decreases with the mass.

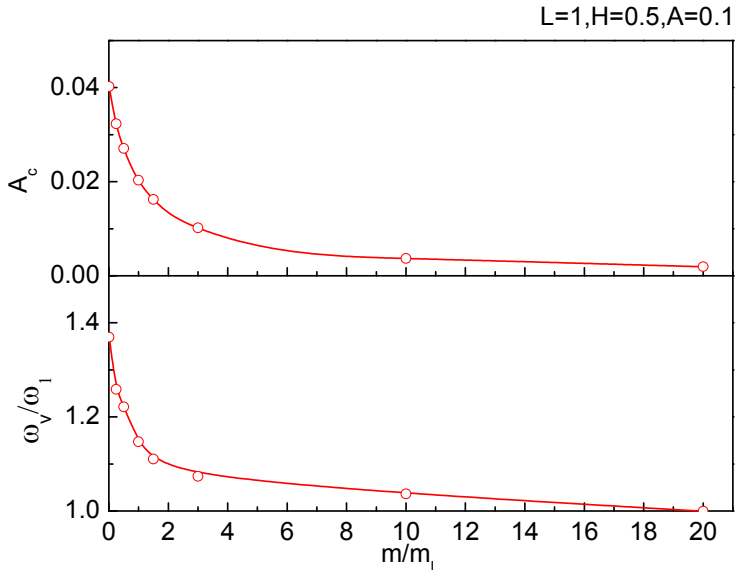

Fig. 9.8 Effect of vessel mass on oscillation amplitude and frequency of single-tank vessel, with initial free-surface deformation of Mode-1

9.4.3 Effect of tank configuration

In Fig. 9.2 and Fig. 9.8, the mass ratio of the liquid and vessel have been taken as variables. However, even for a constant mass ratio, the tank configuration (i.e. tank length L and liquid depth H) could affect the oscillation properties. Thus, this subsection would investigate the effect of the tank configuration on vessel motions. The mass of the vessel and liquid are fixed, and the tank length L is increased from 0.25 to 3.5. Correspondingly,

the liquid depth H decreases from 2.0 to 0.14. It is assumed that the liquid could never spill out or impact the tank roof. The initial free-surface deformation is as in Mode-1 with $A=0.1$. Fig. 9.9 gives the free-surface elevation histories along the right tank wall of different tanks. It shows that sloshing waves in different tanks generally have similar amplitudes, especially for deep-liquid tanks ($H>0.5$). Dominant oscillation frequencies of the free-surface elevation are compared with those in fixed vessels, as shown in Fig. 9.10. The sloshing frequency in the free vessel is always higher than that in the fixed one.

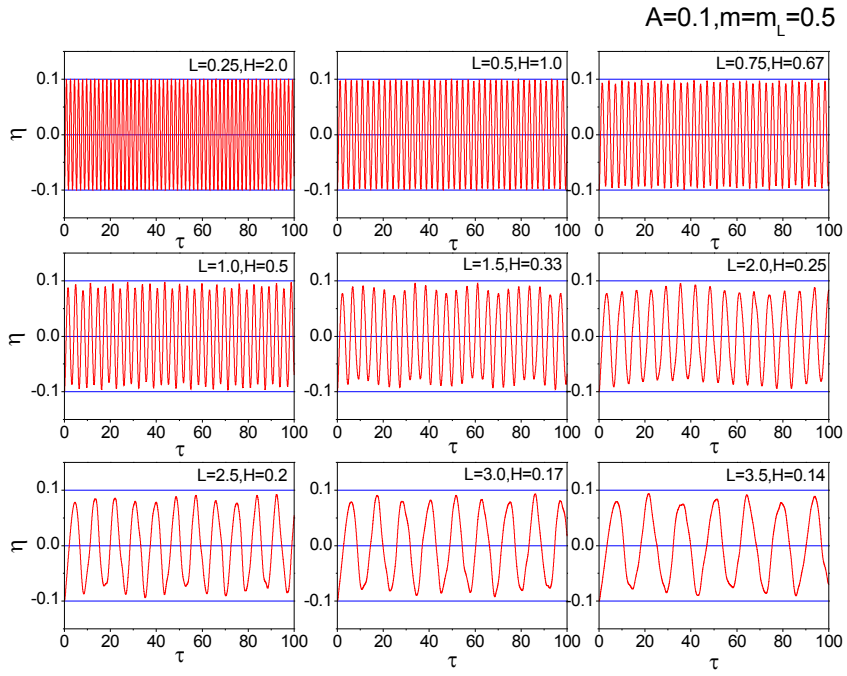

Fig. 9.9 Effect of tank configuration on wave elevation history in single-tank vessel, with initial free-surface deformation of Mode-1

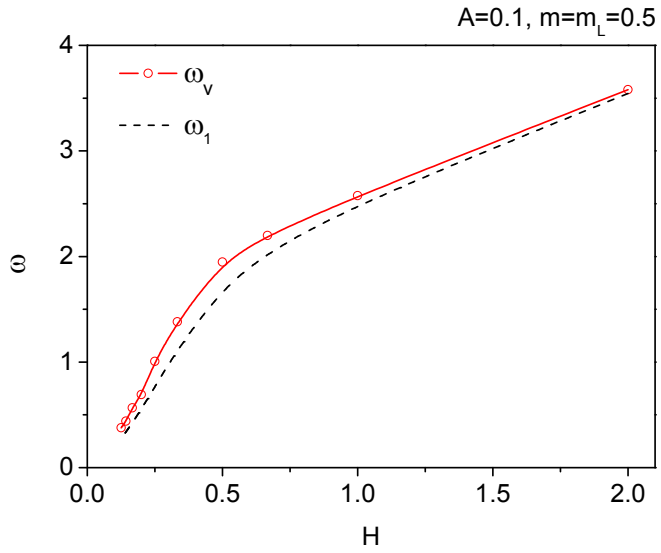

Fig. 9.10 Effect of tank configuration on oscillation frequency of single-tank vessel, with initial free-surface deformation of Mode-1

The vessel motion histories are shown in Fig. 9.11. It is clear that the motion amplitude increases greatly as the liquid gets shallower. Eq. (9.29) can be used to explain this. The analytical expression of the vessel displacement amplitude for this case could be approximated as

$$A_c = \frac{\rho g}{\left(m+m_L\right)} B_j^1 \overline{\zeta}_j^{\,1} = \frac{\rho g}{\left(m+m_L\right)} B_j^1 A \text{, for } \; j=1 . \tag{9.32}$$

Since B_1^1 is of the order $O\left(L^2\right)$ referring to Eqs. (9.16) and (9.21), the vessel with a longer tank (i.e. shallower liquid depth) would have a larger displacement amplitude A_c. From an energy point of view, with the same initial free-surface amplitude, the initial potential energy in the shallower tank has a larger value according to Eq. (9.15). This is confirmed in Fig. 9.12, where the mechanical energy in the tank of depth $H=0.14$ and $H=1.0$ is compared.

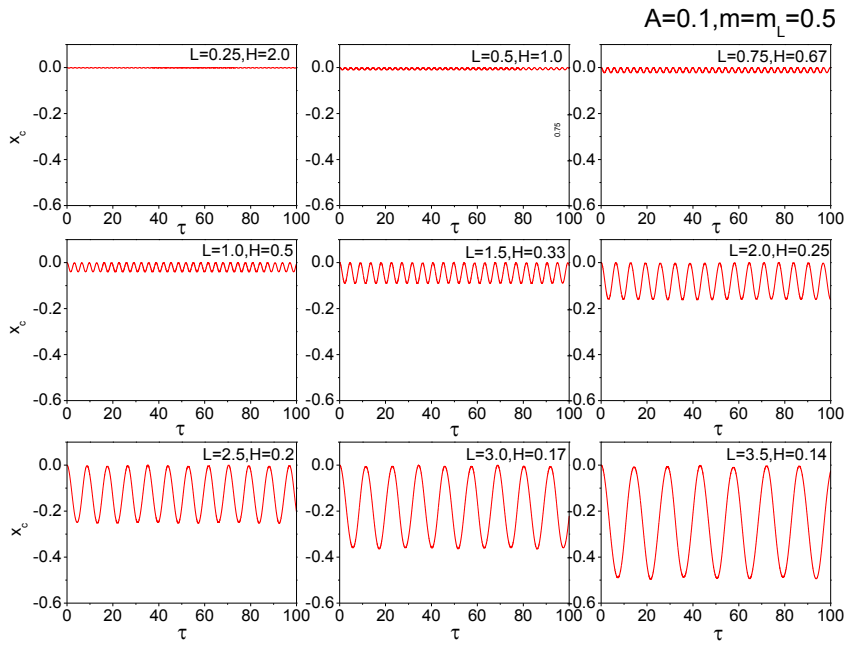

Fig. 9.11 Effect of tank configuration on displacement of single-tank vessel, with initial free-surface deformation of Mode-1

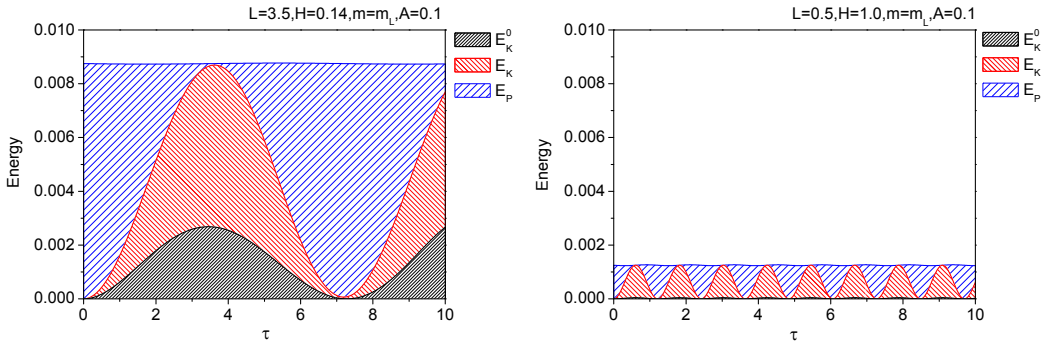

(a) (b)

Fig. 9.12 Energy analysis for single-tank vessel, with initial free-surface deformation of Mode-1, for $m = m_L = 0.5$, $A = 0.1$ and (a) $H = 0.14$; (b) $H = 1.0$

Since the initial potential energy of the fluid could be totally transformed to the kinetic energy of the vessel and fluid, it is interesting to discuss the partition of the vessel's and fluid's kinetic energy after this transformation. Fig. 9.13 shows the percentage of the fluid's and vessel's kinetic energy. It is observed that a major proportion of the initial potential energy is transformed to the fluid kinetic energy. As the liquid depth decreases, the percentage of

the vessel's kinetic energy grows. In other words, even with the same amount of potential energy input, the vessel with a longer tank (i.e. shallower liquid depth) could also have a larger displacement amplitude. This could be understood with the help of Eq. (9.32). The expression of the initial potential energy of Mode-1 could be derived easily. With the same potential energy input, the wave amplitude A is inversely proportional to the tank length L, while B_1^1 is of order $O\left(L^2\right)$. Thus, the vessel displacement amplitude A_c is proportional to L.

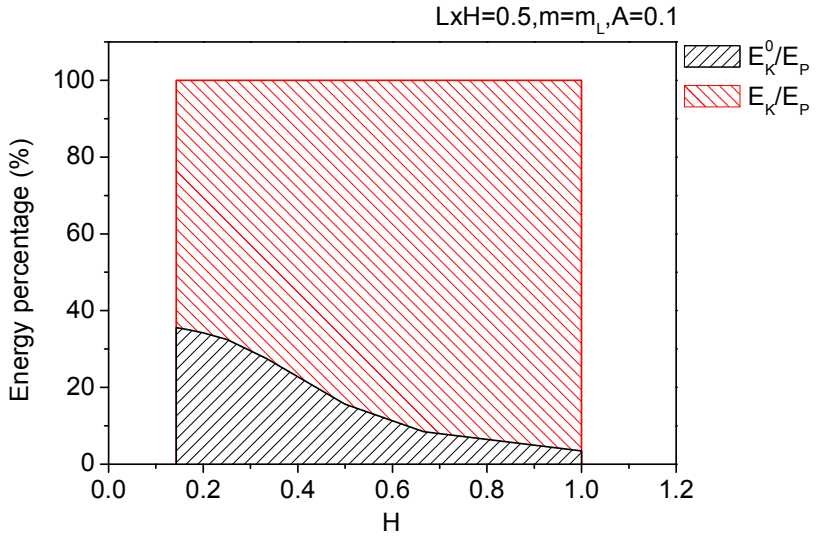

Fig. 9.13 Effect of tank configuration on percentage of maximum kinetic energy for single-tank vessel, with initial free-surface deformation of Mode-1

9.4.4 Effect of initial condition

In the above three subsections, the initial free-surface deformation is of Mode-1, which leads to a nearly harmonic vessel motion. In this subsection, the effects of the initial free-surface profile on the vessel motion are investigated. The vessel with a liquid tank of dimensions $L = B = 1$ and mean liquid depth $H = 0.5$ is considered. The initial free-surface profiles are of different modes with $j = 1$, 3, 5 and 7 in Eq. (9.31). Fig. 9.14 illustrates the initial liquid geometry in terms of the first four modes. The amplitude of the profiles is still fixed at $A = 0.1$, and the vessel mass satisfies $m = m_L$.

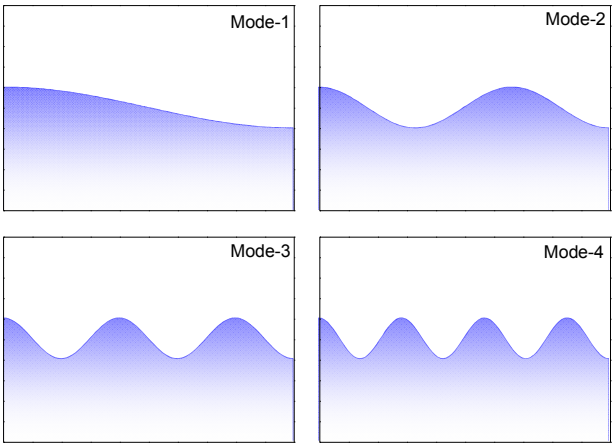

Fig. 9.14 Liquid geometry with free-surface deformation of Mode-1, Mode-2, Mode-3 and Mode-4

Fig. 9.15(a) shows the free-surface elevation histories along the right tank wall. The free-surface amplitudes are of the same order regardless of the modes. Fig. 9.15(b) shows the vessel displacement histories. It is found that the vessel with a higher-mode initial free-surface deformation has a smaller displacement amplitude, even though these vessels have the same initial potential energy input referring to Fig. 9.16. Fig. 9.16 also indicates that the vessel of Mode-1 has the largest kinetic energy, compared with higher-order cases. This can be explained using Eq. (9.32) as that, the value of B_j^1 decreases as j grows, leading to the reduction of the displacement amplitude. Alternatively from a physical point of view, during the leftward motion, the vessel of Mode-1 has the greatest averaged pressure amplitude on the tank wall as well as the longest acting time due to the oscillation period. Thus, according to the theorem of the conservation of momentum, the vessel of Mode-1 could have the largest motion amplitude.

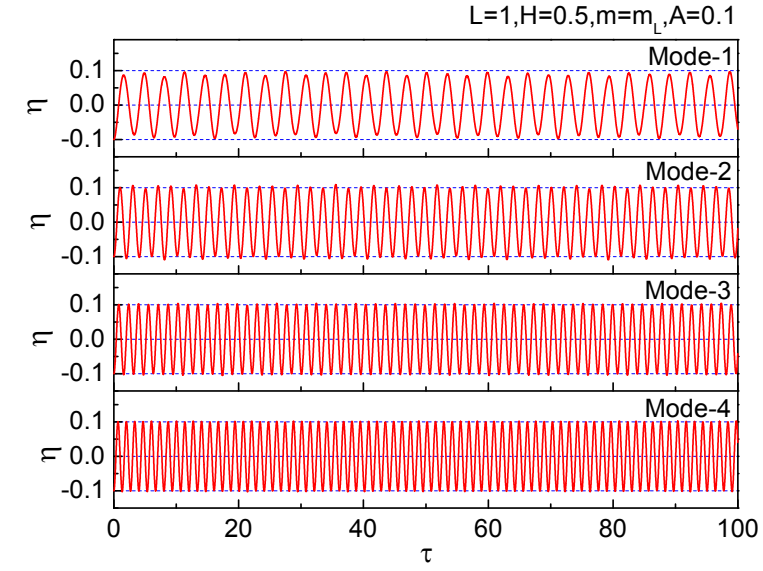

(a)

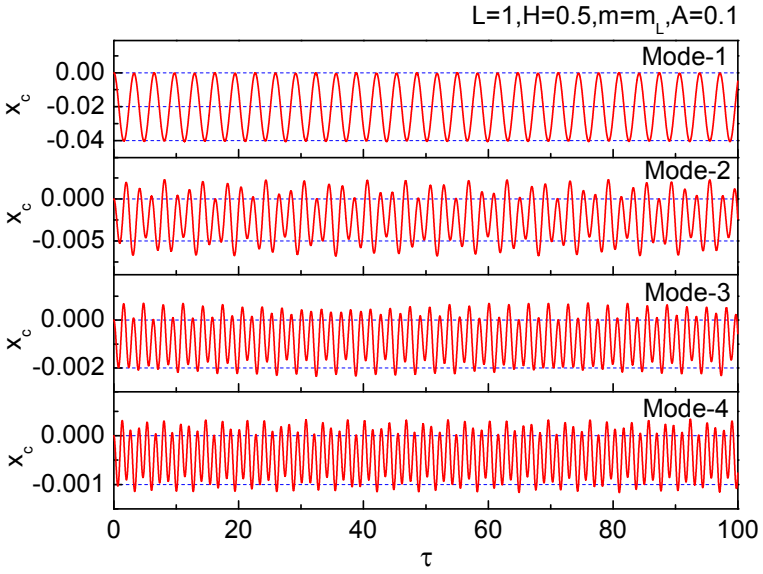

(b)

Fig. 9.15 Effect of initial free-surface deformation on single-tank vessel: (a) wave elevation along the right tank wall; (b) vessel displacement

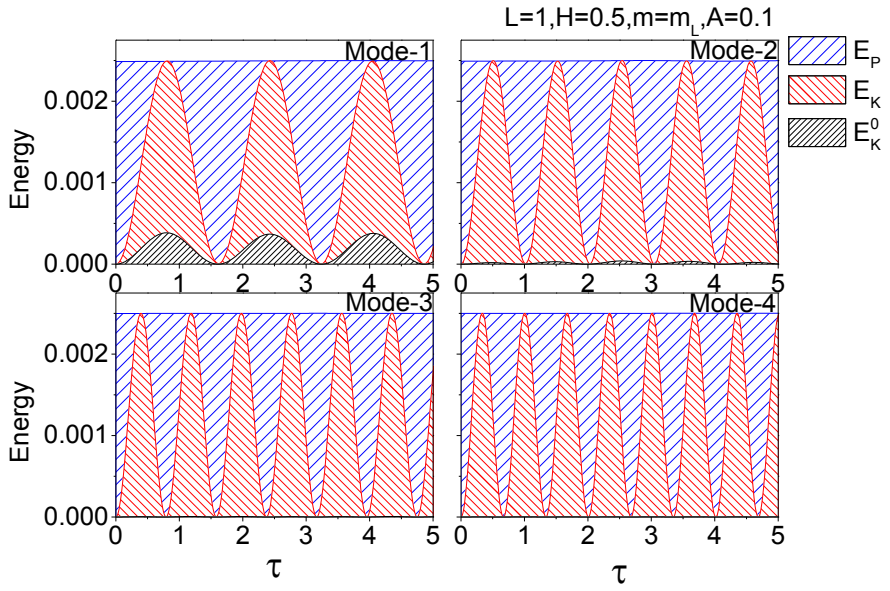

Fig. 9.16 Effect of initial free-surface deformation on energy components of single-tank vessel

It is noticed that vessels of Mode-2, Mode-3 and Mode-4 are undergoing evidently non-harmonic oscillations. The spectra of these displacement histories are shown in Fig. 9.17. Natural frequencies of this coupling system shown in Fig. 9.6(b) are also marked in Fig. 9.17. It is observed that the natural frequency that is closest to the corresponding natural sloshing frequency ω_i of Mode-i dominates the vessel motion. For cases of Mode-2 to 4, the natural frequency ω_{v1} is also visible, because the defined initial free-surface deformation is not the 'true' free-surface mode of this coupling system. The coexistence of multiple frequency components also explains the amplitude modulations in vessel displacement histories in Fig. 9.15.

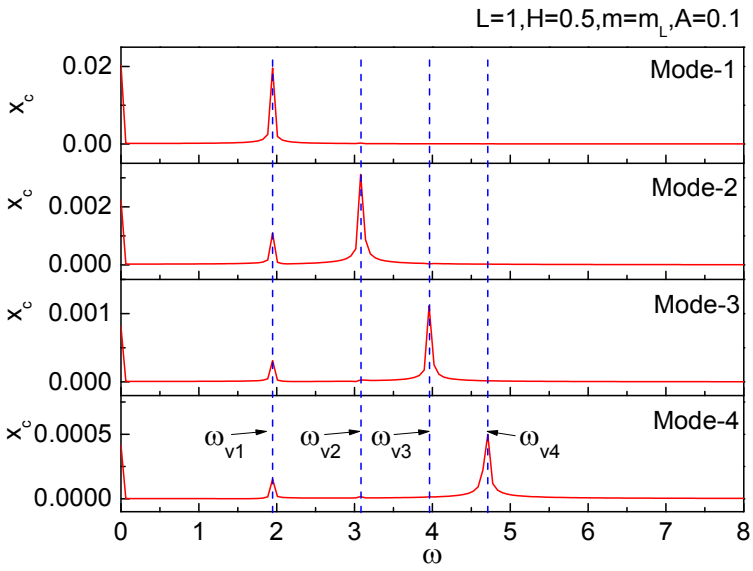

Fig. 9.17 Effect of initial free-surface deformation on spectrum of single-tank vessel oscillation

9.5 Free motion of multiple-tank vessel

In this section, the coupling between the vessel motion and liquid sloshing in multiple rectangular tanks is considered. For convenience sake, tanks with the initial free-surface deformation are called ‘drive tanks’ and the rest tanks are ‘response tanks’. In fact, these definitions may have a practical background. For example, during the offshore loading or unloading operations, LNG tanks with liquids injected or drawn can be taken as drive tanks, while the other tanks are response tanks. In this section, each drive tank has the free-surface deformation of Mode-1 with the amplitude $A = 0.1$.

9.5.1 Effect of number of tanks

In this subsection, the effect of the number of liquid tanks are investigated. All tanks have the same dimensions $L^k = B^k = 1$ and mean liquid depth $H^k = 0.5$. Tank-1 is set as the drive tank, and the vessel mass equals to the overall liquid mass. Fig. 9.18 gives the vessel displacement and wave elevation histories for 2-, 3-, 4- and 9-tank vessels. It is found that vessel motions are still nearly harmonic as the single-tank case. As the tank number increases, the vessel motion amplitude tends to reduce. This is mainly because the vessel with more tanks has a larger mass. The wave elevation histories in all tanks have apparent envelopes as a feature of the

'beating behaviour'. Fig.9.19 also shows the wave elevation history in Tank-1 and that in the rest of the tanks. The envelopes of these elevation histories are highlighted. The vessels with 2, 3, 4, 5, 7 and 9 sloshing tanks are considered, respectively. Tank-1 is the only drive tank, with an initial free-surface deformation. The rest of the tanks are response tanks. It is found that all envelopes have the same period. The maximum envelope amplitude in Tank-1 of all vessels is the same. The envelope in response tanks is half-period phase delayed compared with that in Tank-1. As the number of tanks increases, the variation of the envelope curve in Tank-1 becomes gentler, and the envelope amplitude in the rest tanks decreases. Fig. 9.20 shows several typical free-surface profiles in the 2-tank vessel within the first two periods for an illustration purpose.

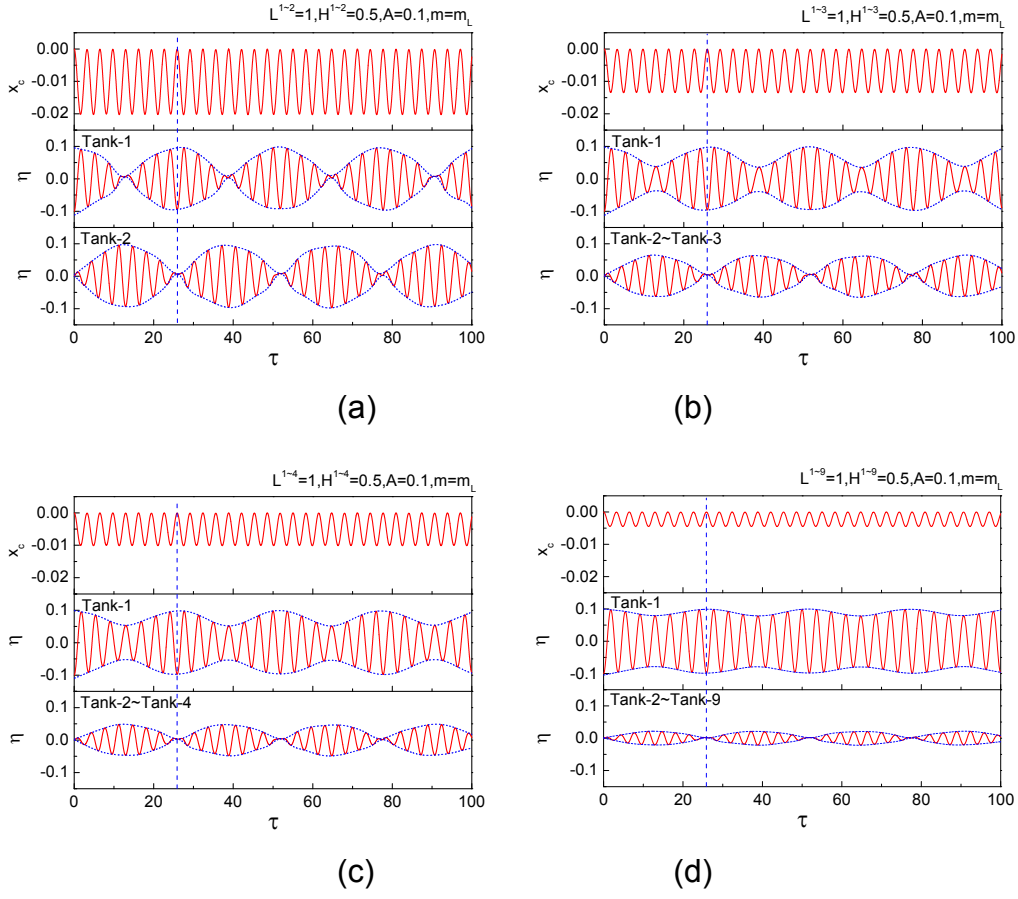

Fig. 9.18 Displacement of multiple-tank vessel and wave elevation along the right tank wall, with initial free-surface deformation of Mode-1 in Tank-1: (a) 2-tank vessel; (b) 3-tank vessel; (c) 4-tank vessel; (d) 9-tank vessel

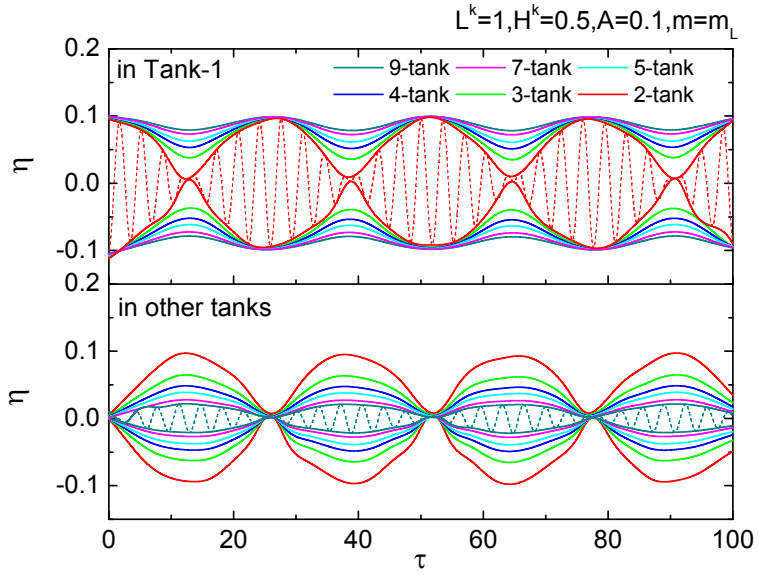

Fig. 9.19 Effect of tank number on wave elevation envelopes in multiple-tank vessel, with initial free-surface deformation of Mode-1 in Tank-1

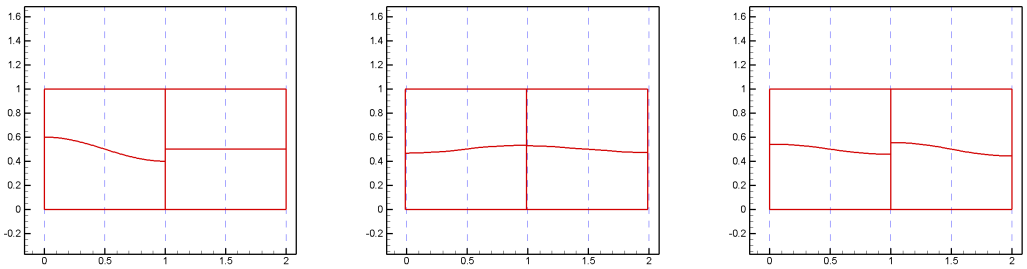

(a) (b) (c)

Fig. 9.20 Position and free-surface profiles of 2-tank vessel, with initial free-surface deformation of Mode-1 in Tank-1 at: (a) $\tau = 0$; (b) $\tau = 2.4$; (c) $\tau = 6.4$

It is known that the envelope suggests that more than one wave components coexist in the fluid system. In Fig. 9.21, the FFT is performed on the time history curves of Fig. 9.18. The frequency ω_v in Fig. 9.21 indicates the natural frequency of the oscillation system, whose value can be obtained from the diagram of $\det\left[M(\omega)\right]$ in Fig. 9.22. It can be seen that, in all cases, the vessel oscillates at the same frequency ω_v. From the diagram of $\det\left[M(\omega)\right]$ in Fig. 9.22, it can also be confirmed that ω_v is a natural frequency of the coupling system. Thus, assuming that all tanks have the

same dimensions and the mass ratio between the liquid and vessel remains the same, the value of ω_v is independent of the number of tanks. However, the wave elevation in all tanks is dominated by both the natural sloshing frequency ω_1 and vessel motion frequency ω_v. The period of the envelope is determined by the period difference of two wave components. Also, in Tank-1, the amplitude of the wave component at ω_1 increases as the tank number grows. In the response tanks, two wave components have similar amplitudes.

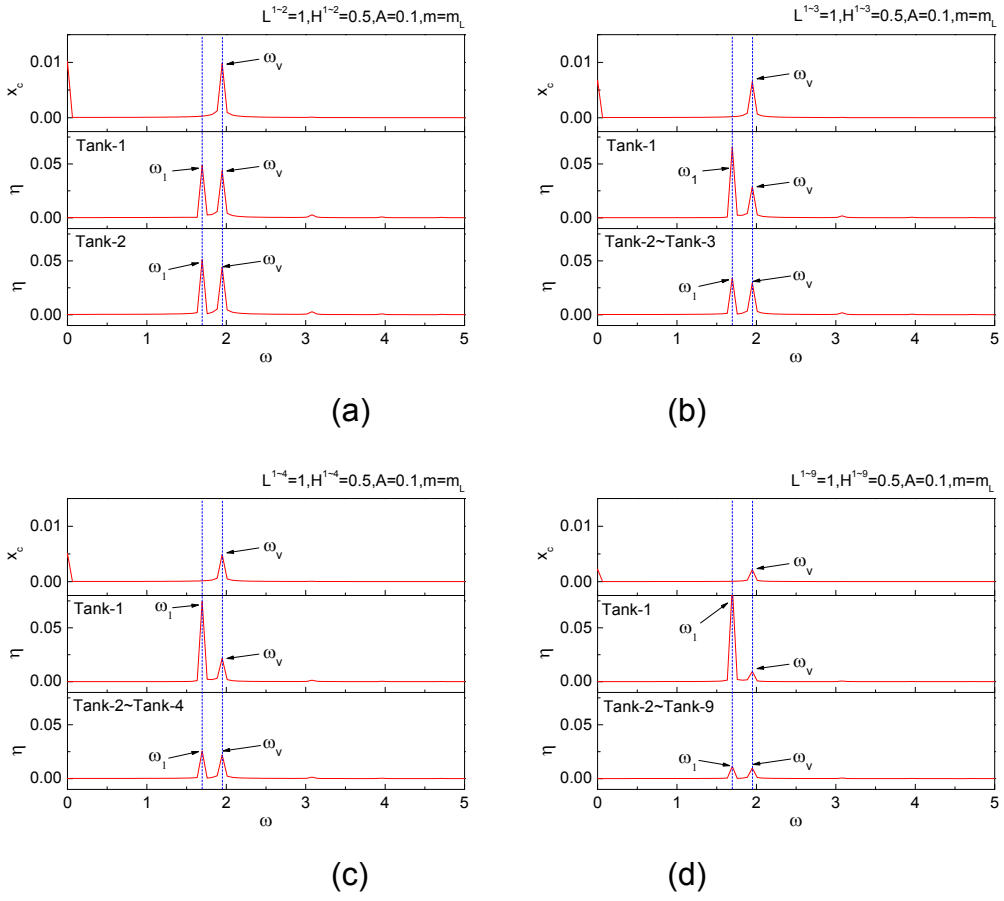

Fig. 9.21 Spectrum of displacement of multiple-tank vessel and wave elevation in tanks, with initial free-surface deformation of Mode-1 in Tank-1: (a) 2-tank vessel; (b) 3-tank vessel; (c) 4-tank vessel; (d) 9-tank vessel

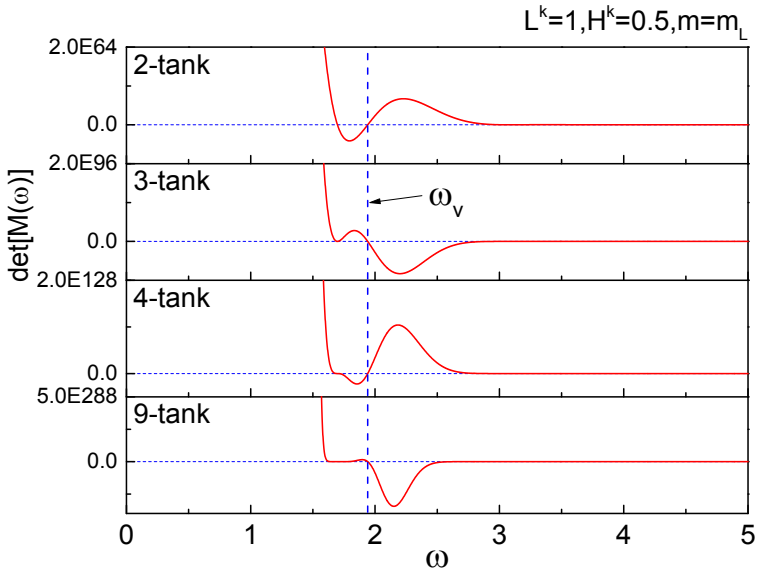

Fig. 9.22 Diagram of $\det\left[M\left(\omega\right)\right]$ of multiple-tank vessel

Fig. 9.23 further gives the time history of liquids' mechanical energy in tanks. The mechanical energy shown in Fig.9.23 is a summation of the kinetic and potential energy of the fluids. According to Fig.9.21, the history of the mechanical energy should contain two frequencies, the natural sloshing frequency and vessel oscillation frequency. Thus, the histories of the mechanical energy in Fig. 9.23 are no longer harmonic. For the 2-tank vessel, the mechanical energy in Tank-1 could totally transfer to Tank-2. This explains the observation in Fig. 9.18(a) that the maximum wave amplitudes in two tanks are the same. However, for the vessel with more than two tanks, the mechanical energy in Tank-1 could not reach zero. In other words, the mechanical energy in Tank-1 could not totally transfer to the rest of the tanks. Fig. 9.24 gives the maximum percentage of the mechanical energy that could transfer out of Tank-1. It is found that, for the vessel with more tanks, the mechanical energy is less likely to transfer out of Tank-1. Thus, even for the vessel with identical liquid tanks, the initial input of the mechanical energy does not have to distribute equally in all tanks.

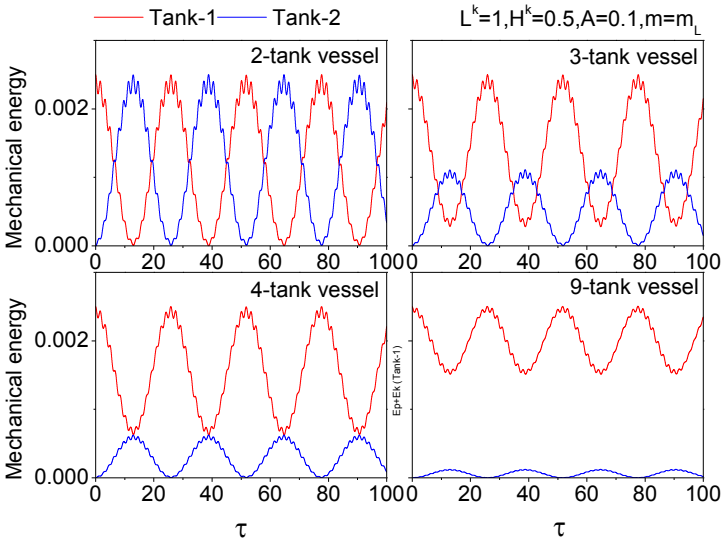

Fig. 9.23 Mechanical energy of liquid in Tank-1 and Tank-2 of multiple-tank vessel, with initial free-surface deformation of Mode-1 in Tank-1

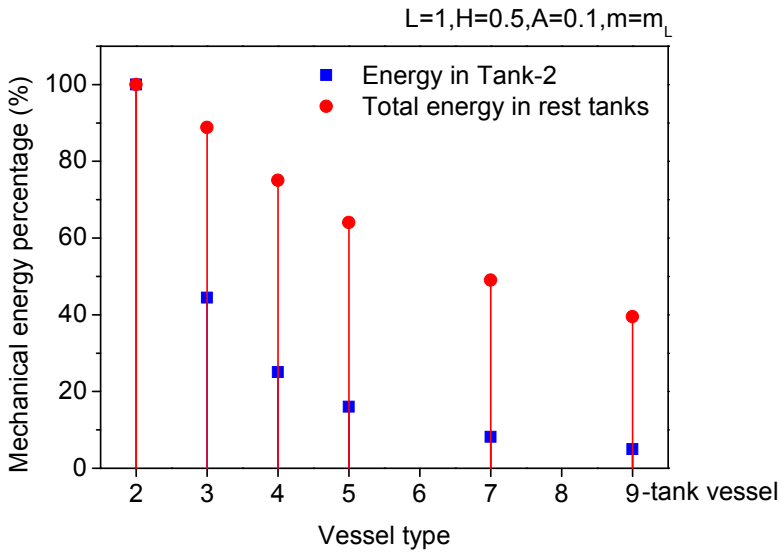

Fig. 9.24 Maximum mechanical energy of liquid in response tanks of multiple-tank vessel, with initial free-surface deformation of Mode-1 in Tank-1

9.5.2 Effect of vessel mass

Fig. 9.23 has shown that the mechanical energy in Tank-1 of the 2-tank vessel could transfer totally to Tank-2. It is necessary to investigate whether this property is affected by the vessel mass. Fig. 9.25 shows four different cases when the vessel mass changes from $m = 0.25m_L$ to $m = 20m_L$. In all cases, the vessel oscillates nearly harmonically. Wave elevation histories in both tanks have shown evident beating behaviour. For different vessel

masses, the wave elevation envelopes in both tanks have the same maximum amplitude but different periods. Generally, the envelope period for a heavier vessel is larger. The fluid's mechanical energy in two tanks is compared in Fig. 9.26. For the vessel with two tanks that have the same dimensions and mean liquid depth, there could be an instant when the mechanical energy in one tank totally transfers to the other.

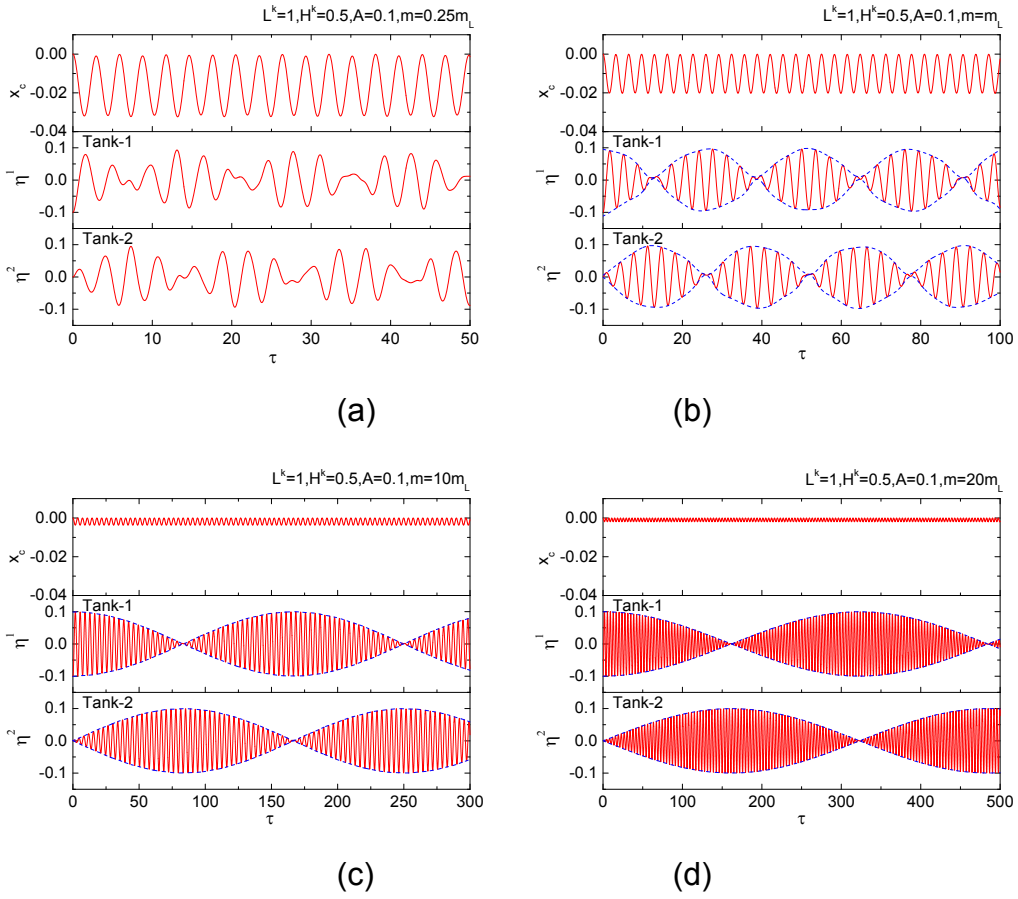

Fig. 9.25 Effect of vessel mass on displacement of 2-tank vessel and wave elevation in tanks, with initial free-surface deformation of Mode-1: (a) $m = 0.25m_L$; (b) $m = m_L$; (c) $m = 10m_L$; (d) $m = 20m_L$

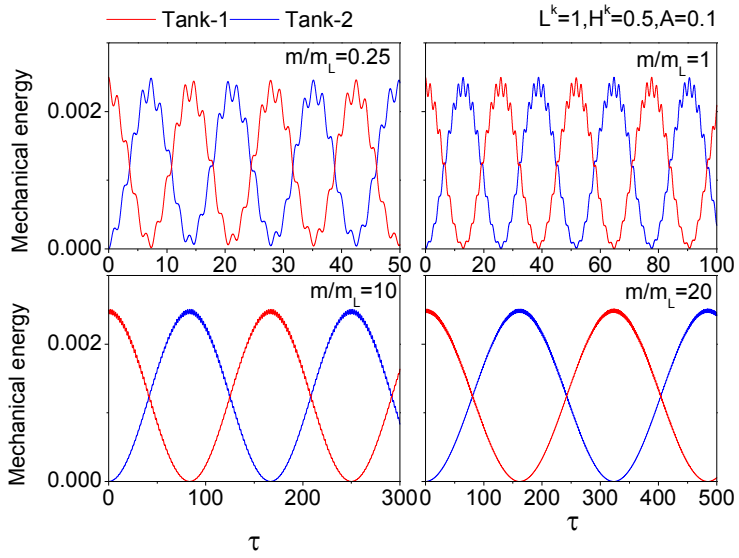

Fig. 9.26 Effect of vessel mass on mechanical energy of liquid in 2-tank vessel, with initial free-surface deformation of Mode-1 in Tank-1

Vessels with more than two tanks are further concerned. Frequencies and amplitudes of the vessel motion are shown in Fig. 9.27. For vessels with tanks that have the same dimension and mean liquid depth, if the mass ratio between the vessel and overall liquid is fixed, the vessel motion frequency is independent of the number of tanks. Meanwhile, if the motion amplitude of the single-tank vessel is A_c, the motion amplitude of the vessel with N tanks is A_c/N. Thus, for this linear problem, as the total mass of the vessel and liquid becomes N times larger, the motion amplitude of the vessel becomes N times smaller.

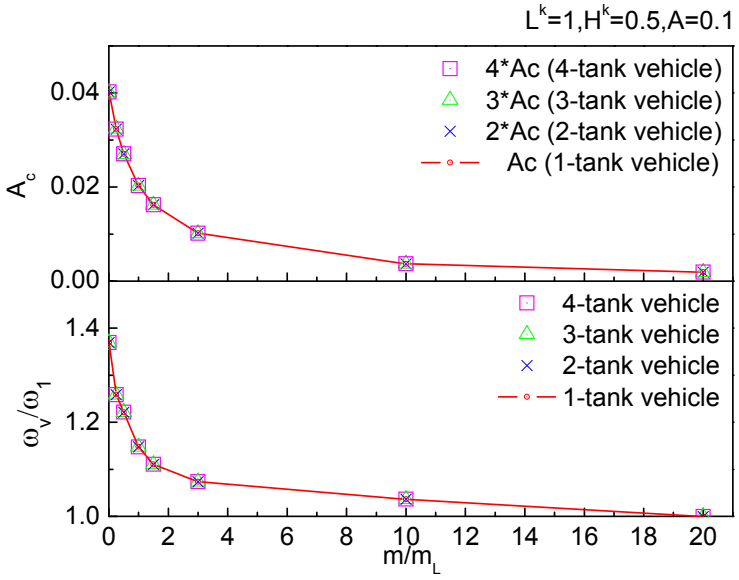

Fig. 9.27 Effect of vessel mass on oscillation amplitude and frequency of multiple-tank vessel, with initial free-surface deformation of Mode-1 in Tank-1

9.5.3 Effect of number of drive tanks

This subsection concerns the vessel with a different number of drive tanks. Fig. 9.28 shows histories of the vessel displacement and wave elevations in all tanks for the 4-tank vessel with 1, 2 or 3 drive tanks. It is found that the vessel displacement amplitude increases as the number of drive tanks increases. This is to be expected because more drive tanks provide larger initial potential energy input. These vessel oscillations have the same frequencies, which is not affected by the number of drive tanks. In different tanks, wave elevation histories show the beating behaviour. The maximum wave elevation in drive tanks is the same. But in the response tanks, the maximum wave amplitude grows as the number of drive tanks increases. Here, N_{dri} and N_{res} are used to denote the number of drive and response tanks, respectively. It is found that, for the case of $N_{dri} < N_{res}$, the maximum wave amplitude in response tanks is smaller than that in drive tanks. On the other hand, for the case of $N_{dri} > N_{res}$, the maximum wave amplitude in response tanks is greater than that in drive tanks. A special situation is when $N_{dri} = N_{res}$, where the maximum wave amplitudes in all tanks are the same.

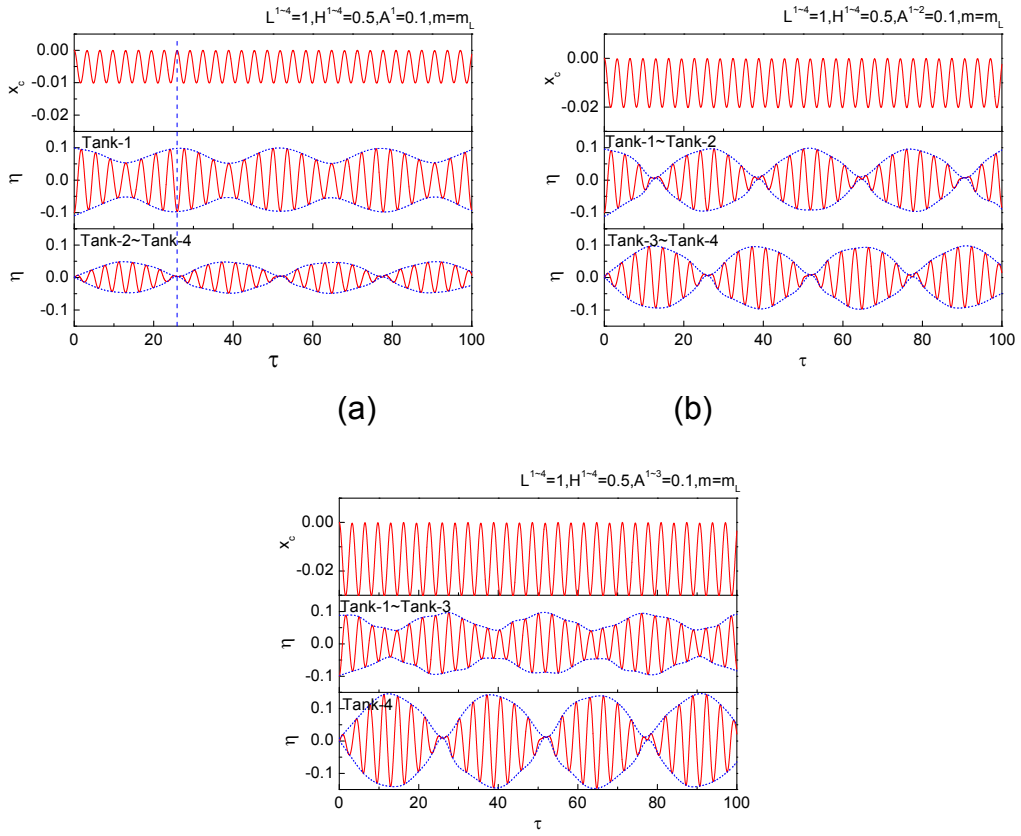

Fig. 9.28 Effect of number of drive tanks on displacement of 4-tank vessel and wave elevation in tanks, with initial free-surface deformation of Mode-1: (a) $A^{1}=0.1$; (b) $A^{1\sim2}=0.1$; (c) $A^{1\sim3}=0.1$

Histories of the fluids' mechanical energy in each tank are shown in Fig. 9.29. It is found that when the vessel has fewer drive tanks, the maximum fluid mechanical energy in any response tank is smaller than that in each drive tank. As the number of drive tanks becomes larger, the fluid energy in each response tank would increase. For a vessel with more drive tanks, the fluid energy in a response tank could exceed the maximum mechanical energy in a drive tank. This is linked to the vessel motion amplitudes. For the special case of $N_{dri}=N_{res}$, the mechanical energy in drive and response tanks would have the same maximum amplitude.

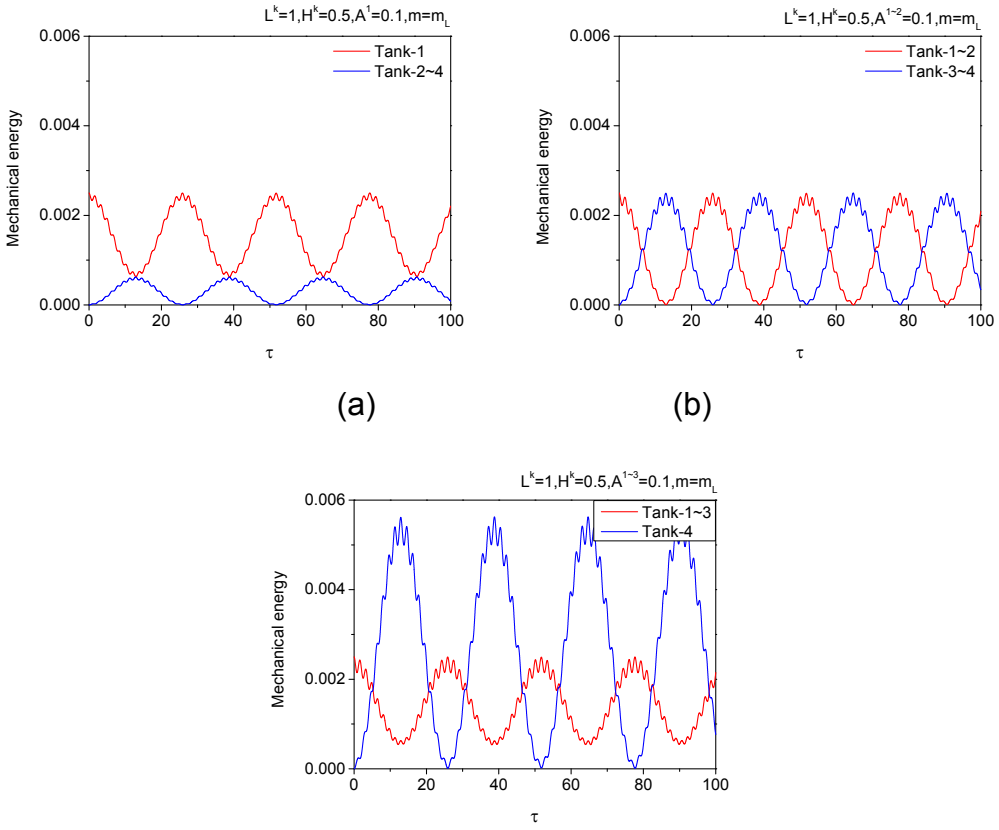

Fig. 9.29 Effect of number of drive tanks on mechanical energy of liquid in 4-tank vessel, with initial free-surface deformation of Mode-1: (a) $A^{1}=0.1$; (b) $A^{1\sim 2}=0.1$; (c) $A^{1\sim 3}=0.1$

9.5.4 Effect of tank configuration

In this subsection, the vessel has tanks of different length. The vessel mass is equal to the total liquid mass. The liquid in all tanks has an average depth $H=0.5$, so that the tank configuration is only determined by the tank length. Firstly consider the 2-tank vessel. Vary the length of Tank-1 from 0.7 to 1.0, and correspondingly the length of Tank-2 from 1.3 to 1.0. Fig. 9.30 (a) and (b) give the spectra of the vessel displacement histories when the drive tank is set as Tank-1 and Tank-2, respectively. Two frequency components primarily contribute to the vessel oscillations. From the diagram of $\det\left[M(\omega)\right]$ in Fig. 9.31, it is confirmed that both of them are natural frequencies of the coupling system. For Fig. 9.30(a), the natural sloshing frequency ω_1 associated with Mode-1 in Tank-1 is closest to the natural

frequency ω_{v2} of the system, so that the natural mode at ω_{v2} has the maximum amplitude. For Fig. 9.30(b), ω_1 is closest to ω_{v1} as indicated by Fig. 9.21, and the maximum natural mode occurs at ω_{v1}. It is also found that these two dominant frequencies become more dispersed, as the length difference of two tanks increases.

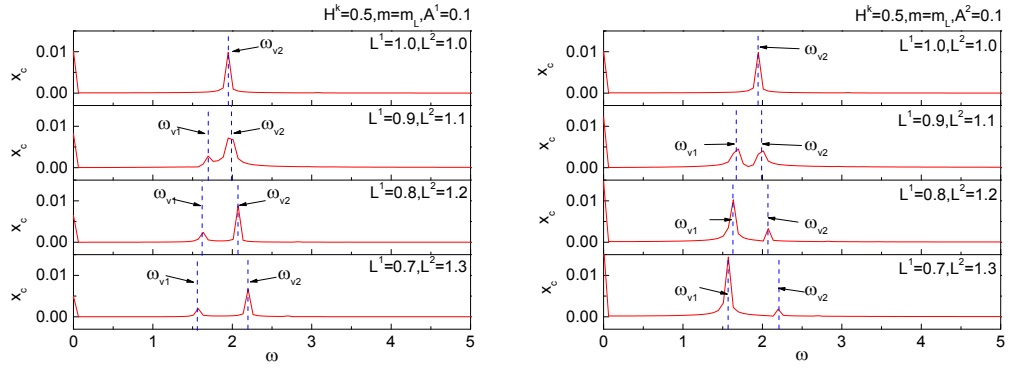

(a) (b)

Fig. 9.30 Effect of tank configuration on spectrum of displacement of 2-tank vessel, with initial free-surface deformation of Mode-1: (a) $A^1 = 0.1$; (b) $A^2 = 0.1$

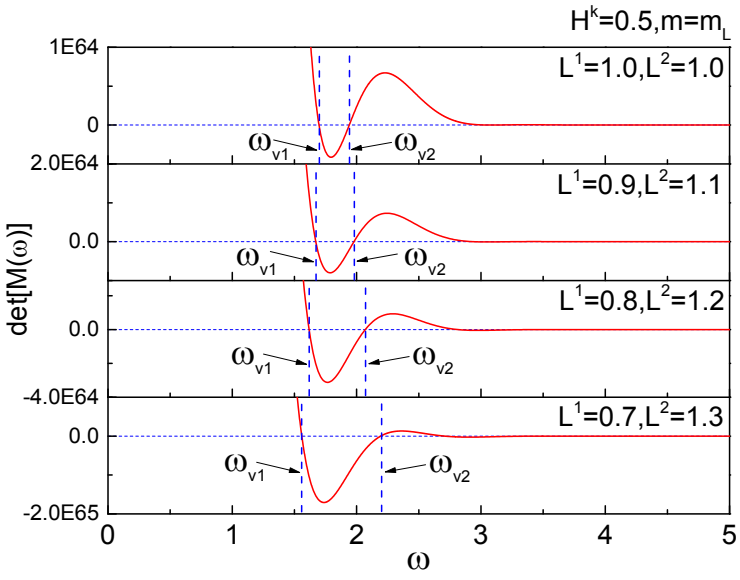

Fig. 9.31 Effect of tank configuration on diagram of $\det\left[M\left(\omega\right)\right]$ of 2-tank vessel

Then, Fig. 9.32 compares the time variation of the fluid mechanical energy in each tank. Sub-figures (a) and (b) illustrate the situation when the

drive tank is Tank-1 and Tank-2, respectively. For both situations, the fluid mechanical energy in one tank is less likely to transfer to the other, as the two tanks become more distinctive. Only when these two tanks are the same, the fluid mechanical energy in one tank could transfer totally to the other. This means that, at an instant, the liquid's mechanical energy must be zero in one tank and reach the maximum value in the other tank. In this situation, the liquid in two tanks should oscillate at the same oscillation frequency, and this can only happen when two tanks are the same.

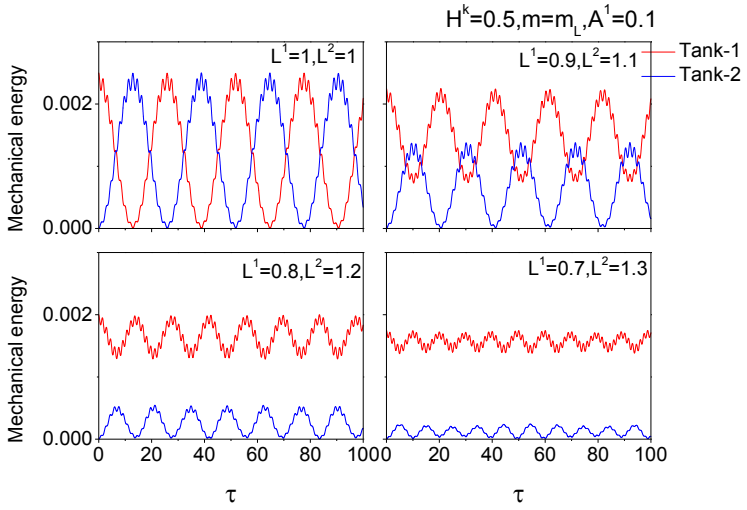

(a)

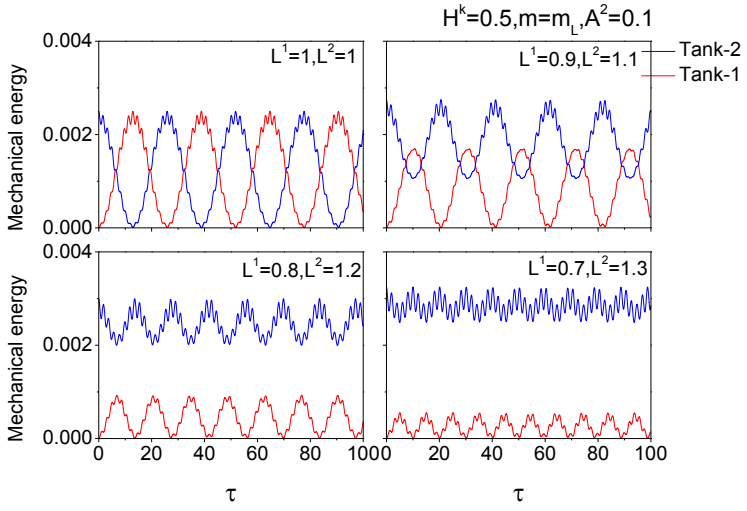

(b)

Fig. 9.32 Effect of tank configuration on mechanical energy of liquid in 2-tank vessel, with initial free-surface deformation of Mode-1: (a) $A^1 = 0.1$; (b) $A^2 = 0.1$

Further, consider a 3-tank vessel. The length of each tank is set as $L^1=0.8$, $L^2=1.0$ and $L^3=1.2$. Fig. 9.33(a) shows the histories of the vessel displacement, when the drive tank is chosen to be Tank-1, Tank-2 and Tank-3, respectively. It is clear that the vessel displacement histories are no longer nearly harmonic. A different drive tank may lead to totally different vessel motions. The spectra of these vessel motion histories are shown in Fig. 9.33(b). It can be seen that the vessel motions are governed by three natural frequencies of the system, referring to the diagram of $\det\left[M(\omega)\right]$ in Fig. 9.33(c). As the drive tank varies from Tank-1 to Tank-3, the natural frequency closest to ω_1 becomes ω_{v3}, ω_{v2} and ω_{v1}, respectively. Correspondingly, the natural mode at ω_{v3}, ω_{v2} and ω_{v1} has the maximum amplitude, respectively.

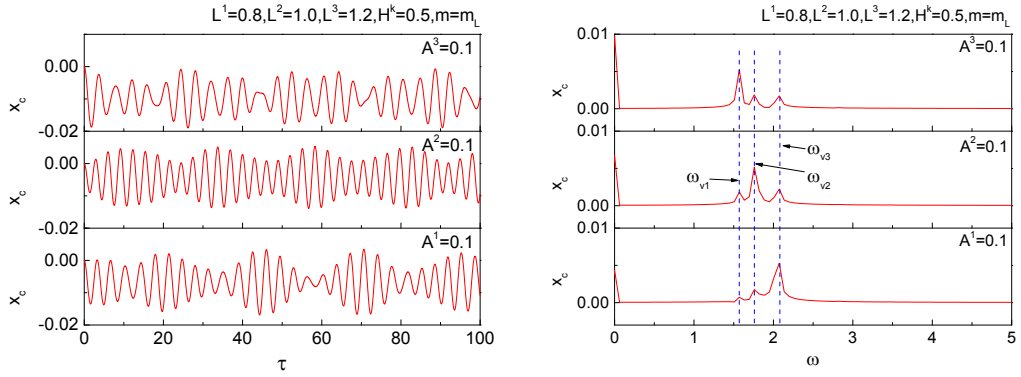

(a) (b)

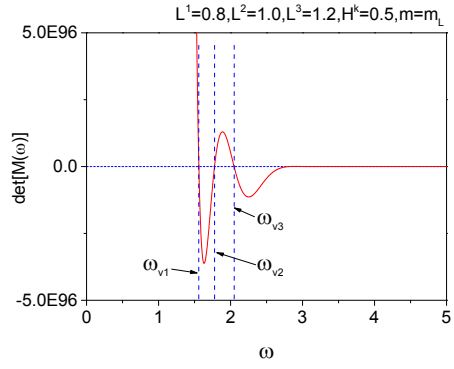

(c)

Fig. 9.33 Effect of tank configuration on displacement of 3-tank vessel, with initial free-surface deformation of Mode-1: (a) vessel displacement; (b) spectrum of vessel displacement; (c) diagram of $\det\left[M(\omega)\right]$

9.6 Conclusions

In this chapter, the coupling between the vessel motion and liquid sloshing in multiple tanks is considered. The vessel could move freely on the horizontal ground and its motion is solely driven by the liquid sloshing in tanks. External disturbance factors (e.g. spring constraint or force field) that might affect oscillation characteristics of the system are not involved. The analytical solution for this coupling problem has been derived based on the potential-flow theory. A method to determine natural frequencies of the coupling system is also given. Then, dynamic properties of the vessel with one or more rectangular tanks are studied systematically. This chapter focuses on the vessel with one degree of freedom.

For the single-tank vessel, effects of the initial free-surface deformation, vessel mass, and tank configuration on the vessel displacement, free-surface elevation, and mechanical energy components of the system have been discussed. When the free surface has an initial deformation of Mode-1, the oscillation frequency of the vessel is always higher than the fundamental natural sloshing frequency in a stationary tank. As the vessel mass grows, both the frequency and amplitude of the vessel motion decrease. For a system with the constant mass ratio between the vessel and liquids, the tank configuration could also affect the oscillation properties. With the same amount of initial potential energy input to the fluid, the vessel with the longer tank tends to have a greater oscillation amplitude. Then, effects of more initial free-surface deformations are investigated. It can be seen that the initial deformation of Mode-1 has the largest influence on the vessel motion.

Then, the vessel with multiple tanks is considered. It is found that even for the vessel with identical liquid tanks, the maximum mechanical energy of the liquid in each tank may not be the same. Only when the drive and response tanks have the same number, the mechanical energy in drive tanks might totally transfer to response ones. For the vessel with different tanks, the fluid mechanical energy in drive tanks is less likely to transfer to response tanks, as the tank configurations become more distinctive. The dominant frequencies of the vessel motion could be predicted accurately by the determinant diagram.

Chapter 10 A motion decoupling method for floating vessel with nonlinear sloshing tanks

10.1 Introduction

As described in Chapter 1, to guarantee the motion safety of an FLNG vessel, two hydrodynamic problems have to be investigated in the design stage. One is the seakeeping problem dealing with the interaction between the floating vessel and external ocean waves, and the other is the sloshing problem related to the free-surface motion in tanks. However, these two hydrodynamic problems are coupled. Because the vessel oscillation due to the excitation of external waves could cause the liquid sloshing in partly filled tanks, while the sloshing dynamics would instantaneously affect the vessel motion and further the external waves in return. The mechanism of this coupling is rather complex.

At present, two groups of numerical approaches have been proposed to investigate the coupling mechanism. The first group is based on the frequency-domain methods. Both the seakeeping and sloshing problems are considered within the linear potential-flow theory. Typical works are Molin (2002), Malenica et al (2003) and Newman (2005), the latter two of which have essentially interpreted the sloshing module of the hydrodynamic software HYDROSTAR and WAMIT, respectively. The frequency-domain methods are generally efficient. However, they have limitations in predicting the effect of near resonance sloshing, due to the stable flow assumption. For example, as the wave excitation frequency ω increases across the lowest natural sloshing frequency ω_n, the principal sloshing-induced added mass would shift from $+\infty$ to $-\infty$ due to the singularity. As a result, the response amplitude operator (RAO, the amplitude ratio of the vessel motion and incident waves) would be zero at $\omega = \omega_n$ and infinity when ω is slightly higher than ω_n. This inaccurate prediction has been confirmed in experiments (e.g. Rognebakke and Faltinsen 2001). To avoid infinite added-mass coefficients, Malenica et al (2003) have introduced an artificial

damping on the tank boundary, although damping coefficients still require experiments for accurate estimation and calibration.

The second group is based on the time-domain methods, with nonlinearities included in the sloshing problem. The nonlinear sloshing could be simulated by a wide range of numerical methods, such as the finite difference method (FDM) for Navier-Stokes (NS) equations in Kim (2002), Nam et al (2006), Kim et al (2007), Lee et al (2007), Lee (2008) and Wang and Arai (2011), moving particle simulation (MPS) method in Hashimoto and Sueyoshi (2010), finite volume method (FVM) based on OpenFOAM in Li et al (2012) and Jiang et al (2015), modal expansion method in Rognebakke and Faltinsen (2001), finite element method (FEM) for potential flows in Mitra et al (2012), and boundary element method (BEM) in Huang et al (2012) and Zhao et al (2014). The seakeeping problem is usually solved by potential-flow solvers based on the impulse-response function (IRF, e.g. in Zhao et al 2014), transient Green's function (e.g. in Huang et al 2012) or time-domain Rankine panel method (e.g. in Kim 2002), or purely NS-equation solvers (e.g. in Yang et al 2006). The time-domain methods may overcome the major disadvantages of the frequency-domain methods, and provide more reliable results. However, time-domain simulations usually require a much greater amount of CPU time as a cost.

For time-domain methods, a great proportion of the CPU consumption is on dealing with the coupling between the sloshing and seakeeping problems. To be specific, at each time step, the calculation of sloshing-induced forces always requires the knowledge of the vessel's acceleration at that instant, either for the NS-equation (e.g. Celebi and Akyildiz 2002) or potential-flow solvers (e.g. Zhao et al 2014). Meanwhile, according to the Newton's Second Law, the vessel's acceleration is dependent on the knowledge of sloshing forces at the same time. An iteration procedure is usually used to determine both acceleration and forces. In practice, the vessel's acceleration may be firstly calculated from the motion equations with approximated sloshing forces. Then, the obtained vessel's acceleration is used in the sloshing module to update the sloshing forces. Once again, the updated sloshing forces are substituted in the motion equations for the acceleration calculation. At any

time step, this iteration lasts for a number of times until the force has reached convergence. When the iteration number is large, the iteration procedure would be rather time-consuming. Besides, the iteration procedure has other limitations. For example, (1) the iteration number to achieve the convergence is uncertain at a single time step; (2) if a maximum iteration number is pre-set, the truncation error might exist; and (3) the convergence of iterations might not be guaranteed, especially for the vessel with multiple tanks.

This chapter would derive an alternative method to decouple the seakeeping and sloshing problems for the time-domain simulation of the floating vessel with nonlinear sloshing tanks. The method could be considered as an extension of the modal decomposition method for floating vessel simulations. Using this method, the exact vessel's acceleration at any instant could be calculated explicitly in one step without iterations, which could greatly reduce the CPU consumption. Meanwhile, other limitations of the iteration procedure (e.g. the uncertain iteration number, truncation error and numerical convergence) could be avoided.

10.2 Problem description

Consider a floating vessel with N_s liquid tanks. There exist (N_s+1) fluid domains V^k $(k=0\sim N_S)$. The external fluid domain V^0 is enclosed by the free surface S_F^0, wetted vessel surface S_B^0, seabed S_D and a far enough open boundary S_C. In Tank-k, the fluid domain, free surface and wetted tank surface are denoted by V^k, S_F^k and S_B^k, respectively. Hereafter, the superscript k would be used to indicate a quantity from the k-th fluid domain. The symbols about the fluids' domains and boundaries are described in Fig. 10.1. For neatness, the earth-fixed coordinate system $O_o-x_oy_oz_o$ and body-fixed system $O-xyz$ that are already illustrated in Fig. 2.1 are not shown in Fig.10.1. The origin O is located at the mass centre of the vessel. Initially, when the vessel is stationary, these two coordinate systems are coincident with each other, with x-axis pointing horizontally to the vessel's stern and z-axis vertically upward.

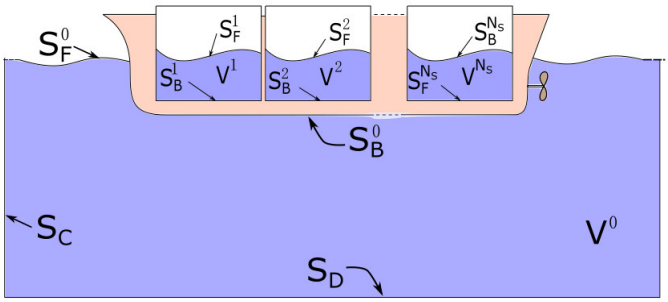

Fig. 10.1 Sketch of floating vessel with liquid tanks

Assume that the vessel is rigid with 6 degrees of freedom (DoFs). Its transversal and rotational motions can be determined by the Newton's equation in $O_o - x_o y_o z_o$ and Euler's equation in $O - xyz$, respectively, i.e.

$$[M]\boldsymbol{a} + \begin{Bmatrix} 0 \\ 0 \\ 0 \\ \boldsymbol{\Omega} \times \left([I] \boldsymbol{\Omega} \right) \end{Bmatrix} = \begin{Bmatrix} \mathbf{F}_d \\ \mathbf{M}_d \end{Bmatrix} + \begin{Bmatrix} \mathbf{F}_s \\ \mathbf{M}_s \end{Bmatrix} + \begin{Bmatrix} \mathbf{F}_e \\ \mathbf{M}_e \end{Bmatrix}, \text{ with}$$

$$[M] = \begin{bmatrix} m & & & & & \\ & m & & 0 & & \\ & & m & & & \\ & & & I_{xx} & I_{xy} & I_{xz} \\ & 0 & & I_{yx} & I_{yy} & I_{yz} \\ & & & I_{zx} & I_{zy} & I_{zz} \end{bmatrix} \text{ and } \boldsymbol{a} = \left\{ \dot{\mathbf{v}}_c, \dot{\boldsymbol{\Omega}} \right\}^T \tag{10.1}$$

where m is the vessel mass, I_{xx} to I_{zz} are moments of the inertia, $\dot{\mathbf{v}}_c = \{a_1, a_2, a_3\} = \{\dot{v}_1, \dot{v}_2, \dot{v}_3\} = \{\ddot{x}_1, \ddot{x}_2, \ddot{x}_3\}$ is the acceleration of the mass centre, $\dot{\boldsymbol{\Omega}} = \{a_4, a_5, a_6\} = \{\dot{v}_4, \dot{v}_5, \dot{v}_6\}$ is the angular acceleration of the vessel, $\{\mathbf{F}_d, \mathbf{M}_d\} = \{F_1, F_2, F_3, F_4, F_5, F_6\}$ denotes the hydrodynamic force/moment from V^0, $\{\mathbf{F}_s, \mathbf{M}_s\}$ is the resultant force/moment due to sloshing, and $\{\mathbf{F}_e, \mathbf{M}_e\}$ represents the resultant force/moment due to gravity, mooring system and so on. The subscript $1 \sim 3$ denotes that the variable is represented in $O_o - x_o y_o z_o$ while the subscript $4 \sim 6$ denotes the expression in $O - xyz$.

The $\{\mathbf{F}_d, \mathbf{M}_d\}$ can be calculated by integrating the pressure over the wetted vessel surface S_B^0. The pressure could be expressed by the Bernoulli's equation within the potential-flow theory. The following expression

could be obtained

$$\begin{Bmatrix} \mathbf{F}_d \\ \mathbf{M}_d \end{Bmatrix} = -\rho^0 \iint_{S_B^0} \left(\frac{\partial \varphi}{\partial t} + \frac{1}{2} \nabla_o \varphi \nabla_o \varphi + g z_o \right) \begin{Bmatrix} \mathbf{n} \\ \mathbf{r} \times \mathbf{n} \end{Bmatrix} dS \tag{10.2}$$

where $\varphi(x, y, z, t)$ is the velocity potential, $\mathbf{r} = \{x, y, z\}$ is the position vector on S_B^0, $\mathbf{n} = \{n_1, n_2, n_3\}$ is the unit normal vector pointing outward from the fluid, and $\mathbf{r} \times \mathbf{n} = \{n_4, n_5, n_6\}$. The velocity potential φ could be determined from the following boundary value problem

$$\nabla_o^2 \varphi = 0 \text{, in } V^0 \tag{10.3}$$

$$\frac{\partial \varphi}{\partial n} = \mathbf{v}_c \cdot \mathbf{n} + \boldsymbol{\Omega} \cdot (\mathbf{r} \times \mathbf{n}) = \sum_{i=1}^{6} v_i \cdot n_i \text{, on } S_B^0 \tag{10.4}$$

$$\frac{\partial \eta_o}{\partial t} = \frac{\partial \varphi}{\partial z_o} - \frac{\partial \varphi}{\partial x_o} \frac{\partial \eta_o}{\partial x_o} - \frac{\partial \varphi}{\partial y_o} \frac{\partial \eta_o}{\partial y_o} \text{, on } S_F^0 \tag{10.5}$$

$$\frac{\partial \varphi}{\partial t} = -g \eta_o - \frac{1}{2} \nabla_o \varphi \cdot \nabla_o \varphi \text{, on } S_F^0 \tag{10.6}$$

$$\frac{\partial \varphi}{\partial n} = \frac{\partial \varphi_I}{\partial n} \text{, on } S_C \tag{10.7}$$

$$\frac{\partial \varphi}{\partial n} = 0 \text{, on } S_D \tag{10.8}$$

where $\eta_o(x_o, y_o, t)$ denotes the free-surface elevation and terms with the subscript I denote variables related to incoming waves. Once the velocity potential and its normal derivative are solved, the gradient of the velocity potential can be obtained. Then, the only unknown on the right-hand side of Eq. (10.2) is the time derivative $\partial \varphi / \partial t$ or φ_t. The φ_t could be obtained by solving the boundary value problem (Wu and Hu 2004)

$$\nabla_o^2 \varphi_t = 0 \text{, in } V^0 \tag{10.9}$$

$$\varphi_t = -g z_o - \frac{1}{2} \nabla_o \varphi \nabla_o \varphi \text{, on } S_F^0 \tag{10.10}$$

$$\frac{\partial \varphi_t}{\partial n} = \sum_{i=1}^{6} a_i \cdot n_i - \mathbf{v}_c \cdot \frac{\partial \nabla_o \varphi}{\partial n} + \Omega \cdot \frac{\partial}{\partial n}[\mathbf{r} \times (\mathbf{v}_c - \nabla_o \varphi)], \text{ on } S_B^0 \tag{10.11}$$

$$\frac{\partial \varphi_t}{\partial n} = \frac{\partial^2 \varphi_I}{\partial n \partial t}, \text{ on } S_C \tag{10.12}$$

$$\frac{\partial \varphi_t}{\partial n} = 0, \text{ on } S_D \tag{10.13}$$

For the sloshing problem in Tank-k, it is convenient to describe the boundary value problem of the velocity potential in the body-fixed system using Eqs. (2.29)-(2.33). The boundary value problem for φ_t is determined by Eqs. (10.9)-(10.11) after replacing V^0, S_F^0 and S_B^0 with V^k, S_F^k and S_B^k, respectively.

From Eq. (10.11), it is clear that the solution of φ_t is determined by the acceleration a_i. However, according to Eq. (10.1)~(10.2), the value of a_i is unknown without the knowledge of φ_t in the expression of F_i. Thus, the hydrodynamic force and vessel motion are essentially coupled through the term φ_t.

10.3 Motion decoupling method

Before taking the sloshing tanks into account, the existing motion decoupling methods for the time-domain simulation of the floating vessel without tanks are firstly reviewed.

The first method is the iteration algorithm (e.g. in Cao et al 1994; and Ma and Yan 2008). The iteration may start with an approximation of the vessel's acceleration or hydrodynamic forces. The equation of motion is solved to update the vessel's acceleration and further the hydrodynamic forces. The iteration stops when the acceleration or force converges to a steady value. This method is simple to apply. However, it has several common disadvantages as mentioned in Section 10.1.

The second method is the so-called 'implicit boundary condition method' by Van Daalen (1993) and Tanizawa (1995). This method does not solve the vessel's acceleration a_i explicitly. Instead, it substitutes the vessel's

acceleration $\mathbf{a}=\left[M\right]^{-1}\left(\mathbf{F}_d+\mathbf{F}_e\right)$ into the boundary condition of φ_t, leading to a relationship between φ_t and $\partial\varphi_t/\partial n$ on S_B^0. Meanwhile, the φ_t and $\partial\varphi_t/\partial n$ are also related, through the Green's third identity. Then, an explicit boundary value problem of φ_t could be formed, and φ_t on $\left(S_B^0+S_F^0+S_C+S_D\right)$ and $\partial\varphi_t/\partial n$ on S_B^0 could be solved simultaneously. Known φ_t, hydrodynamic forces and the vessel's acceleration can be calculated. This method has avoided the iterations, but the BEM matrix for φ_t is different from that for φ and the matrix generation is very complex. This inconvenience would become more evident when multiple floating vessels or liquid tanks exist.

The third method is the modal decomposition method, which is introduced by Vinje and Brevig (1981) and subsequently adopted by the literature such as Cointe et al (1990) and Koo and Kim (2004). With respect to the acceleration and velocity field, the φ_t is decomposed into modes corresponding to the velocity field and each unit acceleration

$$\varphi_t=\sum_{i=1}^{6}\Psi_i\cdot a_i+\overline{\varphi_t} \tag{10.14}$$

Each Ψ_i satisfies the boundary value problem

$$\nabla_o^2\Psi_i=0\text{, in }V^0 \tag{10.15}$$

$$\Psi_i=0\text{, on }S_F^0 \tag{10.16}$$

$$\frac{\partial\Psi_i}{\partial n}=n_i\text{, on }S_B^0 \tag{10.17}$$

$$\frac{\partial\Psi_i}{\partial n}=0\text{, on }S_C\text{ and }S_D \tag{10.18}$$

and $\overline{\varphi_t}$ is determined by

$$\nabla_o^2\overline{\varphi_t}=0\text{, in }V^0 \tag{10.19}$$

$$\overline{\varphi_t}=-gz_o-\frac{1}{2}\nabla_o\varphi\nabla_o\varphi\text{, on }S_F^0 \tag{10.20}$$

$$\frac{\partial\overline{\varphi_t}}{\partial n}=-\mathbf{v}_c\cdot\frac{\partial\nabla_o\varphi}{\partial n}+\Omega\cdot\frac{\partial}{\partial n}\left[\mathbf{r}\times\left(\mathbf{v}_c-\nabla_o\varphi\right)\right],\ \text{on}\ \ S_B^0 \tag{10.21}$$

$$\frac{\partial\overline{\varphi_t}}{\partial n}=\frac{\partial^2\varphi_I}{\partial n\partial t},\ \text{on}\ \ S_C \tag{10.22}$$

$$\frac{\partial\overline{\varphi_t}}{\partial n}=0,\ \text{on}\ \ S_D \tag{10.23}$$

Then, the hydrodynamic forces and moments can be calculated by

$$\begin{aligned}F_i&=-\rho^0\iint_{S_B^0}\varphi_t\cdot n_i dS-\rho^0\iint_{S_B^0}\left(\frac{1}{2}\nabla_o\varphi\nabla_o\varphi+gz_o\right)n_i dS\\&=-\rho^0\iint_{S_B^0}\sum_{j=1}^{6}\Psi_j a_j n_i dS-\rho^0\iint_{S_B^0}\overline{\varphi_t}\cdot n_i dS-\rho^0\iint_{S_B^0}\left(\frac{1}{2}\nabla_o\varphi\nabla_o\varphi+gz_o\right)n_i dS,\\&=-\rho^0\sum_{j=1}^{6}A_{ij}^0a_j-\rho^0U_i^0\end{aligned} \tag{10.24}$$

with $A_{ij}^0=\iint_{S_B^0}\Psi_j n_i dS$ and $U_i^0=\iint_{S_B^0}\overline{\varphi_t}n_i dS+\iint_{S_B^0}\left(\frac{1}{2}\nabla_o\varphi\nabla_o\varphi+gz_o\right)n_i dS$

or

$$\begin{Bmatrix}\boldsymbol{F}_d\\\boldsymbol{M}_d\end{Bmatrix}=-\rho^0\left[A^0\right]\boldsymbol{a}-\rho^0\boldsymbol{U}^0,\ \text{with}$$

$$\left[A^0\right]=\begin{bmatrix}A_{11}^0&A_{12}^0&\cdots&A_{16}^0\\A_{21}^0&A_{22}^0&\cdots&A_{26}^0\\\vdots&\vdots&&\vdots\\A_{61}^0&A_{62}^0&\cdots&A_{66}^0\end{bmatrix}=\begin{bmatrix}\iint_{S_B^0}\Psi_1n_1dS&\iint_{S_B^0}\Psi_2n_1dS&\cdots&\iint_{S_B^0}\Psi_6n_1dS\\\iint_{S_B^0}\Psi_1n_2dS&\iint_{S_B^0}\Psi_2n_2dS&\cdots&\iint_{S_B^0}\Psi_6n_2dS\\\vdots&\vdots&&\vdots\\\iint_{S_B^0}\Psi_1n_6dS&\iint_{S_B^0}\Psi_2n_6dS&\cdots&\iint_{S_B^0}\Psi_6n_6dS\end{bmatrix} \tag{10.25}$$

and $\boldsymbol{U}^0=\left\{U_1^0,U_2^0,U_3^0,U_4^0,U_5^0,U_6^0\right\}^T$

Note that the following relationship is satisfied

$$\begin{aligned}\iint_{S_B^0}\Psi_j\cdot n_i dS&=\iint_{S_B^0}\Psi_j\cdot\frac{\partial\Psi_i}{\partial n}dS=\iint_{S_B^0+S_F^0+S_C+S_D}\Psi_j\cdot\frac{\partial\Psi_i}{\partial n}dS-\iint_{S_F^0}\Psi_j\cdot\frac{\partial\Psi_i}{\partial n}dS\\&=\iint_{S_B^0+S_F^0+S_C+S_D}\frac{\partial\Psi_j}{\partial n}\cdot\Psi_i dS-\iint_{S_F^0}\Psi_j\cdot\frac{\partial\Psi_i}{\partial n}dS=\iint_{S_B^0}\frac{\partial\Psi_j}{\partial n}\cdot\Psi_i dS=\iint_{S_B^0}n_j\cdot\Psi_i dS\end{aligned} \tag{10.26}$$

according to the Green's identity

$$\iint_{S_B^0+S_F^0+S_C+S_D}\left(\Psi_i\frac{\partial\Psi_j}{\partial n}-\frac{\partial\Psi_i}{\partial n}\Psi_j\right)dS=0 \tag{10.27}$$

Substituting Eq. (10.25) to Eq. (10.1) yields

$$\left(\left[M\right]+\rho^0\left[A^0\right]\right)\boldsymbol{a}=-\begin{Bmatrix}0\\0\\0\\\boldsymbol{\Omega}\times\left(\left[I\right]\boldsymbol{\Omega}\right)\end{Bmatrix}-\rho^0\boldsymbol{U}^0+\begin{Bmatrix}\mathbf{F}_e\\\mathbf{M}_e\end{Bmatrix} \tag{10.28}$$

Thus, the vessel's acceleration at any instant could be calculated explicitly. This method is appealing if the BEM solver is adopted. Because coefficient matrices of equation systems for Ψ_i and $\overline{\varphi_t}$ are the same as that for φ. Also, since the boundary value problems of Ψ_i and $\overline{\varphi_t}$ are independent with each other, it is convenient to set the right-hand-side of the equation system as multiple columns and obtain Ψ_i and $\overline{\varphi_t}$ from a single time solution.

The modal decomposition method has a variation which is known as the auxiliary function method developed by Wu and Eatock Taylor (1996). Since both $\overline{\varphi_t}$ and Ψ_i satisfy the Laplace's equation, the following relationship is guaranteed according to the Green's identity

$$\iint_{S_B^0+S_F^0+S_C+S_D}\left(\overline{\varphi_t}\frac{\partial\Psi_i}{\partial n}-\frac{\partial\overline{\varphi_t}}{\partial n}\Psi_i\right)dS=0 \tag{10.29}$$

Regarding the boundary conditions of Ψ_i, the integration of $\overline{\varphi_t}$ can be written as

$$\begin{aligned}\iint_{S_B^0}\overline{\varphi_t}n_i dS&=\iint_{S_B^0}\overline{\varphi_t}\frac{\partial\Psi_i}{\partial n}dS=\iint_{S_B^0+S_F^0+S_C+S_D}\overline{\varphi_t}\frac{\partial\Psi_i}{\partial n}dS-\iint_{S_F^0}\overline{\varphi_t}\frac{\partial\Psi_i}{\partial n}dS\\&=\iint_{S_B^0+S_F^0+S_C+S_D}\frac{\partial\overline{\varphi_t}}{\partial n}\Psi_i dS-\iint_{S_F^0}\overline{\varphi_t}\frac{\partial\Psi_i}{\partial n}dS=\iint_{S_B^0}\frac{\partial\overline{\varphi_t}}{\partial n}\Psi_i dS-\iint_{S_F^0}\overline{\varphi_t}\frac{\partial\Psi_i}{\partial n}dS\end{aligned} \tag{10.30}$$

Then, the Eq. (10.28) can be rewritten as

$$
\begin{aligned}
&\left([M]+\rho^0\left[A^0\right]\right)\boldsymbol{a} \\
&=-\begin{Bmatrix} 0 \\ 0 \\ 0 \\ \boldsymbol{\Omega}\times\left([I]\boldsymbol{\Omega}\right) \end{Bmatrix}-\rho^0\iint_{S_B^0}\frac{\partial\overline{\varphi_t}}{\partial n}\cdot\begin{Bmatrix}\Psi_1\\ \Psi_2\\ \vdots\\ \Psi_6\end{Bmatrix}dS+\rho^0\iint_{S_F^0}\overline{\varphi_t}\cdot\begin{Bmatrix}\partial\Psi_1/\partial n\\ \partial\Psi_2/\partial n\\ \vdots\\ \partial\Psi_6/\partial n\end{Bmatrix}dS \\
&-\rho^0\iint_{S_B^0}\left(\frac{1}{2}\nabla_o\varphi\nabla_o\varphi+gz_o\right)\begin{Bmatrix}\mathbf{n}\\ \mathbf{r}\times\mathbf{n}\end{Bmatrix}dS+\begin{Bmatrix}\mathbf{F}_e\\ \mathbf{M}_e\end{Bmatrix}
\end{aligned}
\tag{10.31}
$$

The original derivation in Wu and Eatock Taylor (1996) applied φ_t instead of $\overline{\varphi_t}$ in Eq. (10.29), which is essentially equivalent to the present formulation. Using the auxiliary function method, the solution of $\overline{\varphi_t}$ is not explicitly required. So Kashiwagi (1998) called this method an 'indirect method'. However, this method does not generate the body-surface pressure directly. If the pressure is required, another boundary value problem for φ_t should be solved after the vessel's acceleration is obtained.

In this study, the mathematical equations related to the sloshing module are further derived as follows, which can be considered as an extension of the modal decomposition method. The sloshing-induced force $\mathbf{F}_s=\mathbf{F}^1+\mathbf{F}^2\cdots+\mathbf{F}^{N_s}$ and moment $\mathbf{M}_s=\mathbf{M}^1+\mathbf{M}^2\cdots+\mathbf{M}^{N_s}$ are further involved in the modal decomposition method. In Tank-k, the sloshing force and moment are obtained from the pressure integration on the wetted tank surface

$$
F_i^k=-\rho^k\iint_{S_B^k}\left(\frac{\partial\varphi^k}{\partial t}+\frac{1}{2}\nabla_o\varphi^k\nabla_o\varphi^k+gz_o\right)n_i dS,\quad k=1,2,\cdots,N_s \text{ and } i=1,2,\cdots,6 \tag{10.32}
$$

In V^k, the φ_t^k could also be decomposed as

$$
\varphi_t^k=\sum_{i=1}^{6}\Psi_i^k\cdot a_i+\overline{\varphi_t^k} \tag{10.33}
$$

The boundary value problem of each Ψ_i^k is

$$
\nabla_o^2\Psi_i^k=0 \text{, in } V^k \tag{10.34}
$$

$$\Psi_i^k = 0 \text{, on } S_F^k \tag{10.35}$$

$$\frac{\partial \Psi_i^k}{\partial n} = n_i \text{, on } S_B^k \tag{10.36}$$

while the boundary value problem of $\overline{\varphi_t^k}$ is

$$\nabla_o^2 \overline{\varphi_t^k} = 0 \text{, in } V^k \tag{10.37}$$

$$\overline{\varphi_t^k} = -gz_o - \frac{1}{2}\nabla_o \varphi^k \nabla_o \varphi^k \text{, on } S_F^k \tag{10.38}$$

$$\frac{\partial \overline{\varphi_t^k}}{\partial n} = -\mathbf{v}_c \cdot \frac{\partial \nabla_o \varphi^k}{\partial n} + \boldsymbol{\Omega} \cdot \frac{\partial}{\partial n}\left[\mathbf{r} \times \left(\mathbf{v}_c - \nabla_o \varphi^k\right)\right] \text{, on } S_B^k \tag{10.39}$$

Then, the resultant sloshing force can be written as

$$\begin{aligned} F_{si} &= \sum_{k=1}^{Ns} F_i^k = -\sum_{k=1}^{Ns} \rho^k \left[\sum_{j=1}^{6} A_{ij}^k a_j + U_i^k\right], \text{ with } A_{ij}^k = \iint_{S_B^k} \Psi_j^k n_i dS \text{ and} \\ U_i^k &= \iint_{S_B^k} \overline{\varphi_t^k} \cdot n_i dS + \iint_{S_B^k} \left(\frac{1}{2}\nabla_o \varphi^k \nabla_o \varphi^k + gz_o\right) n_i dS \end{aligned} \tag{10.40}$$

Thus, the motion equations of the floating vessel with sloshing tanks can be written as

$$\begin{aligned} &\left(\left[M\right] + \sum_{k=0}^{Ns} \rho^k \left[A^k\right]\right)\boldsymbol{a} = -\sum_{k=0}^{Ns} \rho^k \boldsymbol{U}^k - \begin{Bmatrix} 0 \\ 0 \\ 0 \\ \boldsymbol{\Omega} \times \left(\left[I\right]\boldsymbol{\Omega}\right) \end{Bmatrix} + \begin{Bmatrix} \mathbf{F}_e \\ \mathbf{M}_e \end{Bmatrix}, \text{ with} \\ &\left[A^k\right] = \begin{bmatrix} A_{11}^k & A_{12}^k & \cdots & A_{16}^k \\ A_{21}^k & A_{22}^k & \cdots & A_{26}^k \\ \vdots & \vdots & & \vdots \\ A_{61}^k & A_{62}^k & \cdots & A_{66}^k \end{bmatrix} \text{ and } \boldsymbol{U}^k = \left\{U_1^k, U_2^k, U_3^k, U_4^k, U_5^k, U_6^k\right\}^T \end{aligned} \tag{10.41}$$

It is noted that the computation of the second-order differentiation term $\partial \nabla_o \varphi^k / \partial n$ and $\partial\left[\mathbf{r} \times \left(\mathbf{v}_c - \nabla_o \varphi^k\right)\right] / \partial n$ in Eq. (10.39) appears to be difficult. The auxiliary function in Chapter 2 could be used to solve this problem. Since

$$\frac{\partial}{\partial n}\left(\overline{\varphi_t^k}\right) = -\frac{\partial}{\partial n}\left(\mathbf{v}_c \cdot \nabla_o \varphi^k\right) + \frac{\partial}{\partial n}\left[\Omega \cdot \left(\mathbf{r} \times \mathbf{v}_c\right) - \Omega \cdot \left(\mathbf{r} \times \nabla_o \varphi^k\right)\right] \text{ or} \tag{10.42}$$

$$\frac{\partial}{\partial n}\left(\overline{\varphi_t^k}+\mathbf{v}_c\cdot\nabla_o\varphi^k+\nabla_o\varphi^k\cdot\left(\Omega\times\mathbf{r}\right)-\mathbf{v}_c\cdot\left(\Omega\times\mathbf{r}\right)\right)=0$$

the auxiliary function

$$\begin{aligned}\chi^k&=\overline{\varphi_t^k}+\mathbf{v}_c\cdot\nabla_o\varphi^k+\nabla_o\varphi^k\cdot(\Omega\times\mathbf{r})-\mathbf{v}_c\cdot(\Omega\times\mathbf{r})\quad\text{or}\\ \chi^k&=\overline{\varphi_t^k}+\mathbf{v}_c\cdot\nabla_o\varphi^k-\mathbf{\Omega}\cdot\left[\mathbf{r}\times\left(\mathbf{v}_c-\nabla_o\varphi^k\right)\right]\end{aligned}\tag{10.43}$$

can be constructed, with

$$\frac{\partial\chi^k}{\partial n}=\frac{\partial\overline{\varphi_t^k}}{\partial n}+\frac{\partial}{\partial n}\left(\mathbf{v}_c\cdot\nabla_o\varphi^k\right)+\frac{\partial}{\partial n}\left[\nabla_o\varphi^k\cdot\left(\mathbf{\Omega}\times\mathbf{r}\right)\right]-\frac{\partial}{\partial n}\left[\mathbf{v}_c\cdot\left(\mathbf{\Omega}\times\mathbf{r}\right)\right]\tag{10.44}$$

Since all terms of χ^k satisfy the Laplace equation, Eqs. (10.37)-(10.39) can be converted to the boundary value problem with respect to χ^k. Once χ^k is solved, the value of $\overline{\varphi_t^k}$ could be known.

10.4 Impulse-response function method for seakeeping problem

If the amplitude of the vessel motion and external waves are small relative to the characteristic vessel dimension, the S_F^0 and S_B^0 for the seakeeping problem could be assumed to oscillate about their mean position $\overline{S}_F$ and $\overline{S}_B$, respectively (e.g. in Fig. 10.2). Correspondingly, all quantities derivable from the flow (e.g. the velocity potential, free-surface elevation, unsteady translational and rotational vessel motion, pressure, force and moment) are assumed to vary slightly around their mean value. Then, the boundary value problem in Eqs. (10.3)-(10.8) could be linearized.

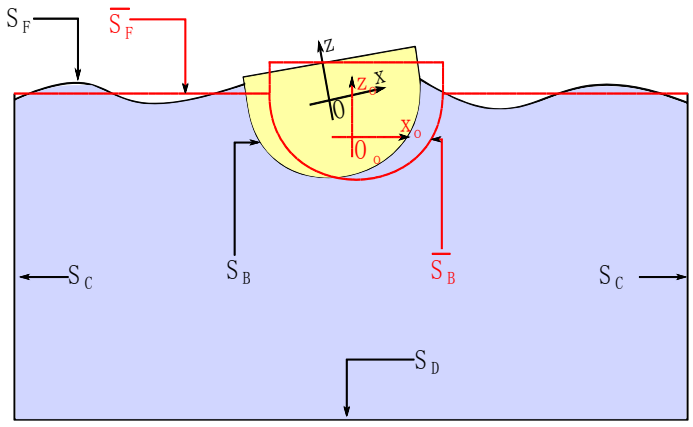

Fig. 10.2 Mean position and instantaneous position of body surface

Firstly expand the quantities on the instantaneous boundary as Taylor series about the mean boundary position. Then, these quantities are expressed by power series with respect to a perturbation parameter ε, e.g. $\varphi=\varphi^{(1)}+\varphi^{(2)}+O\left(\varepsilon^3\right)$, $\eta_o=\eta_o^{(1)}+\eta_o^{(2)}+O\left(\varepsilon^3\right)$, $p=p^{(0)}+p^{(1)}+p^{(2)}+O\left(\varepsilon^3\right)$ and $\mathbf{F}_d=\mathbf{F}_d^{(0)}+\mathbf{F}_d^{(1)}+\mathbf{F}_d^{(2)}+O\left(\varepsilon^3\right)$. Here, the ε is only used to represent the order of the wave steepness and unsteady body motions relative to the characteristic vessel dimensions, which does not necessarily have an explicit definition. The superscripts (0), (1) and (2) indicate that the component is of order $O\left(\varepsilon^0\right)$, $O\left(\varepsilon^1\right)$ and $O\left(\varepsilon^2\right)$, respectively. Substituting the power series into Eqs. (10.3)-(10.8) and omitting terms higher than $O\left(\varepsilon^1\right)$ could lead to the linear boundary value problem

$$\nabla_0^2\varphi^{(1)}=0 \text{, in } \overline{V^0} \tag{10.45}$$

$$\frac{\partial\eta_o^{(1)}}{\partial t}=\frac{\partial\varphi^{(1)}}{\partial z_o} \text{ and } \frac{\partial\varphi^{(1)}}{\partial t}=-g\eta_o^{(1)} \text{ on } \overline{S}_F \tag{10.46}$$

$$\frac{\partial\varphi^{(1)}}{\partial n}=\sum_{i=1}^{6}v_i^{(1)}n_i \text{, on } \overline{S}_B \tag{10.47}$$

$$\frac{\partial\varphi^{(1)}}{\partial n}=\frac{\partial\varphi_I^{(1)}}{\partial n} \text{, on } \overline{S}_C \tag{10.48}$$

$$\frac{\partial\varphi^{(1)}}{\partial n}=0 \text{, on } S_D \tag{10.49}$$

With higher-order terms omitted, the hydrodynamic force/moment from V^0 can be expressed as

$$F_i^{(0)}+F_i^{(1)}=-\rho^0\iint_{\overline{S}_B^0}\varphi_t^{(1)}n_i dS+F_{Bi}=F_i^l+F_{Bi} \tag{10.50}$$

where F_{Bi} is the restoring force and F_i^l is the wave force in the i-th direction. The superscripts (0) and (1) correspond to the steady and linear components of the variable, respectively. The F_{Bi} is determined by the underwater geometry and centre of gravity of the vessel as (Molin 2010)

$$\begin{Bmatrix}\mathbf{F}_B\\ \mathbf{M}_B\end{Bmatrix}=\begin{Bmatrix}F_{B1}\\F_{B2}\\F_{B3}\\F_{B4}\\F_{B5}\\F_{B6}\end{Bmatrix}\approx\begin{bmatrix}0&0&&&&0\\0&0&&&&\\&&C_{33}&C_{34}&C_{35}&\\&&C_{43}&C_{44}&C_{45}&\\&&C_{53}&C_{54}&C_{55}&\\0&&&&&0\end{bmatrix}\begin{Bmatrix}x_1\\x_2\\x_3\\x_4\\x_5\\x_6\end{Bmatrix} \tag{10.51}$$

$$C_{33}=-\rho^0 g\iint_{\bar{S}_F}dS;\quad C_{34}=C_{43}=-\rho^0 g\iint_{\bar{S}_F}ydS;\quad C_{35}=C_{53}=\rho^0 g\iint_{\bar{S}_F}xdS;$$

$$C_{44}=-\rho^0 g\iint_{\bar{S}_F}y^2dS-\rho^0 g\hat{V}z_b;\quad C_{55}=-\rho^0 g\iint_{\bar{S}_F}x^2dS-\rho^0 g\hat{V}z_b; \tag{10.52}$$

$$C_{45}=C_{54}=\rho^0 g\iint_{\bar{S}_F}xydS$$

where $\hat{V}$ is the volume of the vessel's displacement, z_b is the centre of the buoyancy, and $\{x_4,x_5,x_6\}$ are linearized Euler angles. The wave force F_i^l could be further decomposed into the Froude–Krylov (FK) force F_{Ii} due to the pressure field of undisturbed incident waves, diffraction force F_{Di} due to the presence of the restrained vessel by disturbing the incident waves, and radiation forces F_{Ri1} to F_{Ii6} induced by vessel motions in the fluid without incident waves

$$F_i^l=F_{Ii}+F_{Di}+\sum_{j=1}^{6}F_{Rij}\quad\text{or}\quad\mathbf{F}^l=\mathbf{F}_{I1}+\mathbf{F}_{D1}+\sum_{j=1}^{6}\mathbf{F}_{Rj} \tag{10.53}$$

Here, the subscripts $R1$ to $R6$ correspond to mode-1 to 6 of the vessel motion (i.e. surge, sway, heave, roll, pitch and yaw), respectively. The velocity potential could be decomposed correspondingly as

$$\varphi^{(1)}=\varphi_I+\varphi_D+\sum_{j=1}^{6}\varphi_{Rj} \tag{10.54}$$

The IRF method (Cummins 1962) is adopted to calculate the radiation forces, by considering the vessel motion as a succession of impulses. At an instant t, the flow is influenced by the impulsive velocity at and before this instant. The radiation velocity potential could be written as

$$\varphi_{Ri}(x,y,z,t)=\Psi_i(x,y,z)v_i(t)+\int_{-\infty}^{t}\chi_i(x,y,z,t-\tau)v_i(\tau)d\tau \tag{10.55}$$

where Ψ_i is the velocity potential caused by a unit velocity (i.e. Eqs. (10.15)-(10.18)), and χ_i could be considered as an 'impulse-response function'. Then, the radiation force F_{Rij} can be written as

$$\begin{aligned}F_{Rij}&=-\rho^0\iint_{\bar{S}_B^0}\left(\frac{\partial\varphi_{Rj}}{\partial t}\right)n_i dS\\&=\rho^0\dot{v}_j(t)\underbrace{\left(-\iint_{\bar{S}_B^0}\Psi_j(x,y,z)n_i dS\right)}_{A_{Rij}}+\rho^0\int_{-\infty}^{t}v_j(\tau)\underbrace{\left(-\iint_{\bar{S}_B^0}\frac{\partial\chi_j(x,y,z,t-\tau)}{\partial t}n_i dS\right)}_{B_{Rij}}d\tau\\&=\rho^0A_{Rij}\dot{v}_j(t)+\rho^0\int_{-\infty}^{t}B_{Rij}(t-\tau)v_j(\tau)d\tau\end{aligned} \tag{10.56}$$

The time-dependent function B_{Rij} is called the 'retardation function', which is related to the force history induced by each mode of impulsive vessel movement. Replacing τ with $t-\tau$ and changing the integration boundaries yields a more convenient form

$$\int_{-\infty}^{t}B_{Rij}(t-\tau)v_j(\tau)d\tau=\int_0^{+\infty}B_{Rij}(\tau)v_j(t-\tau)d\tau \tag{10.57}$$

Substituting the sloshing, restoring, Froude-Krylov, radiation and diffraction forces into the motion equations yields

$$\begin{aligned}\sum_{j=1}^{6}M_{ij}\ddot{x}_j(t)=&\underbrace{\rho^0\sum_{j=1}^{6}A_{Rij}\ddot{x}_j(t)+\rho^0\sum_{j=1}^{6}\int_0^{+\infty}B_{Rij}(\tau)\dot{x}_j(t-\tau)d\tau}_{F_{Ri}}\\&\underbrace{+\sum_{j=1}^{6}C_{ij}x_j(t)}_{F_{Bi}}\underbrace{-\sum_{k=1}^{Ns}\rho^k\left[\sum_{j=1}^{6}A_{ij}^k a_j+U_i^k\right]}_{F_{si}}+F_{Di}+F_{Ii}+F_{ei}\end{aligned}\quad\text{, for}\quad i=1,2,\cdots,6 \tag{10.58}$$

or

$$\begin{aligned}&\sum_{j=1}^{6}\left[\left(M_{ij}-\rho^0A_{Rij}+\sum_{k=1}^{Ns}\rho^kA_{ij}^k\right)\ddot{x}_j-\rho^0\int_0^{+\infty}B_{Rij}(\tau)\dot{x}_j(t-\tau)d\tau-C_{ij}x_j\right],\\&=-\sum_{k=1}^{Ns}\rho^kU_i^k+F_{Di}+F_{Ii}+F_{ei}\end{aligned}\quad\text{for}\quad i=1,2,\cdots,6 \tag{10.59}$$

where M_{ij} denotes the elements of the matrix $[M]$.

10.5 Coefficients of IRF method

Ogilvie (1964)'s theory is used to solve the coefficients A_{Rij} and B_{Rij} of the IRF method. Consider the vessel undergoing a harmonic oscillation at the frequency ω as

$$\begin{aligned} x_i &= \mathrm{Re}\left[\tilde{x}_i e^{-i\omega t}\right];\ \ v_i = \dot{x}_i = \mathrm{Re}\left[-i\omega\tilde{x}_i e^{-i\omega t}\right] = \omega\,\mathrm{Im}\left[\tilde{x}_i e^{-i\omega t}\right]; \\ a_i &= \ddot{x}_i = \mathrm{Re}\left[-\omega^2\tilde{x}_i e^{-i\omega t}\right] = -\omega^2 x_i \end{aligned} \tag{10.60}$$

where $\tilde{x}_i$ is the complex amplitude of the vessel displacement, and $\mathrm{Re}[\ ]$ and $\mathrm{Im}[\ ]$ denote the real and imaginary part of the complex variable, respectively. Correspondingly, the radiation velocity potential could be expressed as

$$\varphi_{Ri}\left(x_o, y_o, z_o, t\right) = \mathrm{Re}\left[\tilde{\varphi}_{Ri}\left(x_o, y_o, z_o\right)e^{-i\omega t}\right] \tag{10.61}$$

with $\tilde{\varphi}_{Ri}$ as the complex amplitude. Considering the boundary condition on $\overline{S}_B$, $\tilde{\varphi}_{Ri}$ could be further expressed as $\tilde{\varphi}_{Ri}\left(x_o, y_o, z_o\right) = -i\omega\tilde{x}_i\tilde{\varphi}'_{Ri}\left(x_o, y_o, z_o\right)$. Then, the radiation force can be written as

$$\begin{aligned} F_{Rij} &= -\rho^0\iint_{\overline{S}_B^0}\left(\partial\varphi_{Rj}/\partial t\right)n_i dS = -\rho^0\iint_{\overline{S}_B^0}\mathrm{Re}\left[-i\omega\tilde{\varphi}_{Rj}e^{-i\omega t}\right]n_i dS = \rho^0\omega^2\iint_{\overline{S}_B^0}\mathrm{Re}\left[\tilde{x}_j e^{-i\omega t}\tilde{\varphi}'_{Rj}\right]n_i dS \\ &= \rho^0\omega^2\iint_{\overline{S}_B^0}\left(\mathrm{Re}\left[\tilde{x}_j e^{-i\omega t}\right]\mathrm{Re}\left[\tilde{\varphi}'_{Rj}\right] - \mathrm{Im}\left[\tilde{x}_j e^{-i\omega t}\right]\mathrm{Im}\left[\tilde{\varphi}'_{Rj}\right]\right)n_i dS \\ &= \rho^0\omega^2\iint_{\overline{S}_B^0}\left(x_j\,\mathrm{Re}\left[\tilde{\varphi}'_{Rj}\right] - v_j/\omega\,\mathrm{Im}\left[\tilde{\varphi}'_{Rj}\right]\right)n_i dS = \rho^0\iint_{\overline{S}_B^0}\left(-a_j\,\mathrm{Re}\left[\tilde{\varphi}'_{Rj}\right] - v_j\omega\,\mathrm{Im}\left[\tilde{\varphi}'_{Rj}\right]\right)n_i dS \\ &= \rho^0 a_j\left(-\iint_{\overline{S}_B^0}\mathrm{Re}\left[\tilde{\varphi}'_{Rj}\right]n_i dS\right) + \rho^0 v_j\left(-\omega\iint_{\overline{S}_B^0}\mathrm{Im}\left[\tilde{\varphi}'_{Rj}\right]n_i dS\right) = \rho^0\tilde{A}_{Rij}\left(\omega\right)a_j + \rho^0\tilde{B}_{Rij}\left(\omega\right)v_j \end{aligned} \tag{10.62}$$

where $\tilde{A}_{Rij}$ is the added mass and $\tilde{B}_{Rij}$ is radiation damping. In other words, the radiation force has two components, which are in phase with the acceleration and velocity, respectively. For harmonic incident waves, the φ_I and φ_D could also be expressed as

$$\varphi_I\left(x_o, y_o, z_o, t\right) = \mathrm{Re}\left[\tilde{\varphi}_I\left(x_o, y_o, z_o\right)e^{-i\omega t}\right] \tag{10.63}$$

$$\varphi_D\left(x_o, y_o, z_o, t\right) = \mathrm{Re}\left[\tilde{\varphi}_D\left(x_o, y_o, z_o\right) e^{-i\omega t}\right] \tag{10.64}$$

where $\tilde{\varphi}_I$ and $\tilde{\varphi}_D$ are the complex amplitude of the incident and diffraction wave potential. The $\tilde{\varphi}_I$ could be expressed explicitly based on the Airy wave theory

$$\tilde{\varphi}_I\left(x_0, y_0, z_0\right) = \frac{Ag}{i\omega} \frac{\cosh k\left(z_0 + H_0\right)}{\cosh kH_0} e^{ik\left(x_0 \cos\theta + y_0 \sin\theta\right)} \tag{10.65}$$

Correspondingly, the F_{Ii} and F_{Di} become

$$\begin{aligned} F_{Ij} &= -\rho^0 \iint_{\overline{S}_B^0} \left(\partial\varphi_I / \partial t\right) n_j dS \\ &= -\rho^0 \iint_{\overline{S}_B^0} \mathrm{Re}\left[-i\omega\tilde{\varphi}_I\left(x_0, y_0, z_0\right) e^{-i\omega t}\right] n_j dS = \rho^0 \,\mathrm{Re}\left[\left(\left|F_{Ij}\right| e^{i\theta_I}\right) e^{-i\omega t}\right] \end{aligned} \tag{10.66}$$

$$\begin{aligned} F_{Dj} &= -\rho^0 \iint_{\overline{S}_B^0} \left(\partial\varphi_D / \partial t\right) n_j dS \\ &= -\rho^0 \iint_{\overline{S}_B^0} \mathrm{Re}\left[-i\omega\tilde{\varphi}_D\left(x_0, y_0, z_0\right) e^{-i\omega t}\right] n_j dS = \rho^0 \,\mathrm{Re}\left[\left(\left|F_{Dj}\right| e^{i\theta_D}\right) e^{-i\omega t}\right] \end{aligned} \tag{10.67}$$

Then, the frequency-domain motion equation becomes

$$\sum_{j=1}^{6}\left[\left(M_{ij} - \rho^0 \tilde{A}_{Rij}\left(\omega\right)\right)\ddot{x}_j - \rho^0 \tilde{B}_{Rij}\left(\omega\right)\dot{x}_j - C_{ij}x_j\right] = F_{si} + F_{Di} + F_{Ii} + F_{ei}, \quad \text{for } i = 1, 2, \cdots, 6 \tag{10.68}$$

For a special case of $x_i = \cos\left(\omega t\right)$, the frequency-domain motion equations become

$$\sum_{j=1}^{6}\begin{bmatrix} -\omega^2\left(M_{ij} - \rho^0 \tilde{A}_{Rij}\left(\omega\right)\right)\cos\left(\omega t\right) \\ -\rho^0\omega\left(-\tilde{B}_{Rij}\left(\omega\right)\right)\sin\left(\omega t\right) - C_{ij}\cos\left(\omega t\right) \end{bmatrix} = F_{si} + F_{Di} + F_{Ii} + F_{ei}, \text{ for } i = 1, 2, \cdots, 6 \tag{10.69}$$

Meanwhile, the time-domain motion equation Eq. (10.58) becomes

$$\sum_{j=1}^{6}\begin{bmatrix} -\omega^2\left(\left(M_{ij}-\rho^0 A_{Rij}\right)+\rho^0\frac{1}{\omega}\int_0^{+\infty}B_{Rij}(\tau)\sin(\omega\tau)d\tau\right)\cos(\omega t) \\ -\rho^0\omega\left(-\int_0^{+\infty}B_{Rij}(\tau)\cos(\omega\tau)d\tau\right)\sin\omega t - C_{ij}\cos(\omega t) \end{bmatrix}, \text{ for} \quad (10.70)$$
$$= F_{si}+F_{Di}+F_{Ii}+F_{ei}$$

$$i=1,2,\cdots,6$$

Comparing the terms in Eqs. (10.69) and (10.70) leads to the following relations

$$A_{Rij}=\tilde{A}_{Rij}(\omega)+\frac{1}{\omega}\int_0^{+\infty}B_{Rij}(\tau)\sin(\omega\tau)d\tau \quad (10.71)$$

$$\int_0^{+\infty}B_{Rij}(\tau)\cos(\omega\tau)d\tau=\tilde{B}_{Rij}(\omega) \quad (10.72)$$

Through an inverse Fourier transform, the explicit form of $B_{Rij}(\tau)$ could be obtained as

$$B_{Rij}(\tau)=\frac{2}{\pi}\int_0^{+\infty}\tilde{B}_{Rij}(\omega)\cos(\omega\tau)d\omega \quad (10.73)$$

Thus, the coefficients in the time-domain IRF method could be obtained, taking advantage of the frequency-domain results.

10.6 Closure

This chapter has derived a non-iterative method to decouple the seakeeping and sloshing problems. The method may be considered as an extension of the modal decomposition method for floating vessel simulations. Using this method, the exact vessel's acceleration at any instant can be calculated explicitly in one step without iterations, which can greatly reduce the CPU consumptions and avoid other limitations of the iteration procedure. In the next chapter, the numerical scheme based on this method is further developed. A series of numerical simulations on the floating vessel with nonlinear sloshing tanks will be performed.

Chapter 11 Numerical studies of floating vessel with nonlinear sloshing tanks

11.1 Introduction

The implementation of the motion decoupling method derived in Chapter 10 is demonstrated in Fig. 11.1. At a preliminary stage, the coefficients C_{ij} in Eq. (10.52) are calculated, and the frequency-domain solver is used to generate the frequency-dependent coefficients (e.g. $\tilde{A}_{Rij}$, $\tilde{B}_{Rij}$, $\left|F_{Ij}\right|$, θ_I, $\left|F_{Dj}\right|$ and θ_D). The coefficients for the IRF method (i.e. A_{Rij} and B_{Rij}) are obtained subsequently. Then, the time stepping procedure could be started. At each time step, the displacement and velocity of the vessel are already known. The boundary value problem of the velocity potential φ in each tank should firstly be solved. Then, solutions for boundary value problems of Ψ_i and $\overline{\varphi_t}$ in each tank are required. After that, the surface integrations can be performed to generate the coefficients A_{ij}^k and U_i^k. Further taking advantage of the motion equations, the instantaneous vessel's acceleration can be obtained. Then, the vessel motions (velocity and displacement) and boundary conditions for each sloshing tank could be updated to the next time step. It should be pointed out that Fig. 11.1 shows an example when the Euler's time stepping method is used. Higher precision methods, such as the Runge-Kutta and Adams-Bashforth method, could also be applied easily. In the present study, the fourth-order Runge-Kutta method is adopted for the first several time steps, and then the four-step Adams-Bashforth method is used.

This chapter aims to give the numerical results based on the numerical scheme developed in Chapter 10. The simulations of the seakeeping and sloshing problems are firstly verified. The effectiveness of the motion decoupling method is also verified. Then, the floating vessel with the nonlinear sloshing tank is simulated, with experimental data for comparison. The FLNG vessels with four sloshing tanks and three degrees of freedom are further simulated.

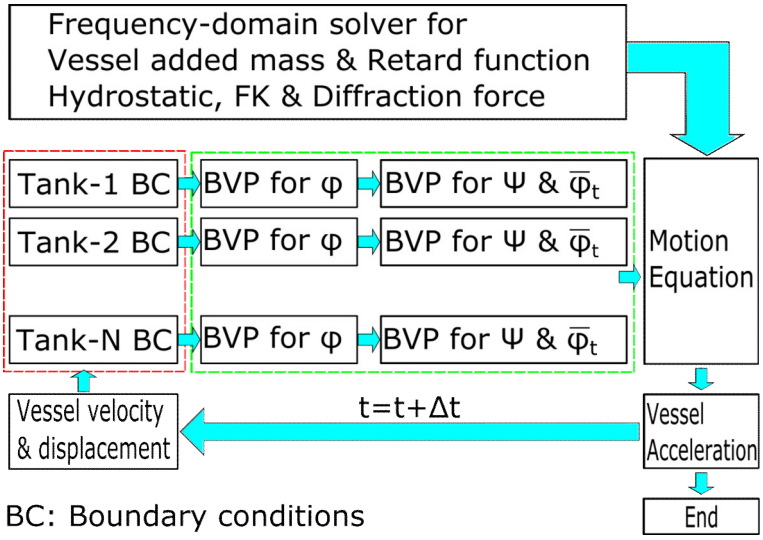

Fig. 11.1 Workflow of motion decoupling method

11.2 Seakeeping problem

This section would firstly verify the simulation of the seakeeping problem i.e. the floating vessel without sloshing tanks. The open source panel method code 'Nemoh' (Babarit 2014) developed by Ecole Centrale de Nantes is adopted as the frequency-domain solver. In this code, the frequency-domain Green's function automatically satisfying the Laplace's equation as well as the linear free-surface and radiation conditions are distributed as sources on vessel-surface panels to approximate the flow field. The source density is determined by the body-surface boundary condition. It is worth mentioning that, for operation convenience, this thesis specially developed an in-house software based on the core of Nemoh, the Microsoft Windows interface of which is shown in Fig. 11.2 for illustration.

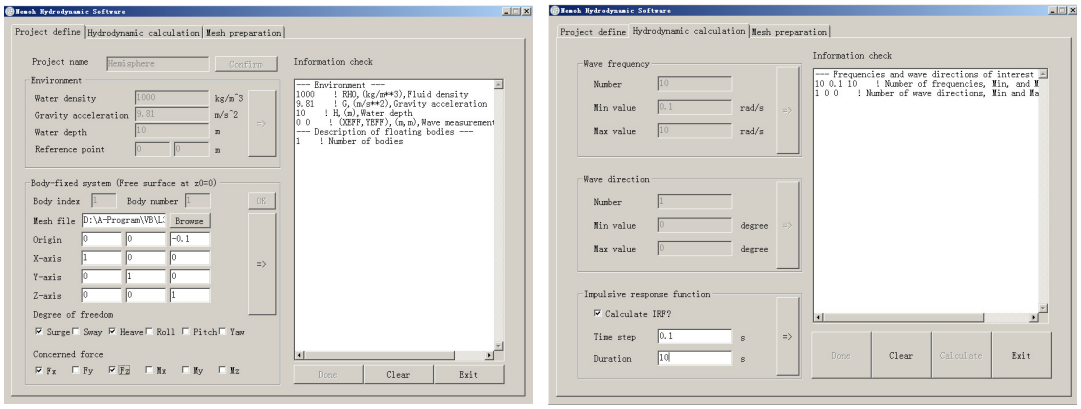

(a) (b)

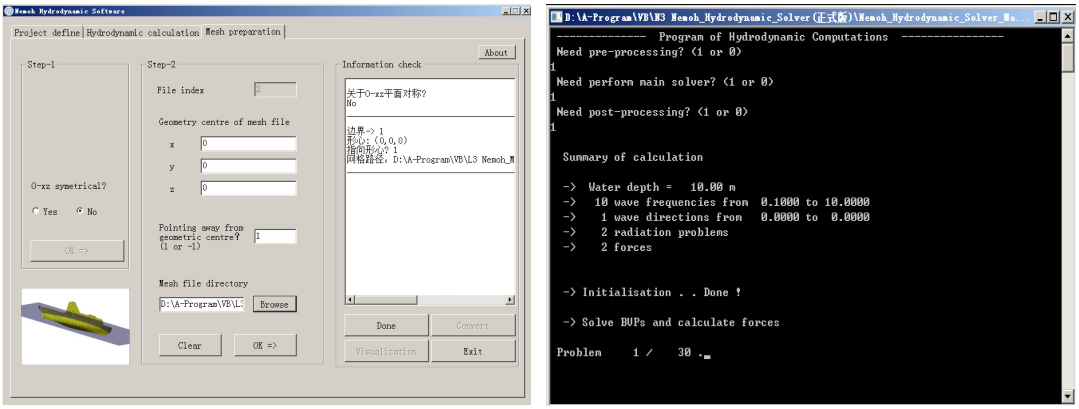

(d) (d)

Fig. 11.2 In-house software based on Nemoh, with Microsoft Windows interface of (a) project definition; (b) calculation parameters; (c) mesh preparation; (d) calculation process

The vessel model is set as a simple truncated circular cylinder. The floating circular cylinder is one of the most classical benchmark test models for 3D floating body simulations. Parameters for the calculation are listed as follows: water density $\rho = 1000\,kg/m^3$, radius $R = 1m$, draught $H = 1m$, vessel mass $m = \rho\pi R^2 H$, pitch inertia $I_{yy} = 0.5\rho\pi R^2 H^3$, the free-surface position with respect to the mass centre $z_f = 0.5m$, and hydrostatic restoring coefficients $C_{33} = \pi$ and $C_{55} = 0.785$. For the panel method calculation, the vessel surface is discretized into mesh elements as in Fig. 11.3. Taking advantage of the geometric symmetry, the mesh can be generated only on half of the surface. There are 1200 mesh elements applied in this case.

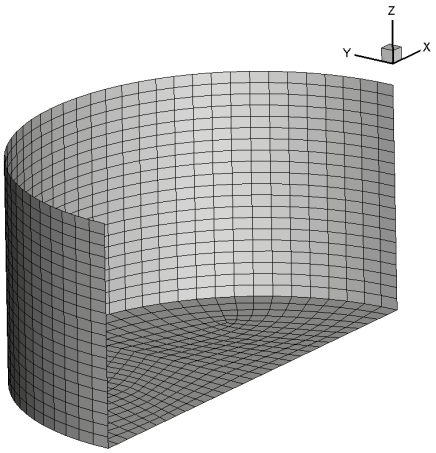

Fig. 11.3 Mesh model for truncated circular cylinder (1200 elements)

Firstly, the frequency-dependent coefficients are verified. The added-mass and damping coefficients $\tilde{A}_{R11}$, $\tilde{B}_{R11}$, $\tilde{A}_{R33}$, $\tilde{B}_{R33}$, $\tilde{A}_{R55}$ and $\tilde{B}_{R55}$ of the vessel are shown in Fig. 11.4. In this chapter, these frequency-dependent coefficients are calculated with the help of the frequency-domain solver Nemoh. It can be seen that all calculated parameters agree well with numerical results of the commercial software WAMIT and Watai (2015).

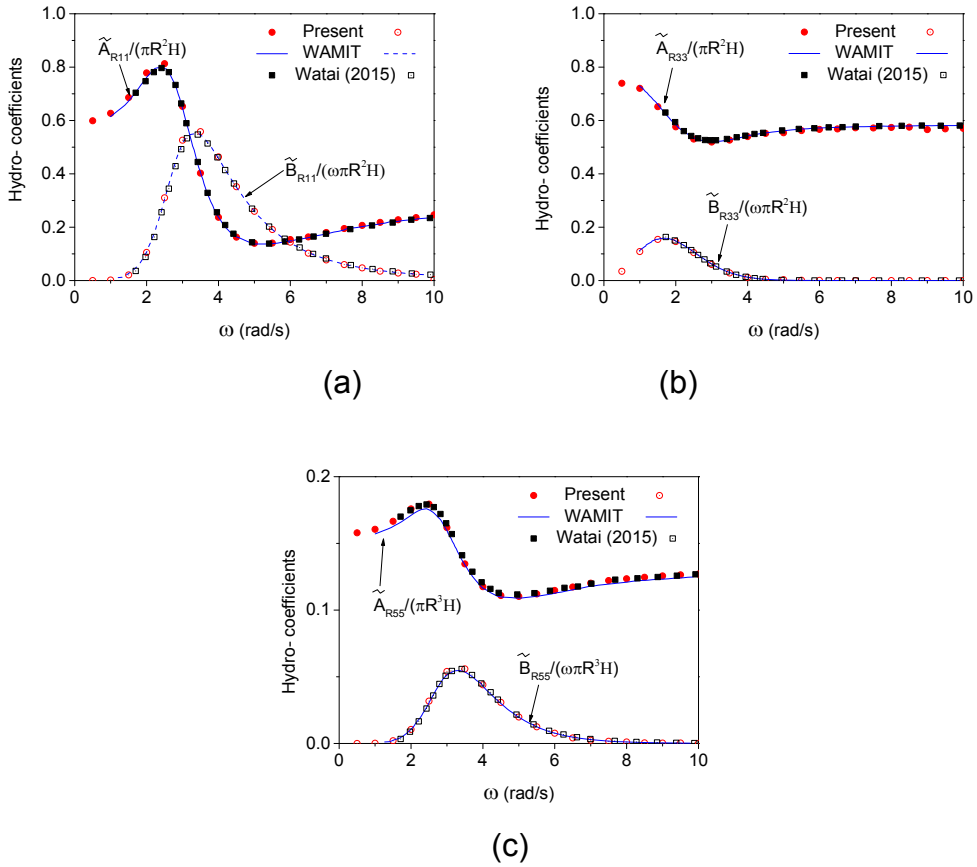

Fig. 11.4 Added-mass and damping coefficients for truncated circular cylinder: (a) $\tilde{A}_{R11}(\omega)$ and $\tilde{B}_{R11}(\omega)$; (b) $\tilde{A}_{R33}(\omega)$ and $\tilde{B}_{R33}(\omega)$; (b) $\tilde{A}_{R55}(\omega)$ and $\tilde{B}_{R55}(\omega)$

The second step tests the IRF-related parameters $B_{Rij}(t)$ and A_{Rij} that are converted from the frequency-dependent coefficients $\tilde{A}_{Rij}(\omega)$ and $\tilde{B}_{Rij}(\omega)$. For B_{Rij}, it is noticed that Eq. (10.73) requires the integration over an infinite frequency range, which is impractical. Kubo et al (1989) proposed a

solution by truncating the frequency range to $0 < \omega \le \omega_{\max}$ and approximating damping coefficients on the rest of the range $\omega > \omega_{\max}$ as

$$\tilde{B}_{Rij}(\omega) = K_{ij}\omega^{-n_{ij}} \text{, for } \omega > \omega_{\max} \tag{11.1}$$

with

$$K_{ij} = \tilde{B}_{Rij}(\omega_{\max})\omega_{\max}^{n_{ij}} \text{, and } \left[n_{ij}\right] = \begin{bmatrix} 3 & 0 & 5 & 0 & 5 & 0 \\ 0 & 3 & 0 & 5 & 0 & 3 \\ 5 & 0 & 7 & 0 & 7 & 0 \\ 0 & 5 & 0 & 7 & 0 & 5 \\ 5 & 0 & 7 & 0 & 7 & 0 \\ 0 & 3 & 0 & 5 & 0 & 3 \end{bmatrix} \tag{11.2}$$

Fig. 11.5 compares two cases when Kubo's method is adopted or not. The damping coefficients and resulted retardation functions are compared, respectively. The solid lines are used to indicate the 'truncated case' when the integration is performed only on the range $0 < \omega \le \omega_{\max}$, and dashed lines are for the 'extended case' when Kubo's method is adopted. In Fig.11.5(a), the damping coefficients on the range of $0 < \omega \le \omega_{\max}$ and $0 < \omega \le \infty$ are marked using the solid and dashed lines, respectively. Correspondingly, in Fig.11.5(b), the solid and dashed lines indicate the retard functions when the integration of the damping coefficient is performed on the range $0 < \omega \le \omega_{\max}$ and $0 < \omega \le \omega_{\max}$, respectively. Evident effects of the truncation on the retard function could be identified. So, Kubo's method would be applied in future simulations. Then, consider A_{Rij}. Fig. 11.6 has shown the value of A_{Rij} computed using each ω. It is clear that, the obtained A_{Rij} at any frequency has almost the same value, which is consistent with Eq. (10.71). Meanwhile, the value of $\tilde{A}_{Rij}(\omega)$ is approaching A_{Rij} as ω increases to infinity, which illustrates the fact that A_{Rij} is essentially the limit case $\tilde{A}_{Rij}(\infty)$.

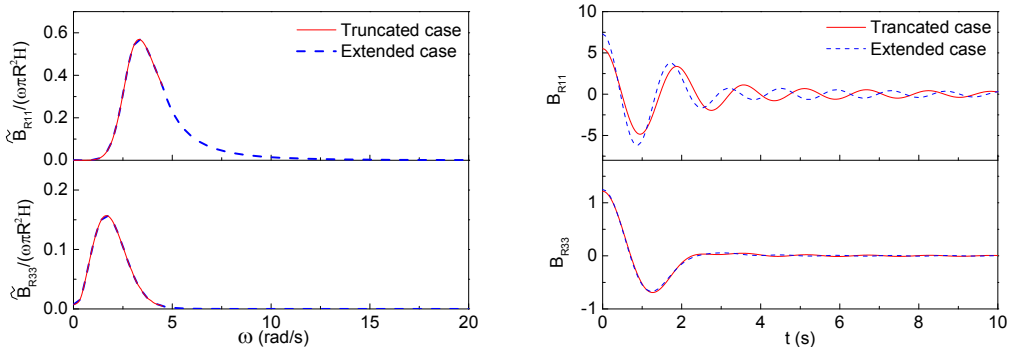

(a) (b)

Fig. 11.5 (a) Damping coefficients and (b) retard functions for truncated circular cylinder

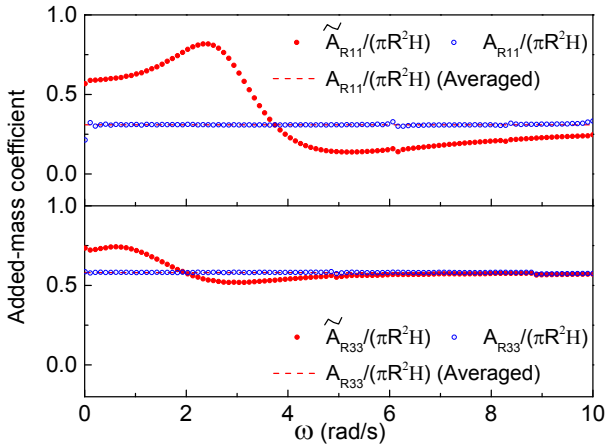

Fig. 11.6 Added-mass coefficients for truncated cylinder

In the third step, hydrodynamic forces acting on the vessel are verified. Firstly, a numerical case is performed to verify the restoring and radiation forces. The vessel of the draught $H = 0.5R$ in the still water is elevated by a height of $A = 0.1R$ from its hydrostatic equilibrium position, and then is set free. The time history of the vessel's vertical displacement is shown in Fig. 11.7. It can be seen that the present result has an excellent agreement with the analytical solution in Newman (1985). Since the vessel's motion is only determined by restoring and radiation forces in this situation, the accuracy of restoring and radiation forces have been verified. Then, the FK force F_{Ii} and diffraction force F_{Di} are to be verified in the diffraction problem when the vessel is fixed in incident waves propagating in the Ox direction. At different wave frequencies, the amplitude of the wave excitation force (a summation of

F_{Ii} and F_{Di}) on the vessel and moment about the centre of its water plane is shown in Fig. 11.8. Results from this numerical scheme compared with the literature show good agreement.

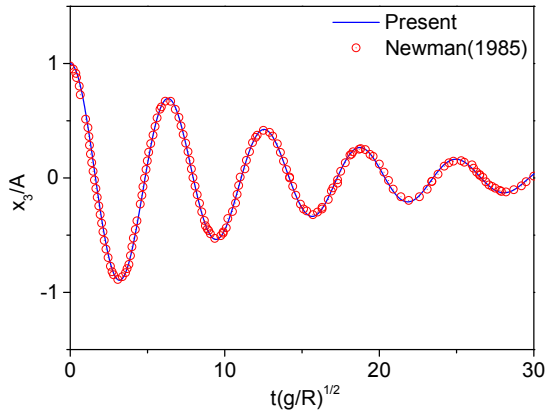

Fig. 11.7 Vertical displacement of floating cylinder in still water

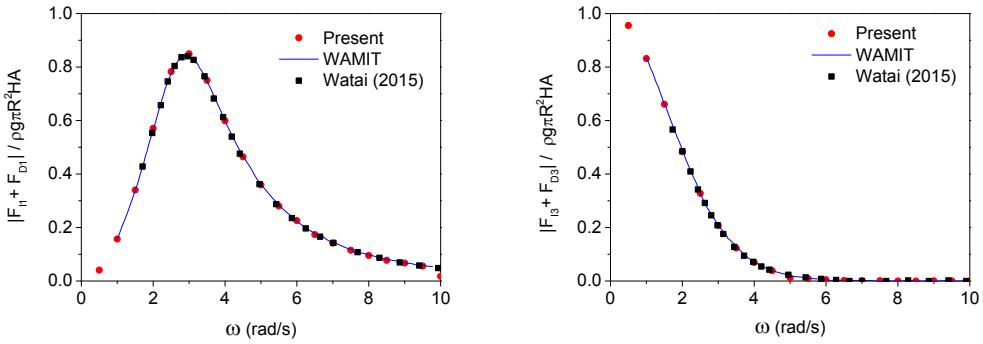

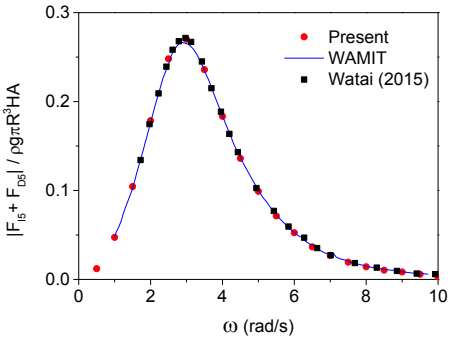

Fig. 11.8 Excitation wave force on truncated circular cylinder: (a) $|F_{I1}+F_{D1}|$; (b) $|F_{I3}+F_{D3}|$; (c) $|F_{I5}+F_{D5}|$ about centre of water plane

Finally, the solution of motion equations is verified. The vessel is initially floating at equilibrium. Then, incident waves with the amplitude $A = 0.1R$ and frequency $\omega = 2.51\ \text{rad/s}$ propagate in the Ox direction. Due to the geometric symmetry, the vessel has a motion with 3 degrees of freedom, i.e. surge, heave and pitch. Since there are nearly no restoring forces acting horizontally on the vessel, the transient effects caused by an abrupt start of the simulation may lead to a mean drift of the vessel motion during the simulation. So a ramp function γ_{ramp} is multiplied on the wave amplitude, to eliminate an abrupt start. The ramp function has the form

$$\gamma_{ramp}(t) = \begin{cases} 1/2\left[1-\cos\left(\pi t/T_{ramp}\right)\right] & ,\text{for } t < T_{ramp} \\ 1 & ,\text{for } t \geq T_{ramp} \end{cases} \tag{11.3}$$

where T_{ramp} is the ramp time which is usually set as several wave periods T. Fig. 11.9 shows time histories of the surge, heave and pitch displacement of the vessel when T_{ramp} is set to be $20T$. It is observed that all these three modes of the vessel motions have reached the steady state after the ramp stage. The heave displacement is also compared with Watai (2015)'s results, where fairly good agreements could still be observed even after about one hundred cycles. Then, incident waves at more frequencies are considered. The surge, heave and pitch RAOs, which are the amplitude ratio between the vessel motions and incoming waves, are shown in Fig. 11.10. Excellent agreements between the present and WAMIT solution can be found.

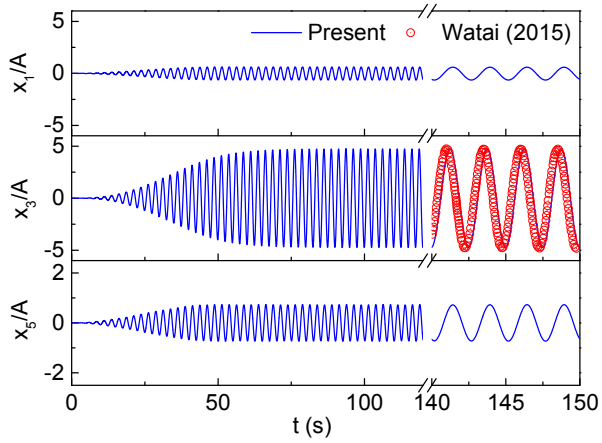

Fig. 11.9 Surge, heave and pitch history of floating truncated cylinder

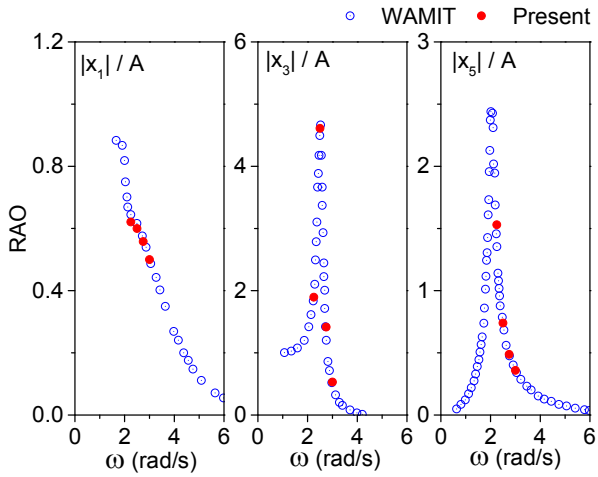

Fig. 11.10 Surge, heave and pitch RAO of floating truncated cylinder

The second vessel model is chosen to be a hemisphere. The hemisphere has the radius $R=1m$, draught $H=1m$, and mass $m=2\rho\pi R^3/3$. Correspondingly, the restoring coefficient has $C_{33}=\pi$. The hemisphere surface is covered by 600 mesh elements as in Fig. 11.11. The frequency-dependent coefficients $\tilde{A}_{R11}$, $\tilde{B}_{R11}$, $\tilde{A}_{R33}$ and $\tilde{B}_{R33}$ of the hemisphere are compared with the analytical solution derived by Hulme (1982) in Fig. 11.12. It is clear that the present results agree well with the corresponding analytical solutions, although curve perturbations exist near $\omega=6$ for $\tilde{A}_{R11}$ and $\omega=5$ for $\tilde{B}_{R33}$. This is a well-known phenomenon of 'irregular frequencies'. The irregular frequencies are attributed to the property of the integral equation of the panel method based on frequency-domain Green's functions as in Nemoh. Because, mathematically, at a discrete set of frequencies, the determinant of the system of equations vanishes (Ursell 1981). Thus, solutions in a narrow vicinity of the irregular frequencies could not represent any physical significance (Mei 1989). However, since irregular frequencies are very high frequencies that are beyond the scope of this study. The extra effort to calculate them will be suspended.

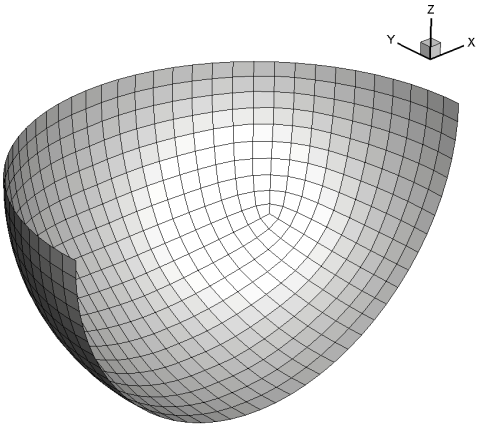

Fig. 11.11 Mesh model for hemisphere (600 elements)

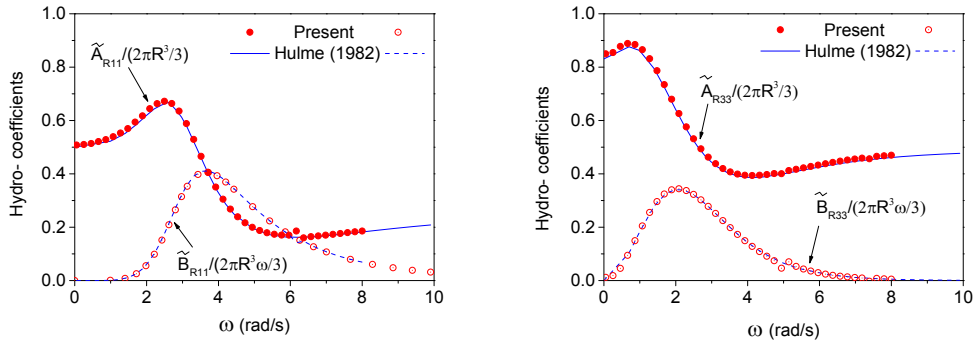

(a) (b)

Fig. 11.12 Added-mass and damping coefficients for hemisphere: (a) $\tilde{A}_{R11}(\omega)$ and $\tilde{B}_{R11}(\omega)$; (b) $\tilde{A}_{R33}(\omega)$ and $\tilde{B}_{R33}(\omega)$

Further, the free motion of a hemisphere in waves is considered. The incident wave with the amplitude $A=0.1R$ and frequency $\omega=3.13$ rad/s propagates in the Ox direction. Fig. 11.13(a) shows time histories of the surge and heave displacement of the vessel when T_{ramp} is set as $20T$. Both the surge and heave motions could reach the steady state after the ramp stage. Even after about one hundred cycles, the heave displacements still agree well with Watai's (2015) results. Fig. 11.13(b) shows the results when the ramp function is not used. It is observed that heave motion reaches a steady state with constant amplitude after several periods. However, the time history of the surge motion has shown an evident drift as time progresses. This is caused by an abrupt start of the simulation. The transient effects could give the vessel a horizontal velocity initially. And during the subsequent

process, there are nearly no restoring forces acting horizontally on the floating vessel to cancel this horizontal velocity, which leads to a mean drift of the vessel motion. Then, more frequencies of incident waves are considered. The surge and heave RAOs are shown in Fig. 11.14. It could be seen that the present results agree well with the WAMIT solutions. The wave excitation forces also agree well with those in the literature as shown in Fig. 11.15.

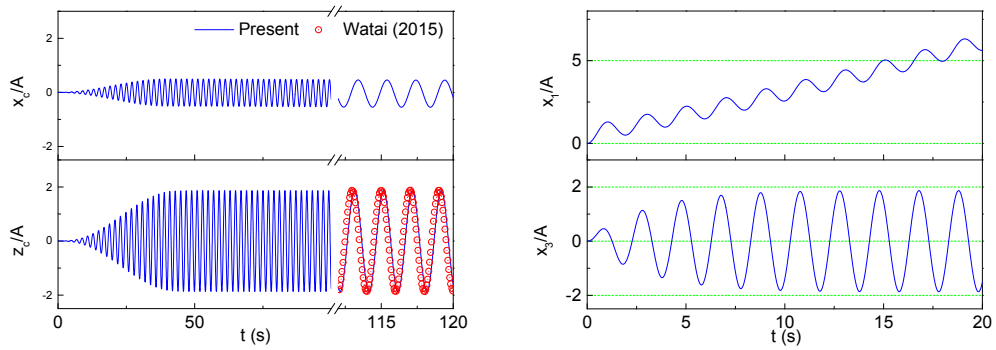

(a) (b)

Fig. 11.13 Surge and heave history of floating hemisphere (a) without ramp; (b) with ramp

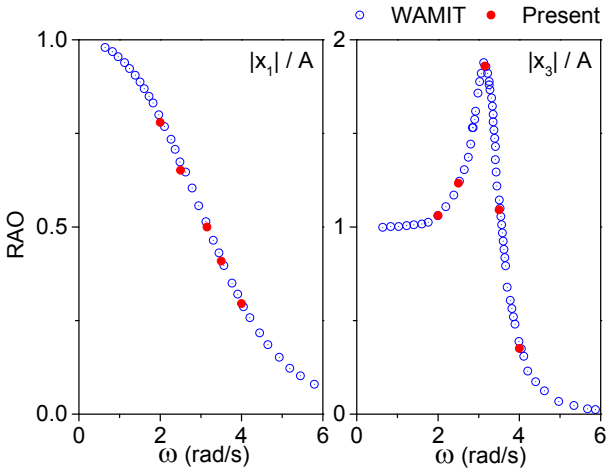

Fig. 11.14 Surge and heave RAO of floating hemisphere

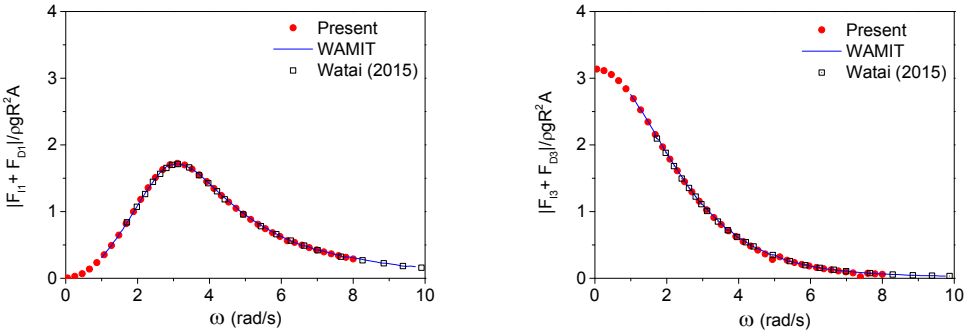

(a) (b)

Fig. 11.15 Excitation wave force on hemisphere: (a) $\left|F_{I1}+F_{D1}\right|$; (b) $\left|F_{I3}+F_{D3}\right|$

Through the above step-by-step verifications, it can be confirmed that the present numerical scheme can provide a reliable simulation for the seakeeping problem.

11.3 Sloshing problem

The accuracy of the nonlinear sloshing simulation has been verified systematically in Chapter 4. In this section, the case when the sloshing tank is mounted on a freely moving vessel on the ground as in Chapter 9 is considered. This case could be used to verify the motion decoupling method. The 3D rectangular tank with length L, width $B=L$ and initial liquid depth $H=0.5L$ is considered. Initially, the vessel is stationary and the free surface has the deformation of

$$\eta(x,y,0)=A_x\cos\left[\pi\left(x+L/2\right)/L\right]+A_y\cos\left[\pi\left(y+B/2\right)/B\right] \tag{11.4}$$

Then, the vessel is set free and allowed to move freely on the frictionless horizontal plane. The tank length L, gravity acceleration g and liquid density ρ are used as bases of the nondimensionalization. The nondimensional time is $\tau=t\sqrt{g/L}$. The mass ratio between the vessel and liquid is $\mu_m=1$. Fig. 11.16(a) shows the vessel's displacement in two directions as well as the wave elevation history at the tank corner $\{L/2,B/2\}$, when $A_x=A_y=0.005$. The linear analytical solution derived in Chapter 9 also shows for comparison. It is clear that the corresponding numerical and analytical solutions have an excellent agreement, which reflects the

effectiveness of the motion decoupling method. To illustrate the nonlinear effects, the initial wave amplitude is further amplified by 10 times with $A_x = A_y = 0.05$. From the comparisons in Fig. 11.16(b), evident distinctions between the linear analytical and nonlinear numerical solutions can be observed. This suggests the necessity of performing the nonlinear sloshing.

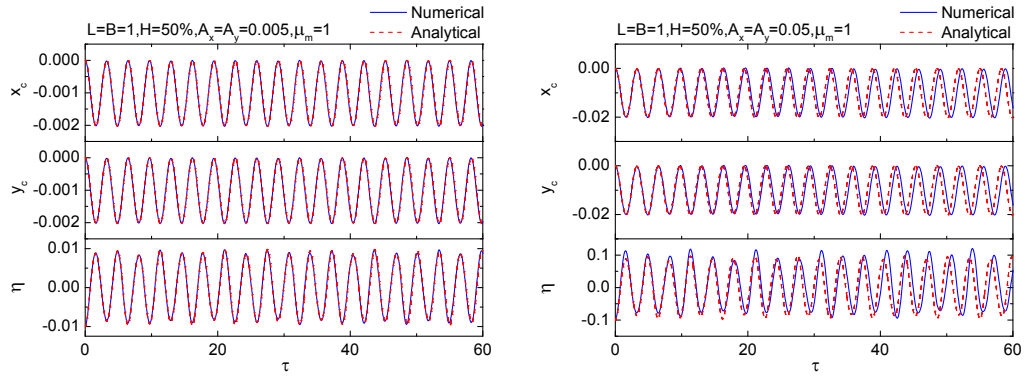

(a) (b)

Fig. 11.16 History of vessel motions and wave elevation at tank corners for (a) $A_x = A_y = 0.005$ and (b) $A_x = A_y = 0.05$

11.4 Coupling of seakeeping and sloshing problem

This section simulates the floating vessel with a nonlinear sloshing tank, which considers the coupling between the seakeeping and sloshing problems. The experiment carried out by Department of Marine Hydrodynamics at NTNU (Rognebakke and Faltinsen 2001) is reproduced by this numerical method. The vessel is floating in the wave flume with the water depth of $1.03m$. As shown in Fig. 11.17, the vessel has a rectangular geometry with length $L_B = 0.4m$, width $B_B = 0.596m$ and draught $H_B = 0.2m$. On the vessel there is a rectangular water tank. Additional weights are placed in the vessel to adjust the draught. The incident wave propagates along the length direction of the vessel while the vessel could move freely in the wave direction along two low-friction rails. To restrain the vessel from drifting off, springs are installed on the vessel. The spring has the stiffness of $30.9\,N/m$, which works as a soft mooring system. The natural frequency of the mooring system is much lower than the considered wave frequencies. It should be noted that, for this case, both the vessel motion and liquid sloshing in the tank only have one

degree-of-freedom.

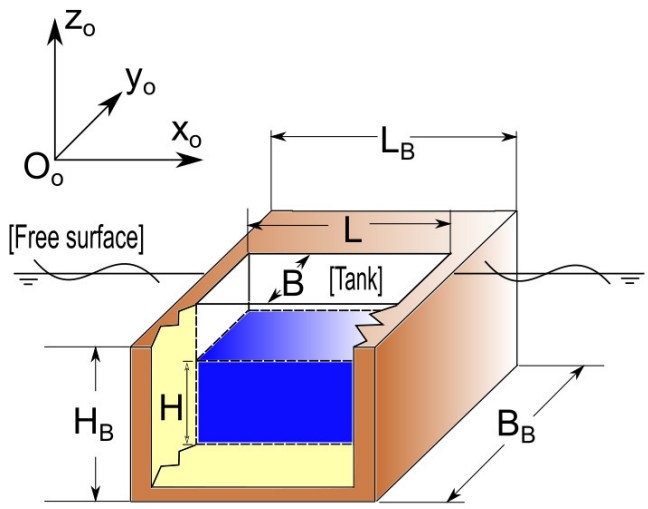

Fig. 11.17 Sketch of vessel with liquid tank

Before considering the sloshing effects on the vessel response, the liquid tank is replaced with the equivalent rigid mass and the tank can be imagined to be frozen. The amplitude of the incident wave is $A = 0.015m$ and the wave frequency is denoted by ω_a. With the help of the springs, in this case, the ramp time can be set to be five wave periods to minimise the transient effects. The surge RAO which means the amplitude ratio between the surge displacement and incident waves is shown in Fig. 11.18. It is clear that the numerical results have a good agreement with the experimental data. This has also validated the present mathematical model for the seakeeping problem.

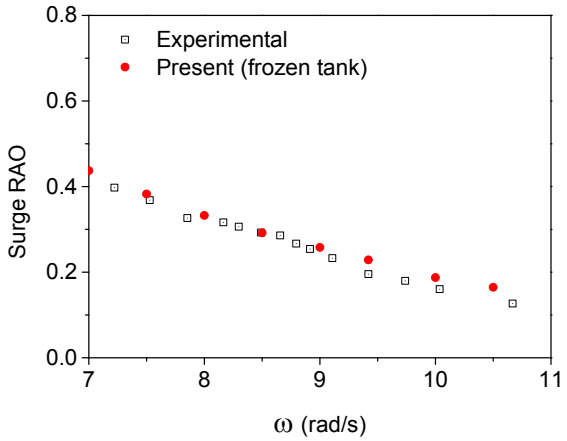

Fig. 11.18 Surge RAO of vessel with frozen tanks

The tank is further filled with water. The tank has the length $L = 0.376m$, width $B = 0.15m$ and water depth $H = 0.184m$. The fundamental natural sloshing frequency of this tank is $\omega_{10} = 8.64\,rad/s$.

In the first case, the incident wave has the amplitude $A = 0.015m$ and frequency $\omega_a = 8\,rad/s$. Note that ω_a is below ω_{10} here. Time histories of the vessel's surge displacement and free-surface run-up along the right tank wall are shown in Fig. 11.19(a). It can be seen that, after a transient state of about 10 seconds, the system gradually gets into a steady stage with nearly constant oscillation amplitude and frequency. From the corresponding FFT analyses in Fig. 11.19(b), it can be observed that both the vessel and liquid oscillations are governed solely by the wave exciting frequency. It is known that, for a forced sloshing problem without damping in the tank, the liquid motion should also be governed by natural sloshing frequencies. Because the sloshing liquid is essentially an oscillation system. As an undamped forced oscillation, the solution can be considered as a sum of harmonic oscillations at the natural frequencies and the excitation frequency. However, when the floating vessel with the liquid tank is placed in incident waves, the system is undergoing the damped forced oscillation, and the solution is only at the external wave frequency. The damping effect is due to the outspread water waves in the external fluid domain. Through the free vessel motion, the sloshing energy in the tank could transfer to the external domain and get dissipated. With a sufficient damping, the liquid sloshing could eventually become the forced oscillation at the excitation frequency. The displacement

history of the vessel with the frozen tank in the same wave condition is also plotted in Fig. 11.19(a). The comparison indicates that the existence of the sloshing tank has reduced the vessel motion amplitude in this case. To explain this, the time history of these forces acting on the vessel by external and sloshing waves is presented in Fig. 11.20. The steady state is also evident from Fig. 11.20(a). Fig. 11.20(b) shows the force histories from $t = 35s$ to $t = 40s$ in detail. It is clear that, during the steady state, the sloshing-induced force is $180°$ out of phase with the force of external waves. In other words, the force from the sloshing liquid acts against the external wave force. The effect of the sloshing tank is similar as that of a passive anti-rolling tank commonly mounted on ships.

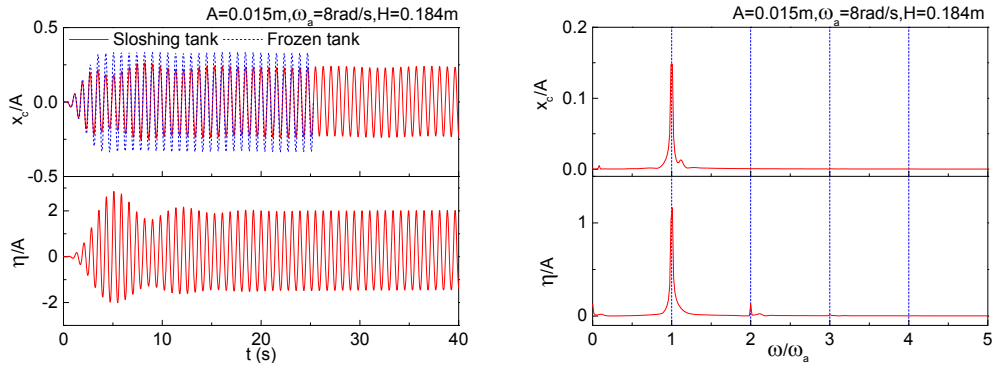

(a) (b)

Fig. 11.19 (a) History of vessel displacement and wave elevation along the right tank wall; and (b) corresponding FFT analyses, for $\omega_a = 8 rad/s$

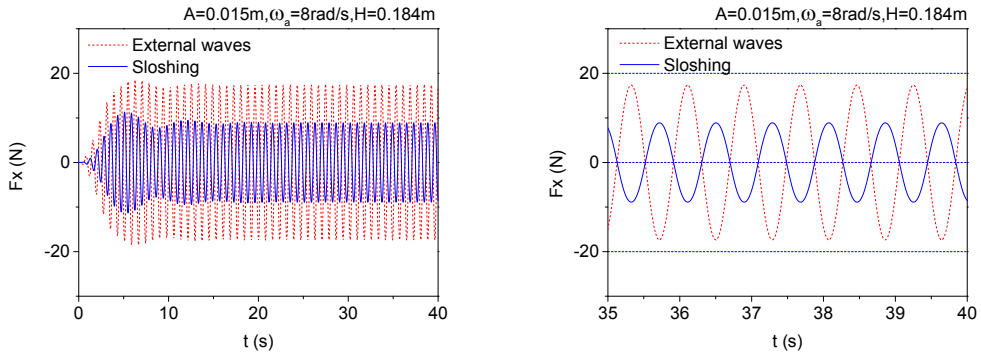

(a) (b)

Fig. 11.20 History of forces acting on the vessel for $\omega_a = 8 rad/s$

The second case considers when the wave excitation frequency is above

ω_{10} , by letting $\omega_a = 10 rad/s$. Histories of the vessel motion and wave elevation along the right tank wall are shown in Fig. 11.21(a). The steady stage could be observed in both time histories. According to the FFT analyses in Fig. 11.21(b), the dominant oscillation frequency of the vessel and liquid in the tank is also the wave excitation frequency. However, unlike the case of $\omega_a = 8 rad/s$, the vessel with a sloshing tank has a larger displacement amplitude than that with the tank frozen. By comparing time histories of the force from external and sloshing waves in Fig. 11.22, it can be found that this time the sloshing-induced force is in phase with the force of external waves.

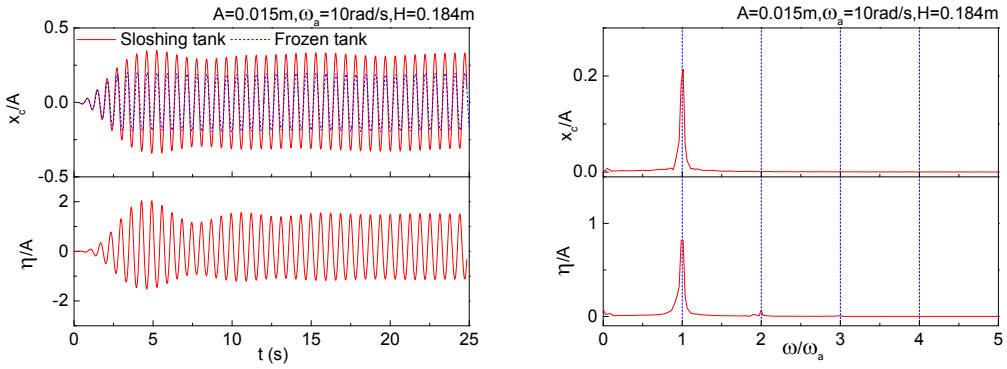

(a) (b)

Fig. 11.21 (a) History of vessel displacement and wave elevation along the right tank wall; and (b) corresponding FFT analyses, for $\omega_a = 10 rad/s$

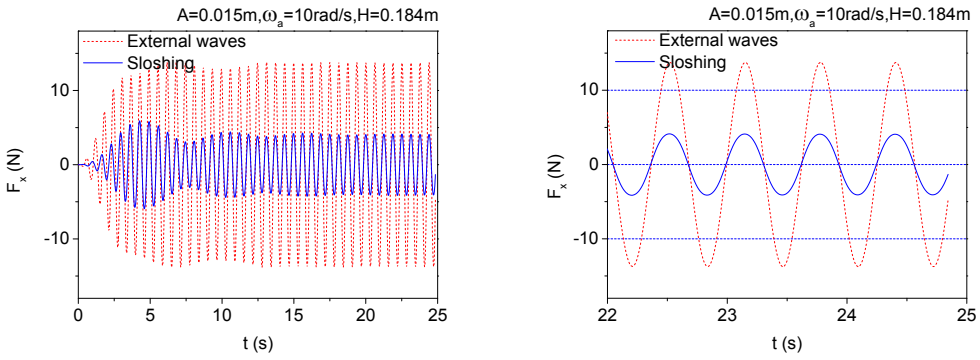

(a) (b)

Fig. 11.22 History of forces acting on the vessel for $\omega_a = 10 rad/s$

From $\omega_a = 8 rad/s$ to $\omega_a = 10 rad/s$, the liquid sloshing acts from reducing to amplifying the vessel motions, due to the phase difference between the sloshing and external wave forces. Then, it would be interesting

to inspect how the phase angle transitions between these two frequencies. So further a series of simulations at frequencies of $\omega_a = 8.2$, 8.3, 8.4, 8.5, 8.64, 8.7, 8.8, 9.0 and $9.5 rad/s$ are conducted.

For cases at $\omega_a = 8 \sim 8.3 rad/s$ and $\omega_a = 8.8 \sim 10 rad/s$, the steady phase could be found from the vessel displacement history. Fig. 11.23 gives the surge RAOs at these frequencies. The calculated results generally have a good agreement with the experimental measurements. It is noticed that at frequencies higher than $\omega = 9 rad/s$, the numerical results are slightly higher than the experimental data. This is because the viscous effect, which normally plays a more evident role for higher frequency situations, is not involved in the present numerical scheme. However, this discrepancy does not affect the general trend of the results. The surge RAOs of the vessel with the frozen tank are also marked in the figure. From the comparison, the great effect of a sloshing tank on vessel motions can be observed. The linear solution calculated by Rognebakke and Faltinsen (2001) is also presented in Fig. 11.23. It can be seen that the linear solution may roughly predict the general trend of the experimental data. However, it could not provide satisfactory RAOs at a wide range of frequencies. This explains why the nonlinearity of the sloshing should be taken into account.

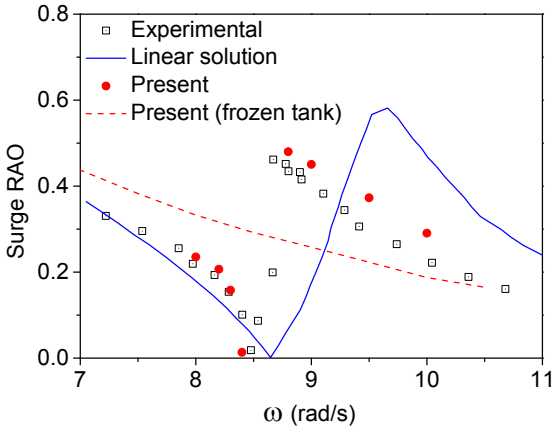

Fig. 11.23 Surge RAO of vessel with sloshing tank

From $\omega_a = 8 rad/s$ to $\omega_a = 8.4 rad/s$ in Fig. 11.23, the motion amplitude of the vessel with the liquid tank is smaller than that of the vessel with frozen tanks. As aforementioned, this is due to the antiphase of the sloshing force

and external-wave force. Also, as ω_a grows and approaches the natural sloshing frequency, the sloshing force increases, which results in the decrease of the surge RAO. A special case of $\omega_a = 8.4 rad/s$ is considered, where the RAO has a very small value. In Fig. 11.24(a), time histories of the vessel displacement and wave elevation in the tank are presented. It is observed that after the transient stage, the displacement amplitude of the vessel with a sloshing tank gradually reduces to a very small value. Correspondingly, the wave elevation amplitude in the tank gradually increases to the maximum and proceeds a steady stage. To explain this, the sloshing and external-wave forces acting on the vessel are compared in Fig. 11.24(b). It is found that two forces have the similar amplitude but are antiphase at the steady state. Thus, the resultant force acting on the floating vessel becomes very small. Further from $\omega_a = 8.8 rad/s$ to $\omega_a = 10 rad/s$, the sloshing-induced force is in phase with the external-wave force, so that RAOs of the vessel with the sloshing tank is larger than that with frozen tanks. Also, as ω_a grows, the sloshing force decreases and the amplification effect of the sloshing tank on the vessel motion reduces.

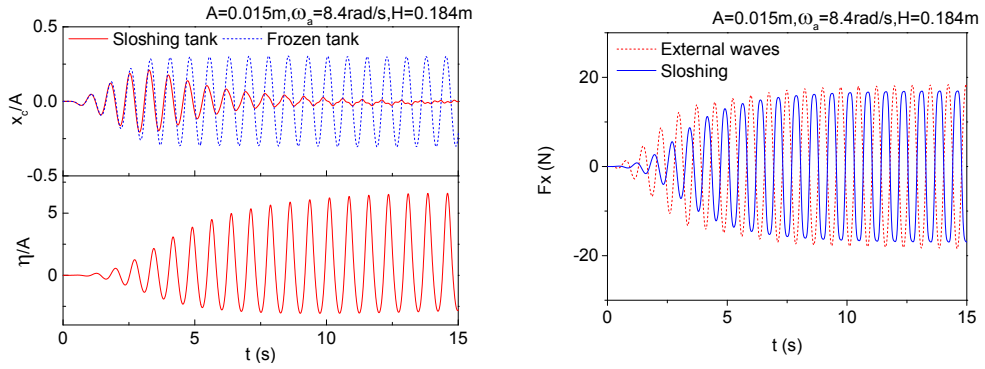

(a) (b)

Fig. 11.24 Time history of (a) vessel displacement and wave elevation along the right tank wall; and (b) forces acting on the vessel, for $\omega_a = 8.4 rad/s$

From Fig. 11.23, it can be seen that an abrupt RAO jump exist in a narrow frequency region between $\omega_a = 8.4 rad/s$ and $\omega_a = 8.7 rad/s$. Three examples with $\omega_a = 8.5$, 8.64 and $8.7 rad/s$ are shown in Fig. 11.25. From the wave elevation histories in Fig. 11.25(a), it can be seen that the sloshing

amplitude keeps increasing until the computation breaks down, which is a near resonance situation. Also in Fig. 11.25(b), the vessel displacement amplitudes show the same increasing trend as time progresses. This is actually a state of instability. To explain this, the hydrodynamics acting on the vessel are compared in Fig. 11.25(c). Firstly, it is found that the phase difference between two force histories is between $0°$ and $180°$, unlike the cases in Fig. 11.19 and Fig. 11.21. In other words, the phase transition exists between the inphase and antiphase states in this frequency range. The phase difference between the sloshing and external forces might make the steady state hard to be observed in the time-domain results. Secondly, after the initial transient stage, the amplitude of sloshing force is always larger than that of the external wave force. The liquid tank does not have any damping function, and the kinetic energy of sloshing waves could only be dissipated after it transfers to the external domain through the vessel motion. However, in the near resonance situation when the sloshing grows to be violent rapidly, the external wave damping might not be efficient enough to dissipate the energy. Then, the mechanical energy in the tank could be accumulated continuously, promoting the unstable state. Given that the sloshing tank has sufficient damping effects, it is still possible for the vessel to reach a steady motion state.

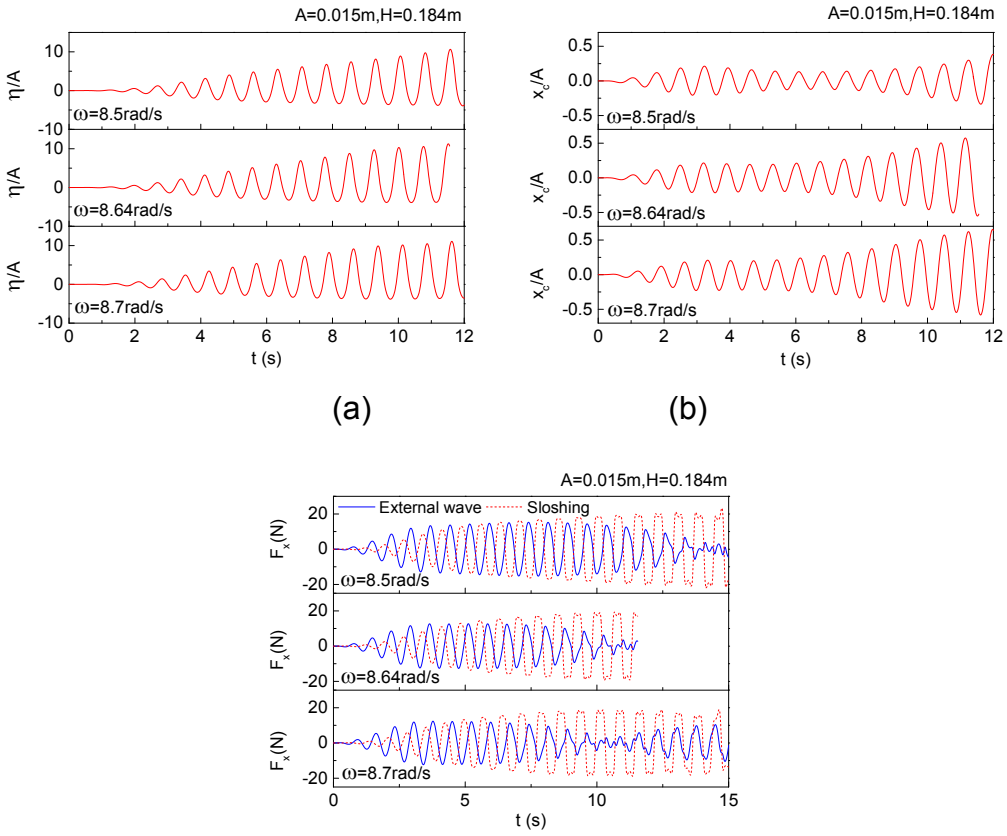

Fig. 11.25 Time history of (a) wave elevation along the right tank wall; (b) vessel displacement; and (c) forces acting on the vessel

11.5 Examples of FLNG vessels

This section would consider the model of FLNG vessels. The vessel is moored to the turret mooring system, so that the vessel is able to rotate freely like the weathervane making its bow against the dominant incident waves. Thus, the FLNG vessel mainly endures the surge, heave and pitch motions. In this section, these three degrees of freedom are considered. Referring to Lee and Kim (2010), the simplified vessel model in Fig. 11.26(a) is adopted. The vessel has a barge shape with the length of $280m$, breadth of $60m$ and draught of $15m$. Four cube tanks with the side length of $40m$ are located symmetrically on the vessel. The bottom of each tank has a $3m$ gap above the vessel keel line. There is also a $3m$ distance between neighbour tanks. Each tank is filled with LNG whose density is about 0.46 times that of the water. The liquid depth in each tank is $20m$. The vessel mass m is set to

maintain the vessel draught. The body-fixed coordinate system $O-xyz$ has its origin O located at the centre of gravity which is $15m$ above the vessel bottom. The Ox axis points to the vessel's stern. The mass radiuses of gyration about the x, y and z axis are $\sqrt{I_{xx}/m}=20m$, $\sqrt{I_{yy}/m}=80m$ and $\sqrt{I_{zz}/m}=80m$, respectively. Additionally, the mooring system with the stiffness of $6.5\times10^5\ N/m$ is applied in the horizontal direction. In the following cases, the amplitude of incident waves is set to be $2m$. The mesh distribution for the hydrodynamic calculations is shown in Fig. 11.26(b). There are 976 and 2218 mesh elements on the vessel surface and fluid boundary of each tank, respectively.

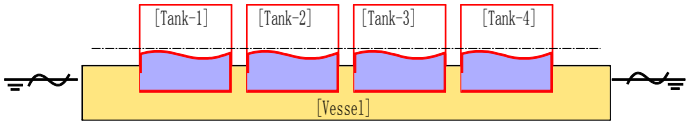

(a)

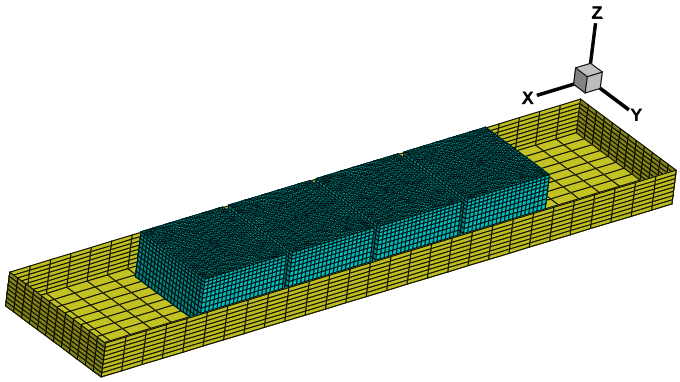

(b)

Fig. 11.26 (a) Sketch of FLNG vessel with cubic tanks; (b) Mesh model of liquid domains

Based on the analytical calculation, it is known that the fundamental natural sloshing frequency of each tank is $\omega_{10}=0.84\,rad/s$. Firstly a specific situation when $\omega_a=0.9\,rad/s$ is considered. The vessel's surge, heave and pitch histories are shown in Fig. 11.27. When all tanks are frozen, the vessel motions after the transient stage are harmonic. Compared with the frozen case, the existence of sloshing tanks has amplified the maximum surge amplitude by about 4 times and the maximum pitch amplitude by about 1.5

times. For the heave motion, it is observed that higher-order oscillations exist in the motion history and the averaged vertical position of the vessel is not constantly zero. These phenomena are due to the effect of nonlinear sloshing tanks. In Fig. 11.28, the forces induced by external waves and sloshing tanks are further compared. It is observed that the horizontal force from the tanks could overtake that from the ocean while the moment by external waves is always larger than the sloshing-induced moment. As time progresses, the sloshing-induced force/moment tends to be inphase with the external-wave force/moment, which explains the amplitude amplification in Fig. 11.27.

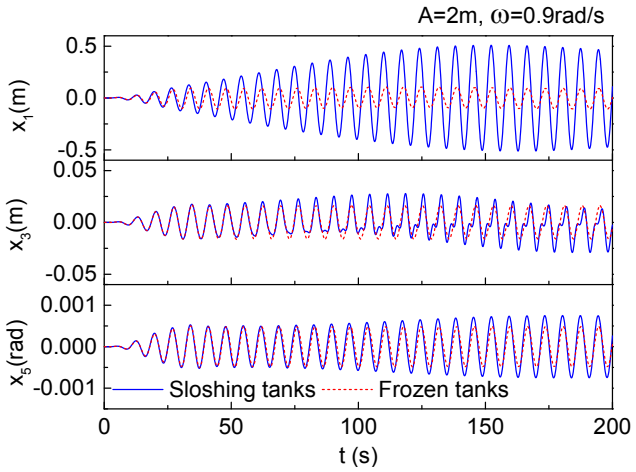

Fig. 11.27 History of vessel surge, heave and pitch for $\omega_a = 0.9 rad/s$

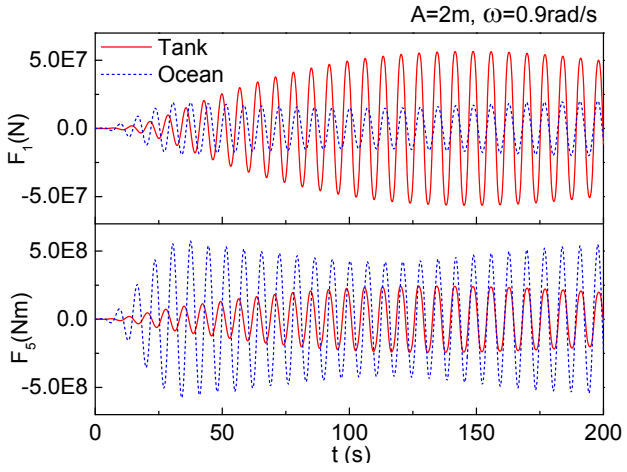

Fig. 11.28 History of force and moment acting on the vessel for $\omega_a = 0.9 rad/s$

Then, incident waves at more frequencies around ω_{10} are employed. The maximum surge, heave and pitch amplitudes of the vessel are plotted in Fig. 11.29. It is observed that, compared with the frozen cases, the existence

of sloshing tanks has evidently affected the vessel's surge amplitude. For $\omega > 0.85 rad/s$, the maximum surge amplitude of the vessel with sloshing tanks overtakes that of the vessel with frozen tanks. The largest effect of sloshing tanks on the vessel's surge occurs at $\omega = 0.88 rad/s$. As ω further increases from $0.88 rad/s$ to $1.0 rad/s$, the maximum surge amplitude of sloshing cases drops from about 7 times to 3 times that of frozen cases. For the heave motion, the sloshing tanks have not changed the heave amplitude much, within the concerned frequency region. For the pitch motion, a critical frequency $\omega_c > \omega_{10}$ exists. Below ω_c, the pitch amplitude is not affected much by sloshing tanks. Above ω_c, the sloshing tanks have amplified the maximum pitch amplitude by about 2 times.

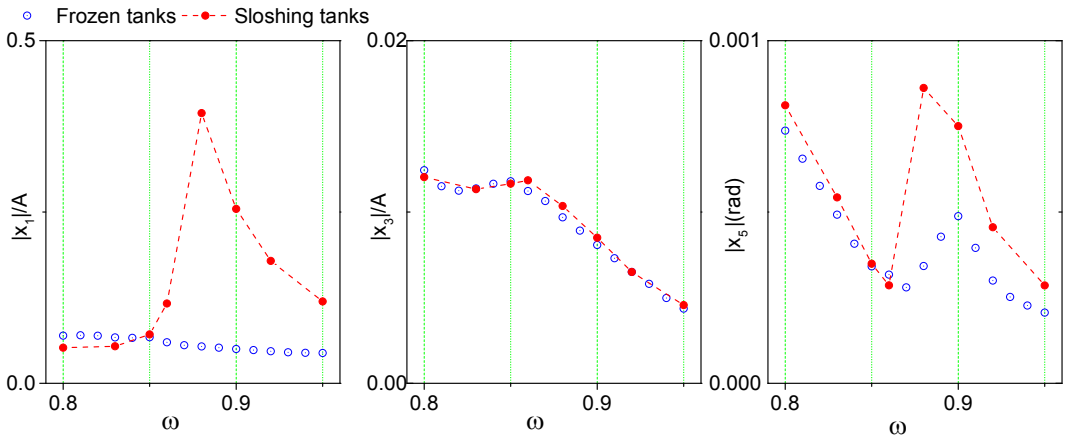

Fig. 11.29 Maximum surge, heave and pitch amplitude of vessel with sloshing tanks

A special situation, i.e. at $\omega = 0.85 rad/s$, could be observed from Fig. 11.29. At this situation, all the surge, heave and pitch amplitudes are not affected much by the existence of sloshing tanks. The vessel motion histories are given in Fig. 11.30, where the surge, heave and pitch displacements are denoted by x_1, x_3 and x_5, respectively. For the heave and pitch motion, the sloshing tanks do not affect the vessel's motion histories much. However, for the surge motion, although the surge amplitudes in both sloshing and frozen cases are similar, they have an evident phase difference. This case shows that the sloshing effects on the vessel motions are not limited to the amplitude.

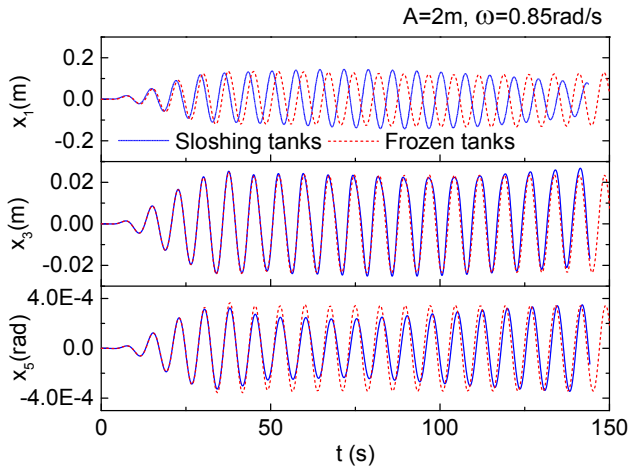

Fig. 11.30 History of vessel surge, heave and pitch for $\omega_a = 0.85\,rad/s$

The coupling of different modes of vessel motions is further studied. Fig. 11.31 compares the vessel surge and pitch histories when one or three degrees of freedom are allowed. It is found that, when the vessel is only allowed to surge or pitch freely (i.e. '1-DoF' in the figure), the motion history tends to be harmonic in this wave environment. However, when three degrees of freedom are released, the maximum amplitude of the vessel motion greatly changes. Thus, when nonlinear sloshing tanks are involved, the surge and pitch modes of the vessel are coupled.

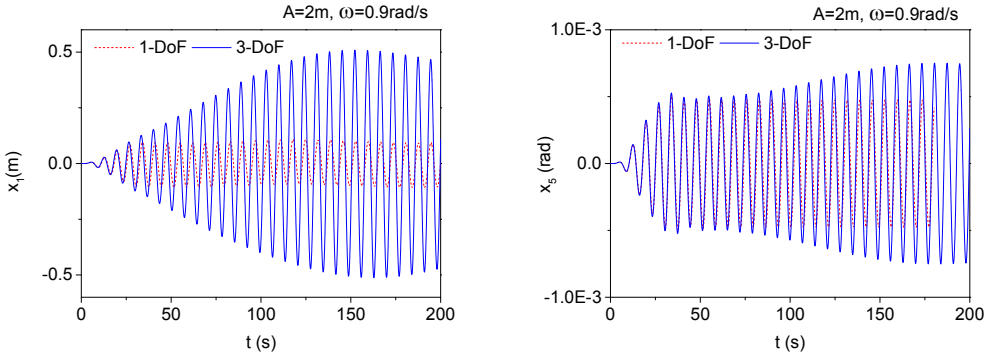

(a) (b)

Fig. 11.31 History of vessel (a) surge and (b) pitch, for $\omega_a = 0.9\,rad/s$

Further the walls between every neighbour tanks are inclined by $\theta = 5\pi/24$, and study the vessel with wedged tanks (as described in Chapter 6). Except for the tank geometry, all the other parameters are kept the same as the previous case. The vessel may surge, heave and pitch freely. The sketch and mesh model for the vessel with wedged tanks are shown in Fig.

11.32. From Chapter 6, it is known that the natural sloshing frequencies of these four tanks are $\omega_{10} = 0.787$, 0.866 , 0.747 and $0.854 rad/s$, respectively.

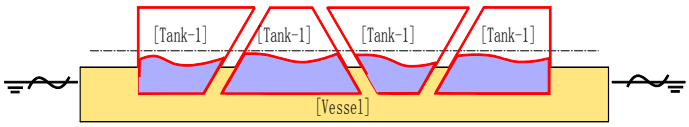

(a)

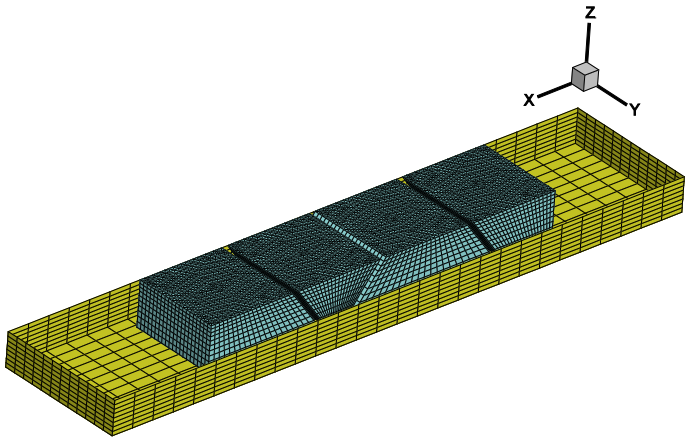

(b)

Fig. 11.32 (a) Sketch of FLNG vessel with wedged tanks; (b) Mesh model of liquid domains

Fig. 11.33 has shown the maximum surge, heave and pitch amplitudes of the vessel in incident waves at different frequencies. It is interesting to find that, the liquid sloshing in wedged tanks does not affect the vessel's motion amplitude as great as that in rectangular tanks. To explain this, the situation of $\omega = 0.9$ is taken for example and the free-surface elevation histories in each tank are compared in Fig. 11.34. The corresponding sloshing-induced forces are shown in Fig. 11.35. Subfigures (a) refer to the case when the tanks are rectangular, and subfigures (b) indicate the situation of wedged tanks. It is found that, the sloshing liquids in all rectangular tanks are always in phase and with similar amplitude, so that the sloshing-induced forces in each tank always have the same direction. However, for the vessel with wedged tanks, the sloshing liquids in all tanks are neither inphase nor of similar amplitude. According to the resultant forces from all tanks in Fig. 11.35, it can be observed that the amplitude of the resultant force from the rectangular tanks

is about two times larger than that from wedged tanks. For the near resonance cases, this difference would be more evident. Using the wedged tanks, even though the large-amplitude sloshing occurs in one tank, the sloshing in the rest of the tanks could still be gentle with a different phase. This would reduce the resultant forces at any instant, and further minimises the sloshing effects on the vessel motions. This observation is consistent with the prediction in Chapter 6. Thus, the design of the FLNG vessel with wedged tanks is preliminarily verified to be effective.

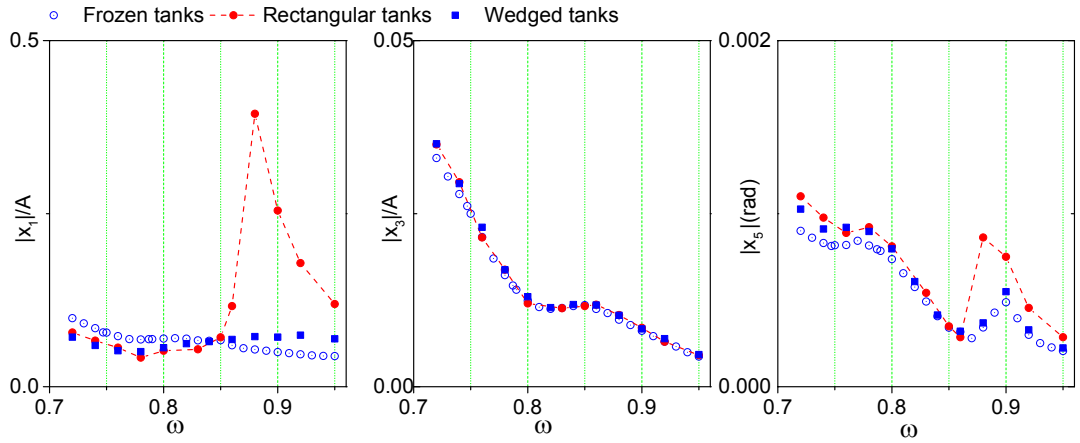

Fig. 11.33 Maximum surge, heave and pitch amplitude of vessel with sloshing tanks

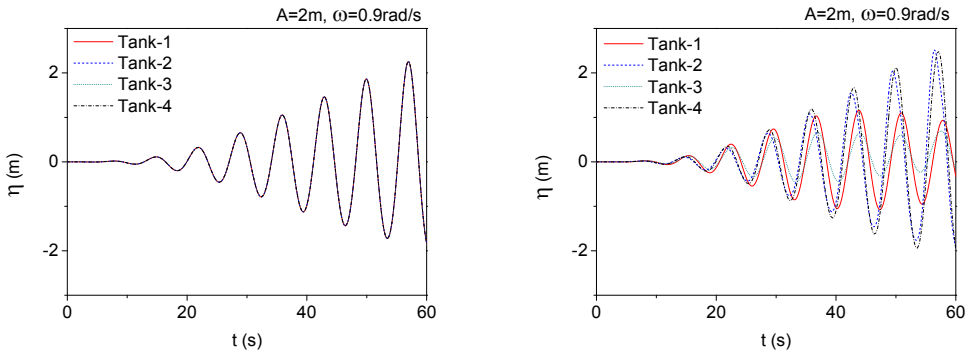

(a) (b)

Fig. 11.34 Histories of free-surface elevations in (a) rectangular tanks and (b) wedged tanks of floating vessel

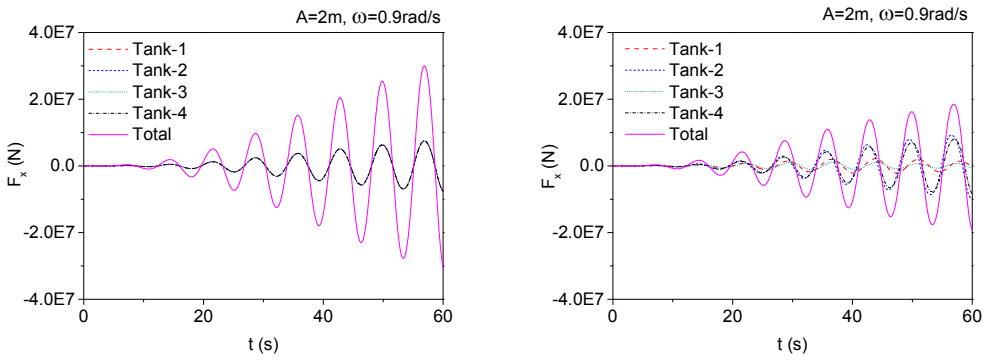

(a) (b)

Fig. 11.35 Histories of sloshing forces in (a) rectangular tanks and (b) wedged tanks of floating vessel

11.6 Conclusions

This chapter performs the time-domain simulation of the floating vessel with nonlinear sloshing tanks. The motion decoupling method derived in Chapter 10 is used, so that the exact vessel's acceleration at any instant could be calculated explicitly in one step without iterations. A potential-flow numerical scheme based on this method is developed, which simulates the seakeeping and sloshing problems using the impulse-response function and boundary element method, respectively. Simulations of the seakeeping and sloshing problems are firstly verified step by step.

Then, the floating vessel with a single tank is investigated. The vessel is allowed to surge freely. The calculated surge RAOs have a good agreement with the experimental measurements. Effects of the sloshing-induced forces on vessel motions are analysed in details. It is found that there is a special narrow frequency region around the natural sloshing frequency. If the wave frequency ω is outside this region, the vessel motion could reach a steady state. For ω at the lower side of the region, the sloshing-induced force is $180°$ out of phase with the external-wave force, so that the existence of the sloshing tank could reduce the vessel motion. At a certain frequency, the sloshing and external-wave forces might even greatly cancel each other leading to a small vessel displacement. For ω at the higher side of the region, the sloshing-induced force is in phase with the external-wave force, and the vessel with a sloshing tank has a larger displacement amplitude than

that with tanks frozen. Within the narrow region, the uncertain phase transition exists between the inphase and antiphase states, making the steady state hard to be observed in time-domain results.

Two examples of the FLNG vessel are simulated. The first example concerns the vessel with four rectangular sloshing tanks. It is found that the sloshing tanks could change the vessel's surge and pitch behaviour evidently, but have no evident effects on the heave motion. The phase of the vessel motions may also be affected. Due to the existence of nonlinear sloshing tanks, the surge and pitch modes of the vessel are coupled. The second example considers the vessel with four wedged sloshing tanks. It is found that, unlike the case of rectangular tanks, the sloshing-induced forces in wedged tanks are neither inphase nor with the similar amplitude. Even though the large-amplitude sloshing occurs in one tank, the sloshing in the remaining tanks could still be gentle with a different phase. This would reduce the resultant forces at any instant, and further minimise the sloshing effects on the vessel motions.

Chapter 12 Concluding remarks

12.1 Summary and conclusions

This thesis considers the hydrodynamic problems related to a new ocean engineering application, the floating liquefied natural gas (FLNG) vessel. The nonlinear liquid sloshing in tanks and its coupling with vessel motions are studied within the potential-flow theory. The main body of the research is constituted by three parts: sloshing in wall-sided tanks, sloshing in non-wall-sided tanks, and coupling of sloshing and vessel motions. The key contributions of this thesis can be listed as follows:

1. Study on the second-order sloshing resonance in 3D tanks (Ch 5)
2. Development of a BEM technique for natural sloshing frequencies/modes (Ch 6)
3. Development of the improved semi-Lagrangian method for the free surface updating near non-vertical wall (Ch 7)
4. Study on the resonant sloshing in wedged tanks (Ch 8)
5. Derivation of the analytical solution for the coupling between sloshing and vessel motions (Ch 9)
6. Derivation of a motion decoupling method for floating vessel with nonlinear tanks (Ch 10)
7. Study on the floating vessel with nonlinear sloshing tanks (Ch 11)
8. Study on an improved design of FLNG vessel (Ch 1, 6 and 11)

The contributions of Item 5 and 6, Item 2 and 3, and Item 1, 4, 7 and 8, are mainly focusing on the mathematical derivations, numerical techniques, and physical observations, respectively.

The detailed conclusions drawn from this study can be summarized as follows.

- **Nonlinear simulation of sloshing in 3D rectangular tanks (Chapter 4)**

In-house FORTRAN codes based on BEM are developed to simulate the nonlinear sloshing in 3D wall-sided tanks. Nonlinear boundary conditions satisfied on the instantaneous free surface are taken into account. In-house Delaunay triangulation codes are developed to generate the 3D surface mesh for BEM computations. A local surface fitting method is used to calculate tangential spatial derivatives of the velocity potential and wave elevation on the free surface. A shared-memory parallel procedure based on OpenMP has been utilised for the efficiency improvement.

A series of classical sloshing problems in 3D rectangular tanks are simulated. The sloshing problems in either fixed or forced oscillating tanks have been considered. The present BEM results are compared with the analytical solution, experimental data or results from other numerical methods (e.g. FEM and FDM). In all cases, the comparisons have shown good agreements. Thus, the mathematical model of the numerical scheme has been validated, and the numerical accuracy has been verified.

- **Second-order resonance in 3D rectangular tanks (Chapter 5)**

Associated with the sloshing phenomenon, the resonance is of major concern. The classical resonance actually indicates the first-order resonance which is triggered by the tank oscillation at certain natural sloshing frequencies. This study further verifies that a distinct resonance (i.e. the 'second-order resonance') also exists in 3D rectangular tanks, using the developed numerical scheme. It is found that after a sufficiently long time, the second-order resonance could become as dominant as the first-order resonance. Increasing the excitation amplitude could evidently accelerate its occurrence. By these observations, it could be confirmed that the resonant sloshing does not have to be triggered at the natural frequencies.

- **Modal analysis for sloshing in wedged tanks (Chapter 6)**

For the FLNG vessel, one of the most dangerous situations is when the resonant sloshing occurs simultaneously in all tanks, which endangers vessel motions. In order to mitigate this risk, this study proposes an alternative design. The wall-sided tanks are replaced with various wedged ones, aiming to diversify resonance conditions (i.e. natural sloshing frequencies) in

different tanks.

A numerical approach with the help of BEM is developed to calculate the natural sloshing frequencies and corresponding modes for these wedged tanks. Effects of the inclined tank wall on natural sloshing frequencies/modes are identified. It is found that, in general, the fundamental natural frequencies of four tanks become more dispersed as the incline angle increases. The natural frequencies of diverging tanks are more sensitive to the incline angle compared with those in converging tanks. The vessel is further excited by sway, roll, surge and pitch motions at the resonance condition of each sloshing tank. The linear sloshing behaviours in these wedged tanks are studied. The observations suggest that using this design, even though the resonance occurs in one tank, the sloshing in remaining tanks could still be gentle. This is expected to minimise the sloshing effect on the vessel motion.

- **Improved semi-Lagrangian free-surface updating procedure (Chapter 7)**

The semi-Lagrangian (SL) procedure is conventionally used for updating the nonlinear free surface in the time domain, which is also adopted by Part I of this thesis. However, the SL procedure is only available to cases when the body surface is vertical near the waterline. Thus, this thesis introduces an improved SL procedure which avoids the 'vertical-wall' limitation of the SL procedure. The reliability and accuracy of the improved SL procedure together with the BEM solver have been verified by comparing with the OpenFOAM CFD software, through the simulation of the nonlinear sloshing in wedged tanks.

- **Resonant sloshing in wedged tanks (Chapter 8)**

The improved SL free-surface updating procedure together with the BEM solver is used to investigate the resonant sloshing in 3D wedged tanks. Two types of resonances are mainly considered. One is the classical resonance induced by a lateral tank oscillation at the lowest natural sloshing frequency in the length or width direction of the tank. Featured sloshing phenomena in wedged tanks are observed. The other type is Faraday waves due to the tank heave. Effects of the excitation frequency, acceleration amplitude, unstable

regions and initial free-surface disturbance on behaviours of Faraday waves in wedged tanks are investigated systematically.

It is particularly found that, due to the geometric nonlinearity caused by inclined tank walls, the actual natural sloshing frequency keeps changing as waves running up. So, during the resonance, the wave amplitude in diverging tanks may increase to a peak and then start to drop. In all considered cases, the maximum wave amplitude in the diverging tank is generally smaller than that in the corresponding rectangular tank in the same condition. For converging tanks, the wave peak has an evident trend to overturn as the wave amplitude grows. In practice, the resulted wave breaking is expected to dissipate the energy and reduce the sloshing violence. Thus, the wedged tanks have shown the possibility to deduce the maximum wave amplitude or the sloshing violence during the resonance.

- **Analytical study of coupling between sloshing and vessel motions (Chapter 9)**

The transient coupling between the vessel motion and liquid sloshing in multiple tanks is investigated. External ocean waves are not involved, so that the vessel motion is only excited by the liquid sloshing in tanks. The analytical solution for this coupling problem has been derived based on the potential-flow theory. The approach to determine natural frequencies of the coupling system is also given. The vessel with one or more rectangular tanks is considered for cases studies. Effects of factors, such as the vessel mass, number of tanks, tank configuration, and initial free-surface deformation on the vessel motion, liquid sloshing, and mechanical energy components of the system are studied systematically.

Among conclusions drawn in Chapter 9, the followings are highlighted. (1) Natural frequencies of the complete coupling system may not be identical to natural sloshing frequencies in tanks. (2) The free-surface deformation of Mode-1 in a tank has the major influence on vessel motions. (3) As the vessel mass grows, both the natural frequency and response amplitude of the vessel oscillations decrease. (4) Consider a system with the constant mass ratio between the vessel and liquids. With the same mechanical energy as input,

the liquid sloshing has greater effects on the motion of the vessel with a shallower tank. (5) For the vessel with different tanks, the fluid's mechanical energy is less likely to exchange among tanks as the tank configuration becomes more distinctive.

- **Motion decoupling method for floating vessel with nonlinear sloshing tanks (Chapter 10)**

For the floating vessel with nonlinear sloshing tanks, time-domain methods have to be used for the simulation. In time-domain simulations, the sloshing and seakeeping problems are coupled. To be specific, at each time step, the calculation of sloshing-induced forces always requires the knowledge of the vessel's acceleration at that instant. Meanwhile, the vessel's acceleration is dependent on the knowledge of sloshing forces at the same time. An iteration procedure is usually used to solve this mutual determination. However, the iteration procedure has limitations such as time-consuming, uncertain iteration number to achieve the convergence, truncation error and unguaranteed convergence for multiple domains.

So, this thesis has derived an alternative method to decouple the seakeeping and sloshing problems. The method could be considered as an extension of the modal decomposition method for floating vessel simulations. Using this method, the exact vessel's acceleration at any instant could be calculated explicitly in one step without iterations, which could greatly reduce the CPU consumptions and avoid other limitations of the iteration procedure. The numerical scheme based on this method is further developed, which models the seakeeping and sloshing problems using the impulse-response function and boundary element method, respectively.

- **Simulation of floating vessel with nonlinear sloshing tanks (Chapter 11)**

Time-domain simulations of the floating vessel with nonlinear sloshing tanks are performed based on the motion decoupling method derived in Chapter 10. The floating vessel with a single tank is firstly investigated. The vessel is allowed to surge freely. The calculated RAOs have a good agreement with the experimental measurements. From detailed analyses, it is

found that the sloshing-induced force could be $180°$ out of phase or in phase with the external-wave force, so that the existence of the sloshing tank could reduce or amplify the vessel motion. At a certain frequency, the sloshing and external-wave forces might even greatly cancel each other, leading to a small vessel displacement. Within a narrow region around the natural sloshing frequency, the uncertain phase transition exists between the inphase and antiphase states.

Two examples of the FLNG vessel are further simulated. The first example concerns the vessel with four rectangular sloshing tanks. It is found that the sloshing tanks could change the vessel's surge and pitch behaviour evidently but have no evident effects on the heave motion. Due to the existence of nonlinear sloshing tanks, the surge and pitch modes of the vessel are coupled. The second example considers the vessel with four wedged sloshing tanks. It is found that, even though the large-amplitude sloshing occurs in one tank, the sloshing in remaining tanks could still be gentle with a different phase and amplitude. This would reduce the resultant sloshing forces and further minimise the sloshing effects on the vessel motion. In other words, the design of the FLNG vessel with wedged tanks has been verified to be effective.

12.2 Limitations and suggestions for future work

The findings presented in this thesis have provided some new insights into the nonlinear sloshing and its interaction with vessel motions. However, the range of applicability of the present numerical schemes should also be stated explicitly here.

Firstly, all studies in this thesis are based on the potential-flow theory. So the observations in this thesis are limited to ideal and flow-irrotational fluids. In practice, the LNG is normally mixed with a cluster of gas bubbles, and may have the viscosity and compressibility. At present, the property of this complex liquid is still unclear. So, far more efforts are still needed to make clear at what extent this type of liquid can be well described by the potential-flow theory.

Secondly, this thesis mainly focuses on the global motion of the

non-violent sloshing liquid. So, the amplitude of the excitation acting on the tank is usually set to be very small, in order to avoid violent local effects. At a violent situation, the liquid in a low-filling tank may easily run up along the tank wall and impact on the side wall. The waves in a high-filling tank may impact on the tank top. During these impact events, violent local phenomena such as the wave breaking, splashes, and air pockets are often generated. To investigate these violent local phenomena and their effects on the global vessel motions, the NS-based CFD software may be a better option than the present numerical scheme.

Thirdly, it is about the improved-SL free-surface updating procedure. This method could only deal with the nearly single-valued free-surface deformation. Large overturning waves are left out of consideration. The free-surface jet flows are not considered, neither. Because, at the slope of a steep wave, the boundary elements might be highly stretched, which could affect the numerical accuracy.

Practical applications of the present work, along with some guidelines recommended for designers, can be summarised as follows. Firstly, the BEM scheme developed for nonlinear sloshing simulations in Chapter 4 and 7 can be used to model the transient LNG sloshing in a tank. Long time simulations (e.g. over hundreds of excitations) are not recommended, due to the accumulation of numerical errors. In practice, the viscosity effect of the liquid may also be important and affect the sloshing behaviour after a sufficiently long time. Secondly, besides the natural sloshing frequencies, excitation frequencies that can trigger the second-order resonance (as in Chapter 5) should also be considered during the verification stage of the tank design. Thirdly, the BEM technique developed in Chapter 6 can be used to estimate the natural sloshing frequencies in a practical LNG tank without difficulty. Further, for the floating vessel simulations, the present numerical scheme is reliable for the calculation of surge, heave and pitch motions, when the external wave length is smaller than about two times of the vessel length. Additionally, for the vessel with wedged tanks, the tank length at half height of each wedged tank is recommended to be the same. Then, the incline angle of the tank wall can be recommended to be as large as possible.

Continued to the progress in this study, some suggestions for the future research directions are made as follows.

- **Violent sloshing**

Before docking for inspection and overhaul, the FLNG vessel is continuously moored at the location for around 20-25 years. So it could experience any complex sea state including cyclones, during the period of service. So it is necessary to further investigate the effects of violent sloshing (including the wave breaking, wave slamming, formation of air pocket and gas bubbles, and elastic vibration of local tank walls). In this situation, the Navier-Stokes solvers should be adopted for the sloshing simulation.

- **Multiple floating bodies**

During the offloading operations, the FLNG vessel and LNG carrier may be arranged in a side-by-side configuration. This multi-body system is expected to have complex interactions with ocean waves. So the responses of these two vessels should be investigated to guarantee the operation safety during the LNG offloading in real sea states.

- **Complex environment**

The FLNG vessel could be applied in a complex ocean environment, with the wind, current and floating ice. So effects of these environmental elements on the dynamic properties of the floating vessel with sloshing tanks should be identified.

- **Hydroelastic problem**

The FLNG vessel is so huge that the lowest natural frequency of the structure may fall into the range of wave encounter frequencies. Therefore, effects of the structural vibrations should be investigated. The hydroelastic problems involve the mutual interaction of the elastic vessel hull with external ocean waves and sloshing in tanks.

Appendix A Solid angle calculation for BEM

The solid angle at each mesh node could be calculated geometrically (Mantic 1993). Take the $i-$th mesh node as the centre and construct a spherical surface with a small radius ε, as in Fig. A.1. Then, the solid angle at the node is defined as

$$c_i = \left(S_\varepsilon / 4\pi\varepsilon^2 \right) \cdot 4\pi = S_\varepsilon / \varepsilon^2 \tag{A.1}$$

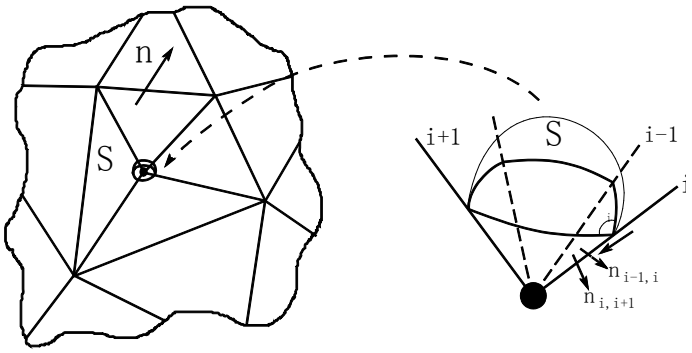

Fig. A.1 Description of solid angle

where S_ε is the area of the spherical surface truncated by N neighbour elements in the fluid domain. The S_ε can be calculated as

$$S_\varepsilon = \varepsilon^2 \left(\sum_{i=1}^{N} \theta_i - (N-2)\pi \right) \tag{A.2}$$

The θ_i is the included angle between two adjacent elements, which could be expressed as

$$\begin{aligned} \theta_i &= \pi + \operatorname{sgn}\left[\left(\mathbf{n}_{i-1,i} \times \mathbf{n}_{i,i+1} \right) \cdot \tau_i \right] \arccos\left(\mathbf{n}_{i-1,i} \cdot \mathbf{n}_{i,i+1} \right) \quad \text{with} \\ \operatorname{sgn}(x) &= \{-1, x<0; 0, x=0; 1, x>0\} \end{aligned} \tag{A.3}$$

where $\mathbf{n}_{i,i+1}$ and $\mathbf{n}_{i-1,i}$ are unit normal vectors of two adjacent elements, and τ is the unit vector on their shared edge pointing to the node. The application of this technique could be found in literature such as Shao (2010).

Appendix B Surface mesh generation technique

To generate the mesh on a surface, a $\xi-\varsigma$ plane is firstly set, based on which the surface could be considered as a single-valued function. The surface projection on the plane could be discretized into mesh elements. Then, the 2D mesh is mapped back to the surface. In this study, the mesh generation algorithm is based on the Delaunay triangulation (e.g. Yu et al 1999).

Take the surface projection of Fig. B.1 for example. The boundary of the projection is expressed by a series of boundary nodes $P_i(i=1,2,\cdots,N)$. The density of the node distribution could reflect the expected mesh coarseness. Coordinates of P_i on the plane are expressed as (ξ_i,ς_i).

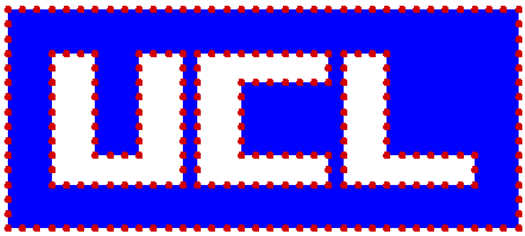

Fig. B.1 Boundary nodes of a concerned domain

Then, a background square which could cover all the boundary nodes is set up. Two diagonal vertexes of the square are connected as in Fig. B.2(a), forming two initial triangular elements. The first node P_1 is inserted in the square. All existing triangles whose circumcircle could cover P_1 consist the 'covering polygon'. Then, all triangular elements within the polygon are deleted, and new elements are created by connecting P_1 with each polygon vertex. Further, other boundary nodes are inserted one by one. The same rule is applied on each P_i to delete and create triangular elements. Fig. B.2(b) to (e) have shown the generated mesh when the first four nodes are inserted. Having processed all boundary nodes, the initial triangular mesh elements can be obtained as in Fig. B.2(f).

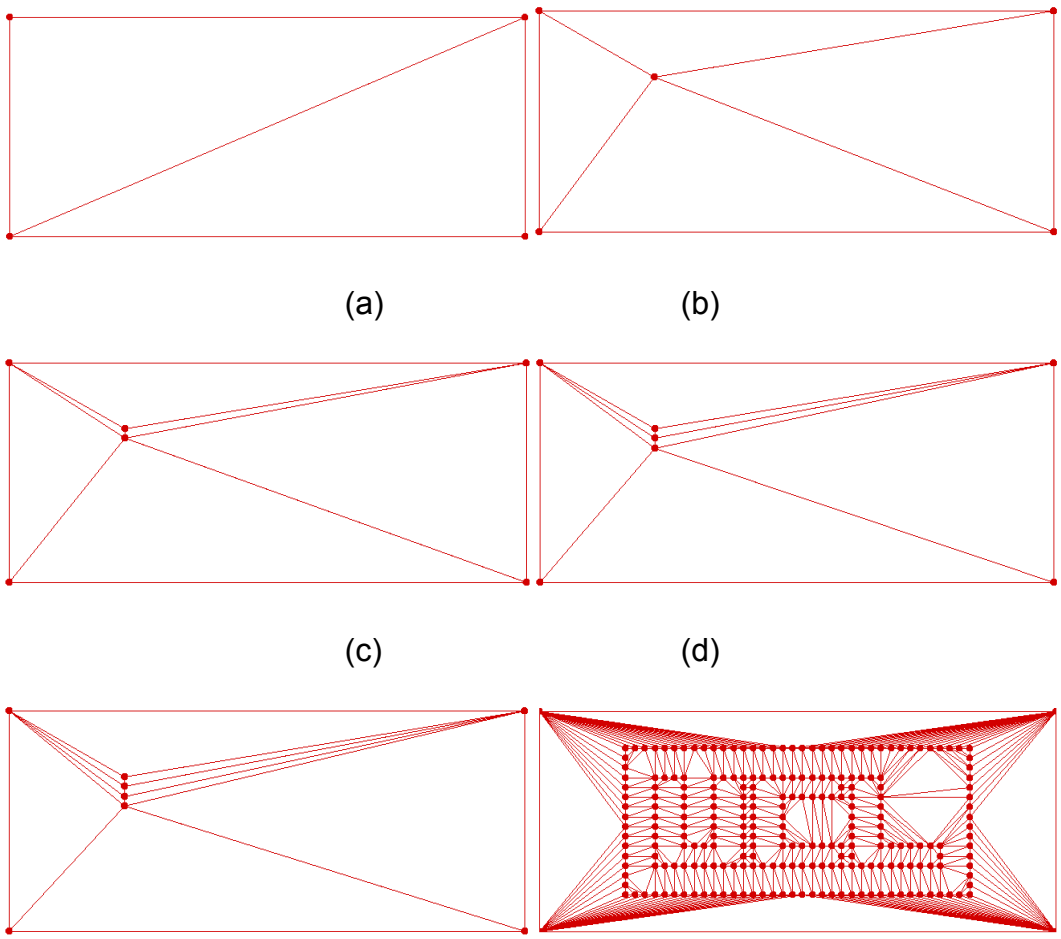

Fig. B.2 Initial triangulation

As shown in Fig. B.2(f), not all triangular elements are located within the surface projection. Mesh elements outside the area of the projection should be deleted. The following rules are further set. The (x_p, y_p) is used to denote the centroid of each triangular element. Draw a vertical line $x = x_p$ through the centroid and it would intersect with a certain number of boundary segments. Count the number of intersection points whose y coordinate is smaller than y_p. If the number is odd, this triangular element must be outside the projection area. Fig. B.3(a) has distinguished the elements inside and outside the surface projection. Removing the irrelevant elements yields an initial rough mesh as in Fig. B.3(b).

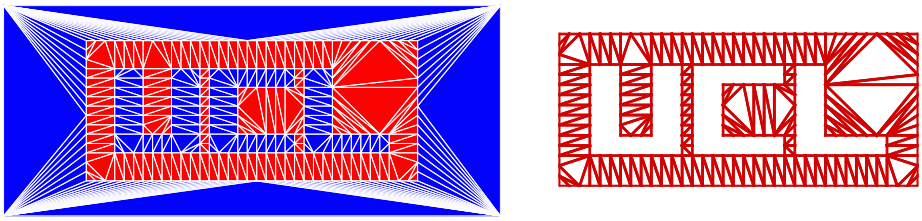

(a) (b)

Fig. B.3 Separation of elements

Since the initial mesh is too coarse to be used for numerical computation purposes. Further refinement on the mesh is necessary. Before moving forward, two terms are firstly introduced. The first one is the 'characteristic length (CL) of a node' which denotes the characteristic length of edges around a node. For a boundary node, the CL is defined as the averaged length of its two neighbour segments. For any internal node P within the triangle $V_1V_2V_3$, its CL is defined as

$$L(P)=\frac{L(V_1)/l_1+L(V_2)/l_2+L(V_3)/l_3}{1/l_1+1/l_2+1/l_3} \tag{B.1}$$

where $L(V_i)$ denotes the CL of the vertex V_i and l_i is distance between P and V_i. The other term is 'characteristic circumcircle radius (CCR)' of a triangular element. The CCR is defined as

$$C_R=r/L(P) \tag{B.2}$$

where r is the circumcircle radius of the triangle and $L(P)$ is the CL of its circumcenter P. The minimum value of CCR is $1/\sqrt{3}$, in the situation of an equilateral triangle. Then, the CL of all boundary nodes and CCR of all triangles are calculated. Figure out the triangle with the maximum CCR and create an internal node at its circumcenter. Delete all triangles whose circumcircle could cover P_1 and create new elements within the covering polygon. Thus, the list of the mesh elements has been updated. Repeat this procedure of searching the largest CCR, inserting new node and create new elements. The iteration stops if the maximum CCR is smaller than a given limitation such as 1.0. The first five steps of the mesh refinement are illustrated in Fig. B.4 (a) to (e) and Fig. B.4 (f) presents the final mesh.

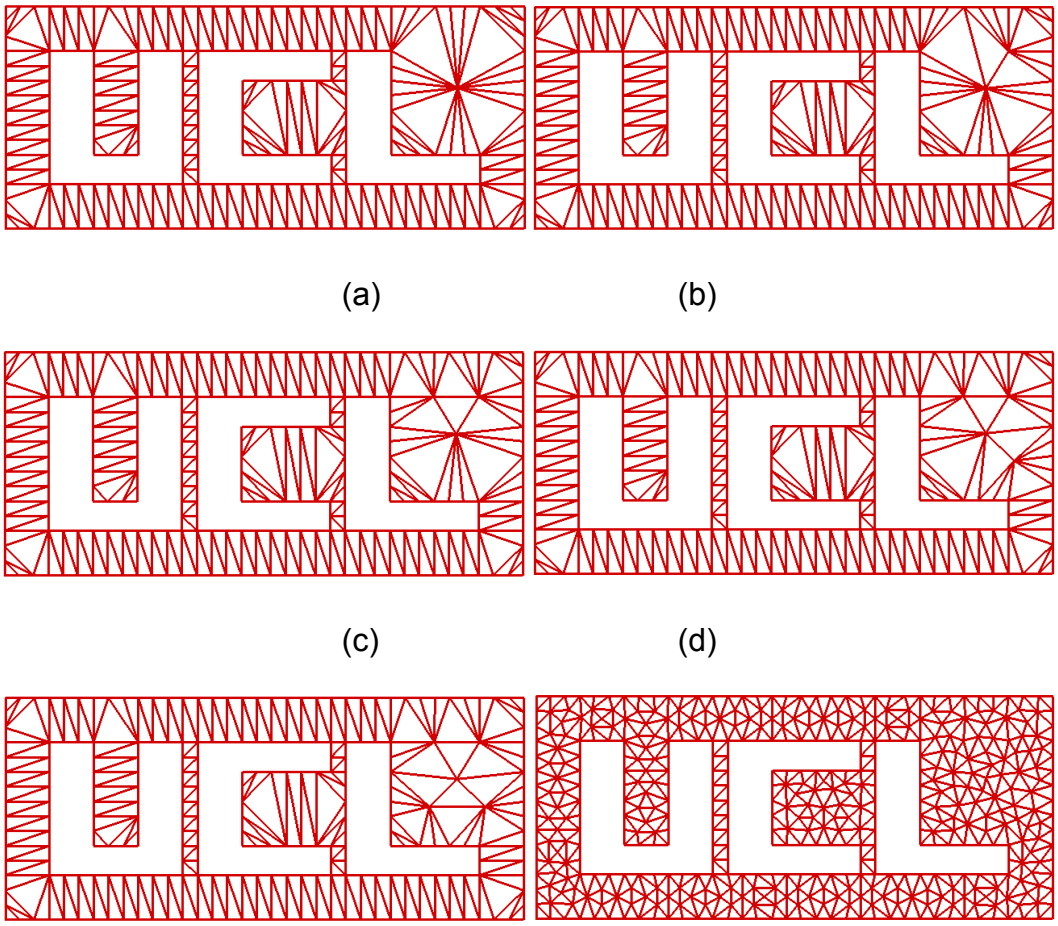

Fig. B.4 Mesh refinement

References

Abramowitz, M., I. A.Stegun, Handbook of mathematical functions with formulas, graphs, and mathematical tables, Dover Publications, New York, 1964.

Abramson, H.N., Dynamic behavior of liquids in moving containers, NASA-SP-106, 1966.

Alemi Ardakani, H., T.J. Bridges, Dynamic coupling between shallow-water sloshing and horizontal vehicle motion, Eur. J. Appl. Math. 21 (2010) 479-517.

Alemi Ardakani, H., T.J. Bridges, M. R. Turner, Resonance in a model for Cooker's sloshing experiment, Eur. J. Mech. B-Fluid. 36 (2012) 25-38.

Aliabadi, S., A. Johnson, J. Abedi, Comparison of finite element and pendulum models for simulation of sloshing, Comput. Fluids 32 (2003) 535-545.

Atluri, S.N., T. Zhu, A new Meshless Local Petrov-Galerkin (MLPG) approach in computational mechanics, Comput. Mech. 22 (1998) 117-127.

Babarit, A., NEMOH BEM documentation, Technical Report, Ecole Centrale de Nantes, 2014, URL: http://lheea.ec-nantes.fr/doku.php/emo/nemoh/start.

Bai, W., R. Eatock Taylor, Fully nonlinear numerical simulation of fixed and floating flare structures, Ocean Eng. 36 (2009) 223-236.

Becker, A.A., The boundary elements method in engineering: a complete course, McGraw-Hill Book Company, UK, 1992.

Behr, M., F. Abraham, Free-surface flow simulations in the presence of inclined walls, Comput, Methods Appl. Mech. Engrg 191 (2002) 5467-5483.

Benjamin, T.B., F. Ursell, The Stability of the Plane Free Surface of a Liquid in Vertical Periodic Motion, Proc. R. Soc. Lond. A. 225 (1954) 505-515.

Cao, Y., R.F. Beck, W.W. Schultz, Nonlinear computation of wave loads and motions of floating bodies in incident waves, 9th IWWWFB, 1994.

Celebi, M.S., Computation of transient nonlinear ship waves using an

adaptive algorithm, J. Fluid Struct. 14 (2000) 281-301.

Celebi, M.S., H. Akyildiz, Nonlinear modeling of liquid sloshing in a moving rectangular tank, Ocean Eng. 29 (2002) 1527-1553.

Chapman, G.J.D., R. Porter, Second-order sloshing over an arbitrary bed, J. Fluid Mech, 524 (2005) 331-355.

Chen, B.F., H.W. Chiang, Complete 2D and Fully Nonlinear Analysis of Ideal Fluid in Tanks, J. Eng. Mech. 125 (1999) 70-78.

Chen, B.F., R. Nokes, Time-independent finite difference analysis of fully non-linear and viscous fluid sloshing in a rectangular tank, J. Comput. Phys. 209 (2005) 47-81.

Chen, B.F., C.H. Wu, Effects of excitation angle and coupled heave-surge-sway motion on fluid sloshing in a three-dimensional tank, J. Mar. Sci. Technol. 16 (2011) 22-50.

Chen, W., M.A. Haroun, F. Liu, Large amplitude liquid sloshing in seismically excited tanks, Earthq. Eng. Struct. D. 25 (1996) 653-669.

Chen, Y., W. Hwang, C. Ko, Sloshing behaviours of rectangular and cylindrical liquid tanks subjected to harmonic and seismic excitations, Earthq. Eng. Struct. D. 36 (2007) 1701-1717.

Chen, Y.G., K. Djidjeli, W.G. Price, Numerical simulation of liquid sloshing phenomena in partially filled tank, Comput. Fluids 38 (2009) 830-842.

Chern, M., et al, Pseudospectral solution of three-dimensional nonlinear sloshing in a shallow water rectangular tank, J. Fluid. Struct. 35 (2012) 160-184.

Chern, M., N. Vaziri, A.G.L. Borthwick, Fully non-linear simulation of second-order resonance in a three-dimensional tank using the PSME method. Appl. Ocean Res. 37 (2012) 22–32.

Chern, M.J., A.G.L. Borthwich, R. Eatock Taylor, A pseudo-spectral sigma-transformation model of 2D nonlinear waves, J. Fluid. Struct. 13 (1999) 607-630.

Chern, M.J., A.G.L. Borthwick, R. Eatock Taylor, Simulation of nonlinear free

surface motions in a cylindrical domain using a Chebyshev Fourier spectral collocation method, Int. J. Numer. Meth. Fluids 36 (2001) 465-496.

Chung, T.J., Computational Fluid Dynamics, Cambridge University Press, Cambridge, 2002.

Cointe, R., et al, Nonlinear and linear motions of a rectangular barge in a perfect fluid, 18th Symposium on Naval Hydrodynamics, 1990.

Cooker, M.J., Water waves in a suspended container, Wave Motion 20 (1994) 385-395.

Cummins, W.E., The impulse response function and ship motions, Schiffstechnik 9 (1962) 101-109.

Dai, L., L. Xu, A numerical scheme for dynamic liquid sloshing in horizontal cylindrical containers. Proc. IMechE Part D: J. Auto. Eng. 220 (2006) 901-918.

Damatty, A.A.E., A.M.I. Sweedan, Equivalent mechanical analog for dynamic analysis of pure conical tanks. Thin Wall. Struct. 44 (2006) 429-440.

Damattya, A.A.E., M.S. Saafana, A.M.I. Sweedan, Experimental study conducted on a liquid-filled combined conical tank model. Thin Wall. Struct. 43 (2005) 1398-1417.

Davis, C., The Principle of Least Action, Retrieved from http://www.idlex.freeserve.co.uk/idle/evolution/ref/leastact.html, 1998.

Dodge, F.T., The new 'dynamic behavior of liquids in moving containers', Tech. Rep. Southern Research Institute, San Antonio, Texas, 2000.

Dommermuth, D.G., D.K.P. Yue, Numerical sinulations of nonlinear axisymmetric flows with a free surface, J. Fluid Mech. 178 (1987) 195-219.

Faraday, M., On the forms and states of fluids on vibrating elastic surfaces, Philos. Trans. Roy. Soc. London 52 (1831) 319-340.

Faltinsen, O.M., A numerical non-linear method of sloshing in tanks with two-dimensional flow, J. Ship Res. 22 (1978) 193-202.

Faltinsen, O.M., et al, Multidimensional modal analysis of nonlinear sloshing in a rectangular tank with finite water depth, J. Fluid Mech. 407 (2000)

201-234.

Faltinsen, O.M., O.F. Rognebakke, A.N. Timokha, Resonant three-dimensional nonlinear sloshing in a square-base basin, J. Fluid Mech. 487 (2003) 1-42.

Faltinsen, O.M., O.F. Rognebakke, A.N. Timokha, Resonant three-dimensional nonlinear sloshing in a square base basin. Part 2. Effect of higher modes, J. Fluid Mech. 523 (2005) 199-218.

Faltinsen, O.M., A.N. Timokha, Adaptive Multimodal Approach to Nonlinear Sloshing in a Rectangular Tank. J. Fluid Mech. 432 (2001) 167-200.

Faltinsen, O.M., A.N. Timokha, Asymptotic modal approximation of nonlinear resonant sloshing in a rectangular tank with small fluid depth, J. Fluid Mech. 470 (2002) 319–357.

Faltinsen, O.M., A.N. Timokha, Sloshing, Cambridge University Press, New York, 2009.

Ferrant, P., Simulation of strongly nonlinear wave generation and wave-body interactions using a 3-D MEL model, 21st Symposium on Naval Hydrodynamics (1997) 93-108.

Firouz-Abadi, R.D., M. Ghasemi, H. Haddadpour, A modal approach to second-order analysis of sloshing using boundary element method. Ocean Eng. 38 (2011) 11–21.

Firouz-Abadi, R.D., H. Haddadpour, M. Ghasemi, Reduced order modeling of liquid sloshing in 3D tanks using boundary element method. Eng. Anal. Bound. Elem. 33 (2009) 750-761.

Frandsen, J.B., Sloshing motions in excited tanks, J. Comput. Phys. 196 (2004) 53-87.

Frandsen, J.B., Numerical predictions of tuned liquid tank structural systems, J. Fluid. Struct. 20 (2005) 309-329.

Frandsen, J.B., A.G.L. Borthwick, Simulation of sloshing motions in fixed and vertically excited containers using a 2-D inviscid σ-transformed finite difference solver, J. Fluid. Struct. 18 (2003) 197-214.

Gao, M., Numerical simulation of liquid sloshing in rectangular tanks using consistent particle method and experimental verification, National University of Singapore, Singapore, 2011.

Gavrilyuk, I., M. Hermann, I. Lukovsky, O. Solodun, A. Timokha, Natural sloshing frequencies in rigid truncated conical tanks, Eng. Computation. 25 (2008) 518-540.

Gavrilyuk, I.P., I.A. Lukovsky, A.N. Timokha, Linear and nonlinear sloshing in a circular conical tank, Fluid. Dyn. Res. 37 (2005) 399-429.

Gavrilyuk, I., et al, Multimodal method for linear liquid sloshing in a rigid tapered conical tank, Eng. Computation. 29 (2011) 198-220.

Gavrilyuk, I.P., et al, Weakly nonlinear sloshing in a truncated circular conical tank, Fluid Dyn. Res. 45 (2013) 1-30.

Gingold, R.A., J.J. Monaghan, Smoothed particle hydrodynamics - Theory and application to non-spherical stars, Mon Not R Astron Soc 181 (1977) 375-389.

Godderidge, B., S.R. Turnock, M. Tan, A rapid method for the simulation of sloshing using a mathematical model based on the pendulum equation, Comput. Fluids 57 (2012a) 163-171.

Godderidge, B., S.R. Turnock, M. Tan, Evaluation of a rapid method for the simulation of sloshing in rectangular and octagonal containers at intermediate filling levels, Comput. Fluids 57 (2012b) 1-24.

Gomez-Gesteira, M., B.D. Rogres, A.J.C. Crespo, State-of-the-art of classical SPH for free-surface flow, J. Hydraul. Res. 48 (2010) 6-27.

Greaves, D.M., A.G.L. Borthwick, G.X. Wu, R. Eatock Taylor, A moving boundary finite element method for fully nonlinear wave simulation, J. Ship Res. 41 (1997) 181–194.

Gui, F., S. Jiang, Numerical Simulation of Liquid Sloshing Problem under resonant excitation, Adv. Mech. Eng. 2014 (2014) 1-7.

Guyenne, P., S.T. Grilli, Numerical study of three-dimensional overturning waves in shallow water, J. Fluid Mech. 547 (2006) 361-388.

Hasheminejad, S.M., A. Mostafa, Transient sloshing in half-full horizontal elliptical tanks under lateral excitation. J. Sound. Vib. 330 (2011) 3507-3525.

Hashimoto, H., M. Sueyoshi, Numerical Simulation Method for a Coupling Motion of Ship and Tank Fluid, 25th IWWWFB, 2010.

Hernandez-Barrios, H., E. Heredia-Zavoni, A.A. Aldama-Rodriguez, Nonlinear sloshing response of cylindrical tanks subjected to earthquake ground motion, Eng. Struct. 29 (2007) 3364-3376.

Herczynski, A., P.D. Weidman, Experiments on the periodic oscillation of free containers driven by liquid sloshing, J. Fluid Mech. 693 (2012) 216-242.

Hirt, C.W., B.D. Nichols, Volume of Fluid (VOF) method for the dynamics of free boundaries, J. Comput. Phys. 39 (1981) 201-225.

Huang, S., W. Duan, H. Zhang, A Coupled Analysis of Nonlinear Sloshing and Ship Motion, J. Marine Sci. Appl. 11 (2012) 427-436.

Hulme, A., The wave forces acting on a floating hemisphere undergoing forced periodic oscillations. J. Fluid Mech. 121 (1982) 443-463.

Ibrahim, R.A., Liquid Sloshing Dynamics: Theory and Applications, Cambridge University Press, Cambridge, 2005.

Ibrahim, R.A., Recent advances in physics of fluid parametric sloshing and related problems, J. Fluid Eng. - T. ASME 137 (2015) 090801-52.

Ibrahim, R.A., M.A. EL-Sayad, Simltaneous parametric and internal resonances in systems involving strong nonlinearities, J. Sound Vib. 225 (1999) 857-885.

Ikeda, T., N. Nakagawa, Non-linear vibrations of a structure caused by water sloshing in a rectangular tank, J. Sound Vib. 201 (1997) 23-41.

International Gas Union (IGU), News, views and knowledge on gas-worldwide, World LNG report-2013 edition, 2014.

Jiang, S., et al, Numerical simulation of coupling effect between ship motion and liquid sloshing under wave action, Ocean Eng. 108 (2015) 140-154.

Kashiwagi, M., M. Inada, T. Momoda, A time-domain nonlinear simulation method for wave-induced motions of a floating body, J. Jpn. Soc. Nav. Archit.

Ocean Eng. 184 (1998) 139-148.

KBR, Floating LNG, 2016, https://kbr.com/Documents/Brochures /2016_FLNG_brochure_3-22.pdf#search=FLNG

Khayyer, A., H. Gotoh, A higher order Laplacian model for enhancement and stabilization of pressure calculation by the MPS method, Appl. Ocean Res. 32 (2010) 124-131.

Kim, Y., A numerical study on sloshing flows coupled with ship motion: the anti-rolling tank problem, J. Ship Res. 46 (2002) 52-62.

Kim, Y., et al, Study on coupling effects of ship motion and sloshing, Ocean Eng. 34 (2007) 2176-2187.

Kim, M., et al, A spectral method for free surface flows of inviscid fluids, Int. J. Numer. Meth. Fluids 28 (1998) 887-902.

Kishev, Z.R., C. Hu, M. Kashiwagi, Numerical simulation of violent sloshing by a CIP-based method, J. Mar. Sci. Technol. 11 (2006) 111-122.

Koo, W., Fully nonlinear wave-body interactions by a 2D potential numerical wave tank, Texas A&M University, 2003.

Koo, W., M. Kim, Freely floating-body simulation by a 2D fully nonlinear numerical wave tank, Ocean Eng. 31 (2004) 2011-2046.

Koshizuka, S., A. Nobe, Y. Oka, Numerical analysis of breaking waves using the moving particle semi-implicit method, Int. J. Numer. Meth. Fluids 26 (1998) 751-769.

Koshizuka, S., Y. Oka, Moving-particle semi-implicit method for fragmentation of incompressible fluids, Nucl. Sci. Eng. 123 (1996) 421-434.

Koshizuka, S., H. Tamako, Y. Oka, A particle method for incompressible viscous flow with fluid fragmentations, Comput. Fluid D. 4 (1995) 29-46.

Kubo, M., N. Shimoda, S. Okamoto, The time domain analysis on moored ship motions, 21st International Conference on Coastal Engineering, ASCE, Costa del Sol-Malaga, Spain, 1989.

La Rocca, M., G. Sciortino, M.A. Boniforti, A fully nonlinear model for sloshing in a rotating container. Fluid Dyn. Res. 27 (2000) 23-52.

La Rocca, M., G. Sciortino, M.A. Bonifortib, Interfacial gravity waves in a two-fluid system. Fluid Dyn. Res. 30 (2002) 31-66.

La Rocca, M., et al, Experimental and theoretical investigation on the sloshing of a two-liquid system with free surface. Phys. Fluids 17 (2005) 062101.

Lamb H., Hydrodynamics, Cambridge University Press, Cambridge, 1945.

Lee, B., et al, Step-by-step improvement of MPS method in simulating violent free-surface motions and impact-loads. Comput. Methods Appl. Mech. Engrg. 200 (2011) 1113-1125.

Lee, S.J., The effects of LNG-sloshing on the global responses of LNG-carriers, Texas A&M University, Texas, 2008.

Lee, S.J., et al, The effects of LNG-tank sloshing on the global motions of LNG carriers, Ocean Eng. 34 (2007) 10-20.

Lee, S.J., M.H. Kim, The effects of inner-liquid motion on LNG vessel responses, J. Offshore Mech. Arct. 132 (2010) 021101-8.

Li, Y., et al, Simulation of tank sloshing based on OpenFOAM and coupling with ship motions in time domain, J. Hydrodyn. 24 (2012) 450-457.

Liu, D., P. Lin, A numerical study of three-dimensional liquid sloshing in tanks. J. Comput. Phys. 227 (2008) 3921-3939.

Liu, Z., Y. Huang, A New Method For Large Amplitude Sloshing Problems. J. Sound Vib. 175 (1994) 185-195.

Livaoglu, R., Investigation of seismic behavior of fluid rectangular tank-soil foundation systems in frequency domain. Soil Dyn. Earthq. Eng. 28 (2008) 132-146.

Longuet-Higgins, M.S., C.D. Cokelet, The deformation of steep surface waves on water: I. A numerical method of computation. Proc. R. Sco. Lond. A 19 (1976) 235-249.

Love, J.S., M.J. Tait, Non-linear multimodal model for tuned liquid dampers of arbitrary tank geometry. Int. J. Nonlinear Mech. 46 (2011) 1065-1075.

Love, J.S., M.J. Tait, Nonlinear multimodal model for TLD of irregular tank geometry and small fluid depth. J. Fluid. Struct. 43 (2013) 83-99.

Lucy, L., A numerical approach to the testing of fusion process. J. Astronomical 82 (1977) 1013-1024

Lukovsky, I.A., A.N. Timokha, Modal Modeling of Nonlinear Fluid Sloshing in Tanks with Non-Vertical Walls Non-Conformal Mapping Technique. Inter. J. Fluid. Mech. Res. 29 (2002) 216-242.

Ma, Q., Numerical simulation of nonlinear interaction between structures and steep waves, University College London, London, 1998.

Ma, Q.W., S. Yan, QALE-FEM for numerical modelling of non-linear interaction between 3D moored floating bodies and steep waves, Int. J. Numer. Meth. Engng. 78 (2008) 713-756.

Malenica, S., M. Zalar, X.B. Chen, Dynamic coupling of seakeeping and sloshing, 13th ISOPE, Hawaii, USA, 2003.

Mantic, V., A new formula for the C-matrix in the Somigliana identity, J. Elasticity 33 (1993) 191-201.

Marsh, A., et al, A numerical investigation of energy dissipation with a shallow depth sloshing absorber. Appl. Math. Model. 34 (2010) 2941-2957.

Marsh, A., M. Prakash, E. Semercigila, O. Turana, A study of sloshing absorber geometry for structural control with SPH. J. Fluid. Struct. 27 (2011) 1165-1181.

Matthiessen, L., Acoustic experiments concerning the smallest transverse waves of liquids(in German), Annalen der Physik 134 (1868) 107–117

McIver, P., 1989. Sloshing frequencies for cylindrical and spherical containers filled to an arbitrary depth. J. Fluid Mech. 201 (1989) 243-257.

Mei, C.C., The applied dynamics of ocean surface waves, World Scientific, Singapore, 1989.

Mitra, S., P.P. Upadhyay, K.P. Sinhamahapatra, Slosh dynamics of inviscid fluids in two-dimensional tanks of various geometry using finite element method. Int. J. Numer. Meth. Fluids. 56 (2008) 1625–1651.

Mitra, S., et al, A 3D fully coupled analysis of nonlinear sloshing and ship motion, Ocean Eng. 39 (2012) 1-13.

Modaressi-Tehrani, K., S. Rakheja, I. Stiharu, Three-dimensional analysis of transient slosh within a partly-filled tank equipped with baffles. Vehicle Syst Dyn. 45 (2007) 525-548.

Molin, B., et al, LNG-FPSO's: frequency domain, coupled analysis of support and liquid cargo motion, IMAM Conference, Rethymnon, Greece, 2002

Molin, B., Hydrodynamique des structures offshore (in Chinese), National Defence Industry Press, Beijing, 2010.

Monaghan, J.J., Simulating Free Surface Flows with SPH. J. Comput. Phys. 110 (1994) 399-406.

Murakami, Y., M. Chikano, Two-dimensional direct numerical simulation of parametrically excited surface waves in viscous fluid, Phys. Fluids 13 (2001) 65-74.

Nakayama, T., K. Washizu, Nonlinear analysis of liquid motion in a container subjected to forced pitching oscillation. Int. J. Numer. Meth. Eng. 15 (1980) 1207-1220.

Nakayama, T., K. Washizu, The boundary element method applied to the analysis of two-dimensional nonlinear sloshing problems. Int. J. Numer. Meth. Eng. 17 (1981) 1631-1646.

Nam, B.W., Y. Kim, D.W. Kim, Nonlinear effects of sloshing flows on ship motion, 21th IWWWFB, 2006.

Newman, J.N., Transient axisymmetric motion of a floating cylinder, J. Fluid Mech. 157 (1985) 17-33.

Newman, J.N., Wave effects on vessels with internal tanks, 20th IWWWFB, Norway, 2005.

Ning, D., W. Song, Y. Liu, B. Teng, A boundary element investigation of liquid sloshing in coupled horizontal and vertical excitation. J. Appl. Math. 2012 (2012) 1–20.

Ogilvie, T. F., Recent progress toward the understanding and prediction of ship motions, 5th Symposium on Naval Hydrodynamics, 1964.

Okamato, T., M. Kawahara, Two-dimensional sloshing analysis by lagrangian

finite element method. Int. J. Numer. Meth. Fluids 11 (1990) 453-477.

Pal, P., S.K. Bhattacharyya, Sloshing in partially filled liquid containers-Numerical and experimental study for 2-D problems. J. Sound Vib. 329 (2010) 4466-4485.

Pan, X., H. Zhang, X. Sun, Numerical simulation of sloshing with large deforming free surface by MPS-LES method. China Ocean Eng. 26 (2012) 653-668.

Pilipchuk, V.N., R.A. Ibrahim, The dynamics of a non-linear system simulating liquid sloshing impact in moving structures. J. Sound Vib. 205 (1997) 593-615.

Ramaswamy, B., Numerical simulation of unsteady viscous free surface flow. J. Comput. Phys. 90 (1990) 396-430.

Rayleigh, J.W.S., On the crispations of fluid resting upon a vibrating support, Phil. Mag. 15 (1883) 229-235

Rognebakke, O.F., O.M. Faltinsen, Coupling of sloshing and ship motions, J. Ship Res. 47 (2003) 208-221.

Rognebakke, O.F., O.M. Faltinsen, Effect of sloshing on ship motions, 16th IWWWFB, 2001.

Rudman, M., P.W. Cleary, Modelling sloshing in LNG tanks, in 7th International Conference on CFD in the Minerals and Process Industries, CSIRO, Melbourne, Australia, 2009.

Santos, C.M.P.S., D.M. Greaves, A mixed Lagrangian-Eulerian method for non-linear free surface flows using multigrid on hierarchical Cartesian grids. Comput. Fluids 36 (2007) 914-923.

Sriram, V., S.A. Sannasiraj, V. Sundar, Simulation of 2-D nonlinear waves using finite element method with cubic spline approximation. J. Fluid. Struct. 22 (2006) 663-681.

Shao, J.R., et al, An improved SPH method for modeling liquid sloshing dynamics. Comput. Struct. 100-101 (2012) 18-26.

Shrimali, M.K., R.S. Jangid, Earthquake response of isolated elevated liquid

storage steel tanks. J. Constr. Steel Res. 59 (2003) 1267-1288.

Shrimali, M.K., R.S. Jangid, Non-linear seismic response of base-isolated liquid storage tanks to bi-directional excitation. Nucl. Eng. Des. 217 (2002a) 1-20.

Shrimali, M.K., R.S. Jangid, Seismic response of liquid storage tanks isolated by sliding bearings. Eng. Struct. 24 (2002b) 909-921.

Souto-Iglesias, A., L. Perez-Rojas, R. Zamora-Rodriguez, Simulation of anti-roll tanks and sloshing type problems with smoothed particle hydrodynamics. Ocean Eng. 31 (2004) 1169-1192.

Souto-Iglesias, A., et al, Liquid moment amplitude assessment in sloshing type problems with smooth particle hydrodynamics. Ocean Eng. 33 (2006) 1462-1484.

Sussman, M., P. Smereka, S. Osher, A level set approach for computing solutions to incompressible two-phase flow. J. Comput. Phys. 114 (1994) 146-159.

Takizawa, A., S. Koshizuka, Generalization of physical component boundary fitted co-ordinate (PCBFC) method for the analysis of free-surface flow. Int. J. Numer. Meth. Fluids 15 (1992) 1213-1237.

Tanizawa, K., A nonlinear simulation method of 3-D body motions in waves, J. Jpn. Soc. Nav. Archit. Ocean Eng. 178 (1995) 179-191.

Tanizawa, K., The state of the art on numerical wave tank, in 4th Osaka Colloquium on Seakeeping Performance of Ships, Osaka, Japan, 2000.

Turnbull, M.S., A.G.L. Borthwick, R. Eatock Taylor, Numerical wave tank based on a -transformed finite element inviscid flow solver. Int. J. Numer. Meth. Fluids 42 (2003a) 641-663.

Turnbull, M.S., A.G.L. Borthwick, R.E. Taylor, Wave-structure interaction using coupled structured-unstructured finite element meshes. Appl. Ocean Res. 25 (2003b) 63-77.

Turner, M.R., T.J. Bridges, Nonlinear energy transfer between fluid sloshing and vessel motion, J. Fluid Mech. 719 (2013) 606-636.

Turner, M.R., H. Alemi Ardakani, T.J. Bridges, Instability of sloshing motion in a vessel undergoing pivoted oscillations, J. Fluid. Struct. 52 (2015) 166-180.

Turner, M.R., T.J. Bridges, H. Alemi Ardakani, Dynamic coupling in Cooker's sloshing experiment with baffles, Phys. Fluids 25 (2013) 112102.

Ursell, F., Irregular frequencies and the motion of floating bodies, J. Fluid Mech. 105 (1981) 143–156

Ushijima, S., Three-dimensional arbitrary Lagrangian–Eulerian numerical prediction method for non-linear free surface oscillation. Int. J. Numer. Meth. Fluids 26 (1998) 605-623.

Van Daalen, Numerical and theoretical studies of water waves and floating bodies, University of Twente, Netherlands, 1993.

Vinji, T., P. Brevig, Numerical simulation of breaking wave, 3rd International Conference on Finite Elements in Water Resources, 1981.

Wang, X., M. Arai, Research on computational method of coupled ship motions and sloshing, J. Jpn. Soc. Nav. Archit. Ocean Eng. 14 (2011) 97-104.

Wang, C.Z., B.C. Khoo, Finite element analysis of two-dimensional nonlinear sloshing problems in random excitations. Ocean Eng. 32 (2005) 107-133.

Wang, C.Z., G.X. Wu, Analysis of second-order resonance in wave interactions with floating bodies through a finite-element method. Ocean Eng. 35 (2008) 717–726.

Wang, C.Z., G.X. Wu, Interactions between fully nonlinear water waves and cylinder arrays in a wave tank, Ocean Eng. 37 (2010) 400-417.

Wang, C.Z., G.X. Wu, B.C. Khoo, Fully nonlinear simulation of resonant motion of liquid confined between floating structures. Comput. Fluids 44 (2011) 89–101.

Watai, R.A., A time-domain boundary elements method for the seakeeping analysis of offshore systems, University of Sao Paulo, Sao Paulo, 2015.

Wright, J., S. Yon, C. Pozrikidis, Numerical studies of two-dimensional Faraday oscillations of inviscid fluids, J. Fluid Mech. 402 (2000) 1-32.

Wu, C., B. Chen, Sloshing waves and resonance modes of fluid in a 3D tank

by a time-independent finite difference method. Ocean Eng. 36 (2009) 500-510.

Wu, G.X., Second-order resonance of sloshing in a tank. Ocean Eng. 34 (2007) 2345-2349.

Wu, G.X., R. Eatock Taylor, Finite element analysis of two-dimensional non-linear transient water waves. Appl. Ocean Res. 16 (1994) 363-372.

Wu, G.X., R. Eatock Taylor, Transient motion of a floating body in steep water waves, 11th IWWWFB, 1996.

Wu, G.X., R. Eatock Taylor, D.M. Greaves, Viscous effect on the transient free surface flow in a two dimensional tank. J. Eng. Math. 40 (2001) 77-90.

Wu, G.X., Z.Z. Hu, Simulation of nonlinear interactions between waves and floating bodies through a finite-element-based numerical tank, Proc. R. Soc. A 460 (2004) 2797-2817.

Wu, G.X., Q.W. Ma, R. Eatock Taylor, Numerical simulation of sloshing waves in a 3D tank based on a finite element method. Appl. Ocean Res. 20 (1998) 337-355.

Xue, M., et al, Computations of fully nonlinear three-dimensional wave-wave and wave-body interactions. Part 1. Dynamics of steep three-dimensional waves, J. Fluid Mech. 438 (2001) 11-39.

Yang, C., R. Lohner, H. Lu, An unstructured-grid based volume-of-fluid method for extreme wave and freely-floating structure interactions, Conference of Global Chinese Scholars on Hydrodynamics, 2006.

Yu, J., Effects of finite water depth on natural frequencies of suspended water tanks, Stud. Appl. Math. 125 (2015) 337-391.

Zhang, H., Wu P., Yue W., The analysis of second-order sloshing resonance in a 3D tank. J. Hydrodyn. 26 (2014) 309-315.

Zhao, W., J. Yang, Z. Hu, L. Tao, Coupled analysis of nonlinear sloshing and ship motions, Appl. Ocean Res. 47 (2014) 85-97.

Zhao, W., J. Yang, Z. Hu, Y. Wei, Recent developments on the hydrodynamics of floating liquid natural gas (FLNG), Ocean Eng. 38 (2011)

1555-1567.

Zhou, H., J.F. Li, T.S. Wang, Simulation of liquid sloshing in curved-wall containers with arbitrary Lagrangian-Eulerian method. Int. J. Numer. Meth. Fluids. 57 (2008) 437-452.

Zhu, T., J. Zhang, S.N. Atluri, A meshless local boundary integral equation (LBIE) method for solving nonlinear problemd. Comput. Mech. 22 (1998) 174-186.